University of Wollongong
Research Online

University of Wollongong Thesis Collection 2017+
University of Wollongong Thesis Collections

2022

3D Printing StarPore® for Bone Tissue Engineering

Jeremy Nicolas Dinoro

Follow this and additional works at: https://ro.uow.edu.au/theses1

University of Wollongong

Copyright Warning

You may print or download ONE copy of this document for the purpose of your own research or study. The University does not authorise you to copy, communicate or otherwise make available electronically to any other person any copyright material contained on this site.

You are reminded of the following: This work is copyright. Apart from any use permitted under the Copyright Act 1968, no part of this work may be reproduced by any process, nor may any other exclusive right be exercised, without the permission of the author. Copyright owners are entitled to take legal action against persons who infringe their copyright. A reproduction of material that is protected by copyright may be a copyright infringement. A court may impose penalties and award damages in relation to offences and infringements relating to copyright material. Higher penalties may apply, and higher damages may be awarded, for offences and infringements involving the conversion of material into digital or electronic form.

Unless otherwise indicated, the views expressed in this thesis are those of the author and do not necessarily represent the views of the University of Wollongong.

Research Online is the open access institutional repository for the University of Wollongong. For further information contact the UOW Library: research-pubs@uow.edu.au

3D Printing StarPore® for Bone Tissue Engineering

Jeremy Nicolas Dinoro
BSc MPhil MSc

This thesis is presented as part of the requirements for the conferral of the degree:
Doctor of Philosophy

Supervisor(s):
Zhilian Yue, Stephen Beirne, Gordon Wallace

The University of Wollongong
Intelligent Polymer Research Institute

August 2022

This research has been conducted with the support of an Australian Government Research Training Program Scholarship and Anatomics Pty Ltd.

Declaration

I, Jeremy Nicolas DiNoro, declare that this thesis is submitted in partial fulfilment of the requirements for the conferral of the degree of Doctor of Philosophy, from the University of Wollongong, is wholly my own work unless otherwise referenced or acknowledged. This document has not been submitted for qualifications at any other academic institution.

Jeremy Nicolas DiNoro

August 22, 2022

Acknowledgements

First and foremost I would like to thank my parents and their parents for the sacrifices they have made to provide me with a fulfilling life full of love, joy and happiness. My achievements and accomplishments are as much theirs as they are mine, they are nothing without you.

I would also like to thank my academic supervisors, Professor Gordon Wallace, Associate Professor Stephen Beirne and Dr. Zhilian Yue, for the opportunity to conduct research in world-class facilities, their ongoing encouragement, support and invaluable perspicacity.

This research was conducted with the support of an Australian Research Council Industrial Transformation Training Centre in Additive Biomanufacturing (ARC ITTC ABM) Scholarship, and Anatomics Pty Ltd. The support from Anatomics, specifically Dr Phillip Lewis and Robert Thompson, has provided exceptional insights into the translational aspects of research, inherently shaping the direction of this work for real-world applications.

Collaborators from the Biofabrication & Tissue Morphology Group (Queensland University of Technology, Brisbane) Dr Naomi Paxton and Professor Mia Woodruff literally gave this work meaning. It's an understatement to say I am merely grateful for the opportunity to use this printing platform to generate implants. The direction and outcomes provided by the work you conducted genuinely shaped the whole project.

A significant portion of this work would not have been achievable without the deep insight from fellow students and colleagues at the University of Wollongong's Innovation Campus (IC) – both the Intelligent Polymer Research Institute (IPRI) and Australian National Fabrication Facility (ANFF) - within the Australian Institute for Innovative Materials Centre (AIIM) and The Translational Research Initiative for Cell Engineering and Printing (TRICEP) to everyone, you know who you are, I thank you.

In no specific order, I would like to thank Benjamin Fillipi, Kuan Phang Chan, Daniel Lawrence, Josh Daniher, Malachy Maher, Sam Findlay, Elvis Smugreski, Dr Dave Shepherd, Dr Patricia Hayes, Dr Sepidar Sayar, Dr Sepehr Talebian and Ali Jeiranikhameneh for their expertise with all the tools, insights, techniques and technical training involved in this work.

Publications

DiNoro, J.N., Paxton, N.C., Skewes, J., Yue, Z., Lewis, P.M., Thompson, R.G., Beirne, S., Woodruff, M.A. and Wallace, G.G., 2022. Laser Sintering Approaches for Bone Tissue Engineering. Polymers, 14(12), p.2336.

Paxton, N.C., **DiNoro, J.N**, Ren, J., Ross, M.T., Daley, R., Zhou, R., Bazaka, K., Thompson, R.G., Yue, Z., Beirne, S. and Harkin, D.G., 2021. Additive manufacturing enables personalised porous high-density polyethylene surgical implant manufacturing with improved tissue and vascular ingrowth. Applied Materials Today, 22, p.100965.

In preparation for Submission

DiNoro, J.N, Paxton, NC, Chan, KP, Lewis, P.M, Thompson RG, Yue Z, Beirne S, Woodruff MA, Wallace GG. Sintering star-shaped HDPE particles towards additive manufacturing patient-specific implants.

Abstract

Since the advent of Tissue Engineering (TE) in the late 1980's, significant progress has been made within the biomedical landscape. A recently established branch within TE is biofabrication, a field that aims to automate the fabrication of biologically functional materials through the use of additive manufacturing or three-dimensional (3D) printing, among other techniques. Additive manufacturing offers fine control over part porosity, with the capacity to match the complex internal architecture of human bone. Coupled with clinical 3D scanning techniques, 3D printing has the capacity to generate implants that accurately match defected areas. However, due to the limited number of regulatory approved devices for human implantation and high cost of sophisticated powder bed fusion printers, the printing techniques are restricted.

To be compatible with regulatory requirements, this work aims to utilise a widely accessible and regulatory approved device, high-density polyethylene (HDPE) to generate bone substitutes. HDPE in the form of StarPore® supplied by industry collaborator Anatomics Pty Ltd, a three-pronged star or trilobal shape, is an established material approved by both the Federal Drug Administration (FDA) in the United States of America and the Therapeutic Goods Administration (TGA) in Australia as a bone substitute for human implantation.

To mitigate printer accessibility constraints, a modular system was developed to interface with commercially available laser engravers. The recoater allows for the homogenous distribution of powder layers onto a heated print bed, with adjustable recoating velocity, feed rate, layer height and blade design. Once a thin layer of StarPore® has been spread across the build area, the laser engraver scans a pattern to selectively fuse adjacent powder particles together and is followed by redistribution of powder above the scanned layer. The laser then repeats a scanning of a cross section, fusing to the previous layer, this continues until a 3D object is realised. This process, part of powder bed fusion, is called SLS.

A range of physicochemical measurements were used to assess StarPore® printability in the context of SLS. Thermogravimetric analysis revealed no significant thermal polymer degradation below typical printing temperatures, nor over an extended timescale of two hours, typical printing duration. Differential scanning calorimetry showed a narrow ‘sintering window’ in which the polymer has to remain for efficient particle coalescence. A theoretical sintering model served as a template for establishing scan parameters, such as laser power, scan velocity, hatch spacing and layer height. *In situ* thermal imaging was used to decipher optimal scanning strategy for homogenous energy distribution throughout the powder bed. Physical characterisation through micro computed tomography revealed porosities ranging from 77 - 84 % in printed constructs, when compared to 55 % in conventionally moulded StarPore®. The compressive and tensile modulus of printed constructs were also found to be 12 - 28 % the strength of the moulded implants, with slight improvements observed through the use of a slurry-based sintering process. Biologically however, printed scaffolds led to a four-fold increase in tissue ingrowth following an 8-week subcutaneous implantation in rats, when compared to existing market products.

This work serves as a template for the future development of a range of custom 3D printing platforms. With the progress of materials research, along with rapid developments in 3D scanning technologies, methods such as those outlined in this work may provide the tools to enable scientists, engineers and clinicians to generate patient-specific implants of the future.

Abbreviations

HA	Hydroxyapatite
NP	Nanoparticle
SLS	Selective Laser Sintering
SLM	Selective Laser Melting
HT-LS	High-temperature Laser Sintering
FDM	Fused Deposition Modelling
2D	Two Dimensional
3D	Three Dimensional
TE	Tissue Engineering
BMP	Bone Morphogenetic Protein
TCP	Tricalcium Phosphate
PE	Polyethylene
HDPE	High-density Polyethylene
LDPE	Low-density Polyethylene
UHMWPE	Ultra-high Molecular Weight Polyethylene
PA	Polyamide
PCL	Polycaprolactone
ED	Energy Density
IR	Infrared
FDA	Federal Drug Administration
ISO	International Organisation for Standardisation
DAPI	4',6-Diamidino-2-Phenylindole
BG	Bioglass
MSC	Mesenchymal Stem Cell
ADSC	Adipose Derived Stem Cell
μCT	Micro-computed Tomography
CT	Computed Tomography
MRI	Magnetic Resonance Imaging
DSC	Differential Scanning Calorimetry
TGA	Thermogravimetric Analysis
FT-IR	Fourier Transform Infrared
SEM	Scanning Electron Microscopy
SBF	Simulated Body Fluid
SD	Standard Deviation
HR	Hauser Ratio

"Science is more than a body of knowledge.
It is a way of thinking; a way of sceptically
interrogating the universe with a fine
understanding of human fallibility.

If we are not able to ask sceptical questions,
to interrogate those who tell us that something is true,
to be sceptical of those in authority, then,
we are up for grabs for the next charlatan
(political or religious) who comes rambling along."

- Carl Sagan

"The master has failed more times
than the beginner has even tried."

- Stephen McCranie

List of Figures

group B after 2, 4, and 8 weeks of surgery (SM: scaffold material; NB: new bone; MB: mature bone). (f) Quantitative analysis of new bone (*P < 0.05, **P < 0.01). Adapted from [157].

Figure 2.1 Timeline of the impacts on a polymer’s physical properties during the SLS process.

Figure 2.2 Thermal camera (FLIR C2) set up for monitoring StarPore® sintering. The usb cable was routed through a hole in the laser cutter to a windows PC that was used to record IR video in real-time.

Figure 2.3 (a) Render ULS laser engraver [206], (b) Render of the K40 system [207], (c) & (d) Solidworks renders of the front and rear of the recoating system.

Figure 2.4 (a) Render of the recoater with labelled components, scale bar = 20 mm, (b) Ultimaker V 1.5.7 board, (c) Arduino Uno board.

Figure 2.5 (a) Render of the recoater with labelled components, scale bar = 20 mm, (b) Ultimaker V 1.5.7 board, (c) (d) Exhaust port adaptor from 5 inch to 6 inch.

Figure 2.6 Schematic of laser path and re-coating schematic, with an outline of the laser path through StarPore®.

Figure 2.7 (A) Particle size distribution as a weight percentage of 20g batches, where n=5 (red represents the standard deviation). (B) Scanning Electron Microscope image of the face (left) and depth (right) of a typical StarPore® particle, where yellow = arm width, blue = arm length, green = body area and pink is the particle depth, where n = 50.

Figure 2.8 Recoating bed density at a layer thickness of 0.5 mm (a), 0.75 mm (b) and 1 mm (c) as a function of blade speed, given as average ∓ S.D. where n = 10.

Figure 2.9 Theoretical sintering simulations (a) Laser power in watts as a function of speed in mm/s, at room temperature with a layer height of 0.75 mm and beam diameter or spot size of 127 μm (b) Laser power in watts as a function of single layer height of powder in mm, at room temperature with a beam diameter or spot size of 127 μm (c) Laser power in watts as a function of laser beam diameter or laser spot size in mm, simulated with a layer height of 0.75 mm, at room temperature and scan speed of 57 mm/s (d) Laser power in watts as a function of build chamber temperature, simulated with a layer height of 0.75 mm, at room temperature and scan speed of 57 mm/s and a spot size of 127 μm.

Figure 2.10 (a) Thermogravimetric Analysis of HDPE. (b) Thermogravimetric Analysis isotherm of HDPE over 2 hours at 200 °C.

Figure 2.11 Cycling DSC measurements of StarPore® accompanied by the defined melting temperature (red) and the recrystallisation temperature (blue).

Figure 2.12 In situ microscopy images of StarPore® particles, scale bar = 500 µm.

Figure 2.13 (a) 3D model of a single sintered strut re-constructed from micro CT imaging, scanned at 18 watts, 100 mm/s, with a 127 µm beam diameter at room temperature, (b) strut thickness (mm) as a function of laser speed (mm/s) and (c) strut thickness (mm) as a function of porosity (% void space calculated within the strut).

Figure 2.14 Schematic of (a) & (b) uni-directional scanning strategy, where 10 lines are scanned horizontally, then vertically at 1 mm spacing over 10 x 10 mm. (c) IR camera images of 4 scanned 10 x 10 mm regions of StarPore®, with associated heat map range, scale bar = 5 mm. (d) & (e) are the schematics of the bi-directional scanning strategy where 10 lines are scanned continuously, first vertically, then vertihorizontalled at 1 mm spacing over 10 x 10 mm and (f) IR camera images of 4 scanned 10 x 10 mm regions of StarPore®, with associated heat map range, scale bar = 5 mm.

Figure 2.15 (a) Light microscopy images of a range of StarPore® powder beds following laser exposure (i) shows slightly adhered particles, (ii) sintered particles, (iii) partially molten particles and (iv) completely molten bed, scale bar = 500 µm. (b) Heat maps determined by real-time IR camera images during scanning at a range of energy densities with (v) corresponding heatmap temperatures, where n = 5. (c) A comparison of bed coalescence with 0.5 mm hatch spacing with (d) 0.75 mm hatch spacing and (e) 1 mm hatch spacing. Printing was conducted with 2 watt laser energy and 10 mm/s scan velocity increments, where n = 3.

Figure 2.16 (a) Roughness profile of dual layer printed StarPore® scaffolds 20 x 20 above the second deposited layer, printed in a dry state without heating (1), printed in a slurry state without substrate heating (2), printed in a slurry with substrate heating (3), printed in a slurry state with substrate heating with dual laser passes (4) and printed in a slurry state with substrate heating with triple laser passes. (b) In situ optical images taken to determine polymer behaviour during sintering in , scale bar = 2 mm.

Figure 2.17 Transmittance infrared spectra of neat HDPE and HDPE following laser exposure, measured through ATR. Spectra were vertically shifted for comparison .

Figure 3.1 Hierarchical structure of human bone, from the macroscopic down to the nanoscale components. Adapted from [283].

Figure 3.2 Schematic of the dimensions of the dumbbell die used to cut tensile samples, in line with ASTM D638-82 (Type IV).

Figure 3.3 The influence of SLS energy density on scaffold porosity, the green region (a) corresponds to adhered particles with high porosity, the yellow region (b) relates to homogeneous particle coalescence and (c) represents over sintering and caking. Scaffolds were printed with the following parameters laser energy 18W, laser velocity 20 mm/s

List of Tables

Table of Contents

CHAPTER 1

PRINTING BONE

Chapter 1: Printing Bone

Overview

The research described in this dissertation was conducted in collaboration with Anatomics Pty Ltd (Melbourne, Victoria) and the Biofabrication & Tissue Morphology Group (Queensland University of Technology, Brisbane) as part of the Australian Research Council Industrial Transformation Training Centre in Additive Biomanufacturing (ARC ITTC ABM).

Portions of this chapter have been published in the following article:

DiNoro, J.N., Paxton, N.C., Skewes, J., Yue, Z., Lewis, P.M., Thompson, R.G., Beirne, S., Woodruff, M.A. and Wallace, G.G., 2022. Laser Sintering Approaches for Bone Tissue Engineering. Polymers, 14(12), p.2336.

Author Contributions: Conceptualization, investigation, writing—original draft preparation, J.N.D.; Conceptualization, investigation, writing—original draft preparation, N.C.P.; writing—original draft preparation, J.S.; writing—review and editing, supervision, Z.Y.; writing—review and editing, supervision, funding acquisition, P.M.L.; writing—review and editing, supervision, funding acquisition, R.G.T.; writing—review and editing, supervision, funding acquisition S.B.; writing—review and editing, supervision, funding acquisition, M.A.W.; supervision, funding acquisition, G.G.W. All authors have read and agreed to the published version of the manuscript.

1.1 Motivation

Currently, bone related diseases, such as osteoporosis, osteopenia and bone fractures cost the Australian healthcare system $3.44 billion dollars annually [1]. This cost is expected to increase with the growing ageing population and a shift towards sedentary lifestyles. The gold standard for many bone implants involves the use of autologous bone grafting or autografts, where bone is taken from other parts of the patient and used to replace the defect. More recently, alloplastic implants have been used to circumvent some of the shortcomings of autografts such as dual interventions, pain and high infection rates. While alloplasts are a useful alternative to traditional grafting techniques, they fail to match the physical and biological characteristics of native bone [2]. In recent times, additive manufacturing has emerged as a promising technology to fabricate patient-specific implants in biomedicine. As the techniques continue to develop, so does our understanding of the relationship between engineering, chemistry and biology. The translation of new printers and novel materials into the clinic will ensure medical advances can be delivered directly to patients. This dissertation presents the development of a novel additive manufacturing or 3D printing technique for the generation of patient-specific implants.

1.2 Context

The work is based on a polymeric material developed by Anatomics and the Commonwealth Scientific and Industrial Research Organisation called StarPore®. Made from high-density polyethylene (HDPE), an established implant material with over three decades of use in facial augmentation (Fig. 1.1 a) or even as human ears (Fig. 1.1 b), StarPore® is dye extruded into a novel trilobular shape (Fig. 1.1 c) to more accurately match the porosity of human bone. Implants made from StarPore® are fabricated through a vibrational injection moulding technique that densely packs particles into a custom silicon or nylon mould and gradually heats them to fuse it all together. Instead of manufacturing implants with a mould, this work aimed to investigate the use of these particles in additive manufacturing.

Figure 1.1 (a) StarPore® cranial implant placed within a human skull model, scale bar = 10 mm, (b) StarPore® human ear implant, scale bar 25 mm, (c) StarPore® trilobal HDPE particles used within the implant, scale bar = 1 mm.

1.3 Introduction and Literature Review

Scaffolds for tissue engineering have historically been used as structures to support cell attachment, vascularisation, tissue growth and regeneration [3,4]. Bone tissue engineered scaffolds can mimic the role of native tissue, as substitutes [5], and/or encourage tissue ingrowth from surrounding bone [6]. The "ideal" bone tissue engineered scaffold should also modulate cellular interactions, promote vascularisation and replicate the mechanical properties at the target site [7,8]. Additionally, the preparation and sterilisation techniques need to comply with industry and regulatory standards [9]. To this end, this review explores the structure and function of bone as well as current strategies used to treat defects. It outlines the history of selective laser sintering (SLS) technology and how it can be utilised in bone tissue engineering, including the use of SLS in the generation of scaffolds with defined porosities and interconnected pores that enable nutrient and waste diffusion. Each SLS material is discussed in the context of their chemical, physical, mechanical, and biological properties. Finally, the review examines the use of composite materials that more closely resemble native bone tissue by addressing some of the shortcomings associated with single phase materials, including weak mechanical properties, lack of functionality and their bioinert nature.

1.3.1 Bone Tissue Regeneration & Engineering

Bones provide structural integrity to the human body, protecting vital organs and facilitating mobility [10]. Bones are fundamental in maintaining homeostasis and play a role in energy metabolism [11], thus it is critical to preserve both their structural [12], and biological integrity [13]. Bone-related fractures directly cost the US economy $19 billion (USD) annually. The ageing and growing population along with a shift towards sedentary lifestyles suggests this burden will undoubtedly continue [14]. Additionally, indirect costs such as loss of productivity and associated social implications highlight that bone-related diseases have significant health and economic repercussions [15].

Current treatments for bone defects resulting from congenital abnormalities, injury or trauma typically utilise grafting. Bone grafting is a surgical procedure in which bone is replaced with other bone from the patient, donor or animal. To date, the ‘gold standard’ in bone grafting is autografting, where bone is harvested from non-essential bones such as the iliac crest or mandibular symphysis and used to replace defective bone. A shortcoming of autografts stems from the difficulty in preserving or obtaining specific geometrical features, particularly for maxillofacial reconstruction. Additionally, other issues arise due to donor site morbidity, increased risk of infection, haemorrhage, poor integration, nerve damage and associated pain from multiple surgeries [16,17]. The most significant drawback with autografting arises when a significant amount of bone needs replacing and there is simply insufficient graft available within the same patient for transplant. Beyond autografting exists allografting, where tissue is extract from either living humans or cadavers and transplanted; xenografting, where tissue is transplanted across species, typically from bovine, porcine or equine origins; alloplastic material grafting, where biomaterials are implanted as bone substitutes and composite grafts, including xenohybrids that combine synthetic biomaterials and xenograft bone grafts as well as composites of multiple biomaterials such as polymers, metals and ceramics. Each technique is associated with shortcomings, ranging from broad ethical concerns to immunological inadequacies risking tissue rejection [18,19].

Alloplastic materials, for instance, eliminate the need for a donor site; thus, limiting potential infections. They can be classified into nonporous, porous, and absorbable materials. Depending on the implant location, the type of material can vary. Typical alloplastic materials used in craniomaxillofacial applications are silicone, expanded polytetrafluoroethylene (Gore-Tex®) (Surgiform Technology, Lugoff, SC, USA), and High-Density Polyethylene Medpor® (Stryker Corporate, Kalamazoo, MI, USA). Silicone is a nonporous material that prevents tissue infiltration, often leading to capsule formation and subsequent infection. Gore-Tex® contains nodes and fibrils with a low porosity and a pore size ranging from 10–30 µm. Medpor®, made from high-density polyethylene, has a larger average pore size of 160–368 µm [20], although it lies in the lower end of porosity of human cancellous bone [21].

Common to many of the more successful bone graft substitutes is the integration of biomimicry into the scaffold design: closely replicating the natural composition, function, morphology, and mechanical properties of native bone to limit stress shielding, improve integration into surrounding tissue and, at times, instigate bone regeneration and remodelling proportional to implant degradation [4,5,15].

1.3.1.1 Bone Structure and Repair

The structure of bone is primarily made up of calcium crystals (hydroxyapatite ≈70 wt%) interspersed in a matrix of collagen among other mineralised extracellular matrices (ECM) and cellular components. There are two types of mature human skeletal bone, both of which are made up of osteons: cortical, and cancellous bone; sometimes also referred to as compact and spongy or trabecular bone, respectively [22].

Cortical bone is highly mineralised and dense with a typical void porosity of approximately 10 % with a range of 5 - 30 %, resulting in a higher elastic modulus (17 GPa) [23] at the expense of toughness [24]. Cortical bone's structure is made up of compact cylinders that serve to protect the inner cancellous bone. Cancellous bone is highly porous (30 - 90 %) with a lower elastic modulus and tensile strength (< 2 MPa) [25]. The irregular sponge-like structure [26], acts to absorb load while creating a microenvironment for biological activity, surrounded by several organic components including marrow, blood vessels and cellular components (< 2%) [24] (Fig. 1.2 a).

With the exception of sesamoid bones, bones found in the human body can be categorised into long bones, short bones, flat bones, and irregular bones. Long bones, typically found in the arms and legs (humerus, femur, tibia, etc.), are a hollow shaft or diaphysis made up of cortical bone and filled with bone marrow and adipose tissue. This is flanked by the epiphysis, which is made up of cancellous bone surrounded by a thin layer of cortical bone and acts to connect adjacent bones to form joints. Short bones act to reinforce joints while facilitating movement in areas such as the wrists and ankles (tarsals and carpals). They are made up of cancellous bone, surrounded by cortical bone. Likewise, flat bones are also made up of cancellous bone surrounded by cortical bone, though flat bones' primary action is to provide structure and protection and thus are found in the cranium, scapula, sternum, ribs and ilium. Irregular bones, found in facial regions and the spinal column, have complex geometries that aid in anchoring and protecting soft tissues, including providing an attachment point for the tongue and acting as a barrier for the spinal cord.

The ratio of cortical bone to cancellous bone varies depending on bone type and location. For instance, the cortical:cancellous ratio of vertebrae is 25:75, with the femoral head having 50:50 and radial diaphysis showing a 95:5 ratio. The quantity and proportion of cortical and cancellous bone at various sites affect the strength of bone independently. Additionally, most bone is anisotropic [27], where the response of bone to load depends on the direction of load application. For instance, longitudinally, bone is strong, yet when load is applied to the surface of bone it is noticeably weaker. Thus, "strength of bones are dependent upon the material, the microscopic structure and the shape of the whole bone" [28].

Bone is a dynamic tissue that undergoes continuous growth, modelling, and re-modelling, from foetal development until death. During development, bone growth occurs longitudinally along growth plates, where cartilage mineralisation forms primary new bone. Modelling occurs as a response to mechanical pressures, gradually adjusting bone structure in response to stimuli in-line with Wolff's law [29]. The process does not involve the coupling of bone formation and resorption. Modelling occurs less frequently in adults than remodelling. Remodelling, on the other hand, is a continuous process that maintains bone mineral homeostasis with osteogenic cells. It includes the resorption of old bone tissue by osteoclasts and the synthesis and mineralisation of protein matrix by osteoblasts. In cortical bone, remodelling lasts approximately 120 days, while within cancellous remodelling lasts 200 days [30]. Regulating these processes are osteocytes, which are terminally differentiated osteoblasts that connect to and act as bone support structures at the bone surface (Fig. 1.2 b). Bone metabolism is a continual process and is regulated by these specialised cells and hormones, in order to preserve tissue strength and integrity, if compromised, scaffolds can be used to restore balance.

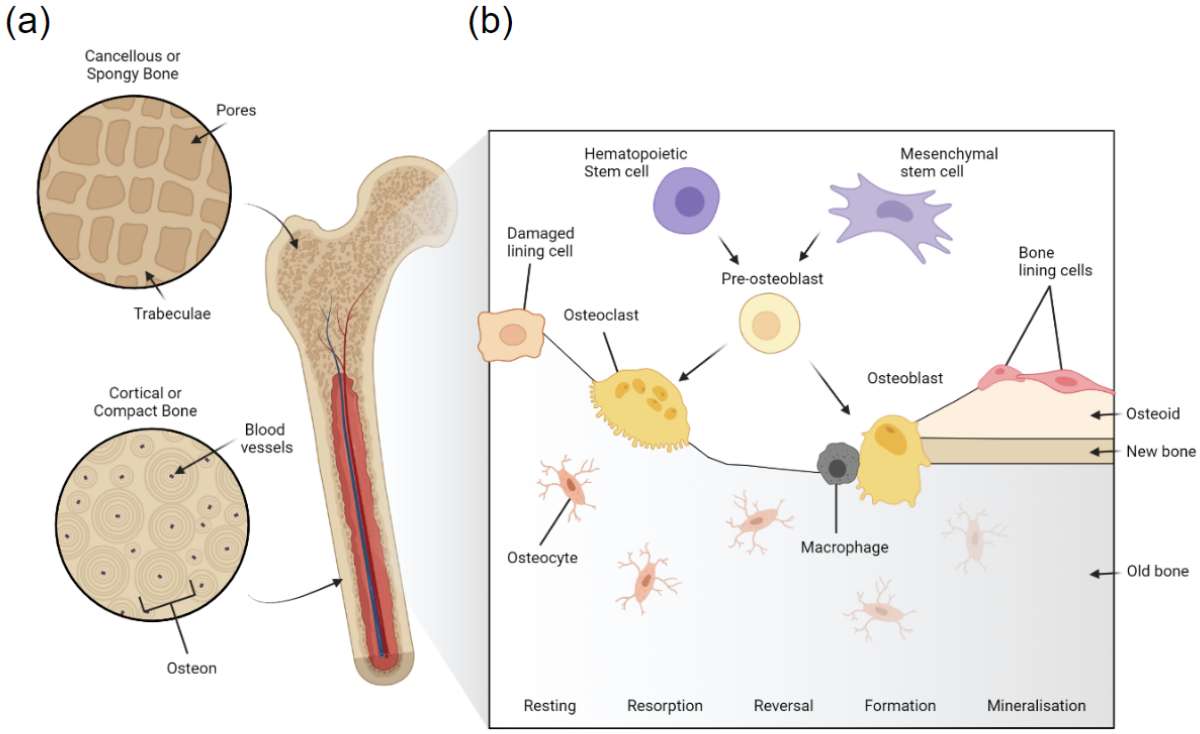

Figure 1.2 (a) Internal structure of human bone (b) bone remodelling and the stem cell pathway, including bone resorption by osteoclasts, bone formation and mineralisation by osteoblasts, after which, osteoblasts become either new lining cells or mature into osteocytes.

1.3.1.2 Scaffold Design

Like native bone, biomimetic bone scaffolds need to balance biological requirements with architectural intricacies and mechanical performance. Porosity, independent of material properties, is the percentage of void space in a solid. It is well established that highly porous (> 75 %) constructs, with interconnected pores, aid tissue ingrowth by providing a high surface area for cells to attach and proliferate into, whilst enabling nutrient and waste transfer [31]. Increases in porosity, however, are inversely proportional to compressive strength [32], with a 10 - 20 % porosity increase known to decrease strength up to four fold [33,34]. Instead, other physical attributes such as pore size, shape and orientation can be manipulated to improve biological outcomes while maintaining mechanical stability. Macropores, larger than 100 µm [35], have been shown to promote osteogenesis and angiogenesis [35], whereas micropores, smaller than 20 µm, can stimulate mineralisation through improvements in cell recruitment and attachment [36,37]. The rate of tissue regeneration has been shown to be proportional to pore curvature, with concave pores observed to be better than flat or convex pores [38–40]. Fibroblasts have been shown to favour small pores over large pores. For example, beta-tricalcium phosphate (β-TCP) scaffolds with 100 µm pores and lowest porosity (38%) showed improved bone ingrowth both *in vitro* and *in vivo* compared to scaffolds with 250 µm and 400 µm pore sizes and larger porosities [41]. In general, a distribution of pore shapes and sizes, a high porosity that is well interconnected, without jeopardising the mechanical properties, will contribute to improved bone tissue engineering outcomes.

The mechanical properties of implants should closely match that of the bone at the target site [42]. In load-bearing scenarios, discrepancies between bone and implant hardness can lead to stress shielding. Stress shielding is a phenomenon associated with implants that are harder or stiffer than bone (typically metallic implants) that prevent the mechanical load transferring to the surrounding bone tissue, provoking bone absorption. The absorption of bone from stress reduction gradually leads to bone resorption and the subsequent loosening of implants [43–45]. This loosening can lead to excessive oscillations of the implants, reducing osseointegration and causing chronic inflammation, pain, discomfort and ultimately implant failure [46,47]. Thus, scaffold design should aim to incorporate materials with a similar Young's modulus to native bone/tissue to circumvent the possibility of stress shielding.

For rapid osseointegration, stimulating the interaction between implants and the surrounding tissue is imperative. Known as the bone-implant interface, this contact area has been shown to be the site of initial cell recruitment and adhesion. Thus, the surface characteristics down to the nanoscale can influence scaffold performance [48]. For instance, the surface roughness of metallic implants has been shown to be inversely proportional to biological fixation. Additionally, surface roughness has been shown to promote MSC proliferation, osteoblast differentiation, bone mineralisation and growth factor production [49–51]. Though, smoother surfaces have been shown to promote osteoblast spreading [52], at the expense of osseointegration [53]. In practice, varying surface finishes can be productive in stimulating rapid cell attachment, though challenges remain in optimising the application of these techniques. The use of computational stem cell proliferation and differentiation modelling may provide the necessary insights into understanding the interactions at the bone-implant interface [54,55]. Combining extensive practical approaches with computational models will aid in advancing the field of bone tissue engineering.

1.3.1.3 Regulatory Requirements for the Future of Bone Tissue Engineered Scaffolds

One of the most important requirements of any bone tissue engineered scaffold or implant, apart from mechanical stability, is its biocompatibility. To ensure safety, medical device regulations prescribe requirements for demonstrating biocompatibility based on the intended use of the device which determines both the location and duration of implantation. Guidance on meeting these requirements are provided by regulators themselves, for example in guidance documents published by the US Food and Drug Administration (FDA), with reference to standards such as ISO 10993: Biological evaluation of medical devices [56]. While risk classification rules vary geographically, with the exception of most dental devices, permanent implants are classified as medium to high risk and fall within Class IIb/III according to the European Medical Devices Regulations (MDR)[57] and Class II/III by the FDA [58]. The risk classification then informs the required biocompatibility studies. For instance, implantable medical devices require toxicological risk assessment of their chemical characteristics, as well as assessment of their nature, degree, frequency and duration of contact with the body with a range of *in vitro* and animal implantation studies. Device contact duration is categorised as Limited (<24 hrs), Prolonged (24hrs to 30 days) or Long Term (>30 days) [56,59]. Resorbable implantable devices have further specific requirements to demonstrate their degradation profiles are safe. Regarding 3D printed personalised implants, MDR classifies them as custom made devices, where each individual device must be made using a MDR compliant technical file, typically under the control of an ISO13485 certified quality management system. In the USA, personalised 3D printed implants require pre-approval via the 510(k) premarket notification pathway with objective evidence proving substantial equivalence to an existing FDA approved device with a similar risk profile and intended use case. Risk management of personalised implants can be categorised into verification and validation of safety and performance with reference to implant specifications and clinical use scenarios. The former for instance, can use mechanical testing and finite element analysis to determine implant compressive strength as well as fixation requirements, from length, thickness, quantity, and trajectory of screws. Surgically, cadaveric or model trial surgery can aid in implant validation, in-line with requirements for traditionally manufactured implants. Compliance with regulatory requirements and international standards ensures a balance between innovation and safety, while also supporting the commercialisation and ultimately delivery of bone tissue engineered scaffolds to patients [60].

1.3.1.4 Advancing the Field of Bone Tissue Engineering

The shortcomings of current grafting measures used for bone regeneration dictate that better alternative approaches are needed, especially as these treatments will see increasing demand with our ageing population. Tissue engineering approaches circumvent several shortcomings that arise from grafting such as donor site morbidity and the ethical and immunological concerns associated with xenografting [61]. Among these approaches is the use of additive manufacturing technologies for bone tissue engineering which encompasses the added value of being able to manufacture patient specific implants to better fit and to better treat the patient. This review explores the use of a promising manufacturing technology, selective laser sintering (SLS), for producing robust, personalised tissue engineered alternatives. LS additive manufacturing approaches are highly versatile, enabling the fabrication of scaffolds from a range of biomaterials including polymers, metals, ceramics, and composites. as outlined in the following sections. The limitations of current methodologies and potential future strategies to circumvent hardware and material shortcomings are also discussed to provide a future-facing perspective of the use of SLS in tissue engineering.

1.3.2 Laser Sintering Bone Tissue Engineering Scaffolds

The mid 1980s saw the development of Additive Manufacturing through the emergence of a technique termed stereolithography. Additive manufacturing technologies have been described as the “process of joining materials to make objects from three-dimensional (3D) model data, usually layer by layer, as opposed to subtractive manufacturing methodologies,” by the ASTM International Committee F42. This form of manufacturing is thought to be part of the next industrial revolution [62]. Additive manufacturing techniques have more recently become known, more generically, as 3D printing. Historically, Additive manufacturing has been used primarily for rapid prototyping for research and development purposes [63] and has been shown to reduce development costs by up to 70% and time to market by 90%; both deemed to be vital in the development and delivery of patient-specific medical implants [64].

The workflow for generating 3D printed medical implants starts with the patient. It involves the development of a 3D model through computer aided design (CAD) or reconstruction of 3D patient anatomical data from medical scans, such as computed tomography (CT/X-rays) or magnetic resonance imaging (MRI) [65] to create a series of 2D slice images, stored in DICOM format (Fig. 1.3). Once a 3D model has been generated and exported, most commonly as a Standard Tessellation Language file, it must be translated into machine readable code (typically g-code which provides sequential machine movement instructions), which separates the model into distinct layers for printers to interpret and control the layer-by-layer fabrication process.

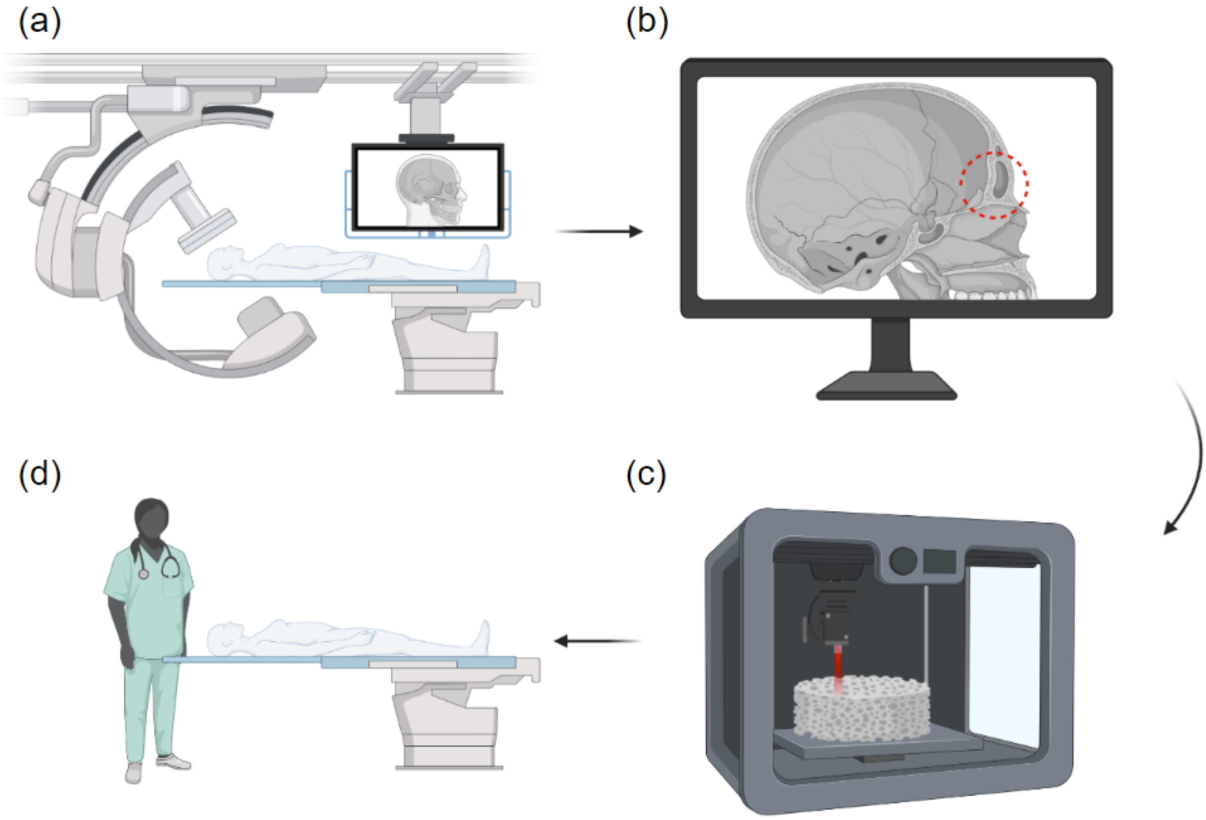

Figure 1.3. A schematic representing the process of 3D printing implants. (a) Initial patient scans from X-ray, CT or MRI. (b) The conversion of medical scan data also known as DICOM files to the generation of a 3D model of the defect. (c) The 3D printing process, in this case light-based printing, to generate an implant to accurately match the patient's defect. (d) Clinical implantation of the patient-specific implant.

3D printing is the layer-by-layer deposition of materials to build a three-dimensional construct. Arguably the most common consumer 3D printing technique involves the controlled deposition of molten polymer achieved by feeding a polymer filament (such as poly lactic acid) through a heated nozzle onto a platform where it solidifies [66]. Subsequent layers are fused on top of previous layers until a 3D object is realised. Other forms of 3D printing involve the use of lasers with curable liquid resins or powder beds. The former stereolithography involves a reservoir of photocurable resin into which laser patterns are traced. Upon adhering to the print platform, subsequent solidified layers are added until constructs emerge from the liquid resin. The latter, utilising a powder bed, termed powder bed fusion, has shown substantial promise as an additive manufacturing technique capable of producing high strength constructs suitable as bone tissue engineered scaffolds and are the focus of this review.

In 1989, a master's student at the University of Texas, Carl R. Deckard, designed, developed, and patented the first Selective Laser Sintering (SLS) system. Following the initial development, the trio of inventors (Joseph J. Beaman and James F. Darrah) went on to create Nova Automation and DTM Corp to industrialise and commercialise their technology. SLS is an additive manufacturing approach that utilises powder bed fusion technology (Fig. 1.4). In essence, both SLS and Selective Laser Melting (SLM) techniques involve the localised heating or melting of a powder bed, with laser energy, which coalesces adjacent particles. For this to work efficiently, powders must absorb the laser irradiation. Typically, both processes utilise infrared (IR) light lasers in a solid or gas state, as well as visible light diodes. Diodes drive solid-state lasers, where active ions of neodymium (Nd3+) are doped in a passive crystal of yttrium aluminium garnet, thus producing an neodymium: yttrium aluminium garnet laser. These lasers can be guided by a fibre to deliver 1064 nm light in concentrated areas for the laser melting of metals such as stainless steel, titanium, and aluminium. Gas lasers lie deeper within the IR spectrum. At a wavelength of 10 600 nm, CO_2 gas lasers are suitable for sintering polymers with high absorptivity, including polyamide and poly(ether ether ketone). More recently polyamide has also been processed through blue diodes at 445 nm, though for efficiency the powder must be black or grey in colour. A detailed review exploring the types of lasers used in additive manufacturing can be found here [67].

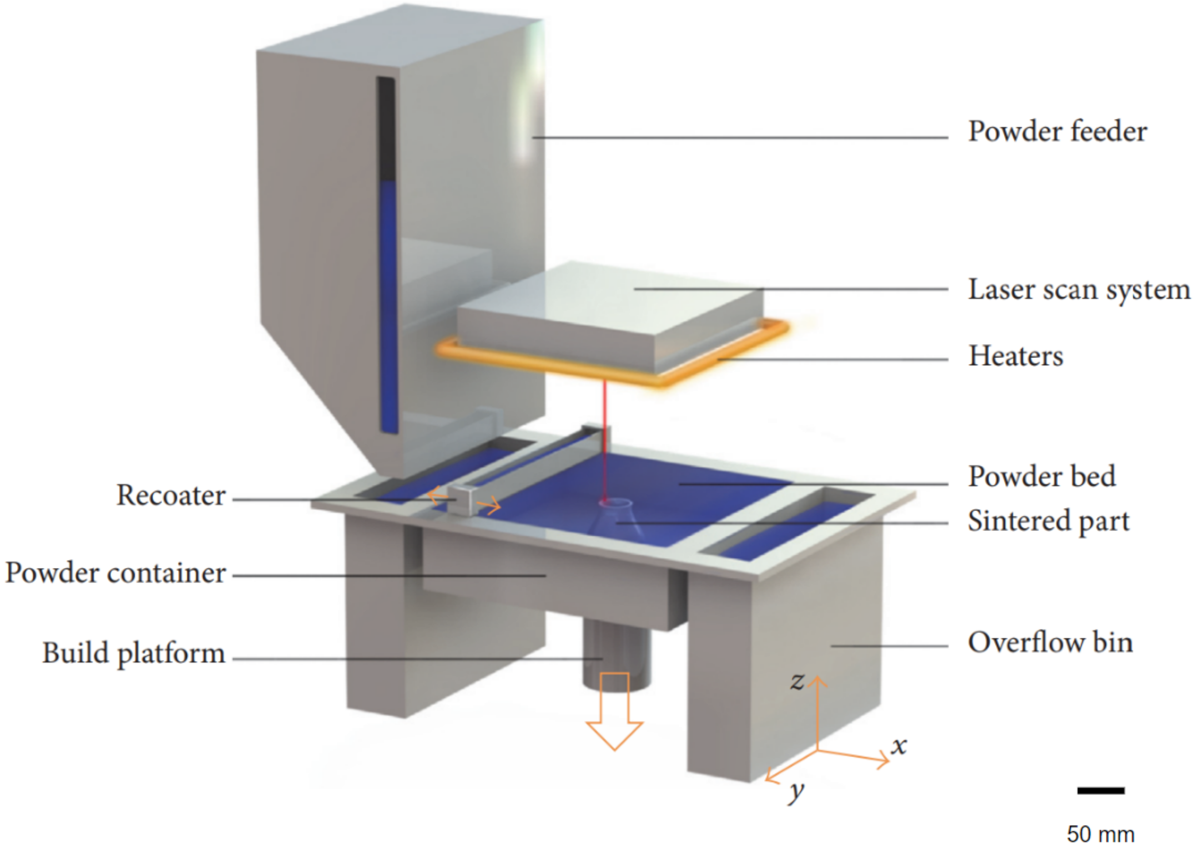

Figure 1.4. Schematic illustration of a typical laser sintering system. Scale bar = 50 mm. Reprinted with permission from [68]**.**

Though material absorptivity is a key component of sinterability [69], laser energy, exposure duration, laser spot size, scan spacing, layer thickness and sintering temperature all play a vital role in effective SLS [70]. In both SLS and SLM, energy density is a fundamental factor that determines print quality. If the energy densities for sintering conditions are not optimised for the specific material used, surface morphology [71] and porosity [72] may be poorly controlled, ultimately risking the production of fragile parts with dimensional inaccuracies [73,74] . To ensure consistency and fine resolution, the intrinsic and extrinsic material properties should be understood in the context of the chosen laser system, previously summarised in the context of polymer SLS [75]. There are five main polymer properties necessary to understand prior to exploring new or novel SLS powders. These properties stem from thermal, optical, and rheological factors down to the material production and processing parameters, explored in depth later in this section.

To optimise the SLS process, an approximation of energy density can be calculated. Nelson, J. C. *et al.* [76] described energy density (E) per unit area (J/mm2) of polymer-coated silicon carbide powders through the relationship of laser power (P) as a function of laser beam velocity (V) and scan spacing (S) (equation 1).

$$E = [P/\ (V \times S)] \tag{1}$$

The equation was later amended to compensate for beam penetration and energy diffusion through a known volume [77], assuming the volume is optically transmissible, where: T = layer thickness, given in (J/mm^3) (equation 2) [78].

$$E = [P/(V \times S \times T)] \tag{2}$$

The model has limitations when modelling SLM, as the metals used radiate substantial energy through conduction [79]. Additionally, the simplicity of the equation cannot account for melt pool depth [80], nor keyhole porosities [81], known phenomenons in SLM [82]. The thermal conductivity of metal powders is important, and whilst it complicates SLM modelling, it has been shown to influence consolidation and part density, directly related to the bulk powder properties [83]. Assuming an evenly packed powder bed, the materials act as a heat transfer medium, capable of reducing thermal gradients and thus overcoming any deformation and warping. Likewise, the continual heating and cooling of the print environment has the same detrimental influence on part properties, including delamination, shrinkage, and warping, leading to morphological inaccuracies and potential mechanical instabilities [84]. Understanding the relationships between material and energy density will improve print resolution, surface finish and overall mechanical properties.

1.3.3 Materials for Laser Sintering

There are many materials with the appropriate physical, chemical and optical properties suitable for SLS. These characteristics can be divided into extrinsic and intrinsic features (Fig. 1.5). Apart from metals (in SLM systems) such as stainless steel, aluminium, and titanium; polyamides, polystyrene, polycarbonate, and ceramics are the most used materials in SLS systems [69]. However, polymers that can be made into a fine powder, also have the capacity to be sintered.

The most typical shape for particles is spherical, as the recoating blades or rollers can evenly distribute subsequent layers, due to their free-flowing capacity. Inconsistent particle size, aspect ratio and shape, like those generated via cryogenic milling, fail to yield dense parts and can result in weak mechanical properties [85,86]. The size of particles for SLS systems range between 20 and 150 µm [87,88], and for SLM, most commonly range between 20 and 60 µm [89]. Small particles are known to have strong electrostatic attractions which can increase friction [90,91], larger particle sizes, on the other hand, can reduce part finish and density [92], thus a range of particle sizes can be beneficial for improving flow and density. Additionally, environmental factors such as humidity also impact isothermal consolidation, but can be controlled with a shield gas such as Ar, N2 or He, among other inert gases.

Intrinsically, the thermal and optical properties need to be sufficiently understood for efficient particle fusion. Typically, semicrystalline polymers have suitable thermal characteristics to be processed through SLS. For new materials, a ‘sintering window’ can be established through differential scanning calorimetry. Ideally, a distinct sintering window exists between the polymer melting point (Tm) and the crystallisation point (Tc). If the sintering window is narrow, printed constructs can deform or lateral growth can occur (Fig. 1.6) [93]. Optically, many polymers contain aliphatic compounds (C-H) capable of absorbing portions of infrared radiation, particularly at the wavelength of 10 600 nm. Rheologically, appropriate SLS materials require a low melt viscosity and a low surface tension. A low melt viscosity is essential as there is no compaction of polymer particles during the SLS process, when compared with injection moulding.

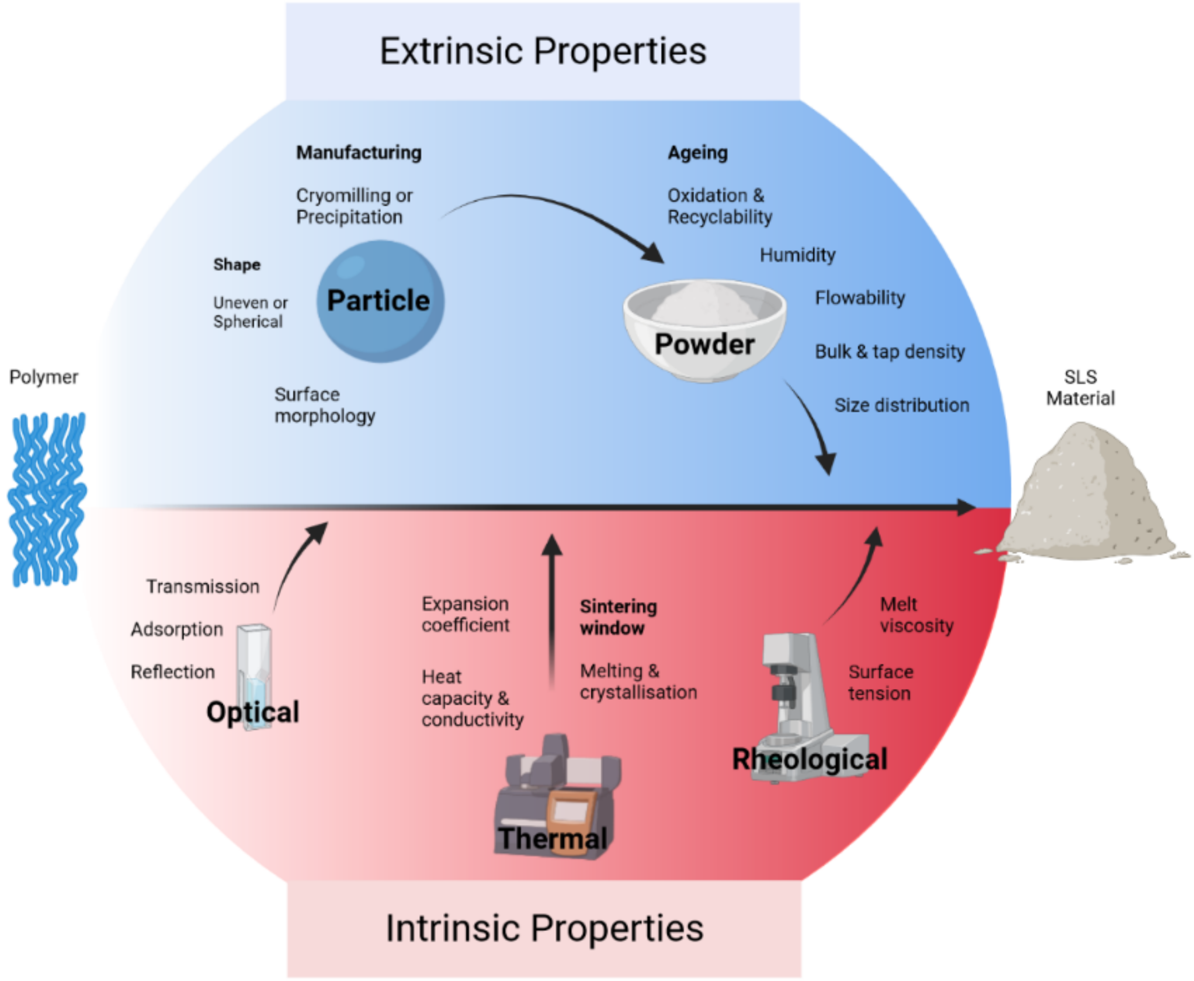

Figure 1.5. A summary of the extrinsic and intrinsic properties associated with the powder and process parameters that have an influence on materials used to produce parts via SLS.

The ageing of polymer powders must also be considered when generating implants, with polyamide chain length being shown to grow with increasing build time and high build chamber temperature [94,95] . Due to the use of high energy lasers, materials processed via SLS should undergo comprehensive physical and chemical analysis, as deformation [96] and chain scission [87] can be detrimental to scaffold and polymer stability. When compared to the bulk properties of the polymer, the tensile strength and modulus are comparable to sintered constructs, however sintered parts are typically more brittle with a reduced elongation at break [68,94].

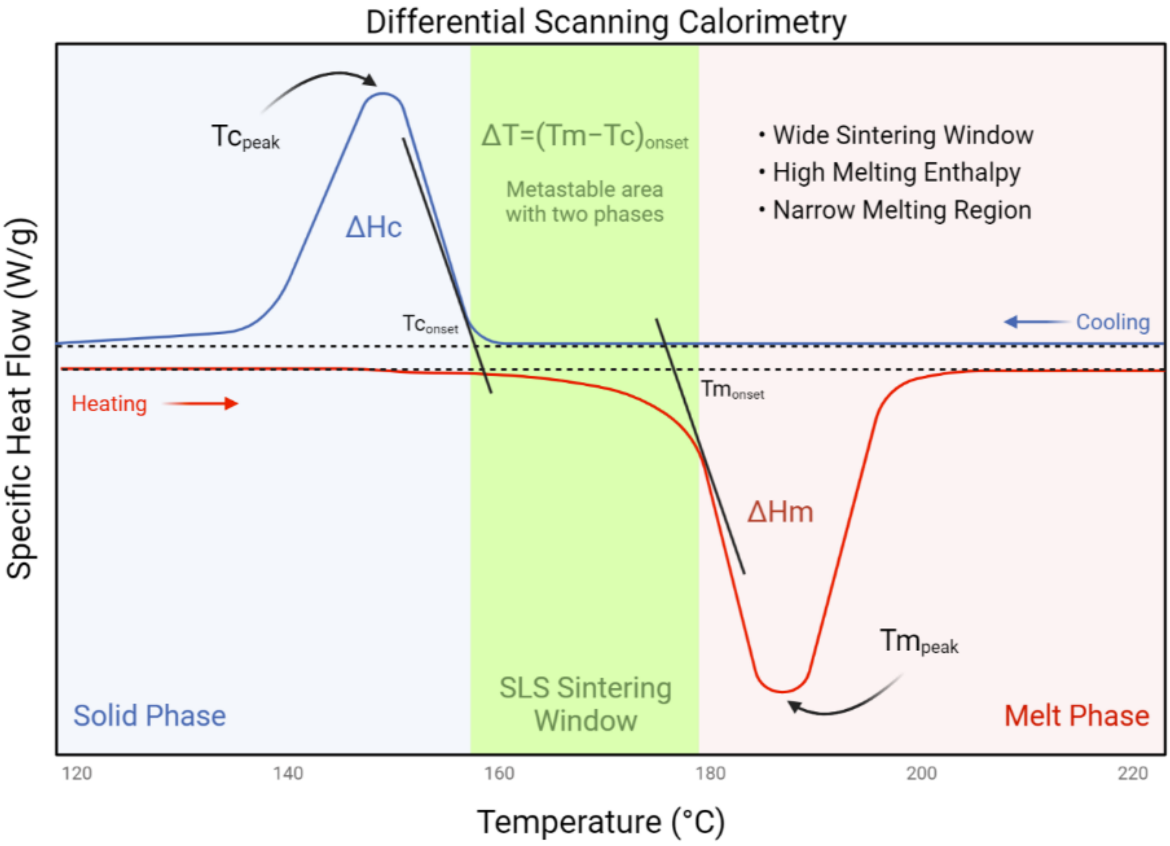

Figure 1.6. An ideal heat flow curve from differential scanning calorimetry analysis in the context of SLS printing, including a melt phase and solid phase determined from a typical heating and cooling rate of 10℃/min. Adapted from [93]**.**

1.3.4 Polymers

1.3.4.1 Polyamide

Nylons are biocompatible polymers that belong to the family of polyamides (PAs) [97], used in a myriad of applications, extending from textiles [98] to biomedicine [99]. They are either derived from petroleum or natural sources such as castor oil [100]. Synthesis involves ring opening or condensation polymerisation. Nomenclature is based on the number of carbon atoms within each monomer, of which there are 8 types. The most common commercially available type for SLS is PA-12 (90 - 95% of the market), known under the trade names of PA 2200 (EOS) and Duraform® PA (3D Systems) [101–103]. They are linear, thermoplastics traditionally used in injection moulding. PA-12 has a broad processing window or 'sintering window', making it useful for SLS [104]. Additionally, it has a low melting viscosity and moisture absorption, superior elongation, wide range of melting and crystallisation temperatures, high flexibility and UV protection when compared to the various other forms of nylon. However, PA-12 has a reduced elongation at break [105] and is more expensive when compared to other powdered polymers, particularly when producing suitable powder homogeneity for SLS [106]. This expense is due to the novel powder processing methods for making consistent powders for SLS, either by precipitation [107] or polymerisation [108].

Other forms of polyamides used in SLS are PA-6 and PA-66, as they are known to have a molecular structure resembling that of collagen found in human bone [109,110]. On a larger scale, biomimetic architectures of trabecular human bone can extend outside the achievable resolution of typical LS systems (<~50 µm). A previous study rectified this issue by scaling up bone CT/MRI data 4-fold to generate PA-6 scaffolds mimicking that of human bone while broadening the porosity and interconnectivity requirements for adequate bone regeneration [111]. Printed scaffolds were tested both *in vitro* and *in vivo* with porcine bone marrow stromal cells and in a porcine mandible, respectively. Bone tissue infiltration after 6 weeks was 43.2%, compared to 50.3 - 65% observed following implantation of HA scaffolds with the same pore geometry [112]. The reduction in tissue growth was thought to be associated with material leaching due to partial sintering. Additionally, the bioinert nature of PA could have played a role in reducing tissue ingrowth. Similarly, PA was used in a recent study that employed an SLS technique to overcome stress shielding by generating porous, biomimetic trabecular-like bone scaffolds [113]. To address this, a porous honeycomb structure was generated through SLS from PA-66. The elastic modulus of scaffolds was found to be within the range of trabecular human bone (50 - 500 MPa). The mechanical data was then applied to a finite element simulation to predict how changes in porosity (between 59 and 96 %) influence elastic modulus. A nonlinear relationship was found between an increase in elastic modulus and decreased porosity. This model could also be applied to a patient's CT data to predict the mechanical properties of bone at a defect site to avoid stress shielding.

1.3.4.2 Polycaprolactone

Polycaprolactone (PCL) has been widely used in bone tissue engineering strategies. PCL is produced by polymerisation of ε-caprolactone via cationic, anionic, or radical polymerisation methods [114,115]. It is a biodegradable [116,117], semicrystalline, aliphatic thermoplastic with a glass transition temperature (Tg) of -60 ℃ [118] with a typical melting point of ~60 °C [119–121], tunable down to 46 °C [122]. The availability of different molecular weight PCL's results in tailorable degradation kinetics over months or years, depending on the tissue engineering application [120]. Its low cost and favourable physicochemical attributes make it suitable for a wide range of additive manufacturing techniques, including FDM [123], melt electrowriting [124], and SLS applications.

One novel study by Kinstlinger *et al.* [125] explored interfacing a custom recoating platform (Fig. 1.7 a & b) with a laser cutter to process PA-12 and PCL. They were able to reproduce sophisticated lattice structures recapitulating bone structures (Fig. 1.7 c & d). Additionally, the study explored the influence of post processing SLS prints on mechanical properties and studied the biocompatibility of the structures using human MSCs (hMSCs). Following 5 minutes of vapour smoothing with dichloromethane, scaffold surface roughness was significantly reduced while elastic modulus and yield stress were improved (Fig. 1.7 k & l). Following 10 days of *in vitro* cell culture, seeded hMSCs showed minimal morphological change (Fig. 1.7 g) compared to the elongation and spindle-like morphology observed on the vapour-smoothed surface (Fig. 1.7 h). A similar study by Mazzoli, *et al.* [126] utilised a Sinterstation CO_2 laser system to fabricate PCL discs (15 mm diameter) with 500 µm pores. The print parameters used included a bed temperature of 50 ℃, a laser power of 12 W and a 0.1 mm layer thickness. This resulted in a compressive strength of 3.6 MPa at 48 % porosity, the lower range of trabecular bone [127]. Additionally, seeded hMSC demonstrated spherical and branched morphology, confirming biocompatibility *in vitro*.

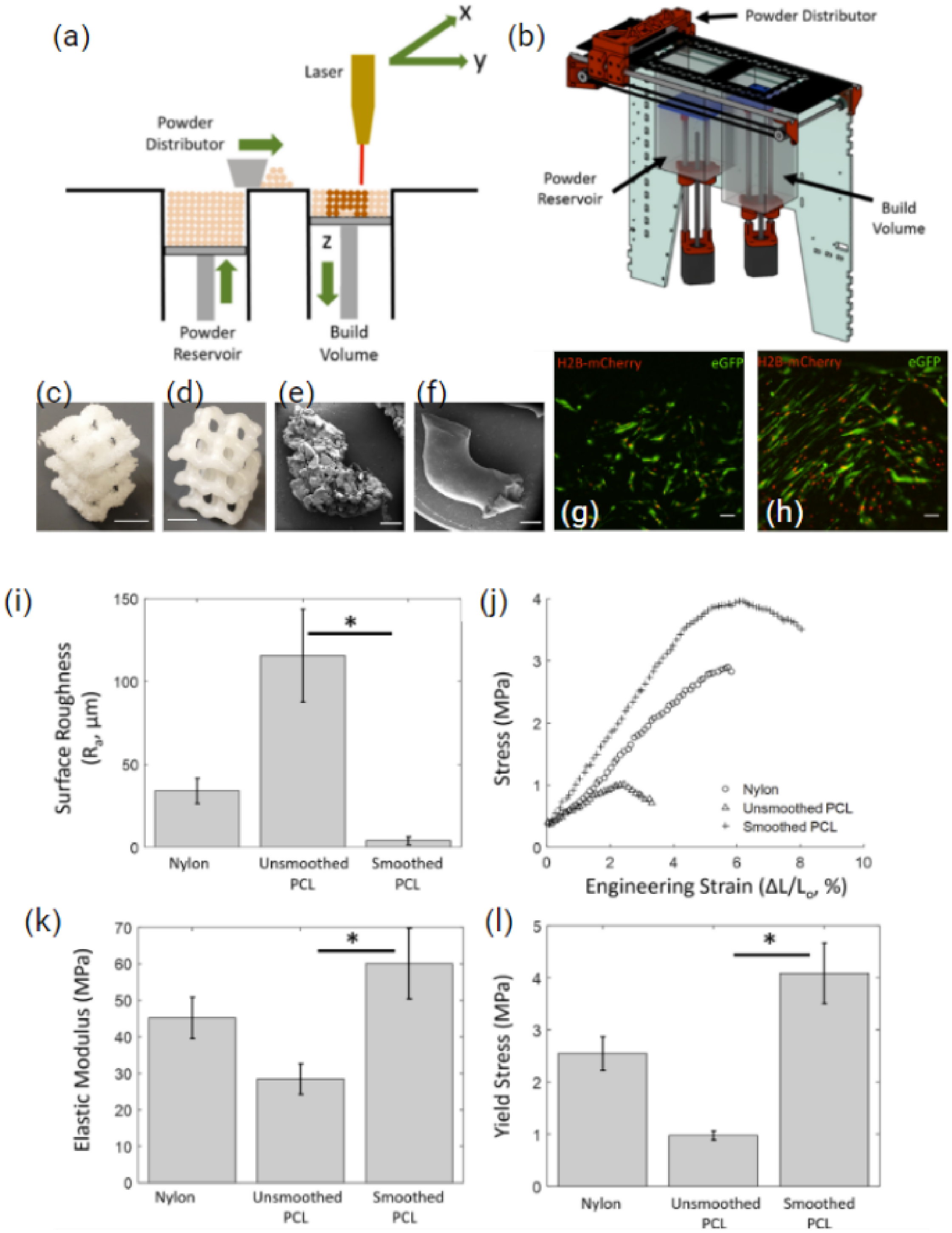

Figure 1.7. (a-b) A schematic and 3D render of the custom re-coating platform developed to build up PA 12 and PCL powder in the Z direction with the use of a laser cutter. Surface finish of PCL sintered diamond lattice, before (c & d) and after vapour smoothing (e & f) (scale bars = 1 mm), (g) shows hMSC morphology on sintered PCL and (h) shows hMSC morphology on vapour-smoothed sintered PCL (scale bar = 1000 µm). (i) Surface roughness and (j, k, l) mechanical properties of sintered PA 12 and PCL as well as vapour-smoothed sintered PCL. Adapted from [125]**.**

More recently, Gu *et al.* [128] utilised small (50 µm) and large (150 µm) PCL microspheres to create bilayered cartilage and subchondral bone scaffolds. They compared three different structures, non-channel, consecutive-channel and inconsecutive-channel. The biomimetic hierarchical structure with varying channels was designed to prevent vascularisation on the dense surface while the porous phase beneath was used to promote osteogenesis and vascularisation. The dense, non-channel scaffold had a compressive strength of 18.27 MPa, with the consecutive-channel and inconsecutive-channel resulting in 5.91 and 10.26 MPa, respectively. The native osteochondral tissue of rabbits is measured to be 20 - 30 MPa [129]. *In vitro* all scaffolds supported MSC adhesion, proliferation and spreading. Interestingly, *in vivo* the inconsecutive-channel scaffold showed a significantly higher bone volume fraction and trabecular number. This was in contrast to the non-channel scaffolds that showed limited tissue integration, with the consecutive-channels revealing inconsistent tissue ingrowth. Overall this hybrid SLS printing approach demonstrates a novel way of tuning mechanical and biological properties of scaffolds without the need of cell or growth factor loading, expanding the potential of PCL in bone tissue engineering applications.

1.3.4.3 Polyethylene

Polyethylene (PE) is a thermoplastic polymer of ethylene with a variable crystalline structure. PEs are produced at almost 5 million tonnes per annum [130], making it the world's most common plastic. They have a broad range of applications due to ease of production, ranging from packaging [131] to biomedicine [132]. PE is classified by its branching and density and exists as ultra-high, high, medium, and low molecular weight varieties. Each form of PE varies in mechanical, chemical, thermal, optical, and electrical properties, broadening its applicability. Due to its long-term stability and biocompatibility [133], PE is one of the most used materials for alloplastic surgical implants and has been used in hundreds of products ranging from facial implants [134], through to coatings for esophageal stents [135], as well as in total hip arthroplasty [136].

SLS of PE is challenging due to its narrow sintering window that can impact print accuracy [137]. Without fine tuning the energy density, laser energy can broadly radiate into surrounding particles leading to lateral growth and warping, in turn filling voids [138] and reducing part porosity [139]. Additionally, in its native state, PE is white or semi-transparent, making it highly reflective to visible (445 nm) or near infrared (1064 nm) light. Using CO_2 lasers (10 600 nm) however, polyethylene appears opaque, improving sintering potential. Additionally, porosity of the printed part can be tuned when printing with a CO_2 laser [140], which can be beneficial for bone tissue engineering applications.

Another component capable of influencing porosity is the size of powder particles. Samoria *et al. [141]* investigated pore size as a function of HDPE powder size, using commercially available HDPE particles with size ranges of 106-125 µm; 150-212 µm and 212-380 µm respectively, and were able to control pore gradients. A larger particle size yielded significantly more closed pores at the expense of mechanical strength, when compared to smaller particles. They concluded that the discrepancies between mechanical properties were a result of limited necking of adjacent particles. A more recent study compared commercially available porous HDPE implants with SLS printed scaffolds *in vivo* [142]. They found that the SLS printed scaffolds demonstrated higher scaffold porosity compared to traditional moulding, and this supported good tissue integration after implantation. Additionally, the functionalisation of the HDPE surface using plasma was also demonstrated to improve the formation of blood vessels within the implant, enabling more rapid tissue ingrowth and maturity [142]. Overall, although PE has been used sparingly in SLS systems due the limitations mentioned, it has established use in biomedicine, warranting further exploration within bone tissue engineering and additive manufacturing landscapes.

Table 1.1 A summary of parameters utilised for SLS different types of PE and composite-based PE materials accompanied by benefits and limitations observed during or after processing

Material	Print Parameters	Benefits	Limitations	Ref
HDPE 106-125 µm 150–212 µm 212-380 µm	CO_2 laser 200/400 µm layers ED= 0.44 J.mm2 95 ℃ bed 44.5 mm/s	Smaller particles higher elastic modulus and ultimate strength, marginal differences between 100 - 200 particles	Reduced necking with larger particles	[141]
PA12/HDPE blends 80/20, 50/50, 20/80	CO_2 laser 150 layers µm 60 ℃ bed 80 mm/s Power: PA = 3W, HDPE = 12W, PA/HDPE = 6 W	PA absorbs energy and transfer to HDPE for coalescence	PA better for sintering than HDPE	[143]
PA12/HDPE blends 80/20, 50/50, 20/80	CO_2 laser as above PA = 3.33W (ED 0.3) bed 140 HDPE = 4.95 (ED 0.445) bed 100	HDPE ultimate strength 73 MPa, compared to 54	HDPE elastic modulus 137, PA12 205	[144]
PA12/HDPE blends 80/20, 50/50, 20/80 PA size = 60 µm HDPE size = 80 - 200 µm	CO_2 laser Parameters as above (approx) 44.5 mm/s 140 bed temp for PA, 100 for HDPE ED PA12 = 0.3 MJ/m2 HDPE 0.445 MJ/m2	Increased PA 6 ratio led to higher plastic deformation,fatigue test the 20/80 and 50/50 blends presented good fatigue resistance	Increased PA 6 reduced elastic recovery,	[145]

UHMWPE 80 x 10 x 4 mm samples	CO$_2$ laser Feed temp 110 - 150 Bed temp 130 - 150 Laser powder 5 - 30 W Scan count 1-2 Speed 5000 mm/s Scan spacing 0.15mm Roller speed 177.8 mm/s Layer thickness 0.1 mm	Able to tune mechanical properties through adjustments in scan parameters and strategies	Determined very narrow processing window, post processing recommended	[146]
UHMWPE < 180 µm particle size	CO$_2$ laser No pre heat 0.2 mm spot size ED 0.65–2.20 Jmm$_{-2}$S^{-1}	Capable of producing relatively dense and continuous constructs	Shrinkage leads to movement due to thermal gradient thus reducing part resolution FT-IR revealed hints of polymer degradation, in the presence of double bonds, from cross-linking and oxidation (although qualitative)	[147]

1.3.4.4 Polyetheretherketone

Polyetheretherketone (PEEK) is a semi-crystalline polymer that is stiff, robust and lightweight [148], with decades of use in the aerospace, medical and dental fields. It has exceptional strength, a Young's modulus of 3.6 GPa and tensile strength of 90 - 100 MPa [149], a high wear resistance and low friction coefficient, rendering it favourable as a biomaterial to mimic the native properties of bone. With a typical glass transition temperature of 143 ℃, a melting point of 343 ℃ [150] and thermal degradation at 575 ℃ [151], it can sustain high temperature exposure for extended periods. Its high melting point inspired the modification of conventional SLS systems [152], leading to the birth of high temperature (>300 ℃) SLS or HT-LS [153,154].

One study explored the generation of patient-specific PEEK cranial implants via SLS. The study compared print orientation and found that vertically-printed SLS constructs were not as accurate or as strong as horizontally-printed SLS constructs, with a 70 % reduced failure rate [155]. Interestingly, when compared to injection moulding, SLS-generated PEEK scaffolds showed a reduced tensile strength but an improved compressive strength.

However, the high temperature processing parameters for PEEK sintering limit reusability. This heightened sensitivity stems from PEEK's cold powder coating preparation, which can lead to crystallisation shrinkage and warping deformation if powder bed temperature fluctuates [156]. The high temperatures and print duration impact the physicochemical properties of the polymer, severely reducing PEEK's reusability even when using an inert gas shield [157,158]. These changes caused by ageing can reduce powder performance, resulting in inconsistencies between printed scaffolds even with the same printing parameters.

To improve the bone-implant interface, intricate internal architectures have been generated via SLS from PEEK [159]. By mimicking trabecular bone and impregnating constructs with a co-culture of ADSCs and BMSCs, scaffolds improved cell morphologies, resembling that of fibroblasts and lead to greater osteogenic differentiation of the ADSCs.

Overall SLS fabricated porous PEEK, combined with novel co-culturing techniques are a promising approach towards generating patient-specific craniofacial implants.

1.3.5 Composites

The primarily homogenous materials explored so far have met the necessary print requirements for LS applications. However, bone itself is a heterogeneous composite material and is perhaps nature's best example of a composite structure which requires different phases for optimal form and function. To satisfy its osteogenic capacity, biomimetic scaffolds for bone tissue engineering need to comply with both the physical and biological attributes of native human bone. Polymers alone are known to be relatively bioinert and mechanically weaker than cortical bone, however they are very easy to form into different shapes and sizes. Ceramics and metals can often be too hard and brittle, resulting in stress shielding or implant instability. One solution involves the use of composite blends of materials to exploit the favourable properties from each and reducing their negative attributes [6]. For instance, the mechanical strength of polymers can be improved through fibre and ceramic reinforcement [176] and their bioinert nature can be enhanced via the addition of bioactive compounds to promote osteogenesis [88].

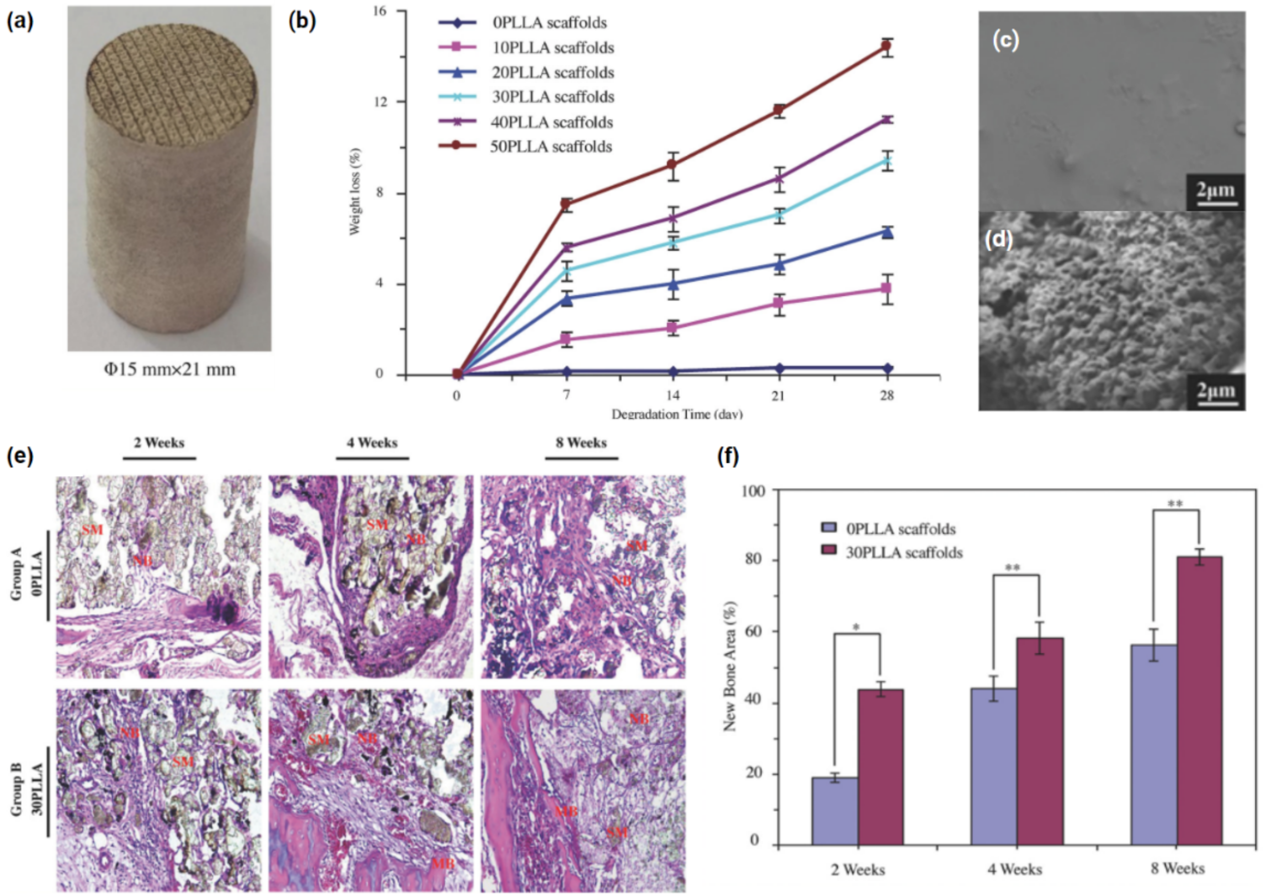

Figure 1.8 (a) Sintered composite cylinder containing PEEK/β-TCP/PLLA (5:2:3 wt/wt/wt), generated with Solidworks 2011 (Solidworks Corporation, USA) and converted to stereolithography (STL) format prior to printing with a CO_2 laser system (Rofin-Sinar Laser GmbH, Germany). A spot size of 500 μm, scan velocity of 120 mm/s, interval of 950 μm and a layer thickness ranging from 0.1 - 0.2 mm was used. (b) Weight loss behaviour of scaffolds during a 28 day PBS immersion, where the number represents the weight percentage of PLLA. (c&d) SEM micrographs of constructs with 0 and 30 wt% PLLA after 28 days in SBF solution. The histological images and quantitative analysis of new bone formation. (e) H&E staining images of the bone defect sections in the experimental group A and experimental group B after 2, 4, and 8 weeks of surgery (SM: scaffold material; NB: new bone; MB: mature bone). (f) Quantitative analysis of new bone (*$P < 0.05$, **$P < 0.01$). Adapted from [160]**.**

One of the first instances of composite sintering without organic solvents was described in 2003, where Tan *et al.* [74] physically blended HA (10-40 wt%) and PEEK powders to form grades of HAPEEK. Through increased laser energy they were able to SLS the composite at much lower part bed temperatures when compared to other studies of HT-LS. Unfortunately, with an increased HA ratio, the constructs became fragile and brittle, suggesting that high HA composition may not be suitable for load bearing implants. On the other hand, when HA particles were embedded into a polymer phase and partially exposed, this is potentially beneficial for improving PEEK's long term mechanical properties and osteogenic capacity. Fent *et al.* [160] incorporated a biodegradable polymer with a bioactive PEEK composite containing β-tricalcium phosphate (β-TCP), the three-phase material was SLS into porous cylinders (Fig. 1.8 a) with a CO_2 laser and a broad 500 µm spot size. The degradation rate was able to be tuned over 28 days by adjusting the concentration of the polymer Poly-L-lactic acid (PLLA) (Fig. 1.8 b), thus improving the apatite forming capacity of the scaffolds due to increased surface area and exposure to integrated β-TCP (Fig. 1.8 c & d). Following an 8-week rabbit implantation, H&E staining reiterated the improved bone forming ability (Fig. 1.8 e & f).

Polyamide (PA 12) has been blended with HA (78 wt%) to overcome modulus mismatching common with homogenous materials [161]. The study found that part porosity was significantly influenced by thickness of deposited powder layers, more so than laser energy density. HA nanoparticles have also been introduced to coat and reinforce PA 12 [162], revealing a 15-20% improved tensile strength and modulus at the expense of reduced elongation at break. Likewise, porous PA-HA composites have been sintered in various orientations to assess the impact on mechanical properties, both practically and theoretically [163]. Interestingly, vertically sintered dog bones had an improved compressive and tensile strength when compared to horizontally sintered, while strength improved overall with increased HA concentration from a 10.6 MPa tensile strength with PA-HA 95%:5% to 24.3 MPa in the PA-HA 80%:20%, similar trends were also observed following compression tests. PA has also been combined with glass beads [164] and carbon nanofibres [165] to improve the storage modulus by 22 % and tensile modulus by 1000 MPa, respectively. The former however, found the morphology of cryo-processed powder to be undesirable for SLS and resulted in uncontrollable surface morphologies.

HA has also been integrated into other polymers for SLS. HAPEX™ is a polyethylene composite containing 40 % Vol of bioactive synthetic hydroxyapatite filler [166]. As a bone analogue, HAPEX™ aims to overcome stress shielding and bone resorption at fixation points. The reinforcement of HDPE with HA improves the fracture toughness, over the purely ceramic material, whilst retaining its osteoconductivity *in vivo* [167]. A study by Savalani *et al.* [168] explored the use of 30 and 40 % HAPEX™ in SLS systems. They compared the use of both CO_2 and Nd:YAG lasers for powder coalescence. Interestingly the 'sintering window' of the CO_2 laser was determined to be wider, thus consistent printability was achievable, though fine optimisations were necessary. Slower CO_2 laser scanning velocities (below 600mm/s at both 3.6W and 7.2W) resulted in polymer degradation as the energy density was too high, on the other hand, at a scan velocity of 4800 mm/s and 7.2W laser energy, SLS parts become too brittle from insufficient necking/coalescence, thus a 1200 mm/s scan velocity was deemed suitable. For a comprehensive review of additive manufacturing approaches using HA composites, the reader is referred to a recent study by Milazzo *et al.* [169].

Composite SLS approaches have been used to improve osteogenesis. One study explored the use of PCL/HA microspheres in SLS. Specifically, they created multi-layered constructs that ranged from pure PCL to PCL + 30 wt% HA nanoparticles in 5 wt% increments throughout seven 400 µm layers [170]. The biomimetic gradient construct, from top to bottom, was intended to replicate articular cartilage and subchondral bone, respectively. Following a 12-week implantation in a rabbit model, gradient constructs showed improved trabecular bone formation when compared to pure PCL scaffolds, after µCT analysis. This was also consistent with both immunohistochemical staining for both cartilage and bone-specific proteins and the upregulation of chondrogenic and osteogenic genes following qRT-PCR analysis. Protein expression for both aggrecan (AGG) and collagen type II (COL II) were observed to be stronger in gradient scaffolds compared to the PCL and untreated control groups. On a genetic level, relative mRNA expression of chondrogenic markers AGG and COL II as well as osteogenic markers collagen type 1 and osteocalcin were all significantly upregulated in the gradient constructs. Another study utilising a PCL/HA composite created using SLS compared a range of nano-HA concentrations (i.e., pure PCL, PCL with 5 wt% nano-HA, PCL with 10 wt% nano-HA, and PCL with 15 wt%

nano-HA). Interestingly, using the same SLS parameters, scaffold porosity reduced, and the compressive strength improved with increased nano-HA concentration. With pure PCL resulting in an approximately 78.5 % porosity and 1.38 MPa compressive strength and PCL with 15 wt% nano-HA showing a porosity of 70 % and a compressive strength of 3.17 MPa. Following a 9-week rabbit femur implantation, the highest concentration of HA resulted in enhanced bone formation [171]. Another study explored the use of biodegradable polymer microspheres with an osteoconductive element. The polymer matrix was made up of either PHBV or PLLA and the bioactive element was either Ca-P or CHAp. The incorporation of calcium phosphate nanoparticles, improved SaOS-2 proliferation and ALP expression over the virgin PLLA scaffolds [88]. Several other papers have explored the use of HA reinforced composites for bone tissue engineering (Table. 1.2).

Table 1.2 Summary of composite sintering approaches outlining the specific print parameters uti-lised, physical attributes and biological outcomes of printed constructs. Where P = Laser Power, λ = Wavelength, S = Scan spacing, T = Layer thickness, V = Scan Velocity, Φ = Beam Diameter, E= Elastic modulus, σUC = Ultimate compressive strength.

Composite formulation(s)	Print specifications	Physical attributes	Biological response	Ref
PCL/HA In wt% ratios of 100:0, 90:10, 80:20 and 70:30	P = 1-1.2 W λ = 10.6 µm S = 152.4 µm T = N/A V = 914 mm/s Φ = 450 µm 50 ℃ bed temp	Increased HA concentration resulted in a higher E but a reduction in σUC	-	[172]
PCL/ β-TCP In wt% ratios of 100:0, 90:10, 50:50, NB 50:50 utilised smaller PCL particles	P = 7 W λ = 10.6 µm S = N/A T = 0.11 mm V = N/A Φ = 410 µm 49 ℃ bed temp	Increasing β-TCP content was found to decrease the strength	*In vivo* bone formation significantly lower in PCL/TCP sintered composite compared to pure β-TCP	[173]
PLLA/GO@Si-HA	P = 3.5 W λ = N/A S = N/A T = N/A V = 180 mm/s	Compressive strength and modulus improved by 85% and 120% after incorporating GO@Si-HA, with a marginal improvement in hardness	4 wk SBF: PLLA minimal, PLLA/GO minimal, PLLA/GO@Si-HA significantly improved apatite formation and MG-63 cell morphology and ALP activity after 7 days	[174]

PEEK PEEK/20%plyglycolicacid (PGA) PEEK/40%PGA	P = 100 W (max) λ = 10.6 µm S = 2.5 mm T = 0.1-0.2 mm V = 400 mm/min Φ = 800 µm	Increase in PGA concentration reduced compressive and tensile strength	PGA had no significant influence on MG-63 cell viability or morphology	[175]
Poly (vinylidene fluoride)/Bioactive glass 58s (PVDF/58s)	P = 100 W (max) λ = 10.6 µm S = 3 mm T = 0.1-0.2 mm V = 500 mm/min Φ = 800 µm	BG was found to be slightly exposed on the surface of scaffolds following EDS analysis	BG 58s addition improved osteoconductivity and osteoinductivity of scaffolds, following SBF and MG-63 cell seeding analysis	[176]
Aliphatic-polycarbonate/HA (a-PC/HA) a-PC a-PC/5 wt% HA a-PC/10 wt% HA a-PC/15 wt% HA	P = 11 W λ = 10.6 µm S = 0.15 mm T = 0.15 mm V = 2000 mm/s Φ = 200 µm 135 ℃ bed temp	Surface roughness and porosity (53 to 82 %) increased with HA content, below 15 wt% ideal 6 - 7 times reduction in scaffold strength with HA compared to pure a-PC	Osteoconductivity unchanged by SLS processing	[177]
Poly[3,6-dimethyl-1,4-dioxane-2,5-dione]/HA	P = 10 W λ = 1.06 µm S = N/A T = N/A V = mm/s Φ = 125 µm	Young’s modulus increased from 6.4 to 8.4 GPa with HA addition	Sintered composite scaffolds improved ATSC attachment and viability, compared to foaming method and virgin polymer	[178]

PVA/HA 90:10 vol % 10 - 75 µm 50 - 100 µm	P = 10 - 20 W λ = 10.6 µm S = N/A T = N/A V = 1270 - 2540 mm/s & 2032 mm/s 65 - 75 ℃ bed temp & 80 ℃ bed temp for larger particles	Ball mixing was found to be best for homogenous blends of PVA and HA when compared to tumbler mixer. Also larger particles prevented clumping during layer deposition	-	[179]
PCL PCL/TCP PCL/TCP/collagen	P = 1 W (PCL) & 2 W (PCL/TCP) λ = N/A S = 0.2 mm T = N/A V = 500 mm/s 40 ℃ bed temp	Significant improvement of compressive modulus with addition of TCP, col no difference	Improved pASC attachment, viability and osteogenic differentiation (ALP and osteocalcin) with TCP and TCP/col addition, ALP activity highest at day 7 for all scaffolds (over 28 days) Woven bone and vasculature observed *in vivo* with composites, pure PCL was full of fibroblasts and granular tissue	[180]

1.4 Conclusion

The incidence of bone related diseases and injuries is growing with the global ageing population. Additive manufacturing strategies currently hold significant promise in addressing many of the shortcomings associated with traditional bone grafting methods to treat these conditions, from constructing patient-specific implants directly from medical scan data to generating intricate internal architectures that recapitulate the hierarchical structure and dynamic mechanical properties of bone. Further, the ability to create composite materials through combination of bioactive materials with structurally robust or elastic materials whilst adding various cell types and biological cues enables a toolbox of options tailored to specific tissue types.

As the additive manufacturing technologies develop, so does our understanding of the relationship between print method, materials, and the human body. Further understandings, both qualitatively and quantitatively, between material and laser interactions may provide insights into the use of new materials for laser sintering. Additionally, new mechanisms for feeding material into the print bed may broaden material applicability. For instance, digital light processing systems have established rotating bed recoating systems to deposit microparticle layers of HA and TCP to produce high resolution parts for bone tissue engineering applications. Similarly, layer-wise slurry deposition has been developed to improve print bed powder density during printing, and thus improve the mechanical properties of prints. Combining these novel deposition techniques to laser sintering systems could hold the key to producing biomimetic bone for generating patient-specific implants.

Promising new advancements such as EBM [181] for metal printing to the use of bioactive coatings [180], antimicrobials and even drug delivery methods for powder bed fusion [182–187], will ensure that novel implants can be provided to patients in a timely manner, with the appropriate legislation and oversight from government and regulators. In creating these personalised implants, humans will be equipped with the necessary tools to mitigate the impact of bone-related illnesses and the overall disease burden. This burden can lead to superfluous stress on the healthcare sector and unpredictable economic impacts. These new additive manufacturing approaches also have the capacity to broaden the accessibility of the technology in the developing world, so that one day we can provide objective patient care and potentially engineer patient-specific tissues on a global scale.

1.5 Thesis Objectives & Outline

To develop new 3D printing techniques researchers and engineers must first identify the applications the printing process will be used for. Whether it be for functional parts in the aerospace field, or medical devices in the clinic. From this, the relevant materials can be established and the printer-material interactions investigated.

Chapter 1, aimed to define the use of additive manufacturing approaches in biomedicine. Specifically, how the use of powder bed fusion techniques, such as selective laser sintering (SLS) can be used to generate scaffolds and implants for bone tissue engineering applications. The chapter outlined the structure and regeneration mechanisms of bone, including how biomimetic bone scaffolds can be regulated and used to advance the field of bone tissue engineering. It also outlined the history of SLS and the most common materials currently used for bone tissue engineering applications, with a specific focus on polymers and composite materials. The work provides insights into how to develop a platform for future SLS systems by characterising the technical parameters used for different material sintering and the resulting physical and biological characteristics of the scaffolds produced.

Chapter 2 aimed to assess how HDPE could be printed. It hypothesised that spot welding through the use of SLS printing would be the most appropriate technique to generate porous implants for bone tissue engineering applications. It describes for the first time, the generation of a novel SLS technique for printing trilobal HDPE particles known as StarPore®. Specifically, a recoating platform that enables the spreading of polymer layers, was developed to interface with laser engravers. To estimate sinterability, a theoretical sintering model provided insights into the required energy density for efficient particle fusion, based on physicochemical attributes of the polymer. Prior to printing, the thermochemical properties of HDPE were investigated under the established theoretical sintering parameters. From this, a 'sintering window' was determined, between the polymers melting and recrystallisation points. Thermogravimetric analysis revealed polymer stability well above the required sintering temperatures. Single strut and single layer printing parameters were compared and quantified through in situ optical and infrared imaging techniques. Additionally, optimisations in laser scan strategies over a single polymer layer were conducted and monitored in real-time to establish a range of sintering parameters that provide sufficient particle coalescence.

Chapter 3 aimed to characterise the physical and mechanical attributes of printed HDPE in the form of StarPore®. It was hypothesised that, due to the inherent thermochemical properties of HDPE, all variables would have to be finely tuned to control porosity. Specifically, the physical and mechanical properties of single-layer and multi-layer printed constructs was tested with a comparison to commercially available moulded implants. Micro computed tomography revealed porosity of moulded constructs to be approximately 64% compared to the 76 - 94 % of printed constructs. The high porosity had a detrimental impact on compression and tensile properties of printed scaffolds showing a reduced welding capacity between particles, when compared to the commercially available moulded scaffolds. Likewise, 3D laser microscopy revealed significantly rougher surfaces and a broader range of strut thicknesses on printed scaffolds when compared to those moulded. Scanning electron microscopy was also used to investigate particle necking and coalescence.

Chapter 4 aimed to test the biological performance of printed implants, compared with market-available moulded implants. It was hypothesised that the increased porosity of printed constructs would improve tissue integration when compared to the moulded constructs. The bioactivity of printed and moulded scaffolds *in vitro* as well as their performance *in vivo*. A simulated body fluid assay revealed no inherent polymer bioactivity, with and without the addition of Bioglass. *In vivo*, however, the highly porous printed scaffolds showed a significantly higher tissue integration when compared to moulded scaffolds, after an 8 week subcutaneous implantation in rats. Additionally, printed scaffold immunohistochemistry provided evidence of initial stages of microvasculature not observed in moulded constructs.

Chapter 5 aimed to summarise all the research conducted through the dissertation and provide insights into the next steps. While each chapter contains a short introduction, methods, results, discussion and conclusion sections, chapter 5 serves to broaden the conclusions and future directions, beyond SLS for bone tissue engineering applications. In doing so, demonstrating the use of innovative 3D printing and materials approaches towards other tissue engineering and regenerative medicine approaches, including drug development and delivery as well as the use of machine learning to streamline progress efficiencies in 3D printing techniques. This is followed by references and the appendix.

1.6 Research Significance

The current state of bone implantation typically uses off-the-shelf products that may not match the defect site. Relying on these pre-manufactured shapes means surgeons often have to manipulate and shape the implants to accurately fit, prolonging surgical time and reducing theatre efficiencies. Mismatches between host tissue and implants, physical and mechanical properties, can result in dislodging and high infection rates, with the requirement of dual interventions. Coupled with the high costs associated with creating the moulds for the pre-made scaffolds, demonstrates the need for new fabrication methods.

Through the use of additive manufacturing, we can tailor scaffolds to accurately match the contours and internal characteristics of tissue lost. Using existing clinical scanning techniques, 3D models can be generated to precisely match defects. Additionally, through the use of finite element analysis, we can tune the mechanical properties to match surrounding tissue, alleviating any potential for stress shielding.

Sophisticated additive manufacturing techniques however, are often expensive and not accessible. This thesis, by employing an interdisciplinary skill set from clinician specialists, chemists, biologists and engineers, provides the template for improving additive manufacturing accessibility. The development of a custom recoating platform serves as a modular approach to powder bed fusion. It allows for existing commercially available laser engraver systems to be turned into 3D printers.

The previous section establishes the context of this work by outlining the need for new innovative approaches to bone tissue engineering. Regulatory hurdles are explored as well as novel SLS systems for the generation of implants with new materials. Identification of materials with favourable printing traits combined with those that have inherent bioactivity has the potential to revolutionise the medical device industry.

The successive chapters explore the development of a customised 3D printing platform capable of printing the regulatory approved HDPE device StarPore®. The material is investigated in the context of SLS printing and characterised in comparison to the current gold standard of moulded bone substitute materials. A focus on the two most important functions of bone is investigated, the mechanical and biological performance of printed implants compared to those made by moulding.

Ultimately, the significance of this body of work provides insight into how the development of novel SLS fabrication methods can be used for the generation of patient-specific bone implants.

CHAPTER

2

DESIGN & PRINTING

Chapter 2: Design & Printing

Overview

Initial inroads into developing a novel 3D printing method should distinguish both the material(s) being used, and the application of the print constructs. In this regard, powder bed fusion technology was deemed the most appropriate, from analysing the current literature landscape, for producing high density polyethylene (HDPE) bone substitutes for craniomaxillo facial (CMF) applications. This chapter explores the fundamental intrinsic and extrinsic HDPE properties, including thermochemical and morphological characteristics, in the context of the powder bed fusion technique, Selective Laser Sintering (SLS). Following which, a theoretical sintering model was used to gauge a broad set of print parameters. With the aid of *in situ* optical and thermal imaging, these parameters were quantified and adjusted appropriately. Single strut and single layer constructs were printed and the physical attributes were examined.

2.1 Additive Manufacturing Technology

The utilisation of additive manufacturing in tissue engineering has inspired the field of Biofabrication. In the context of tissue engineering and regenerative medicine, biofabrication can be defined as '*the automated generation of biologically functional products with structural organisation from living cells, bioactive molecules, biomaterials, cell aggregates such as micro-tissues, or hybrid cell-material constructs, through Bioprinting or Bioassembly and subsequent tissue maturation processes*'[188]. Several technologies have been explored to address bone tissue engineering challenges within the landscape of biofabrication or to generate scaffolds to support tissue regeneration (Table 2.1).

Table 2.1. An outline of additive manufacturing technologies, the materials used and the advantages and disadvantages suitable for generating bone tissue engineered substitutes.

Technique	**Materials**	**Advantages**	**Disadvantages**	**Ref(s)**
Stereolithography (SLA)	Photoactive resins (PEG, GelMA + composites)	Smooth surface finish, high resolution in XYZ, cost	Support removal difficult, resin is messy, limited materials	[189,190]
Digital Light Processing (DLP)	Ceramic -filled photoactive resin (Zirconia, HA, TCP + composites)	High speed printing, high resolution	Cost, support removal difficult, resin or slurry is messy, limited materials, lengthy post-processing	[191–193]
Fused deposition modelling (FDM)	Thermoplastics (PLA, PET, ABS, PCL + composites)	Highly accessible, cost, easy of use	Low resolution, layers visible, limited material choice	[194–196]
Selective laser melting (SLM)	Metals (Titanium, stainless steel, aluminium etc)	High resolution, high strength parts, no supports	Cost, material exchange, high temperature, warping, trapped particles, rough edges, post processing	[197–199]
Selective laser sintering (SLS)	Polymers (PA12, PCL, PEEK, HDPE etc)	Wide range of materials, no supports	Material exchange, trapped particles, rough edges, post processing, warping	[185,200]

2.1.1 Powder Bed Fusion

Arguably the most suitable additive manufacturing methods for bone tissue engineering applications are powder bed fusion techniques. Powder bed fusion employs the localised heating of a powder bed with light energy, typically from diode or CO_2 gas lasers, that fuse or coalesce adjacent particles over a two dimensional cross-section. Subsequent powder layers are deposited on top of the previous layer with either a roller or blade and the process is repeated. The two dimensional cross-sections are bound to the layers beneath until the three dimensional (3D) construct is realised. This method is suitable for bone tissue engineering as the powder bed itself acts as a support material, enabling the generation of hierarchical, internal architectures resembling bone. Additionally, intricate internal architectures can be generated with powder bed fusion, capable of matching the dynamic structure of human bone.

2.1.1.1 Selective Laser Sintering

The two main powder bed fusion technologies are selective laser melting (SLM), and selective laser sintering (SLS). The former typically employs metals such as titanium, stainless steel and aluminium alloys and the latter polymers, including polyamide, polyetherketone and polyethylene. The efficiency of both fabrication methods is measured by (i) scan speed, (ii) laser power, (iii) scan spacing and (iv) layer thickness. How SLM differs from SLS, relates to the laser's interaction with the material. Metals in SLM are completely melted to form a dense melt-pool, and can result in fabricated components with physical properties akin to the same wrought material. SLS on the other hand, doesn’t typically completely melt the material. Laser energy is used to elevate a localised temperature within the powder bed to just below the melting point of the polymer, to a glassy state, softening the material enough to enable fusion with adjacent powder particles.

The types of lasers used in SLS and SLM systems range from visible light diodes in the vicinity of 445 nm wavelength to 1064 nm Nd:YAG or fibre lasers all through the infrared spectrum towards 10 600 nm in the form of CO_2 gas lasers. Depending on the material being sintered different lasers can be used. For example, the common polymer polyamide or nylon (in the form known typically as PA12) can be sintered using either a 445 nm laser diode or a CO_2 gas laser at 10600 nm. Other examples can be found in Table 2.2. CO_2 gas lasers are the most common as several polymers and ceramics (oxides) absorb energy at 10600 nm, while metals and ceramics (carbides) absorb energy more efficiently at 1064 nm [201]. Materials capable of transmitting this wavelength are zinc selenide, used as the focus lens in the majority of laser cutters and ionic crystals such as potassium chloride and sodium chloride. The ionic crystals however, are quite hygroscopic, thus are not typically utilised as windows in laser systems.

Table 2.2 Specifications of lasers used in SLS and SLM approaches, adapted from [67]**.**

Laser type	**CO_2**	**Nd:YAG**	**Yb-fibre**	**Visible light**
Wavelength	10.6 µm (also 9.2, 9.4, 9.6 and 10.2 µm)	1064 nm	1080 nm	445 nm
Lasering medium	Gas	Crystalline rod	Doped fibre	LED
Beam transmission	Mirror, lens	Fibre, lens	Fibre, lens	Mirror
Output power	Up to 20 kW	Up to 16 kW	Up to 20 kW	MW to W
Efficiency	5 - 20 %	Lamp 1 - 3 %, diode 10 - 20%	10 - 30 %	Up to 95 %
Pump source	Electrical discharge	Laser diode or flashlamp	Laser diode	Electro-luminance
Operation	CW & pulse	CW & pulse	CW & puse	CW & puse
Duration	Hundreds of ns - tens µs	A few ns - tens ms	Tens ns - tens ms	Tens ns
Maintenance periods	2000 hrs	Lamp - 200 hrs, diode 10 000 hrs	None (>25 000 hrs)	None (>100 000 hrs)

2.1.1.2 Selective Laser Sintering Process

As outlined in the previous chapter, there are intrinsic and extrinsic properties that impact material printability. With the exception of novel high speed 3D printing techniques [202], printing typically spans hours. Slowly heating the print environment and allowing for powder to gradually get to the desired print temperature can prevent thermal gradients that can often result in part warping. Likewise, the cooling rate also significantly influences part consistency. Thus time and temperature are controllable variables that can drastically impact part quality. A timeline of the sintering process, adapted from [203], can be seen in figure 2.1.

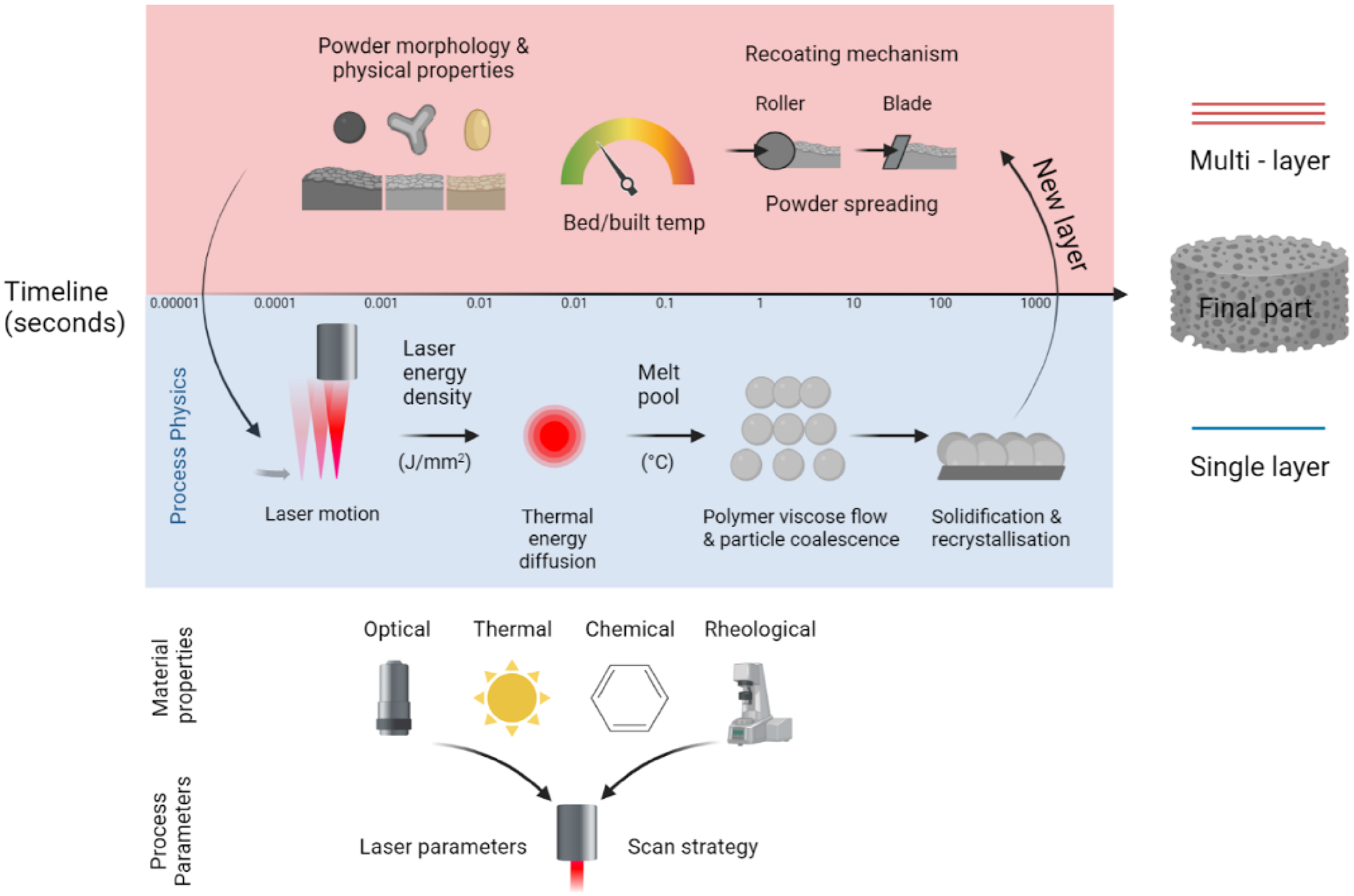

Figure 2.1 Timeline of the impacts on a polymer's physical properties during the SLS process. Adapted from [204]

Understanding the principles of SLS printing allows us to apply it to a broader range of materials. This chapter investigates the development of a custom recoating platform that interfaces with commercially available laser engraving platforms, one stand alone and one desktop system. The desktop system in particular is used as it is relatively accessible throughout the world. The recoater is developed with widely available 3D printing hardware, software and firmware, which is made from laser engraved acrylic and 3D printed components. While the process of HDPE via SLS is not new, no instance of printing trilobular structures as the starting powder has been conducted. Here, for the first time, we explore the generation of highly porous trilobular HDPE structures based on StarPore® for bone tissue engineering applications. The material is characterised physicochemically to accurately develop a set of printing parameters and scan strategies in the context of SLS. A theoretical model is generated to estimate scan strategies, while *in situ* thermal imaging is used to gauge particle behaviour during printing. The physical attributes of the particles are defined including the influence of packing and spreading in the powder bed. Finally, single strut and single layer scaffolds are printed under the established conditions.

2.2 Experimental Section

2.2.1 Materials

HDPE powder in the form of StarPore® was supplied by Anatomics (Melbourne, VIC, Australia).

Sample preparation. A novel selective laser sintering (SLS) technique was employed to fabricate high density polyethylene (HDPE) scaffolds. Trilobal HDPE particles, within the order of 600 µm in diameter, were commercially manufactured and marketed as StarPore®, supplied by Anatomics (Bentleigh East, VIC, Australia). The powder was spread onto a sintering platform in 0.75 - 1 mm layers housed inside a 30 watt CO_2 laser engraver (Universal laser systems). Powders were exposed to a range of laser powers, among other variables (Table 2.3).

Table 2.3 Sintering parameters for scaffolds, NB processing was performed within a humidity and temperature controlled laboratory environment

	Inputs	**unit**	**Lower bound**	**Upper bound**	**Value**
Variables	Laser power	W	16	24	
	Laser velocity	mm/s	50	125	
	Hatch spacing	mm	0.50	1	
	Scan length	mm	10	20	
	Layer thickness	mm	0.5	1	
	Laser spot diameter	µm	127	304	
	Post processing	°C	0	120	
	Laser passes	No.	1	3	
	Bed temperature	°C	Ambient	100	
	Powder preparation	mg/ml	Dry	Slurry (800)	
Constants	Humidity	%			50
	Ambient temperature	°C			22

2.2.2 Laser Systems Design and Software

Two CO_2 laser (λ 10.6 µm) engraving systems were used during this work, a PLS6MW (Universal Laser Systems [ULS] GmbH, Vienna, Austria) and a K40 (VEVOR, Shanghai, China). The ULS utilised a 30-watt laser tube and the K40 a 40-watt laser tube. Both systems utilise a zinc selenide focus lens, resulting in a 127 µm diameter spot size at the focus point. In vector mode the ULS laser head can accelerate up to 500 mm/s with the K40 up to 100 mm/s. The software packages utilised to control the ULS system were Universal Control Panel (UCP) and the Laser System Manager (LSM) (Universal Laser Systems GmbH, Vienna, Austria) and for the K40, K40 Whisperer (Scorch Works) and LightBurn (Pulse Laser Systems). STL's were generated from a variety of software packages including Magics™ and Mimics™ (Materialise, Leuven, Belgium), Inventor (Autodesk, San Rafael, California) and Fusion 360 (Autodesk, San Rafael, California). Software used to generate

G-Code was IceSL Slicer 2.4.0 for the conversion of STL to SVG and Inkscape for SVG manipulation and export.

2.2.3 Re-coating Platform Design and Software

A custom re-coating platform was designed and developed. Inspired by the OPEN-SLS platform (RepRap)[125], the system employs two Z-axis' and one Y-axis with a re-coating blade attached. A heated substrate was added to the print bed and ceramic heaters used to control the surface temperature of both the print and the feeder areas. The print volume was designed to be 60 x 60 x 60 mm (XYZ), with a removable overflow bin to collect excess powder for recycling. Nema17 stepper motors control each axis, custom nylon 3D printed mounts hold the print bed and feeder bed. The whole system is built from 3 mm laser cut acrylic sheets.

The system is based on an Ultimaker™ PCB control board (Ultimaker BV, Utrecht, The Netherlands), Marlin firmware and an Arduino Mega microcontroller (Arduino LLC, Massachusetts, USA). A PC equipped with Repetier-host (Hot-World GmbH & Co. KG, Willich Germany) sends the G-code commands (Appendix 1) to control the re-coating system.

2.2.4 Theoretical Sintering Model

A theoretical sintering model was developed prior to printing to approximate the process parameters at the initial stage of sintering and alleviate extensive trial-and-error testing (Appendix 2). The model assumes a surface heat source, disregarding penetration depth through a porous bed, as gas within voids has a low thermal conductivity when compared to the polymer powder. Thermal gradients observed during multi-layer sintering [204] from the time delay and cooling effect were assumed constant. The model also assumes a Gaussian distribution of laser energy. Additionally, the model ignores the obscure particle shape, as accurately modelling the irregular structure would require excessive computational power, and alternatively assumes the use of homogeneous spherical powder particles. The constants used for HDPE can be found in Table 2.4.

Table 2.4 Material constants of HDPE.

Material constant	**Value**
Density HDPE	0.965 g/cm^3
Density of StarPore® powder bed (ρ_{powder})	0.323 g/cm^3
Specific heat capacity	1.9 J/gK
Melting temperature	132 °C
Thermal conductivity	0.485 W/mK
Beam diameter	0.127 µm

Half neck radius, Initial particle radius, Surface energy, Viscosity, Sintering time

$$y/a \;=\; [P/\,(V\,x\,S)]$$

To optimise the SLS process, an approximation of energy density can be calculated. Nelson, J. C. *et al. [76]* described energy density (E) per unit area (J/mm^2) of polymer-coated silicon carbide powders through the relationship of laser power (P) as a function of laser beam velocity (V) and scan spacing (S) and (equation 1).

$$E \;=\; [P/\,(V\,x\,S)] \tag{1}$$

The equation was later amended to compensate for beam penetration and energy diffusion through a known volume [77], assuming the material thickness is optically transmissible, where: T = layer thickness, given in (J/mm^2) (equation 2) [78].

$$E \;=\; [P/(V\,x\,S\,x\,T)] \tag{2}$$

2.2.5 Intrinsic and Extrinsic Polymer Characterisation

2.2.5.1 Thermal Degradation Kinetics

Thermogravimetric Analysis (TGA) was conducted with the TGA Q500 instrument (TA Instruments) to characterise the thermal decomposition of HDPE before and after laser exposure, to understand the impact of sintering on the polymer chains. The samples were run in the presence of nitrogen 20 ml/min and under an atmospheric environment with nitrogen and oxygen being fed into the chamber at 20 ml/min. Alumina crucibles (Netzsch, Germany) were filled with approximately 10 mg (± 0.2 mg) of polymer. Samples were heated from room temperature (20 °C) to 850 °C at 5 °C/min, where n = 5. Additionally an isothermal test was also conducted to understand polymer stability. Samples were heated from room temperature (20 °C) to 200 °C at a rate of 10 °C/min and held there for 2 hours before being cooled back to room temperature (20 °C).

2.2.5.2 Melting and Re-crystallisation Characteristics

Differential Scanning Calorimetry (DSC) was completed on a DSC Q100 (TA Instruments, New Castle DE, USA) to assess the correlation between the heat flow and the temperature of the HDPE powder. Concavus aluminium pans (Netzsch, Germany) were filled with approximately 5 mg (± 1mg) of polymer and press sealed. An empty reference pan was placed in one furnace adjacent to the polymer. Temperature was cycled from room temperature (20 °C) to 250 °C and back at 5 °C/min and repeated twice to remove any thermal history from the polymer. The reference and sample chambers were both maintained under nitrogen at 20 ml/min. To mimic the sintering environment, the chambers were also filled with oxygen at 20 ml/min without thermal cycling.

2.2.5.3 Chemical Fingerprint

The chemical fingerprint of HDPE before and after sintering was determined through Fourier Transform-Infrared Spectroscopy (FT-IR) on the IRPrestige-21 spectrometer (Shimadzu, Tokyo, Japan) to ascertain whether any chemical changes occurred during lasing. Samples were analysed in their solid state with a diamond attenuated total reflection (ATR) accessory (Shimadzu ATR 8800M, Tokyo, Japan), in the range 4 000 – 600 cm^{-1} at a resolution of 5 cm^{-1}, after 32 sweep scans. Atmospheric corrections were made when processing spectra in Shimadzu IRsolution (Shimadzu, Tokyo, Japan) to eliminate moisture and carbon dioxide from the spectra along with Happ-Genzel apodization, ATR correction, smoothing and baseline correction algorithms.

2.2.6 Physical Characterisation

2.2.6.1 Powder Analysis

StarPore® powder was first sorted with sieves (ASTM E11) from Advantech (Wisconsin, USA) with apertures of 900 µm, 600 µm and 300 µm, known as 60, 30 and 20 mesh sizes respectively. 20g of powder was weighed and sieved through all sieves stacked from 900 - 300 µm. From there, a turbine vibrator was attached onto the sieves and agitated for 5 minutes, with the frequency of vibrations being adjusted by air pressure between 2 - 6 bar, following which the powder remaining on each sieve weighed (as a percentage of 20 grams) this was repeated 5 times. Following sorting, particles within the 600 - 300 µm range were analysed via optical light microscopy (Leica M205A, Wetzlar, Germany) to gauge body diameter, arm length and particle depth, where n = 20.

2.2.6.2 Bed Density

Powder bed density was measured following 3 different re-coating speeds (20, 40, 60 mm/s) over 3 depths (0.5, 0.75, 1 mm), in both a dry state and slurry state 800 mg/ml of StarPore® in water). The powders were spread over a 60 x 60 mm build plate and the dry weight of the powder within the print area was measured.

2.2.6.3 Hauser Ratio

Powder flowability was measured by comparing the tapped powder density to the bulk powder density (Ep. 3), established previously [205,206]. Firstly, a 100 ml plastic measuring cylinder was weighed on a calibrated micro scale. Then StarPore® powder was added to the cylinder and weighed ($\rho bulk$). The full measuring cylinder was then placed on a hard surface and tapped by hand at a frequency of 0.5 Hz for 2 minutes under ambient conditions ($\rho tapped$) and repeated ten times. The HR was determined by Equation 3.

$$HR = \frac{\rho tapped}{\rho bulk} \tag{3}$$

1. HR < 1.25: easily fluidised
2. 1.25 < HR < 1.4: decreasing fluidization behaviour
3. HR > 1.4: fluidisation problems

2.2.6.4 Single Particle Heating

Powder behaviour during heating was visualised by placing a heated peltier plate beneath an optical light microscopy (Leica M205A, Wetzlar, Germany). ImageJ was used to determine the increased particle geometry and surface area during the process, where n = 10.

2.2.7 Printing

2.2.7.1 Single Strut Printing

Initial, single-strut printing involved rastering a straight 40 mm line with laser energy densities ranging from 0.03 - 1.20 J/mm^2. A Leica M205A (Leica Microsystems, Wetzlar, Germany) fitted with a Leica IC80 HD (Leica Microsystems, Wetzlar, Germany) integrated camera and auto montage software (version 3.8) was used to qualitatively assess coalescence a 10 regions along each strut, where n = 5. For single-layer prints, 20 x 20 mm squares were sintered with either 1 mm or 0.5 mm spacing, and examined via light microscopy, μCT and SEM.

2.2.7.2 Single Layer Printing

Thermal imaging with the FLIR C2 (reported accuracy of +/- 2 °C or +/- 2% @ 9 Hz), used in conjunction with the FLIR ThermaCAM Researcher Pro 2.10 Software, (FLIR Systems, Wilsonville, OR, USA) was used to assess temperature of the printed bed during sintering, with the process parameters determined via the model. The camera was placed perpendicular to the laser at a 45 degree angle facing down to the print bed (Fig. 2.2). Optical and infra-red images were overlaid to identify temperature increase for each laser pass. Energy densities of 0.36, 0.40, 0.46 and 0.53 J/mm^2 were compared, where n = 5.

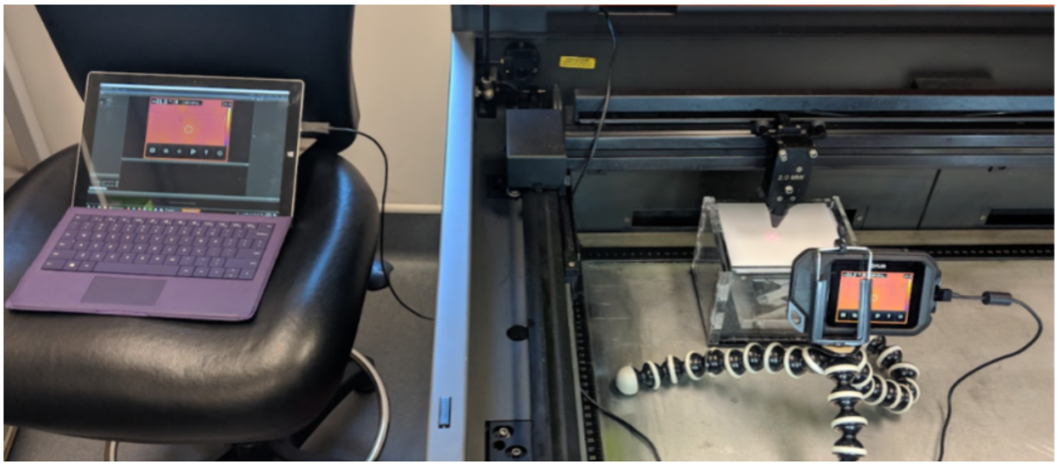

Figure 2.2 Thermal camera (FLIR C2) set up for monitoring SP sintering. The usb cable was routed through a hole in the laser cutter to a windows PC that was used to record IR video in real-time.

2.2.7.3 Multi-layer Printing

Multi-layer printing was conducted under the same parameters of the single layer printing with energy densities of 0.36, 0.40, 0.46 and 0.53 J/mm^3 (n.b. The use of J/mm^3 for multi-layer printing as the layer height varies). A 60 x 60 x 2 mm HDPE square substrate made from a thermal press was added above a 50 x 50 mm ceramic, 20 V thermoelectric peltier chip module TEC1-12720 (Sunyon Industry Co. Ltd Dongguan) and heated to 100 °C prior to printing. 20 x 20 mm (XY) scaffolds were printed at 18 W with a scan spacing of 0.75 mm, with a first layer height of 1 mm and subsequent layers of 0.75 mm.

2.2.7.3 Slurry Printing

A slurry was made by mixing 800 mg/ml of StarPore® in water. Print parameters were the same as above with the exception of double and triple scanning of the same area.

2.3 Results and Discussion

2.3.1 Printer Development

Two laser engravers, a commercial standalone ULS system (Fig. 2.3 a) and a desktop K40 (Fig. 2.3 b), were utilised throughout this work. Both were equipped with the same recoating platform (Fig. 2.3 c & d), controlled by Arduino and Ultimaker boards (Fig. 2.4 b & c). The build volume of the print platform was 60 x 60 x 60 mm (XYZ), with a modular and portable design capable of being placed into any system. Both systems employ CO_2 laser tubes that guide the laser beam through a series of mirrors, in X and Y, toward a laser head that fires directly down through the Z axis. The Z-axis platform on the ULS system was set to its lowest point to ensure the focus point of the laser was at its highest energy. The cone nozzle, used to guide the inert gas shields, had to be removed to prevent obstruction from the recoater.

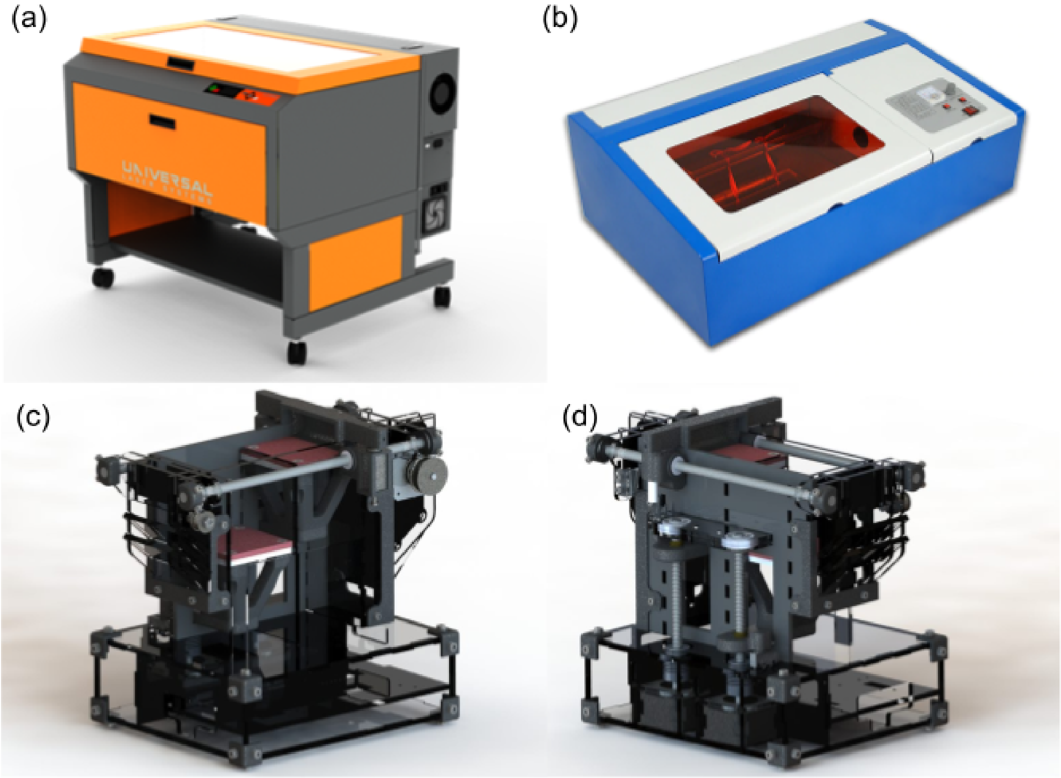

Figure 2.3 (a) Render ULS laser engraver [207], **(b) Render of the K40 system** [208], **(c) & (d) Solidworks renders of the front and rear of the recoating system**

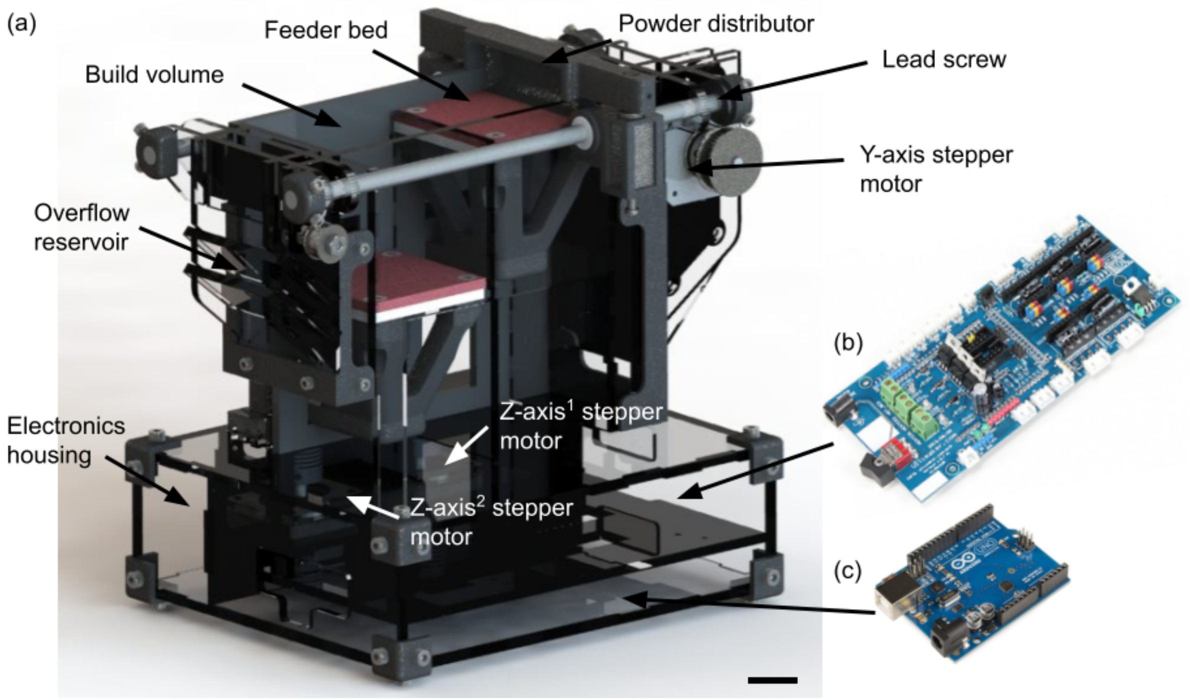

Figure 2.4 (a) Render of the recoater with labelled components, scale bar = 20 mm, (b) Ultimaker V 1.5.7 board, (c) Arduino Uno board.

The bottom of the K40 system was cut out and structural support was added via Extruded aluminium profiles to allow room for the recoating system to be placed beneath the laser head (Fig. 2.5 c). An additional interlocked access point was placed at the front of the system for easy access to the recoater. Safety switches and grounding wires were hardwired into the system to prevent laser operation when doors and access points were open (Fig. 2.5 b). A Raspberry Pie 3+ was mounted to the side of the system to control the software to run both the laser (K40 whisperer) and the recoater (Repetier-host) as well as 3D modelling and G-code generating software. A 3D printed exhaust port was made to interface with the lab exhaust system and an upgraded fan was installed to improve extraction of fumes and smoke and minimise their effect on printing conditions (Fig. 2.5 d)

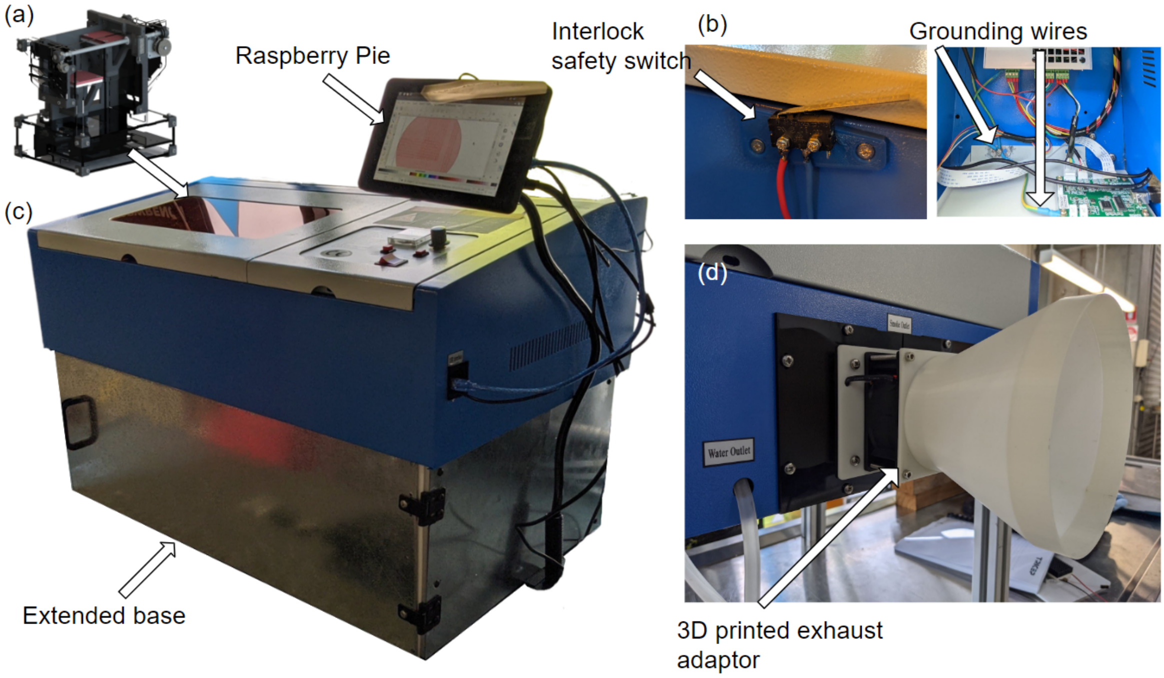

Figure 2.5 (a) Render of the recoater with labelled components, scale bar = 20 mm, (b) Ultimaker V 1.5.7 board, (c) extended base of the system, (d) 3D printed exhaust port adapter from 5 inch to 6 inch.

The laser path throughout both systems followed the same route. Initially, the CO_2 gas tube is excited and irradiated towards a sequence of mirrors followed by focusing by a zinc selenide lens until it converges to a high energy spot on the material, in this case a powder bed (Fig. 2.6). The re-coating system is made up of a supply or feeder chamber and build chamber. Firstly a thin layer of material is dispensed across the build platform from the supply chamber stepping up and a blade spreading material throughout the area. Following laser scanning, the process is repeated until a 3D object is realised.

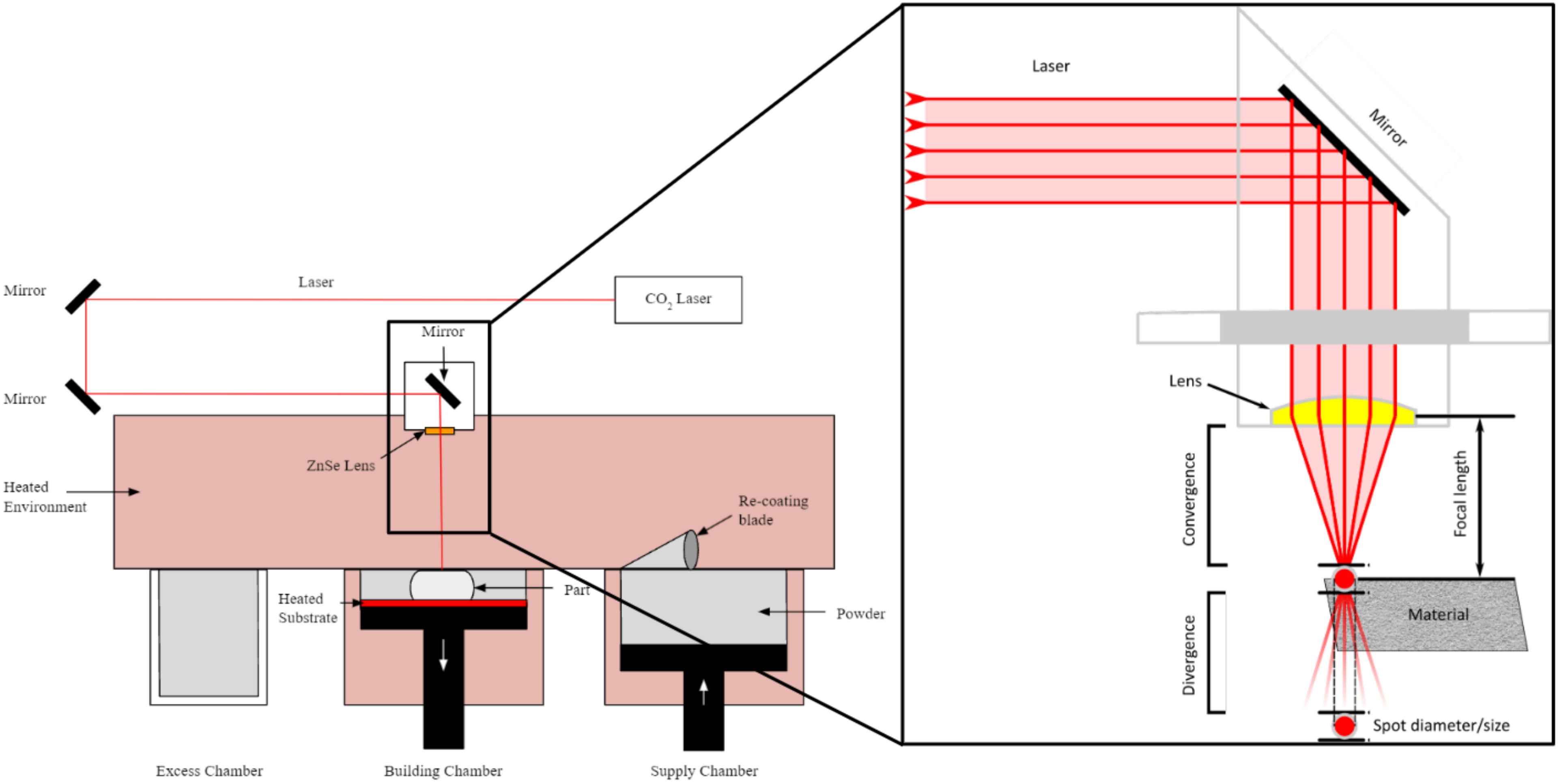

Figure 2.6 Schematic of laser path and re-coating schematic, with an outline of the laser path through StarPore®.

2.3.2 Powder Characteristics

2.3.2.1 Morphology, Size and Spreading

Extrinsically, particle size and shape can influence SLS part properties. Typically, spherical particles are used to ensure consistent flow and spreadability during powder re-coating, preventing stickiness and caking. The three main types of 'spherical' particles most commonly microspheres, potato or elliptical shaped particles and cryomilled particles [75]. The shape and size of these particles directly impacts density and consequently, the mechanical properties of prints. The irregular shape and large size of StarPore® were investigated to determine particle size distribution. Figure 2.7 a shows an average particle size distribution of approximately 500 μm, with 90 % of the 20g samples residing within the 300 - 600 μm range. Characteristics of the irregular shape of the particles were also quantified (Fig. 2.7 a), with an average particle body area found to be 0.087 cm^2, arm length and width of 0.460 mm and 0.232 mm, respectively. The average particle depth or thickness was determined to be 0.315 mm (Table 2.5). While these morphological measurements were derived from two-dimensional scanning electron microscope images, the irregular shape meant that atypical methods were necessary to assess powder morphology, beyond circularity and aspect ratios commonly used to quantify powders in powder bed fusion systems [209–211].

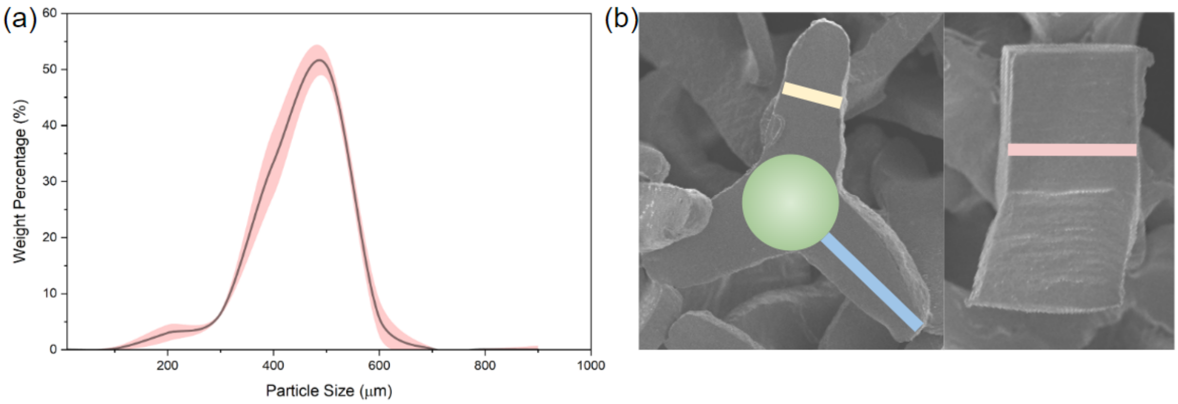

Figure 2.7 (A) Particle size distribution as a weight percentage of 20g batches, where n=5 (red represents the standard deviation). (B) Scanning Electron Microscope image of the face (left) and depth (right) of a typical StarPore® particle, where yellow = arm width, blue = arm length, green = body area and pink is the particle depth, where n = 50.

Table 2.5 A summary of StarPore® shape characteristics, assessed by SEM, where n = 50.

Characteristic	Average size ± S.D
Arm width	0.232 mm ∓ 0.030
Arm length	0.460 mm ∓ 0.065
Body area	0.087 cm^2 ∓ 0.015
Depth	0.315 mm ∓ 0.011

Powder flowability plays a fundamental role in ensuring part consistency [212,213]. It should be noted that "powder flow properties" and "powder flowability" are slightly different phenomena. The former relates to the interactions between powder particles, whereas flowability is the powder-equipment interaction [214]. Thus to understand the behaviour of StarPore® in an SLS system a Hauser Ratio (HR) was first established (Table 2.6). If a material's HR ranges between 1.00 - 1.11 it is considered to have excellent flowability. Virgin, unsintered StarPore particles were found to have a HR of 1.105 ∓ 0.014, residing in the excellent range of flow character. Similarly, the recycled material was also found to have excellent flowability, with a HR of 1.087 ∓ 0.031. Note the higher standard deviation was mostly likely correlated to the presence of partially sintered powder clumps. The cryomilled HDPE powder, on the other hand, was found to have a HR of 1.220 ∓ 0.025, above the excellent and even good range of powder flow character and within the fair range of 1.19 - 1.25 [215].

Table 2.6 Hauser ratios derived from bulk and tapped densities of Starpore® powder, recycled StarPore® material leftover from sintering and cryomilled HDPE pellets, given as average ∓ S.D. where n = 10.

Material	Bulk Density (g/ml)	Tap Density (g/ml)	Hauser Ratio
Starpore®	0.3469 ∓ 0.009	0.3833 ∓ 0.011	1.105 ∓ 0.014
Starpore® (recycled)	0.3342 ∓ 0.021	0.3632 ∓ 0.016	1.087 ∓ 0.031
Cryomilled HDPE	0.2142 ∓ 0.018	0.2612 ∓ 0.029	1.220 ∓ 0.025

If layers are not homogeneously distributed, resulting prints can be irregular, highly porous and weak [216]. The speed and thickness of layer deposition, as well as part size and shape all impact bed density. While part size and shape are not controllable variables, re-coating speed and layer height are. The powder bed density following blade re-coating of StarPore® was found to range between 17.3 - 27.1 % (Fig. 2.8). As expected, this is below the bed densities typically observed in SLS systems [217]. This is as the irregular particle shape can reduce the free-flowing behaviour resulting in particle cohesion and friction. Additionally, uncontrollable shifts in particle orientation were found to dislodge and flick adjacent particles, resulting in a further reduction in bed density, thus no significant differences were observed with increases in re-coating speed from 20 - 60 mm/s. Layer height however, did result in significant bed density variation, with the 0.5 mm step height revealing densities below 20 %. As 0.5 mm below the particle size threshold, thus a step size of 0.75 - 1 mm was deemed more appropriate, approaching the 30 % density known to print useful parts. Interestingly, the 1 mm layer height showed the highest bed densities overall, as voids could be easily filled with more powder. However, a 1 mm step size often resulted in stacked particles which could hinder homogenous coalescence during printing. Therefore, based on these results, a speed of 40 mm/s, with a first layer of 1 mm and subsequent 0.75 mm layers was established as a good balance of speed and thickness to ensure a single particle layer was achieved consistently.

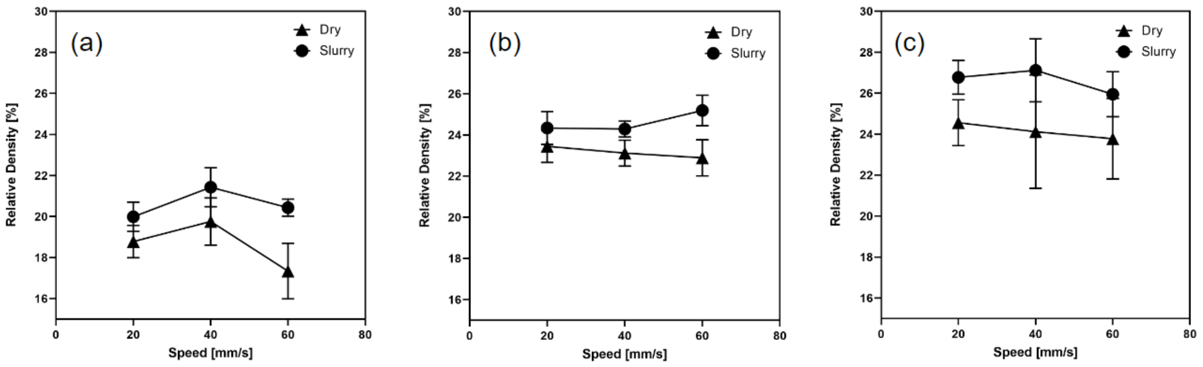

Figure 2.8 Recoating bed density at a layer thickness of 0.5 mm (a), 0.75 mm (b) and 1 mm (c) as a function of blade speed, given as average ∓ S.D. where n = 10.

2.3.3 Theoretical Sintering Model

There are several mechanisms behind SLS powder coalesce all centering around temperature. Thus the binding kinetics can be simplified with regard to temperature. Attempts have been made to model the SLS process with the assumption of a homogeneous spherical powder bed [218–220]. Modelling the necking of polydiverse or nonspherical powders was outlined by [221], where three structural parameters were identified for effective conductivity, namely the powder bed relative density, the mean coordination number and the contact size. The model suggests the thermal conductivity is proportional to the linear dimension of contact.

The outcomes of the SLS process are difficult to predict. While there are established constants for materials, as theoretically, any thermoplastic powder can be sintered, as long as they are softened or melted with heat (by laser radiation) [75,102], distinct variables arise between laser technologies and printing hardware used. The consistent consolidation behaviour however, makes it difficult to fuse certain polymers [126,165]. The two fundamental process parameters used to model SLS are laser powder (W) and laser velocity (mm/s) which equates to an energy density over a known area. Utilising the bed densities determined in the previous section, a theoretical sintering model for HDPE was established (Appendix 2). Four simulations were run to determine particle coalescence as a function of laser power, speed or laser velocity, layer height, beam diameter and build chamber temperature were all compared (Fig. 2.9 a-d). As laser speed increases the amount of power required to melt the polymer also needs to increase. From this we can also determine the range of energy densities required for coalescence. Laser speed, often referred to as scan velocity, between 25 - 150 mm/s will impact necking between HDPE particles at laser power between 18 - 22 watts. Interestingly, the only scenario which required more than 40 watts (W) of laser energy was when layer heights exceeded 1 mm (Fig. 2.9 b). While the K40 is capable of outputting 40 W of laser energy, running it at its highest capacity will accelerate degradation [222,223], thus < 30 W was utilised in all experiments. Additionally, manipulating scan strategies can alleviate the need for increasing energy into the print area [224–226] (this idea will be explored later). It is worth noting that the model assumes spherical particles as the computational power necessary for modelling a bed density for irregular shaped particles may be excessive [227]. Another shortcoming of this basic simulation is the model cannot determine ideal build orientation due to the anisotropy of the SLS process [228], it was merely used as a guide to ensure a streamlined printing approach.

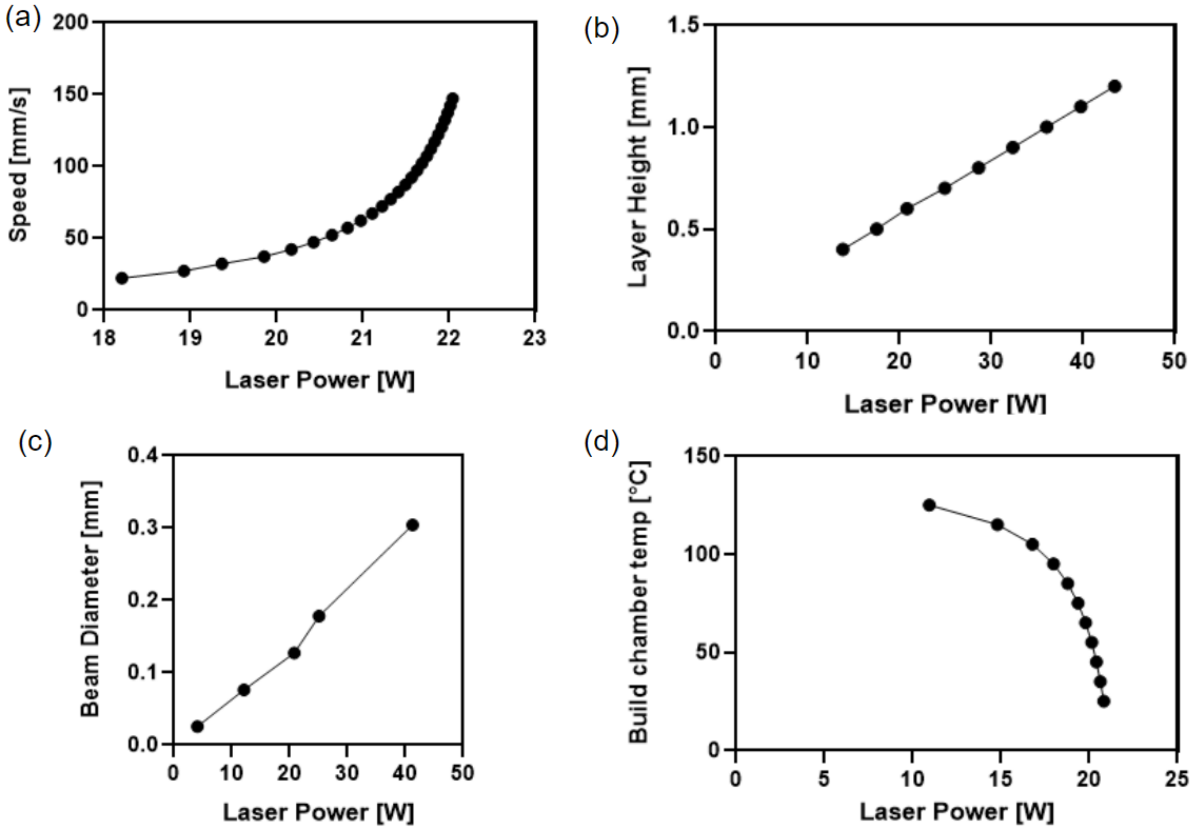

Figure 2.9 Theoretical sintering simulations (a) Laser power in watts as a function of speed in mm/s, at room temperature with a layer height of 0.75 mm and beam diameter or spot size of 127 µm (b) Laser power in watts as a function of single layer height of powder in mm, at room temperature with a beam diameter or spot size of 127 µm (c) Laser power in watts as a function of laser beam diameter or laser spot size in mm, simulated with a layer height of 0.75 mm, at room temperature and scan speed of 57 mm/s (d) Laser power in watts as a function of build chamber temperature, simulated with a layer height of 0.75 mm, at room temperature and scan speed of 57 mm/s and a spot size of 127 µm.

2.3.4 Thermal and Chemical Characterisation

A polymer's thermal behaviour is one factor that dictates sinterability. The upper limits of which can be gauged through TGA. HDPE, the base polymer of StarPore®, was found to degrade 5 % up to 420 °C, with rapid, irreversible degradation beyond this (Fig.

2.10 a), consistent with previous findings [229,230]. This is associated with the decomposition of molecular bonds through oxidation. Vasquez *et al. [231]* suggested that a 1 % reduction in polymer mass was deemed to be the beginning of degradation, which was found to be 373 °C. At 486 °C only 5 % of polymer remains, resulting in complete decomposition above this temperature. To ensure oxidation does not occur within the processing range of SLS, an isothermal analysis was also conducted. From preliminary *in situ* thermal imaging (outlined in the next section), sintering temperature did not exceed 200 °C within the energy density range for effective particle coalescence. Thus, HDPE was maintained at 200 °C for 2 hours without any measurable degradation (Fig. 2.10 b). This is well above the 95 - 100 °C print bed temperatures previously utilised during HDPE sintering [141,144].

To mimic the sintering environment, TGA was also run in the presence of oxygen. A shift in polymer degradation was observed, particularly following laser energy exposure. Prints that were exposed to 0.30 J/mm^2, lost 5 % of their weight by 371 °C and those at a higher energy of 0.40 J/mm^2 at 323 °C (Appendix 3). This can be attributed to thermo-oxidative degradation which can influence the crystallinity of the polymer, as HDPE degradation is well established in literature [232–235]. While degradation did occur, this is well beyond the processing temperatures the polymer is exposed to during printing, and thus may not tarnish material performance after a single print.

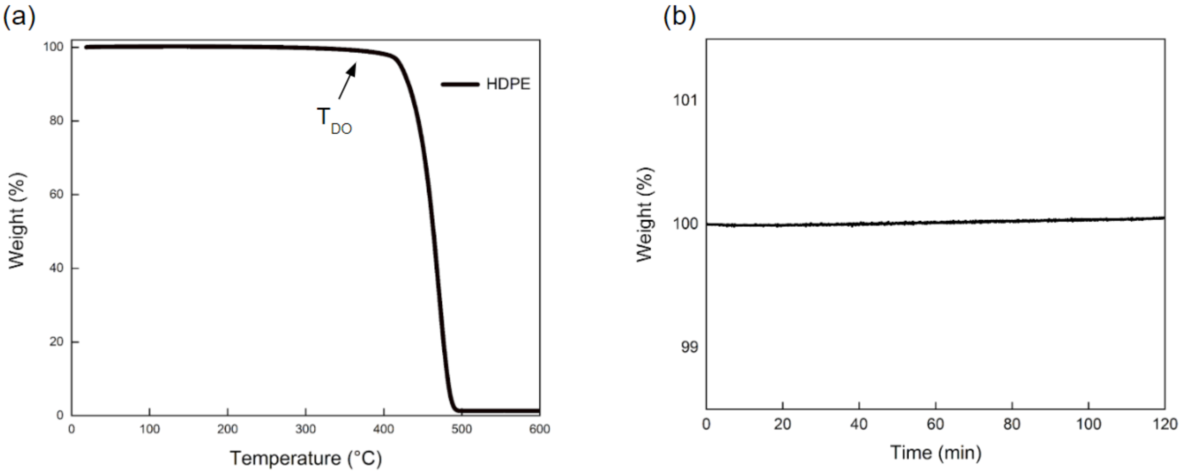

Figure 2.10 (a) Thermogravimetric Analysis of HDPE. (b) Thermogravimetric Analysis isotherm of HDPE over 2 hours at 200 °C.

For efficient SLS of semi-crystalline polymers, dissecting DSC and identifying a ‘sintering window’ is paramount. This temperature ‘window’ exists between the polymer’s endothermal melting point (T_m), where polymeric chains relax and move from a semi-crystalline to amorphous phase, and exothermic re-crystallisation point (T_c), where there is a release of excess free energy as the polymer transitions from an amorphous solid to a semi-crystalline solid. The window for HDPE was determined to be between 119 ℃ and 128 ℃, approximately 9 ℃ (Fig. 2.11), inline with previous findings [236–239]. Additionally, the degree of crystallinity of the polymer did not change during thermal cycles, suggesting no detrimental impacts to the polymer backbone would be instigated while sintering. It should be noted that while DSC measurements are typically taken after the second or third melting and cooling cycle to remove the polymer’s thermal history as well as ensure reliability, this data was derived from the first cycle in order to mimic the print process.

Interestingly, typical sintering windows for polymers utilised in SLS span a broader range, with PE shown to be 14 ℃ [224] and PA 12 extending over 30 ℃ [75,240,241]. A narrow window introduces difficulties such as incomplete fusion from low energy densities, to the trapping of gases within the polymer melt as a result of rapid crystallisation[54], when the energy density exceeds the window. Not only can excessive energy density reduce part resolution and accuracy but also result in powder caking, a phenomenon which fuses adjacent particles to the part through unwanted thermal diffusion [242]. Broadening these sintering windows is possible through the use of IR absorbers such as carbon black [236] or specific thermal treatments, though the procedures are kept confidential by material manufacturers [243].

In the context of SLS the relationship between T_c and T_m can dictate part quality [244]. For instance if the temperature during sintering is too low, and close to the T_c, incomplete coalescence can occur, where particles either partially fuse or don’t fuse at all. The resulting constructs can be brittle and may have loose particles within them that significantly reduce part quality [106,245,246]. On the other hand, if the sintering temperature exceeds the T_m, unpredictable lateral growth and bleeding can occur through a drop in polymer viscosity, which can jeopardise part resolution and porosity. Additionally, rapid cooling can be as detrimental to part quality as rapid heating, leading to warping and curling [247]. The semi-crystalline state of HDPE, is known to exhibit significant shrinkage upon reaching T_m when compared to amorphous polymers. Thus managing the thermal gradients during the printing process can result in consistent print outcomes while ensuring polymer longevity and stability, particularly useful for material recycling, common during SLS.

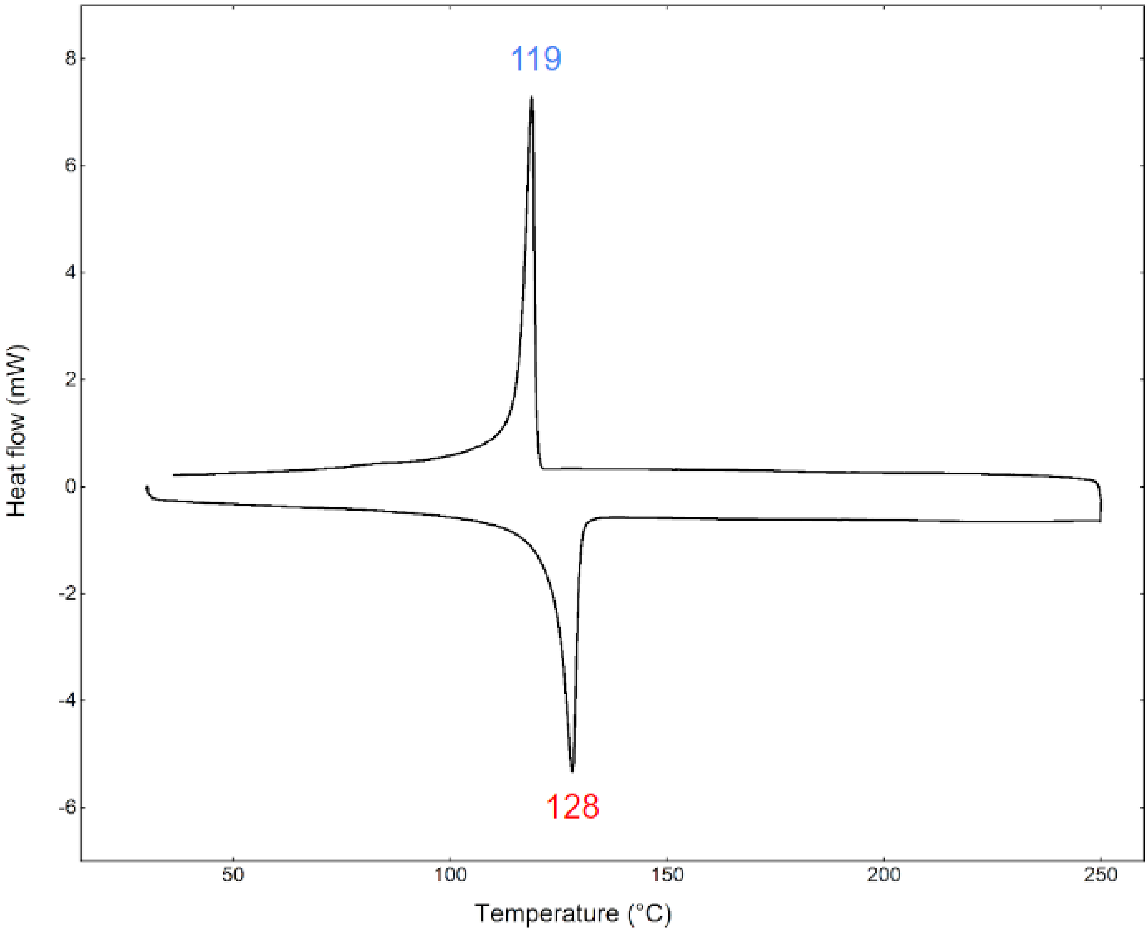

Figure 2.11 Cycling DSC measurements of StarPore® accompanied by the defined melting temperature (red) and the recrystallisation temperature (blue).

Single particle heating revealed an increase in polymer surface area by approximately 110 % (Fig. 2.12). As the StarPore® particles were gradually heated to 125 ℃, a shift in geometry began to appear between 115 ℃ and 120 ℃ as the polymer approached its glassy state, where units began to relax and flatten. An increase in particle width and length from 0.232 mm ∓ 0.030 and 0.460 mm ∓ 0.065 to 0.454 mm ∓ 0.052 and 0.869 mm ∓ 0.075 was observed (Table 2.7). Correspondingly, particle depth was found to flatten from 0.315 mm ∓ 0.011 to 0.234 mm ∓ 0.110.

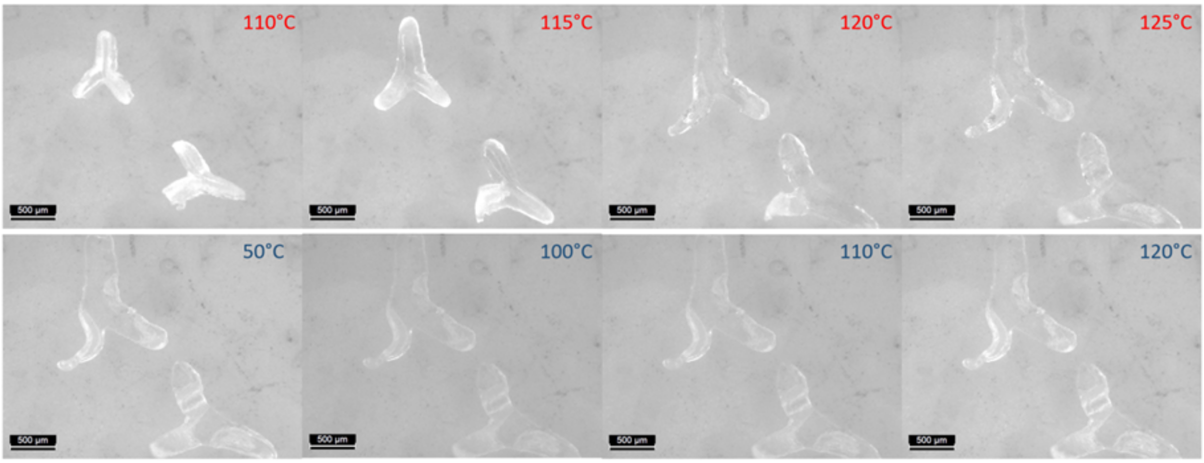

Figure 2.12 *In situ* microscopy images of StarPore® particles, scale bar = 500 µm.

Table 2.7 A summary of StarPore® shape characteristics following heating, assessed by *in situ* heated optical light microscopy, where n = 10.

Characteristic	Average size prior to heating ± S.D	Average size post heating ± S.D
Arm width	0.232 mm ∓ 0.030	0.454 mm ∓ 0.052
Arm length	0.460 mm ∓ 0.065	0.869 mm ∓ 0.075
Surface area	0.087 cm^2 ∓ 0.015	0.157 cm^2 ∓ 0.029
Depth	0.315 mm ∓ 0.011	0.234 mm ∓ 0.110

2.3.5 Single Strut Printing

Utilising the information gathered from the theoretical modelling and physicochemical characterisation, single strut printing was conducted. Micro CT was employed to determine the average strut thickness and porosity of each scan speed used (Fig 2.13 a). The single struts were designed in CAD with a 1 mm diameter. The thickness of each strut was found to reduce with increased laser speed (Fig. 2.13 b). Strut thickness at its thickest point grew beyond 2.7 mm at 25 mm/s and 50 mm/s, a growth of approximately 2.7

fold, thought to be a result of increased energy density and temperature gradient within the print bed. This higher energy density generates a molten pool of polymer whose thermal energy dissipates towards adjacent particles leading to lateral growth [248]. Correspondingly, porosity was also found to increase with laser speed (Fig. 2.13 c). This is associated with a reduction in particle fusion or coalescence at lower energy densities and more substantial melting with higher energy densities. The molten centre of the strut found at 25 mm/s and 50 mm/s is much more dense than the struts at 100 mm/s and 125 mm/s. This phenomenon will become more evident during the single layer sintering in the next section. Another possible method for overcoming rapid thermal gradients and polymer expansion is the addition of a heated substrate and print environment, which may improve print accuracy.

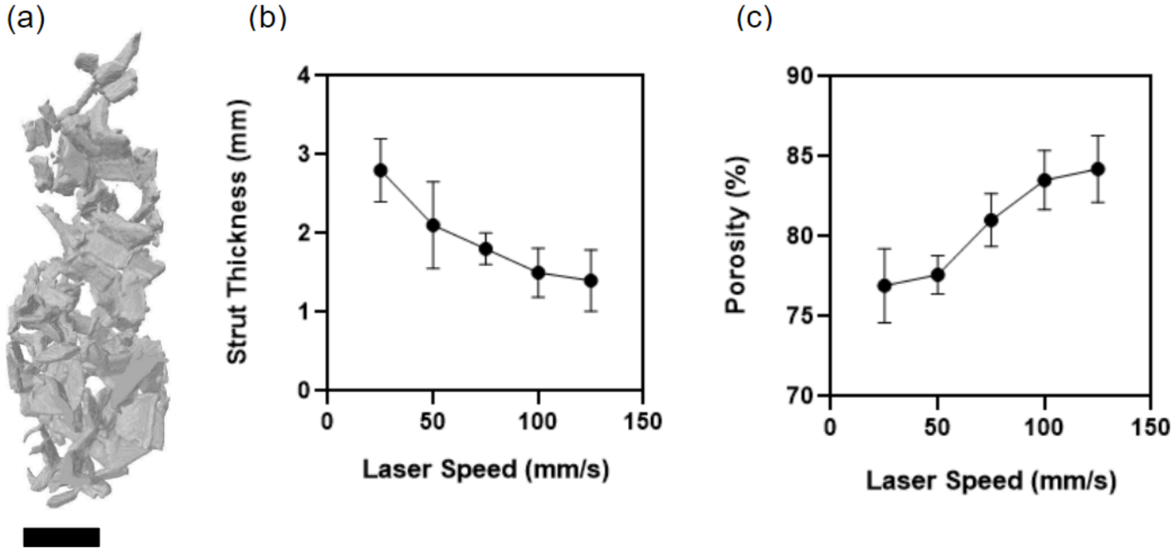

Figure 2.13 (a) 3D model of a single 0.1 mm sintered strut re-constructed from micro CT imaging, scanned at 18 watts, 100 mm/s, with a 127 µm beam diameter at room temperature, (b) strut thickness (mm) as a function of laser speed (mm/s) and (c) strut thickness (mm) as a function of porosity (% void space calculated within the strut).

2.3.6 Single Layer Printing

In situ thermal imaging was set up to monitor the temperature at the laser-material interface, with the energy densities established in the previous section, to optimise scan strategies. The lateral diffusion observed at laser speeds between 25 - 50 mm/s in the single strut sintering was indicative of poor part resolution and dimensional inaccuracy. Coupled with the known melting point, 128 ℃, from the DSC analysis and the 1 mm spreading onto the build platform from the re-coating experiments, the sintering parameters could be tuned. During thermal imaging while sintering 10 x 10 mm cuboid scaffolds temperature variable fluctuations were observed. Uni-directional (Fig. 2.14 a-b) and bi-directional (Fig. 2.14 d-e) scan patterns using the same energy densities revealed spikes of up to 131 ℃ (Fig. 2.14 c) for uni-directional scanning and 154 ℃ (Fig. 2.14 f) for bi-directional, also known as zig-zag or S shape scanning [226]. Due to the longer scan duration of the uni directional scanning and dwell time between each strut, the bed was found to barely exceed the melting point of the polymer. Bi-directional scanning, on the other hand, revealed excessive temperature fluxes well beyond the melting point of the polymer, leading to an overconcentration of laser energy. This can lead to thermal oxidation, reduced part porosity and can affect mechanical properties [249].

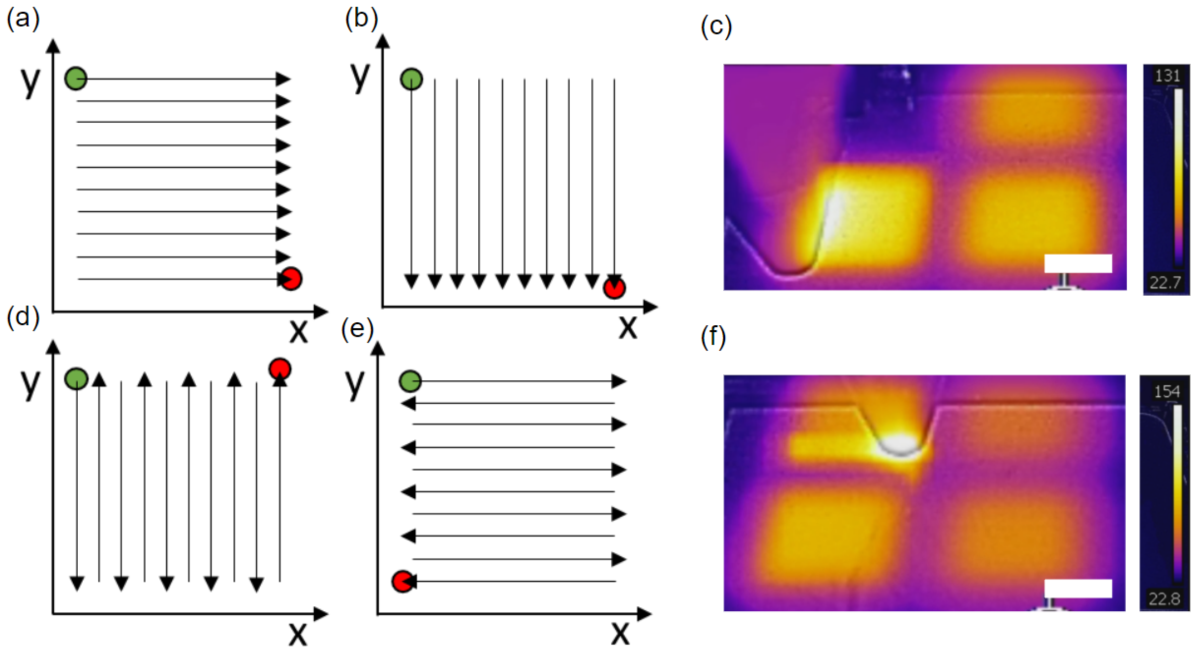

Figure 2.14 Schematic of (a) & (b) uni-directional scanning strategy, where 10 lines are scanned horizontally, then vertically at 1 mm spacing over 10 x 10 mm. (c) IR camera images of 4 scanned 10 x 10 mm regions of StarPore®, with associated heat map range, scale bar = 5 mm. (d) & (e) are the schematics of the bi-directional scanning strategy where 10 lines are scanned continuously, first vertically, then horizontally at 1 mm spacing over 10 x 10 mm and (f) IR camera images of 4 scanned 10 x 10 mm regions of StarPore®, with associated heat map range, scale bar = 5 mm.

The next steps were to investigate how hatch spacing influenced sintering. The *in situ* thermal imaging technique was used in conjunction with high resolution optical microscopy to quantify particle coalescence at different energy densities (Fig. 2.15 ai-iv). These surface micrographs revealed slightly softened or partially adherent particles from an energy density of 0.36 J/mm^2 and below (Fig. 2.15 bi). The onset of particle coalescence began at an energy density of 0.40 J/mm^2 up to 0.46 J/mm^2 with a hatch spacing of 0.75 mm (Fig. 2.15 bii & iii). Beyond 0.46 J/mm^2 revealed a molten phase (Fig. 2.15 biv), as the hatch spacing approached the StarPore® particle diameter of 0.5 mm. Interestingly, air pockets were observed within the molten polymer bed, an established phenomena seen in rotational moulding and within other SLS systems [250–253]. These air pockets or bubbles, commonly referred to as pores or voids, occur due to rapid temperature refluxes where gas bubbles are encapsulated by molten polymer which solidifies faster than the gas can diffuse out. The process is impacted by polymer rheology, thermal properties [254] and powder properties [255,256]. Unfavourable consequences arise from the process, such as a reduction in porosity [252] and brittle mechanical properties [250]. Additionally, higher energy densities can result in lateral growth, where the thermal energy from the laser radiates uncontrolled throughout the print bed, limiting part accuracy and resolution [248]. Without extensive and precise preheating and cooling, these thermal gradients can lead to unpredictable polymer shrinkage and curling. Multiple laser passes during each layer of scanning can help reduce any thermal gradients or bleeding [106,107]. It should be noted that reduced hatch spacings lead to longer print times, as the laser has to scan more of the print area, unless adjustments in spot size can be made. The best scanning parameters over the hatch distance tested, based on homogeneous temperature distribution, were determined to be 0.40 J/mm^2 with a hatch spacing of 0.75 mm. It should be noted that the energy densities in this section are presented as J/mm^2 due to the factor that sintering was conducted throughout a single, constant layer thickness of powder. Subsequent sections outline energy density as J/mm^3 as they are multi-layered constructs, with variations in layer heights.

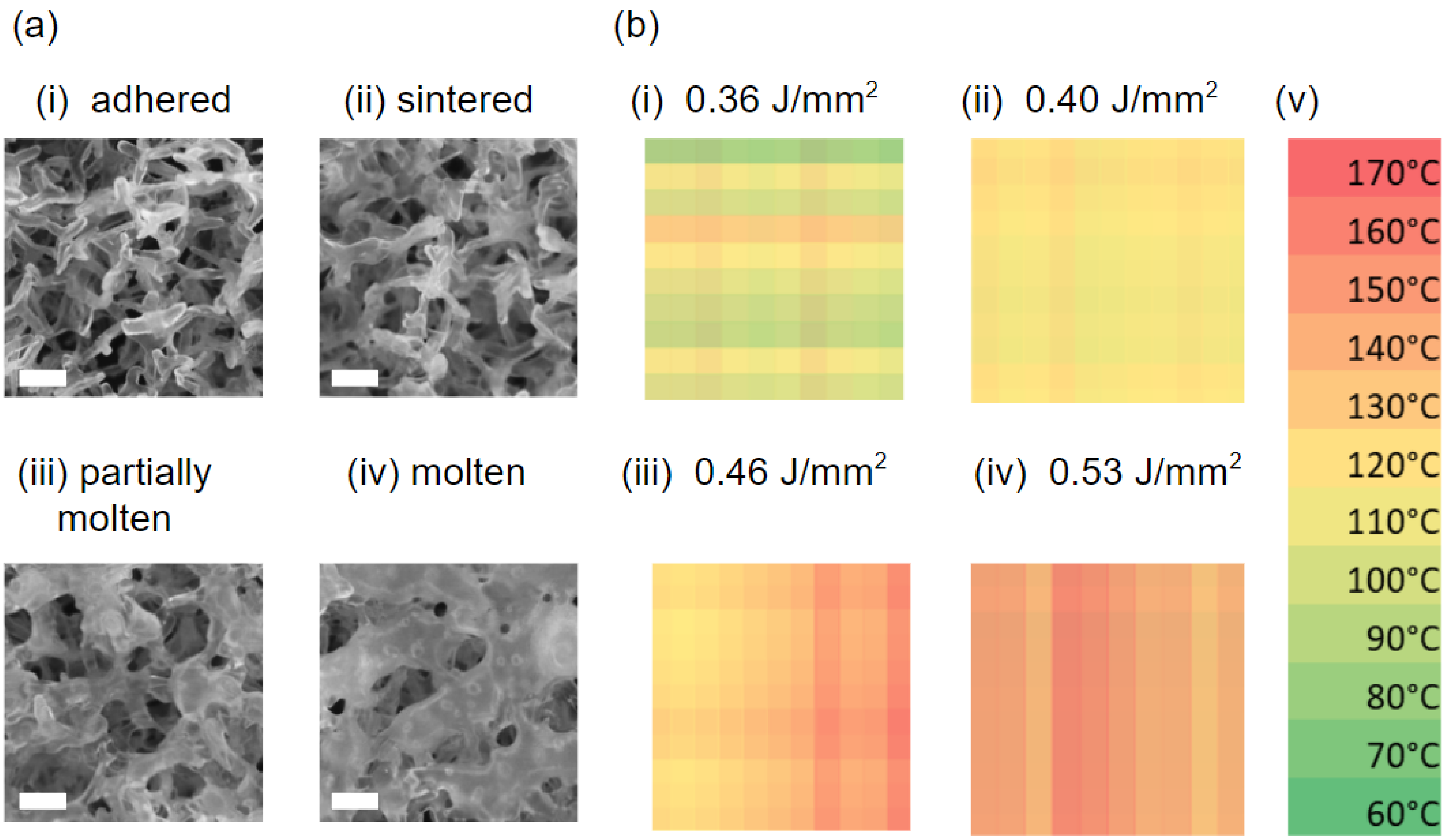
(a)
(i) adhered
(ii) sintered
(iii) partially molten
(iv) molten
(b)
(i) 0.36 J/mm^2
(ii) 0.40 J/mm^2
(iii) 0.46 J/mm^2
(iv) 0.53 J/mm^2
(v)
170°C
160°C
150°C
140°C
130°C
120°C
110°C
100°C
90°C
80°C
70°C
60°C

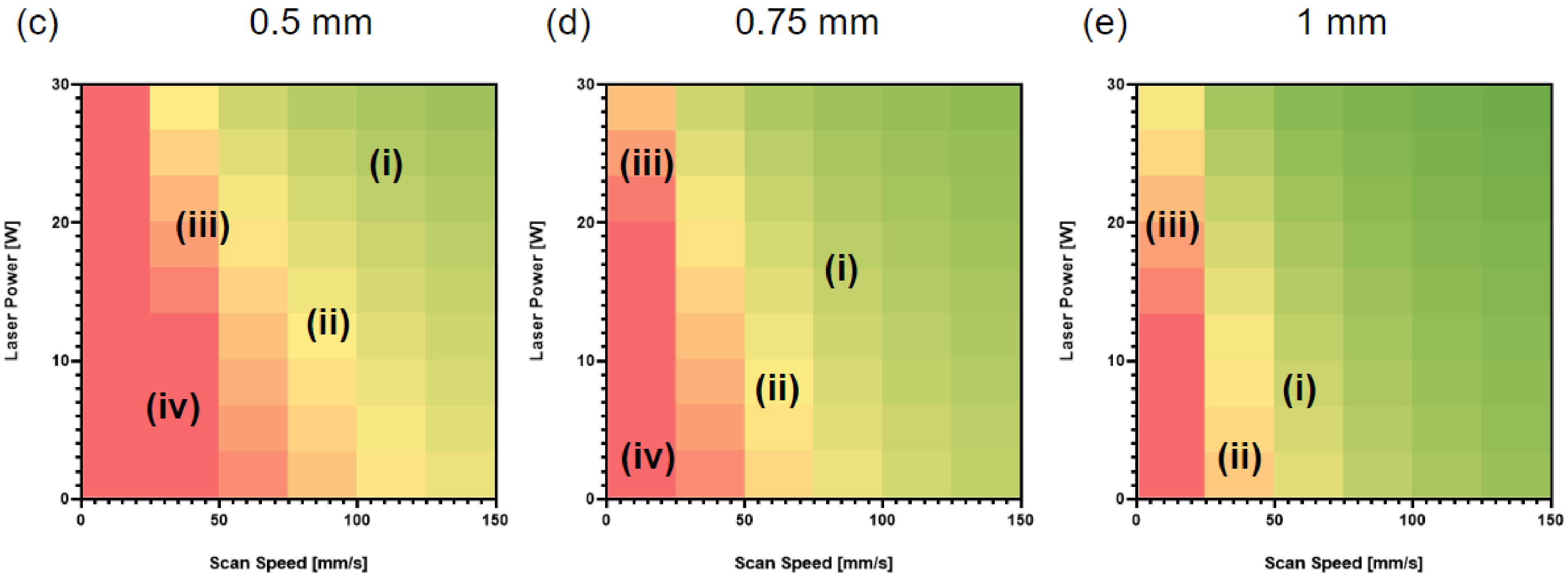

Figure 2.15 (a) Light microscopy images of a range of StarPore® powder beds following laser exposure (i) shows slightly adhered particles, (ii) sintered particles, (iii) partially molten particles and (iv) completely molten bed, scale bar = 500 µm. (b) Heat maps determined by real-time IR camera images during scanning at a range of energy densities with (v) corresponding heatmap temperatures, where n = 5. (c) A comparison of bed coalescence with 0.5 mm hatch spacing with (d) 0.75 mm hatch spacing and (e) 1 mm hatch spacing. Printing was conducted with laser energy ascending in 2-watt increments and 10 mm/s scan velocity increments, where n = 3.

2.3.7 Multi-layer Printing

Dual layer printing was conducted using the print parameters above. Due to polymer shrinkage [147], the powder bed prevented any consistent recoating of the second layer. As the blade moved to deposit a second powder layer, it was found to often dislodge the previous sintered construct. This process is most likely associated with deformation of the first layer which prevents subsequent layer deposition, observed previously in poly (3-hydroxybutyrate) sintering [257]. Spreading experiments did not identify this issue as particles were free flowing. To circumvent this challenge, a HDPE substrate was used above the heated peltier, to ensure first layer fixation. While homogeneous distribution of subsequent layers was realised, the issues associated with polymer shrinkage were not [258].

2.3.8 Slurry Printing

Multi-layer printing was not repeatable via a typical SLS approach, even with adapting the heated substrate to a HDPE-based platform. Thus to alleviate polymer shrinkage and spreadability limitations, a novel slurry-based printing approach was employed. While the shrinkage was initially interpreted as thermal expansion upon heating, it was later realised that it results from polymer crystallisation upon rapid cooling [259]. The preheated polymer bed and use of a slurry-based approach acted as a thermal buffer to gradually increase and decrease the run away temperature gradients upon sintering. Without preheating, sintered second layers of StarPore® were found to grow approximately 1.2 mm in the Z plane (Fig. 2.16 a1). Sintering the slurry resulted in reduced spikes in growth (Fig. 2.16 a2). Cooling the heated substrate with the slurry printing method resulting in slightly better homogeneity (Fig. 2.16 a3). Likewise, using the same processing method but adding another laser pass resulted in a further enhanced sintering performance (Fig. 2.16 a4). A third raster scan over the previously scanned area, also resulted in a reduction in Z-height expansion (Fig. 2.16 a5). The water used in the slurry approach slowly evaporates during laser irradiation, merely acting as a buffer to prevent the polymer shrinking and warping due to temperature gradients. Physical degradation and chemical analysis would not likely be impacted by the addition of water, as water evaporates at 100°C and the polymeric units of HDPE begin to relax at 120°C. More extensive analysis should be conducted if other liquid delivery vehicles were to be utilised. To our knowledge this is the first instance a slurry-based printing approach has been utilised in an SLS system and may have broader applicability for polymers not suitable for SLS.

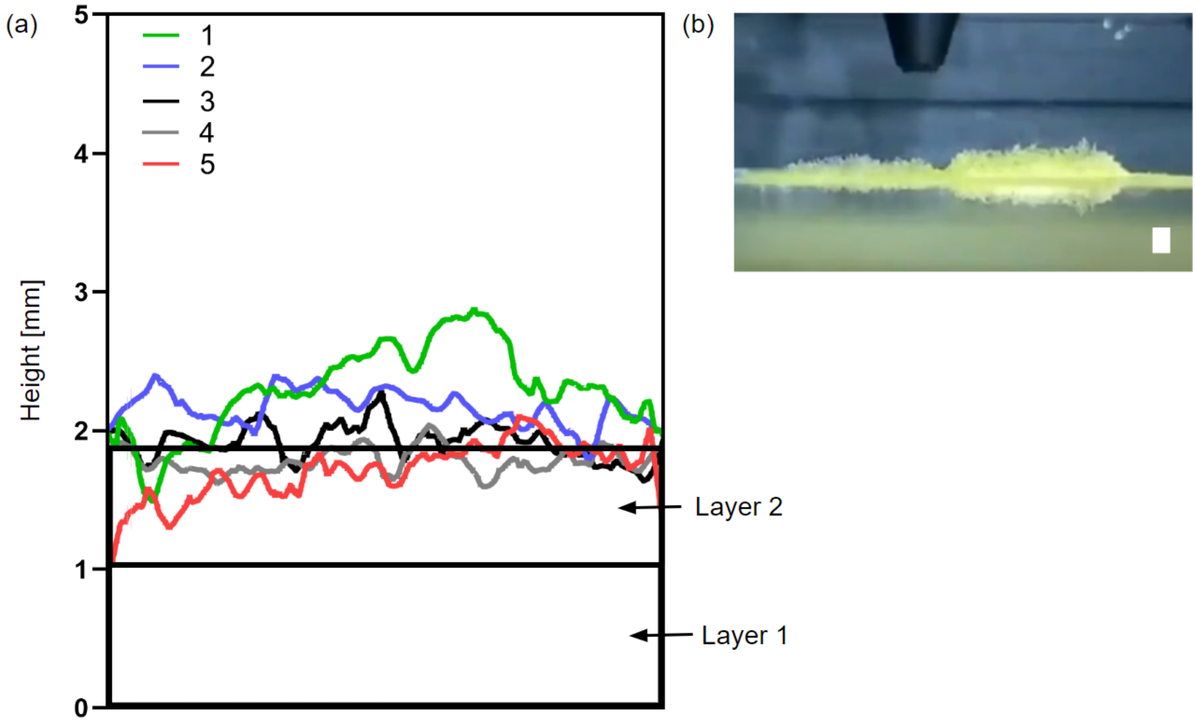

Figure 2.16 (a) Roughness profile of dual layer printed StarPore® scaffolds 20 x 20 above the second deposited layer, printed in a dry state without heating (1), printed in a slurry state without substrate heating (2), printed in a slurry with substrate heating (3), printed in a slurry state with substrate heating with dual laser passes (4) and printed in a slurry state with substrate heating with triple laser passes. (b) *In situ* optical images taken to determine polymer behaviour, shrinkage and warping, during sintering in , scale bar = 2 mm

2.3.9 Chemical Fingerprint

FT-IR was used to assess polymer stability following SLS processing (Fig. 2.17). The chemical fingerprint of neat or virgin HDPE was compared to that of HDPE exposed to energy densities ranging from 0.36 J/mm^2 to 0.53 J/mm^2. Figure 2.17 shows the frequency range ascribed to the stretching vibration of doublet peaks, at 2900 cm^{-1} (-CH_2) and 2850 cm^{-1} (-CH) and that of -CH_2 between 1470 - 1460 cm^{-1}, with the rocking and bending of the -CH_2 band observed at ~700cm^{-1}, comparable to previous studies [260–263]. No obvious differences were observed between samples. Previously, when investigating the influence of energy density on sintered PA12, higher chain mobility caused by chain scission has been observed with increased energy density [264,265], indicative of slight polymer degradation from oxidation. This oxidation could result in reduced mechanical properties of sintered scaffolds. These impacts were not identified in the HDPE following laser exposure.

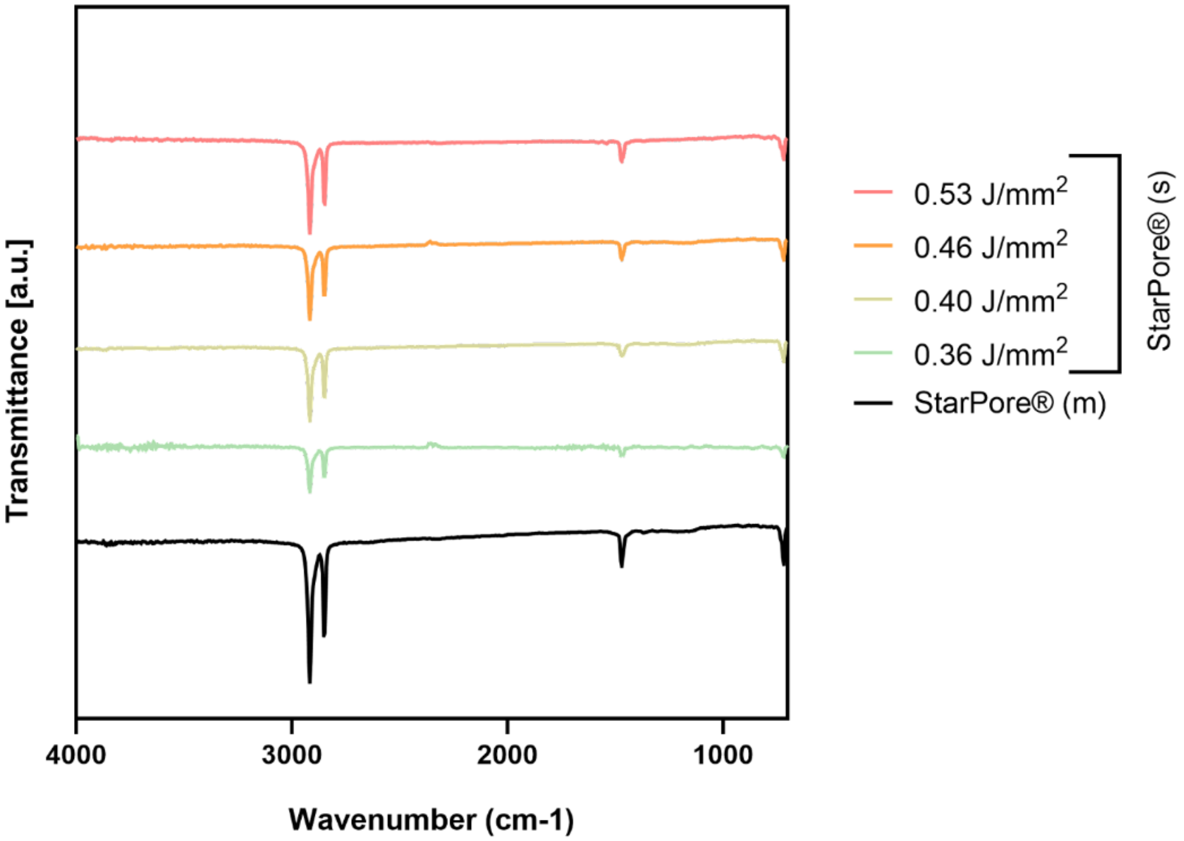

Figure 2.17 Transmittance infrared spectra of neat HDPE and HDPE following laser exposure, measured through ATR. Spectra were vertically shifted for comparison

2.4 Conclusions

This chapter outlines the development of a custom recoating platform capable of interfacing with existing laser engraving systems. The system was developed with 3D printing hardware, such as an arduino, an ultimaker motherboard, nema stepper motors and lead screws, as well as laser cut components and 3D printed components that served as a template for the system. The build volume was 60 x 60 x 60 (XYZ) and custom designed firmware and G-code was developed to control two Z-axis and one Y-axis.

Thermal analysis revealed a narrow sintering window for printing, between the melting point and the crystallisation point, of 9 degrees celsius, much narrower than typical SLS materials. On the other hand polymer thermal stability was high, with degradation only occurring beyond 370 °C, well beyond the sintering window. Additionally, this stability was found to be consistent for over two hours when exposed to 200 °C under atmospheric conditions.

Prior to printing, a theoretical sintering model was established to define a range of scan parameters, including laser energy and laser velocity, for efficient sintering of HDPE. Single particle heating of trilobal HDPE particles known as StarPore® revealed significant deformations as the polymer units transitioned through their glassy state towards their melting point. Likewise, single strut printing demonstrated the unpredictability of the polymer shape in response to thermal gradients. Single layer printing was conducted in conjunction with *in situ* thermal imaging to determine the ideal energy density and scan strategy for efficient particle coalescence.

This chapter irons out many of the issues associated with sintering HDPE in general, including shrinkage and deformation. While the novel trilobal shape is beneficial for creating highly porous implants when fabricated through vibrational moulding, SLS fabrication was not consistent. Initial experiments resulted in large variations in morphology, with unpredictable particle behaviour from thermal stresses instigated by the laser. The introduction of bed heating and a slurry-based approach alleviated thermal runaway for consistent sintering. The water acted as a thermal dissipator while its surface tension enabled homogeneous spreading and levelling of particles. Additionally, SLS printing is known to be sensitive to changes in environmental humidity, the slurry printing method may provide relief to this issue.

The next chapter explores how the established printing methodology compares to the gold standard of moulded HDPE implants, including the use of imaging analysis to determine porosity and surface morphology as well as mechanical tests to compare structure stiffness and ultimate tensile strength against moulded StarPore®.

CHAPTER

3

MECHANICS

Chapter 3: Mechanics

Overview

This chapter explores the use of imaging and mechanical testing techniques to compare how the changing of energy density influences printed StarPore® constructs. The traditionally moulded StarPore® is used as a positive control throughout the experiments. The chapter investigates porosity changes with the use of micro computed tomography as well as 3D laser confocal microscopy and scanning electron microscopy to assess surface morphology. Finally compression and tensile tests are used to establish whether the printed structures can resist the same load as the moulded ones.

3.1 Bone Mechanics

The skeletal system forms the backbone of the human being. As humans age, bone gradually deteriorates, losing its mass and strength leading to osteoporosis [266]. By the end of 2050, it is approximated that 20% of the world's population will be 65 or older [267]. This ageing population could have a significant impact on the healthcare sector [268], particularly with bone related illnesses.

To address these healthcare concerns bone has already become the second most engineered tissue to combat degradation from osteoporosis, trauma and tumours [269]. To accurately engineer such a tissue one must dissect its composition. Natural human bone is a hierarchy of organic, inorganic materials as well as water, mainly 30 % collagen, 60 % mineral and 10 % water, respectively (Fig. 3.1).

The structure of bone can be separated into two components, cancellous and cortical tissues, outlined in the introduction of this thesis. These two tissues are also known as spongy or trabecular and compact bones. Essentially, cancellous or trabecular bone is a highly porous environment conducive to biological processes. Cancellous bone is known to be anisotropic due to its range of porosity and pore sizes, reaching up to 1 mm in diameter [270]. The latter, cortical or compact bone offers the structural integrity comparable to mild steel while being incredibly light and relatively elastic [271]. Hydroxyapatite (HA) crystals provide hardness and rigidity to bone tissue. They support collagen fibres in the osteoid matrix. HA's inherent ceramic properties, however, mean the crystals lack elasticity and have low impact resistance. The ultimate compressive strength is high yet HA is significantly weak when exposed to twisting or bending. Collagen on the other hand provides bone its elasticity, reinforcing any external loads of twisting or bending, though at the expense of compressive strength [272].

The dynamic structure of bone and its composition aspects such as degree of mineralisation, overall porosity, and orientation of collagen fibres leads to high variabilities in defining the mechanical properties of bone [272]. Additionally, the anisotropic nature of bone, where stiffness is higher longitudinally, weak under shear loads and stronger under compression when compared to tension, prevents one simple explanation. It should be noted that the modulus and strength of cortical bone is directly affected by the properties of the adjacent cancellous bone [273]. That said, the stiffness of cortical bone and cancellous bone exhibit strengths of 35-283 and 1.5-38 MPa, respectively [274]. Cortical bone can resist higher ultimate stress than trabecular bone, but is more brittle, failing at strains of 2 % when compared to trabecular bone's ductile 30 % resistance to strain [275–277]. These properties are related to the mineral composition and apparent density of each bone type. The density of cortical bone typically ranges between 1.6 - 2 g/cm^3 [278], which equates to a porosity of approximately 30 %. Cancellous bone has an apparent density with 0.05 - 0.3 g/cm^3 [279], extending up to 0.75 g/cm^3 in the femoral head [280]. Changes in mineral density from osteoporosis can significantly reduce the stiffness of bone and lead to increased risk of fracture [281].

Stiffness is related to bone mineral content and density, toughness is strongly associated with collagen quality and orientation [282]. For instance, if the integrity of collagen is compromised through denaturing or compositional changes, the toughness of cortical bone is significantly reduced [283]. Bone has an inherent viscoelastic nature that can, depending on location, deteriorate with age. Mc Calden *et al.* [284] found the tensile strength of the femur can reduce by 55 MPa between the ages of 20 and 95, as a result of reduction in bone density. On the other hand, the strength of the tibia has been shown to not reduce with age [283,285].

Knowing the complex hierarchical structure of human bone, including the broad range of properties that vary with age, location of the bone etc, new and innovative measures of bone tissue engineering are required. This chapter focuses on characterising 3D printed bone substitutes, via SLS, for the development of patient-specific bone substitutes. Initial experiments explore how adjustments in scan strategy can influence porosity and surface morphology of scaffolds. Additionally, mechanical tests were used to assess whether the porous printed scaffolds can match currently approved HDPE implants, which are used as positive controls throughout each experiment.

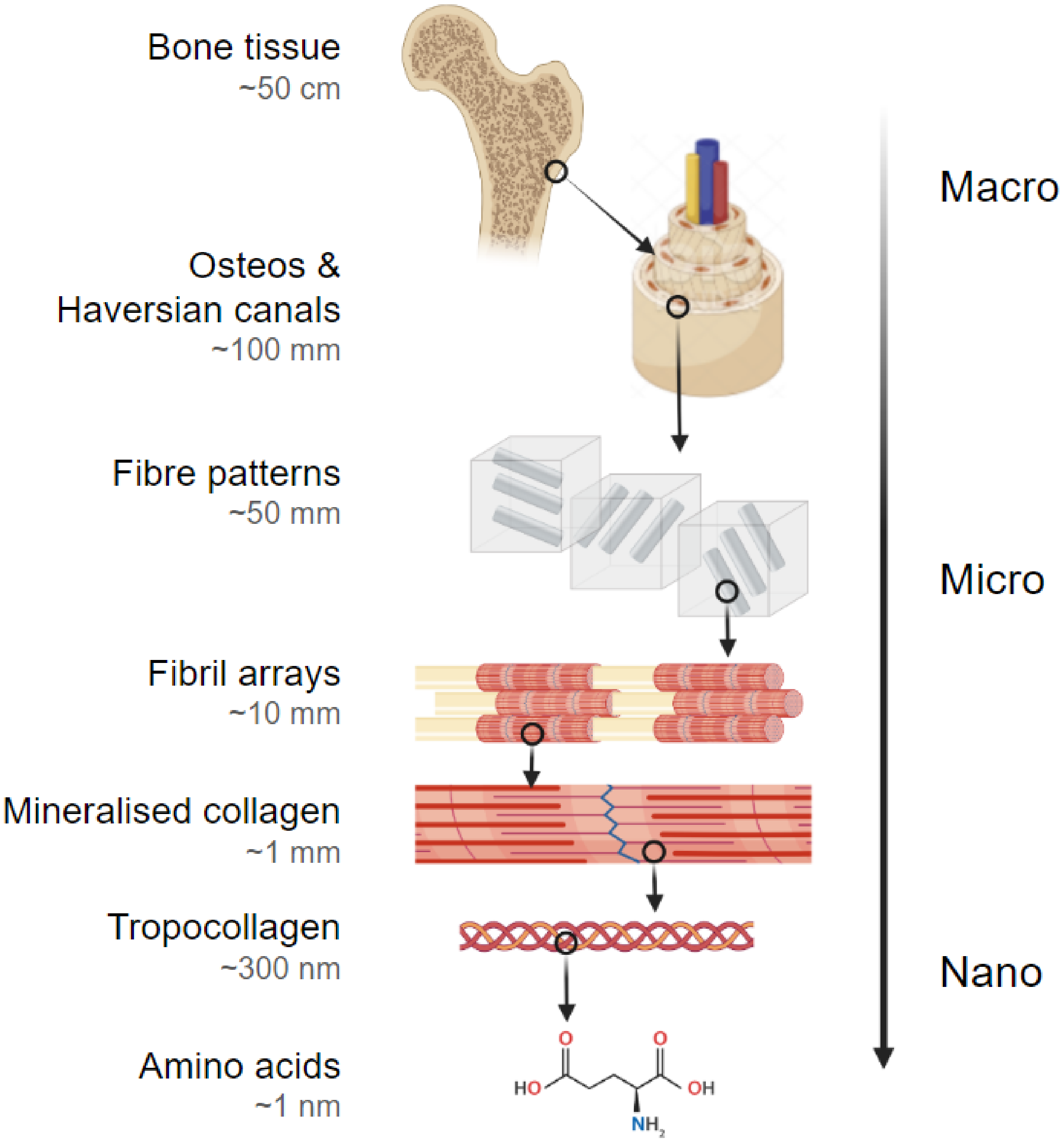

Figure 3.1 Hierarchical structure of human bone, from the macroscopic down to the nanoscale components. Adapted from [286]

3.2 Materials & Methods

3.2.1 Materials

Trilobal high density polyethylene (HDPE), StarPore® (Anatomics Pty Ltd, Melbourne, Australia) was first sieved to remove any particles above 600 µm or below 300 µm.

3.2.2 Sintering systems

The custom recoating system (outlined in previous chapter) was placed in two laser engravers. A PLS6MW (Universal Laser Systems [ULS] GmbH, Vienna, Austria) and a K40 (VEVOR, Shanghai, China) both equipped with CO_2 lasers (λ 10 600 nm). The ULS employs a 30-watt laser tube and the K40 a 40-watt laser tube. Both systems utilise a zinc selenide focus lens, resulting in a 127 µm diameter spot size at the focus point. In vector mode the ULS laser head can accelerate up to 500 mm/s with the K40 up to 100 mm/s.

3.2.3 Scaffold design and Software

Scanning strategies were developed in CorelDraw Graphics Suite X6 (Ottawa, ON, Canada) for the ULS system, controlled by the ULS system were Universal Control Panel and the Laser System Manager (Universal Laser Systems GmbH, Vienna, Austria) and for the K40, K40 Whisperer (Scorch Works) and LightBurn (Pulse Laser Systems). Scan strategies either generated 10 x 10 mm or 20 x 20 mm cuboid scaffolds with layer height and hatch spacing variations outlined in Table 3.1. STL's were generated from a variety of software packages including Magics and Mimics (Materialise, Leuven, Belgium), Inventor (Autodesk, San Rafael, California) and Fusion 360 (Autodesk, San Rafael, California). Software used to generate G-Code was IceSL Slicer 2.4.0 for the conversion of STL to SVG and Inkscape for SVG manipulation and export.

3.2.4 Process parameters

The sintering parameters used to process all scaffolds in this section are given in Table 3.1. Considering the plethora of variables in the SLS process, ambient temperature was recorded each day during printing and a heated substrate was set to 100 °C to reduce any thermal gradients that can jeopardise part quality. The variables tested were laser power, laser velocity, hatch spacing, scan length, layer thickness and laser spot diameter. While there are a variety of other factors, including a diverse range of scan strategies not investigated in the previous chapter that can impact part quality, those chosen were considered most fundamental in establishing coalescence behaviour of the novel trilobal HDPE material.

3.2.5 Microstructure Analysis

3.2.5.1 Porosity Analysis

The porosity of moulded and sintered scaffolds was investigated via X-ray scanning using a benchtop micro computed tomography (μCT) scanner (Bruker, Skyscan 1275, Kontich, Belgium). The samples were scanned with an X-ray beam energy of 40 kV, a beam intensity of 250 uA, an angular step of 0.2 ° for a total of 360 ° rotation, an exposure of 50 ms, a spatial resolution of 10.7 μm and a total scan time 1h:21m:25s, 437 sections were reconstructed with NRecon (Bruker micro-CT, Kontich, Belgium) and a region of interest was analysed with CTAn (Bruker micro-CT, Kontich, Belgium). 3D isosurface renderings were generated using CTVol (Bruker, Kontich, Belgium) software to visualise the structure.

3.2.5.2 Surface Morphology

To determine variations in print the surface morphology of printed and moulded scaffolds were assessed by 3D laser scanning confocal microscopy (Olympus LEXT™ OLS5100 Laser Microscope, Tokyo, Japan). Powder bed and sintered scaffold topographies were also investigated through scanning electron microscopy (SEM) using a JEOL JSM-7500FA. Samples were prepared via sputter-coating to create a ~10 nm gold coating.

3.2.5.3 Light Microscopy and Scanning Electron Microscopy

Printed constructs were investigated via a Leica M205A stereomicroscope. High resolution scanning electron microscopy (SEM) was conducted using a JEOL JSM-6490LV microscope. All scaffolds were sputtered coated with a 10 nm layer of gold. The images were performed under high vacuum mode at an accelerating voltage of 15 kV. All images, measurements and post processing was conducted in ImageJ.

3.2.6 Mechanical properties

3.2.6.1 Compression

Compression tests were conducted on a EZ-L mechanical tester (Shimadzu, Japan) equipped with a 500 N load cell. Discs (⌀ 6 mm x 3 mm) were biopsy punched (Kai Medical, Gifu, Japan) and compressed at a loading rate of 1 mm/min. Young's modulus was determined from the linear elastic region of the stress-strain curve. The compressive load was interpreted from the stress-strain curve, measurements were presented as mean ± SD, where n=5. All tests were carried out at a constant crosshead speed of 1 mm/min, at 22 ± 3°C and relative humidity 50 ± 5%.

3.2.6.2 Tensile

Tensile tests were conducted on a EZ-L mechanical tester (Shimadzu, Japan) equipped with a 500 N load cell. Dumbbell-like samples conforming to ASTM D638-82 (Type IV) were cut out using a cutting die (Fig. 3.2). Samples were mounted into custom 3D printed Y-shaped brackets. Young's modulus was determined from the linear elastic region of the stress-strain curve. All tests were carried out at a constant crosshead speed of 1 mm/min, at 22 ± 3°C and relative humidity 50 ± 5%, where n = 5 for each parameter.

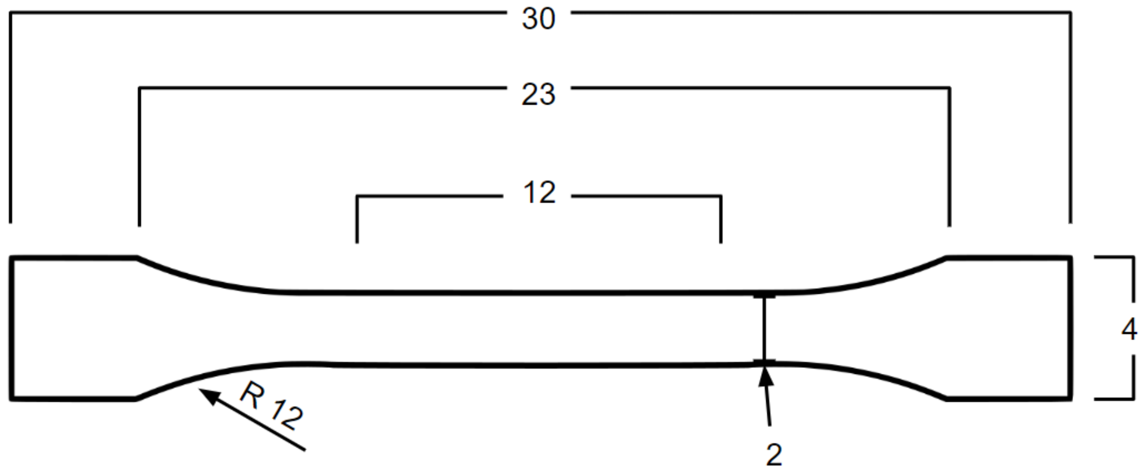

Figure 3.2 Schematic of the dimensions of the dumbbell die used to cut tensile samples, in line with ASTM D638-82 (Type IV).

3.3 Results & Discussion

3.3.1 Microstructure analysis

Energy density plays a vital role in SLS. By combining increased laser power with a reduction in laser scan velocity, as well as narrow hatch spacing we can increase the energy density focused into the powder bed. Figure 3.3 shows the relationship between porosity and energy density of sintered StarPore®. Porosity measurements were quantitatively measured with µCT. The highest porosities of over 91.58 - 92.67 % were found below energy densities of 0.34 J/mm^3 (Fig. 3.3 a) where laser power was < 16 W, laser velocity exceeded 150 mm/s, hatch spacing of 1.5 mm and layer height of 1.5 mm. Between the energy densities of 0.42 J/mm^3 and 0.54 J/mm^3 , where particle coalescence was homogenous throughout the powder bed (Fig. 3.3 b), the porosity was found to reach 76.54 %. As the energy density increases beyond 0.56 J/mm^3 scaffold porosity hits a plateau area 73% porosity. Beyond this range, however, the polymer began to flow from a reduction in melt viscosity [287,288], creating voids that trapped gases (Fig. 3.3 c). Additionally, excessive temperature fluctuations at energy densities above 0.6 J/mm^3 polymer ageing and degradation can occur, along with powder caking [289,290]. The loss of the trilobal shape from over-sintering was also lost within the red region, making the particle shape redundant.

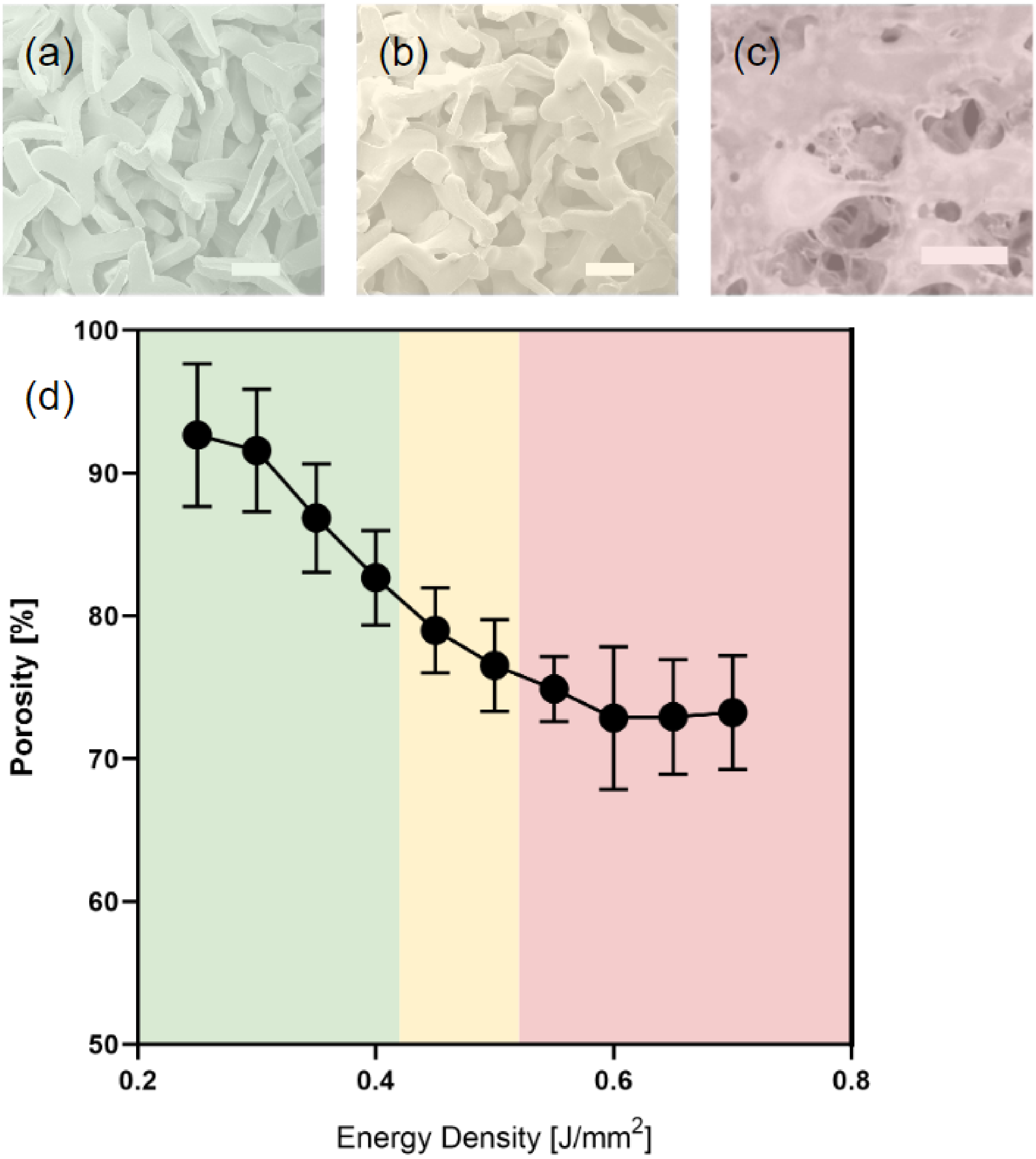

Figure 3.3 The influence of SLS energy density on scaffold porosity, the green region (a) corresponds to adhered particles with high porosity, the yellow region (b) relates to homogeneous particle coalescence and (c) represents over sintering and caking. Scaffolds were printed with the following parameters laser energy 18W, laser velocity 20 mm/s intervals from 20 - 200 mm/s, hatch spacing 0.75 mm, layer thickness 1mm. each data point represents an average ∓ S.D., where n = 3.

While laser velocity has a significant influence on energy density, so does laser power, hatch spacing and layer height. Figure 3.4 outlines how variations in sintering parameters impact part porosity. Porosity was shown to decrease with an increase in laser power, with a porosity of 86.21 % at 16 W, 82.45% at 18 W, 76.23 % at 20 W and 74.81 % at 22 W of laser power (Fig. 3.4 a). High standard deviations were observed at 20 and 22 W due to pockets of complete melting, where the higher energy densities led to over-sintering and inconsistent particle necking, similar to that observed at the energy densities above 0.56 J/mm^2 in the previous figure. A relatively linear trend was observed between porosity and laser scan velocity (Fig. 3.4 b). With scan velocities of 75 mm/s resulting in an average porosity of 78.91 %. As the speed increased to 125 mm/s standard deviation of the 86.9 % porosity was also larger, as partial sintering was observed.

Hatch spacing was found to affect part porosity the most (Fig. 3.4 c). CO_2 laser intensity is not constant throughout the beam diameter as it more closely resembles a Gaussian distribution [76]. As a consequence, both particles in the scan path and adjacent particles can be exposed to inconsistent energy pulses during scanning dependent on laser velocity and scan length [76]. Additionally, the thermal history of the polymer can impart an unpredictable response to laser exposure. Thus a hatch spacing of 0.5 mm resulted in a reduced porosity of 71.34 % (Fig. 3.4 d), associated with a decrease in melt viscosity and loss of particle shape integrity. From these localised melt pool deviations, hatch space accuracy and resolution are both diminished. A porosity range of 82.45 - 91.34 % was observed at hatch spacings of 0.75 mm, 1 mm and 1.25 mm, respectively. We expected similar results when sintering a powder bed with a layer height of 0.5 mm, as the energy density is focused into less material with a higher surface area. Interestingly, the 0.5 mm layer height resulted in a porosity of 87.64 %, well above the 71.34 %. One explanation in the reduced porosity could be associated with particle spreading. Typical SLS materials are spherical, this enables homogenous layer deposition. StarPore®'s novel tilobal structure, while useful for creating highly porosity constructs, limits its ability to be accurately spread across the print bed.

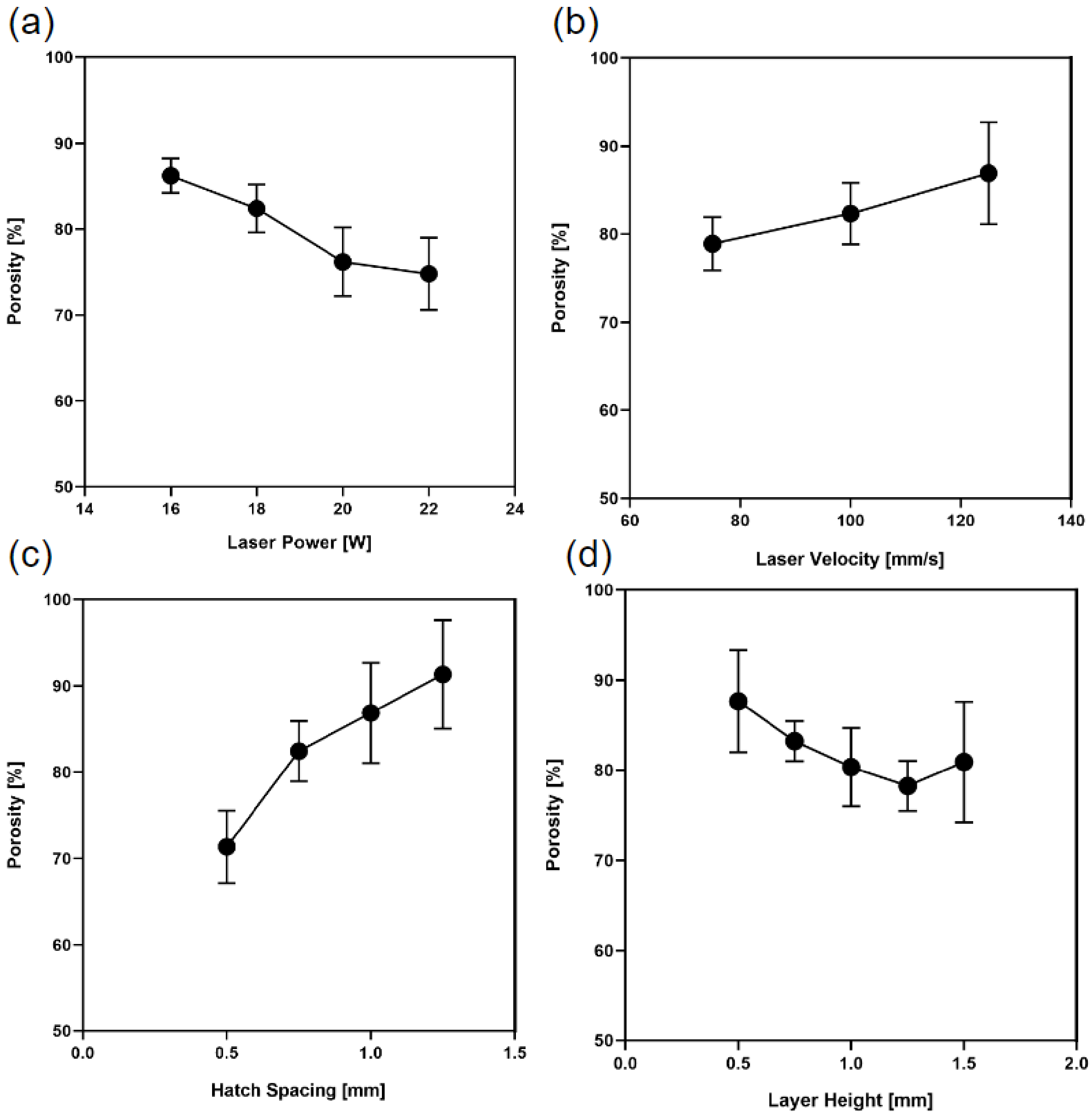

Figure 3.4 Effects of SLS process parameters on sintered StarPore® scaffold porosity, each data point represents an average ∓ S.D., where n = 3.

Sintering parameters also affect internal structural characteristics. A cross section of StarPore® (m) can be seen in Fig. 3.5 a. The internal structure thickness of sintered scaffolds was compared against the moulded StarPore®. Interestingly, we found that with increasing energy the structure thickness distribution became much broader (Fig 3.5 b). The volume of StarPore® (m) thickness resembled a bell curve with a peak between approximately 0.136 - 0.165 mm. While StarPore® (s) printed at 0.40 J/mm^3 shared a similar bell curve with peak thicknesses between the 0.107 - 0.164 mm the volume percentage reduced 14.3 to 8.3 %. Additionally, a second significant portion of structure thickness was observed around 0.5 mm, most likely due to the StarPore® particle geometry. A more linear trend between the peak structure thickness of 0.15 mm down to 0.6 mm was observed in the 0.46 J/mm^3 printed constructs; this could be correlated to more homogenous printing throughout the powder bed. Lastly, the highest energy (0.53 J/mm^3) printing revealed no significant structure thickness peaks, thought to be associated with a melt pool. As outlined in the previous chapter, energy densities beyond 0.5 J/mm^3 structure resulted in temperature gradients well above the melting point of the polymer, leading to loss of particle shape integrity.

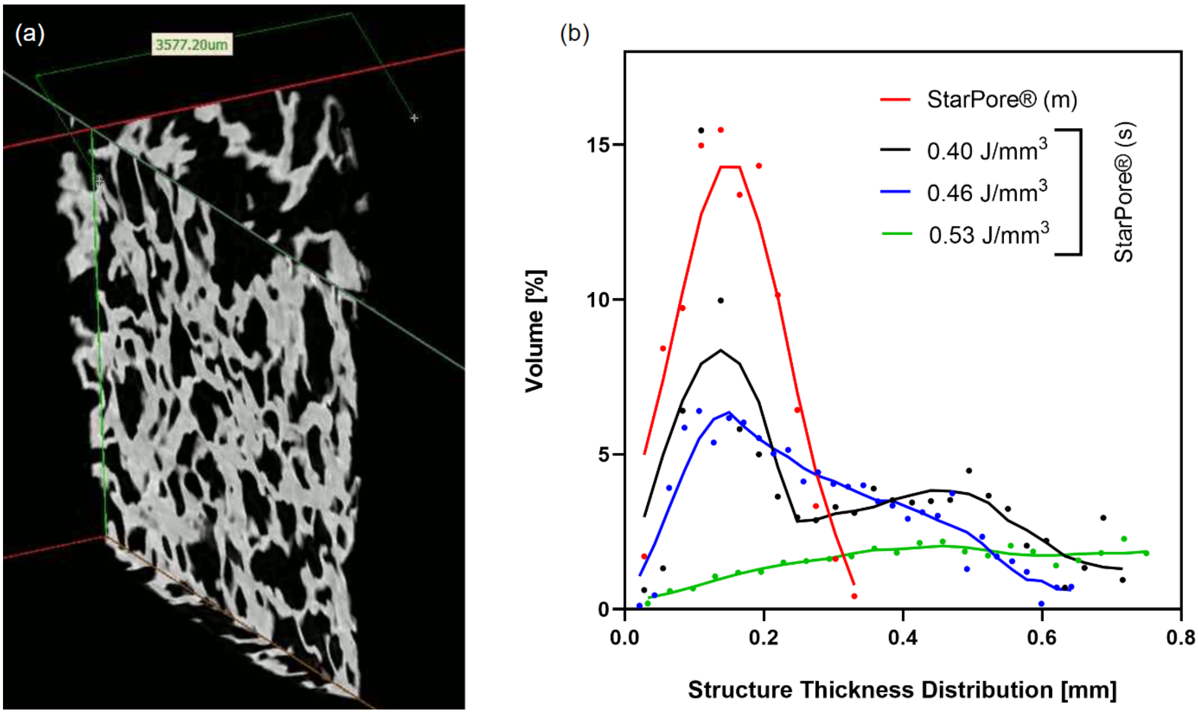

Figure 3.5 (a) A cross section of StarPore® (m) scaffold reconstructed from µCT data. (b) Structure thickness distribution of StarPore® (m) compared to StarPore® (s) constructs generated at 0.40, 0.46 and 0.53^3 energy densities, generated via the 3D analysis tool in CTan (Bruker micro-CT, Kontich, Belgium).

3.3.1.1 Surface Morphology

Fig. 3.6 shows the surface roughness of printed StarPore® (ED 0.42 J/mm^3) compared to that of commercially available moulded implants of StarPore® and MEDPOR®. As expected, the surface roughness of printed scaffolds was much higher than those moulded. The Sa, the arithmetical mean height of a line which relates to the absolute difference in height from each point was found to be 298.5 µm, 140.3 µm and 141.1 µm for StarPore® (s), StarPore® (m), and MEDPOR®, respectively (Fig. 3.6 d). The Sq, which represents the root mean square value, was determined to be 380.6 µm, 179.9 µm and 180.6 µm for StarPore® (s), StarPore® (m), and MEDPOR®, respectively (Fig. 3.6 e). The observed differences between the surface roughness of printed and moulded scaffolds can be attributed to a range of phenomena.

Firstly, SLS fabrication cannot restrict the polymer particles from moving through the Z plane. As the high energy laser focuses on the powder bed, the polymer units begin to relax and the material starts to soften, often shrinking in an unpredictable manner as observed during single strut printing (Chapter 2.3.5). Furthermore, the particle size is much larger than typical SLS materials, over 10-fold in some cases, with a peculiar trilobal shape that results in heterogeneous spreading during layer deposition and sintering. The friction between particles can also result in voids within the powder bed prior to lasing. All of these factors impair the shape and dimensional accuracy of sintered parts. Spherical particles flow more consistently during layer deposition and behave predictably during heating, as heat radiates homogeneously.

Other physical mechanisms at play during the printing process include melting and shrinkage due to rapid solidification or crystallisation, surface tension, melt viscosity and gravity as well as fluid dynamics observed at higher energy densities due to the Marangoni convection effect, though more commonly observed in SLM [104,291]. The moulded scaffolds of StarPore® (m), and MEDPOR® on the other hand had surprisingly low variations in roughness. While both HDPE, the particles are wildly different in size and geometry the roughness differences were insignificant. Due to the moulding method, where polymer particles are restricted in every direction and heated, the surface finish is always glossy and smooth.

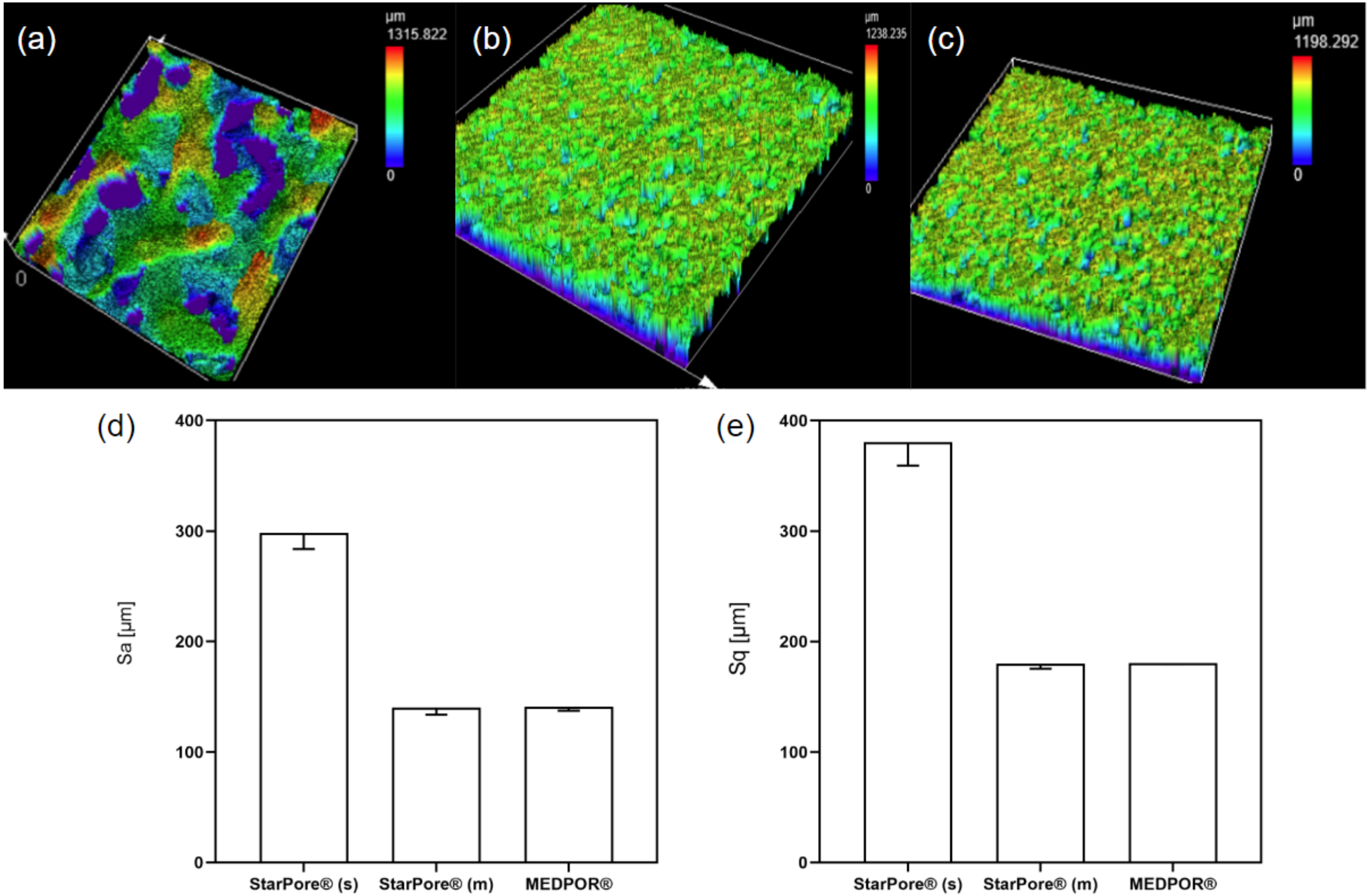

Figure 3.6 (a-c) 3D confocal laser microscopy heatmap images of the surface of StarPore® (s), StarPore® (m) and MEDPOR®. (d) The Sa, arithmetical mean height of a line or each scaffold, (e) Sq, obtained by squaring each height value in the dataset, then taking the square root of the mean. Avg ∓ S.D. where n = 3

The roughness profiles of StarPore® (s) StarPore® (m) and MEDPOR® were also tested along vertical lines (Fig. 3.7). Broader troughs were observed throughout StarPore® (s) (Fig. 3.7 a), with the maximum valley depth (Rv) determined to be 995 µm (Table 3.1). Additionally, the maximum peak height (Rp) was found to be 646 µm, the total height of the roughness profile (Rt) and mean height of roughness profile elements (Rc) found to be 1641 µm and 636 µm, respectively. In comparison, the StarPore® (m) had a peak height of 441 µm and a maximum valley depth of 762 µm. Similarly, the MEDPOR® sample had a peak height of 427 µm and pit depth of 708 µm, suggesting the moulded process yields similar surface finishes on the constructs even if the overall porosities are different. Interestingly, the skewness (Rsk) of all scaffolds was negative, meaning that all surfaces are made up of valleys instead of peaks, they're all porous surfaces. The kurtosis (Rku) or sharpness of the constructs was found to be more rounded on the StarPore® (s) with increased sharpness on both the StarPore® (m) and MEDPOR® scaffolds.

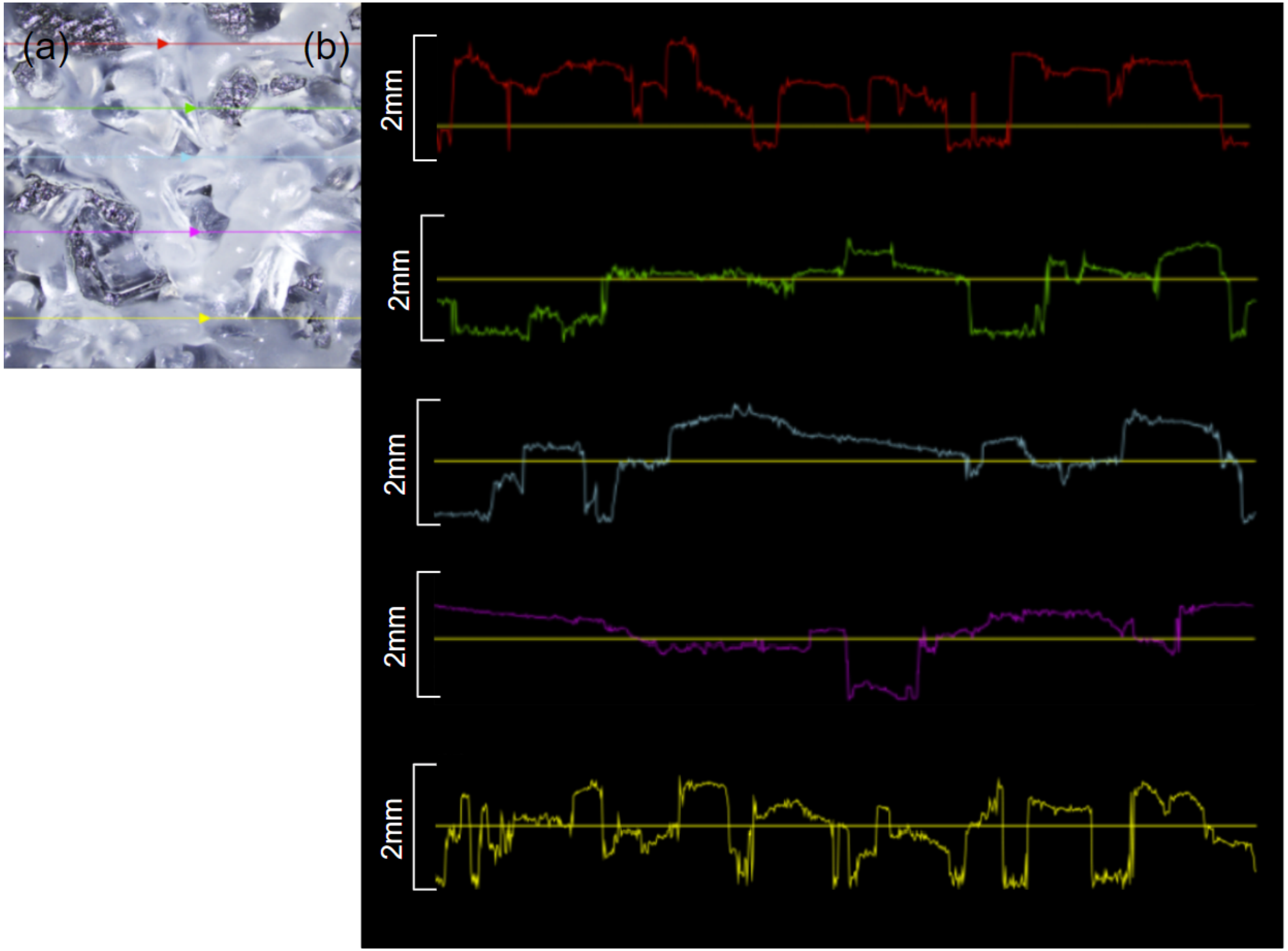
(a)
(b)
2mm
2mm
2mm
2mm
2mm

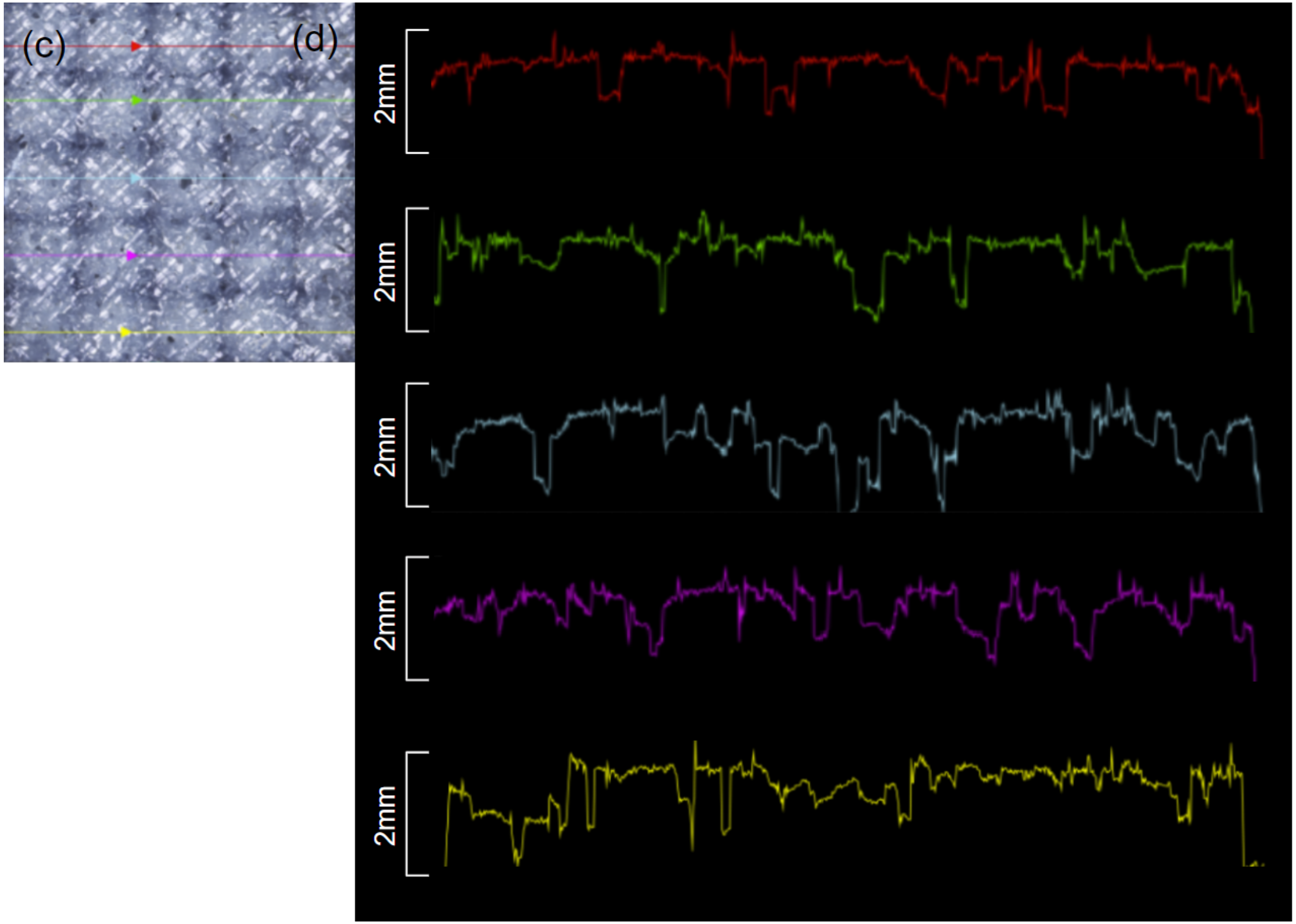
(c)
(d)
2mm
2mm
2mm
2mm
2mm

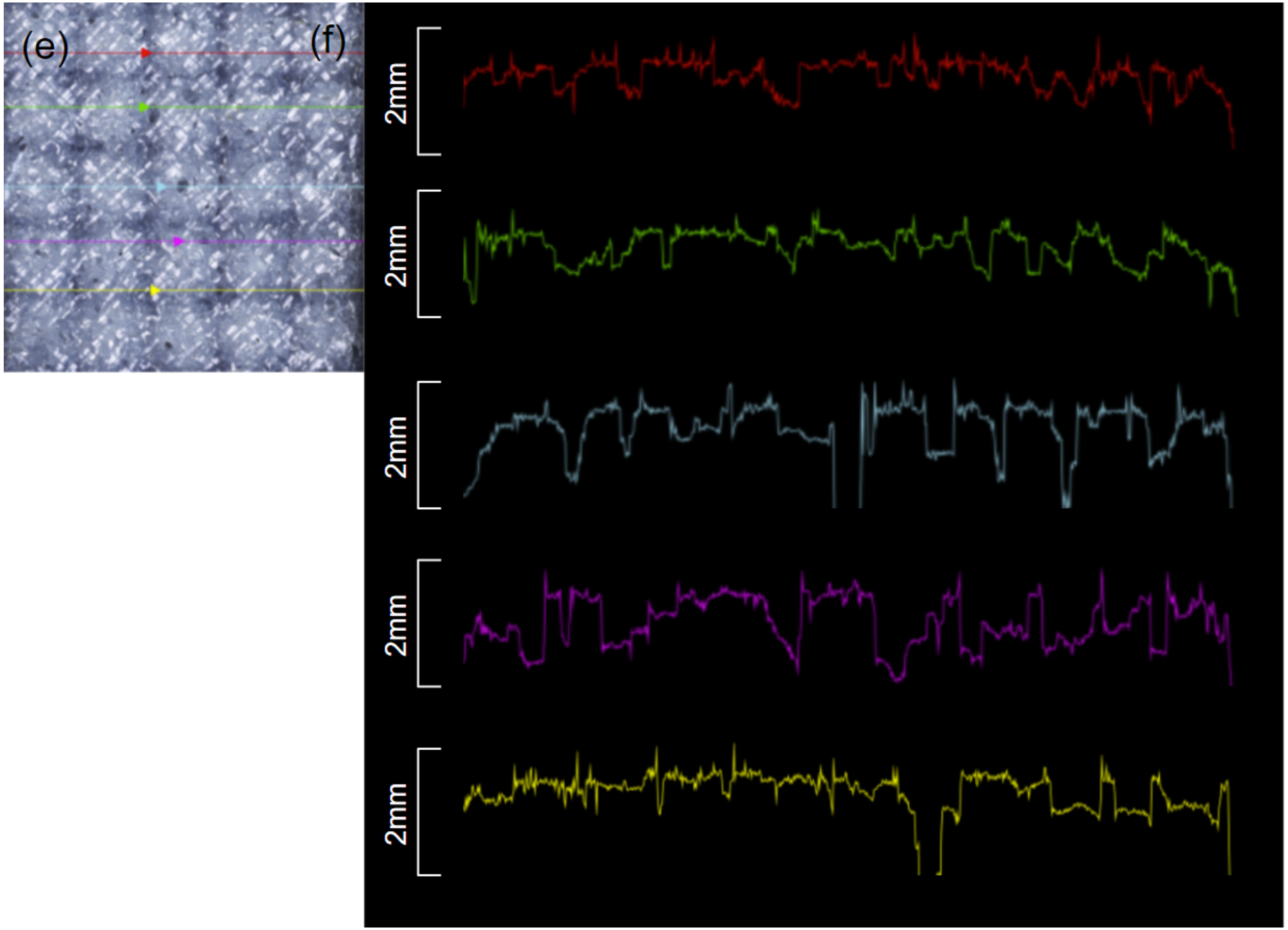

Figure 3.7 Surface roughness measurements of (a & b) StarPore® (s), (c & d) StarPore® (m) and (e & f) MEDPOR®, where each line represents the roughness profile.

Table 3.1 Surface roughness measurements of (a) StarPore® (s) (b) StarPore® (m) (c) MEDPOR®, where each line represents the roughness profile.

Sample Unit	Rp [µm]	Rv [µm]	Rz [µm]	Rc [µm]	Rt [µm]	Ra [µm]	Rq [µm]	Rsk	Rku
StarPore® (s)	646	995	1641	636	1641	306	379	-0.725	2.9
StarPore® (m)	441	762	1203	460	1203	139	178	-1.345	5.3
MEDPOR®	427	708	1136	451	1135	147	184	-1.203	4.1

3.3.1.2 Scanning Electron Microscopy

Scanning electron microscopy was used to visualise the macroscopic morphology of sintered StarPore® scaffolds (Fig. 3.8). 20 x 20 x 1 mm scaffolds were sintered with increasing laser velocities from 60 - 90 mm/s in 10 mm/s intervals, with constants of laser power, scan spacing, layer height, 18 W, 0.75 mm and 0.75 mm, respectively. A softened powder bed, with partial particle curvature was observed at 0.36 J/mm^3 (Fig. 3.8 a). No necking or particle coalescence was seen under these sintering parameters, as there are clear boundaries between each StarPore® unit. Partial melting and particle bonding began at 0.40 J/mm^3, though adhesion was relatively poor due to heterogeneous sintering (Fig. 3.8 b). Adequate coalescence became apparent at 0.46 J/mm^3 at a scan speed of 70 mm/s, while still maintaining particle integrity (Fig. 3.8 c). The powder bed at 0.53 J/mm^3 starts to melt and lose some of its porosity and particle integrity (Fig. 3.8 d).

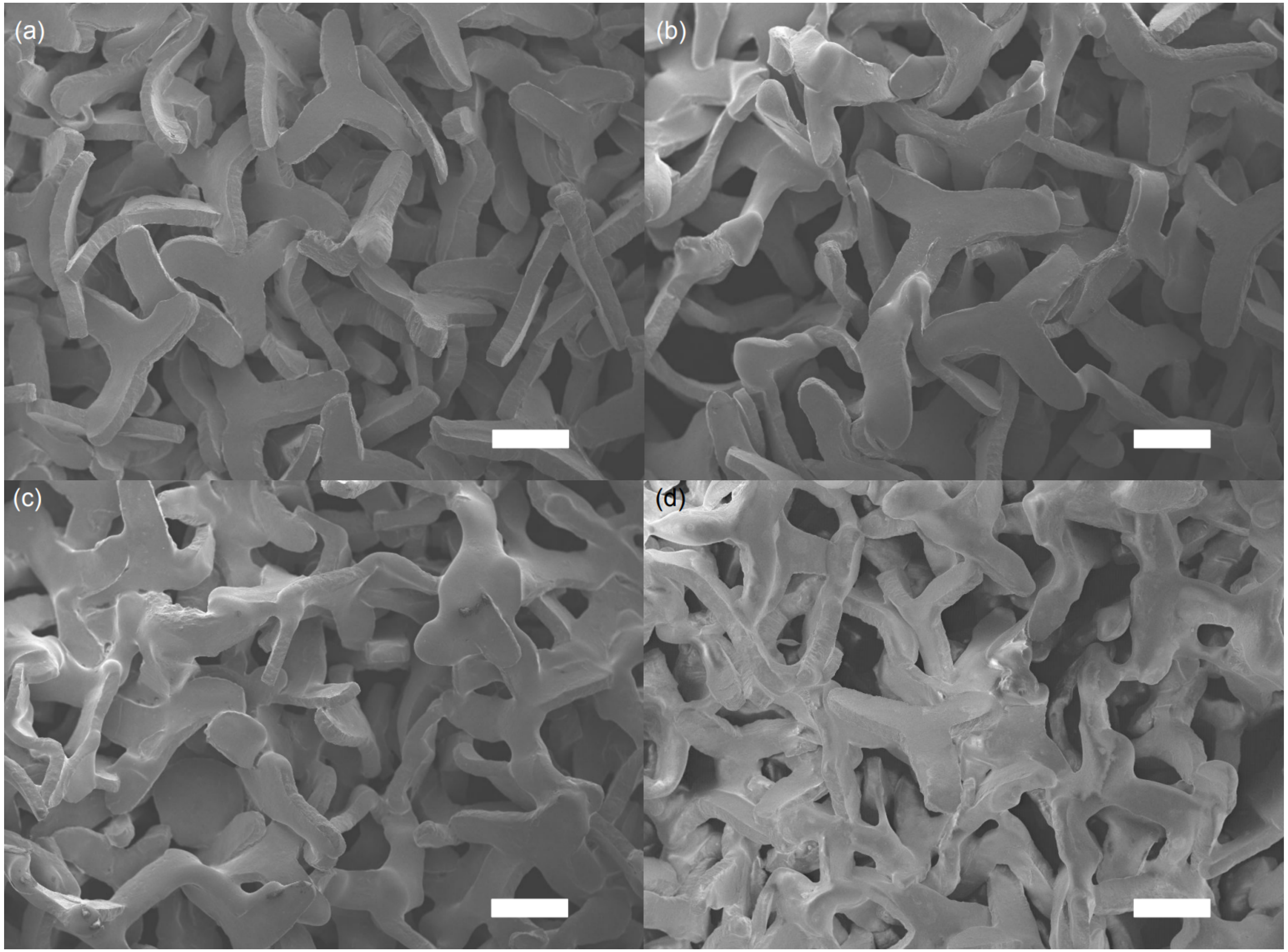

Figure 3.8 Surface morphology of sintered StarPore® scaffolds with increasing energy density. (a) 0.36 J/mm^3 (b) 0.40 J/mm^3 (c) 0.46 J/mm^3 (d) 0.53 J/mm^3. Where scale = 500 µm.

3.3.2 Mechanical properties

3.3.2.1 Compression

The mechanical strength of scaffolds is a fundamental parameter for bone tissue engineered scaffolds. The compressive strength of SLS printed StarPore® was compared to moulded StarPore® scaffolds, printed in a dry and slurry state. Fig. 3.9 shows the modulus determined from the elastic region of the stress strain curves for each scaffold. A slight increase in modulus was observed with increased energy density but was insignificant. The results indicated a shift in mechanical performance when energy density increased from 0.36 to 0.46 J/mm^3 yielding a 51.9% increase in modulus of 0.42 MPa to 0.81 MPa, almost two-fold (Fig. 3.9 a). The highest energy density drove the modulus up to 0.85 MPa, though this was at the sacrifice of particle shape integrity (as outlined in the SEM images above), making the use of the novel StarPore® particle shape redundant as the polymer began to flow and lose all inherent porosity. Printing in a slurry state slightly increased the compression modulus over dry sintering (Fig. 3.9 b). At 0.36 J/mm^3 an increase from 0.42 MPa to 0.58 MPa was observed, with 0.40 J/mm^3 and 0.46 J/mm^3 increasing from 0.64 MPa and 0.81 MPa to 0.74 MPa to 0.89 MPa, respectively. The highest energy density 0.53 J/mm^3 resulted in a slight improvement from 0.85 to 0.92 MPa. Overall the average increase in compressive modulus through the use of slurry printing was found to be 13.9 % throughout all energy densities tested. The limitations of the SLS process however, meant that printed scaffolds were over an order of magnitude weaker in compressive modulus when compared to moulded StarPore®. This was directly related to the much higher porosities generated through printing, as highly porous structures are very sensitive to slight defects, with thin honeycomb structures being shown to halve in structure with only a 5 % strut reduction [292]. Interestingly, the compressive strength of sintered scaffolds at energy densities above 0.40 J/mm^3 lie within the lower range of human trabecular bone [293,294].

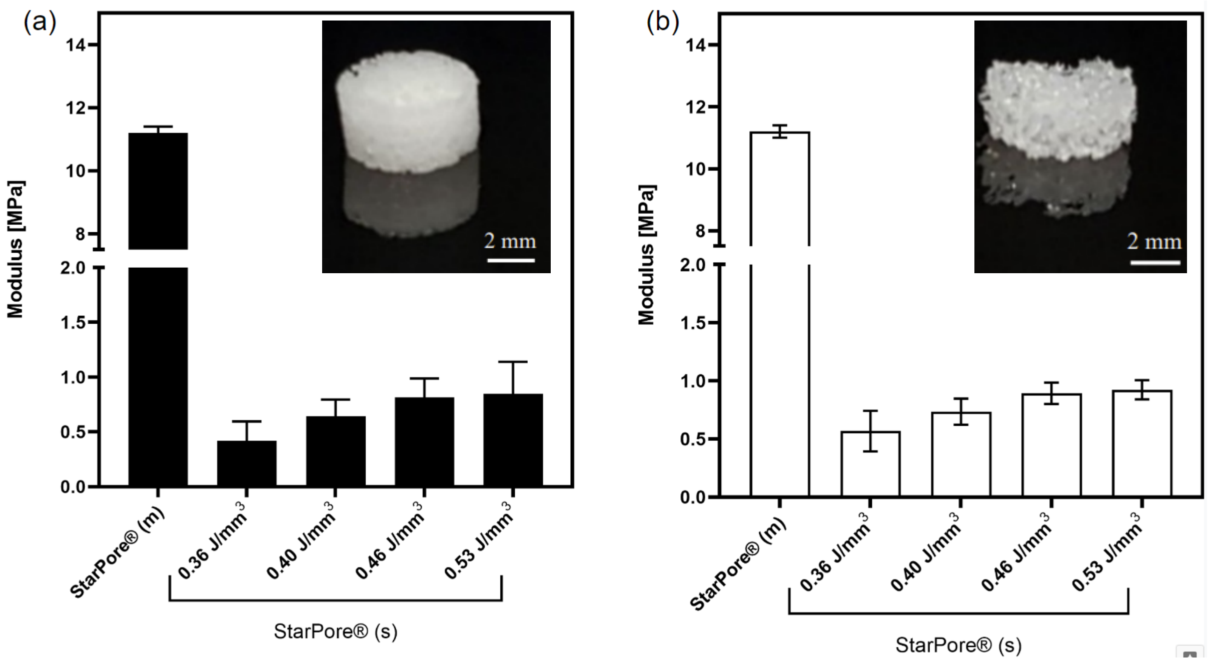

Figure 3.9 Compressive modulus of moulded StarPore® compared to sintered StarPore® in a dry, with an image of a moulded construct (a) and slurry state, with an image of a sintered construct (b). average ∓ S.D., where n = 10.

3.3.2.2 Tensile

To maintain consistency between the printed and moulded constructs, each dumbbell was cut out using the same die conforming to ASTM D638-82 (Type IV). Table 3.2 shows the data extracted from the stress strain curves, comparing StarPore® (m) to a range of StarPore® (s) samples, sintered at different energy densities from 0.36 J/mm^3,0.40 J/mm^3, 0.46 J/mm^3 and 0.53 J/mm^3, in either a dry state or a slurry state. StarPore® (m) showed a significantly higher average ultimate tensile strength of 4.57 MPa when compared to the StarPore® (s) scaffolds which were found to range from 0.99 to 1.54 MPa in a dry and slurry state, respectively. Likewise, the yield point and elongation at break of StarPore® (m) was found to be 3.33 MPa and 32.17 %, respectively. The extended elongation suggests that the moulding process generates highly ductile constructs. The yield strength was found to be slightly higher in the slurry sintered scaffolds when compared to those sintered in a dry state, with an energy density of 0.36 J/mm^3 showing an approximate 50 % improvement. When compared to the moulded scaffolds, sintered scaffolds were found to be very brittle, especially when printed below 0.46 J/mm^3 in both the dry and slurry printing, with yield points well below 1 MPa and elongation at breaks below 10 % [295]. Due to structural heterogeneity from the laser energy Gaussian distribution, large variations were observed in ultimate tensile strength (UTS). The anisotropic nature of 3D printed parts, coupled with the location of the scaffold within the print bed and print orientation, can have a significant influence on mechanical properties [228,296]. For instance, printing constructs at the edges of the substrate has an increased risk of warpage [297,298]. Previous work has overcome these shortcomings by sectioning the scan strategies within the constructs to prevent excessive thermal gradients [299]. Specifically, they separated their dumbbell shaped scaffolds into 7 parts for SLS printing, which ultimately resulted in reduced shrinkage of UHMWPE. Future work should investigate segmented printing approaches, plus how changing the print orientation of constructs impacts compression and tensile strength.

Table 3.2 Tensile strength data comparing StarPore® (m) andStarPore® (s) at a range of energy densities between 0.36 J/mm^3 to 0.53 J/mm^3 both in a dry state and a slurry state. UTS = Ultimate Tensile Strength. Data is shown as average ∓ S.D. Where n = 5

	Sample	**UTS**	**Yield Strength**	**Elongation at break**
	Unit	[MPa]	[MPa]	[%]
	StarPore® (m)	4.57 ∓ 0.32	3.33 ∓ 0.40	32.17 ∓ 1.93
Dry	StarPore® (s) 0.36 J/mm^3	0.18 ∓ 0.03	0.14 ∓ 0.11	2.87 ∓ 1.35
Dry	StarPore® (s) 0.40 J/mm^3	0.34 ∓ 0.09	0.28 ∓ 0.13	4.91 ∓ 2.05
Dry	StarPore® (s) 0.46 J/mm^3	0.56 ∓ 0.14	0.52 ∓ 0.35	6.71 ∓ 3.34
Dry	StarPore® (s) 0.53 J/mm^3	0.99 ∓ 0.21	1.01 ∓ 0.41	9.23 ∓ 4.57
Slurry	StarPore® (s) 0.36 J/mm^3	0.27 ∓ 0.08	0.21 ∓ 0.12	4.17 ∓ 1.55
Slurry	StarPore® (s) 0.40 J/mm^3	0.43 ∓ 0.03	0.35 ∓ 0.07	6.98 ∓ 1.93
Slurry	StarPore® (s) 0.46 J/mm^3	0.91 ∓ 0.12	0.68 ∓ 0.15	10.17 ∓ 2.20
Slurry	StarPore® (s) 0.53 J/mm^3	1.54 ∓ 0.38	1.21 ∓ 0.39	11.10 ∓ 3.45

3.4 Conclusions

Successful fabrication via SLS of trilobal HDPE in the form of StarPore® was achieved. Porosity was found to be significantly higher than commercially available HDPE implants, including moulded StarPore® and MEDPOR®. Adjusting the energy density and scan strategy enabled control over the porosity of printed constructs, not achievable through the traditional fabrication methods used to generate moulded StarPore® and MEDPOR®. Additionally, the surface morphology could also be tuned by manipulating the sintering parameters, whereas the smooth and glossy finish on the moulded implants is fixed.

Printed scaffolds were found to be within the compressive strength range of human cancellous bone. However, sintering resulted in scaffolds that have approximately 21 % the strength of the moulded constructs. This is a known issue in many additive fabrication methods, which struggle to achieve the mechanical properties of traditionally fabricated parts, i.e. injection moulding, due to their anisotropic nature. Through the use of the slurry printing method, printed constructs had a 13.9 % improvement in compressive strength, though this was still only two-thirds that of the moulded scaffolds.

While the increased pore size and porosity of printed constructs lead to reduced mechanical properties relative to moulded constructs, this could be advantageous once implanted. It is established that native tissues can more rapidly infiltrate larger pores and recruit various cell types such as vascular and bone cells, to encourage tissue remodelling. This is a known mechanism for implant support and stabilisation, that is capable of improving implant integration and functional performance. Thus the printed constructs could show beneficial properties over the moulded constructs, once implanted.

Several approaches exist that can overcome the shortfalls associated with SLS, such as adjusting the scan strategy and changing the print orientation of parts, to improve overall strength. Additionally, composite materials can be rapidly tested in new systems that can be used for reinforcement or even bioactivity. Added bioactivity can be beneficial in generating implants that encourage tissue ingrowth and vascularisation, more on this in the next chapter.

The flexibility of additive manufacturing fabrication may hold the key to designing and developing new ways to produce innovative implants of the future. Together with progress in materials science, 3D scanning and additive manufacturing technology, as well as biological testing, researchers can ensure clinicians will be equipped with the best possible scaffolds. The translation of research like this will diversify innovative treatment options and ultimately provide tailored, or patient-specific implants for positive patient outcomes.

CHAPTER 4

BIOLOGY

Chapter 4: Biology

Overview

To accurately gauge the efficacy of newly developed bone substitutes, biological models are necessary for translation to humans. This chapter draws upon the established apatite-forming assay called simulated body fluid or the SBF assay, comparing the bioactivity of MEDPOR®, StarPore® (m) and StarPore® (s), accompanied by an eight week *in vivo* rat study. The subcutaneous implantation was used to quantify tissue ingrowth and vascularisation in all 3 scaffolds, through immunohistochemical stainings and high resolution microscopy.

Portions of this chapter have been published in the following article:

Paxton, N.C., Dinoro, J., Ren, J., Ross, M.T., Daley, R., Zhou, R., Bazaka, K., Thompson, R.G., Yue, Z., Beirne, S. and Harkin, D.G., 2021. Additive manufacturing enables personalised porous high-density polyethylene surgical implant manufacturing with improved tissue and vascular ingrowth. Applied Materials Today, 22, p.100965.

Author contributions: Naomi C. Paxton: Conceptualization, Methodology, Validation, Formal analysis, Investigation, Writing - Original Draft. Jeremy Dinoro: Conceptualization, Methodology, Validation, Investigation, Writing - Review & Editing. Jiongyu Ren: Investigation, Writing - Review & Editing. Maureen T. Ross: Investigation, Writing - Review & Editing. Ryan Daley: Validation, Investigation, Writing - Review & Editing. Renwu Zhou: Investigation, Writing - Review & Editing. Kateryna Bazaka: Resources, Supervision. Robert G. Thompson: Conceptualization, Funding acquisition. Zhilian Yue: Supervision. Stephen Beirne: Funding acquisition, Supervision. Damien G. Harkin: Formal analysis, Writing - Review & Editing. Mark C. Allenby: Writing - Review & Editing, Supervision. Cynthia S. Wong: Formal analysis, Investigation, Writing - Review & Editing, Supervision. Gordon G. Wallace: Conceptualization, Funding acquisition, Resources, Supervision. Maria A. Woodruff: Conceptualization, Funding acquisition, Resources, Supervision.

4.1 Introduction to Human Bone Structure

Musculoskeletal disorders currently cost the US government over $380 billion dollars annually. This cost stems from a growing ageing population, with the financial burden of 45 - 65 year olds equating to $168.8 billion and > 65's attributing to $133.9 billion [300]. Current grafting treatments can lead to further complications, including donor site morbidity, pain and increased risk of infection [301,302]. New grafting innovations are vital to reduce the healthcare burden on society, the workforce, communities and individuals.

As a dehydrated tissue, human bone is made up of 70% inorganic and 30% organic components [303,304]. The inorganic phase is mainly composed of calcium, with the organic phase primarily composed of collagen type I, generated by osteoblasts [304]. The external surfaces of bone are dense and robust. If this outer layer is thin it is called cortical bone, where it is thick, it is known as compact bone (Fig. 4.1) [305]. The outer sheath is rigid, with an approximate ultimate compressive strength of 160 MPa, though due to its anisotropic nature, long bones can range from 131 MPa to 205 MPa in transverse and longitudinal directions, respectively [306]. Internally, cancellous or spongy bone as the name suggests provides dampening to sudden external stress while also housing high levels of metabolic activity [307]. The compressive modulus lies within the range of 0.1 - 30 MPa, depending on bone location, age, and hormone levels of an individual, among other variables [308,309].

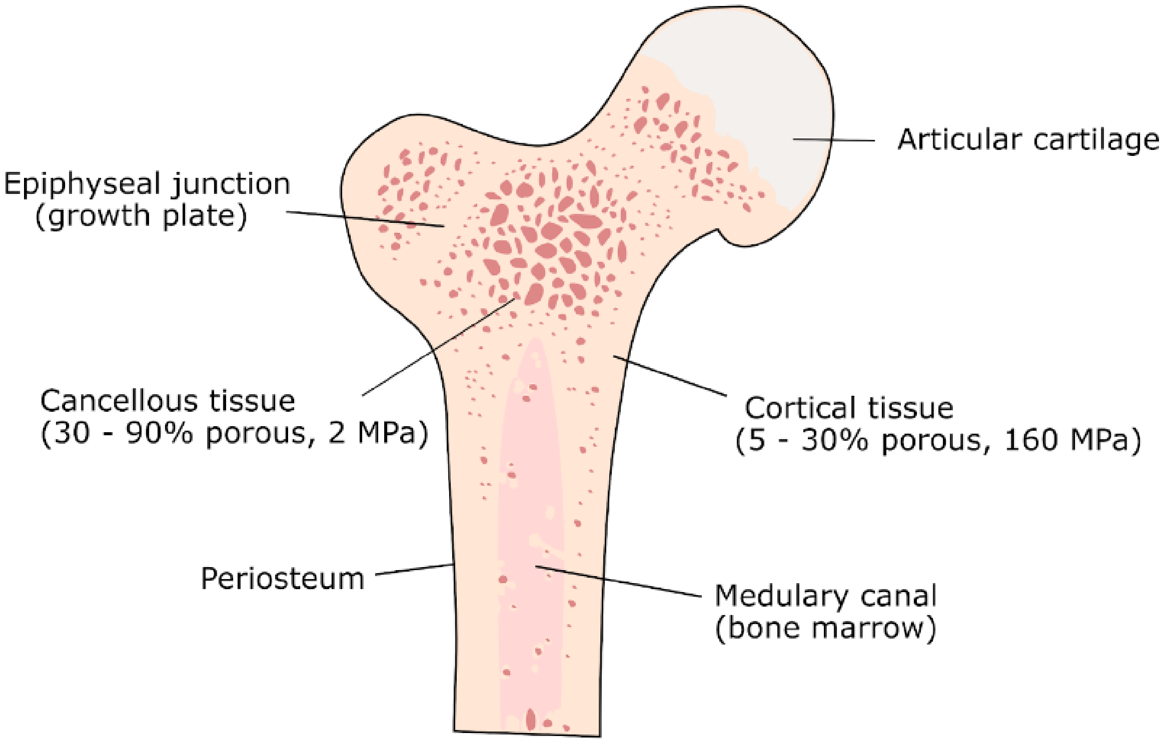

Figure 4.1 Schematic drawing of the end of a human long bone

4.1.2 Treatments and Printed Implants

Bone naturally has a regeneration capacity to heal defects smaller than 20 mm. Exceeding this size, an injury or intervention is known as a critical sized bone defect. The standard treatment for critical sized bone defects is autografting. As outlined in the first chapter, autografting can lead to a range of complications, such as pain and increased risk of infection, thus tissue engineered alternatives need to be explored to improve patient outcomes.

Craniomaxillofacial (CMF) bone supports vital human functions such as mastication, speech, breathing, vision and hearing. Additionally, cranial bone protects the brain from impact. Injury to the CMF region, particularly critical sized defects, can be difficult to repair due to complex architecture, symmetry and aesthetics [310–312]. In the same vein, understanding bone's regeneration process, from initial development to signalling pathways, provides scientists, engineers and clinicians the tools to decipher the interactions between structure, physiology and function. Thus, the ideal implant should both support and promote tissue ingrowth and vascularisation beyond static prosthetics [313]. Furthermore, an implant should match the contours and architecture of the defect [311], including a porous interior to enable tissue infiltration and vascular invasion [314]. As delays in vascularisation can limit gas exchange and waste removal, resulting in hypoxia and cell death [315].

Additive manufacturing offers the ability to fabricate patient-specific implants from clinical scan data that can accurately match the many of the properties of the defect site. The choice to implement additive manufacturing into developing implants circumvents the use of pre-manufactured moulds, delivering implants more efficiently and economically [316]. Additionally, the mechanical properties of the printed constructs can match that of the target site through adjustments to the density and porosity of prints.

The aim of this chapter was to investigate the influence of porosity and fabrication methods on bioactivity, tissue ingrowth and vascularisation of implants. Specifically, a comparison of the current gold standards of HDPE implants, MEDPOR®, StarPore® and sintered StarPore®, with porosities of 35.9%, 67.6% and 82.4% respectively. It was hypothesised that the higher porosity implants would improve tissue ingrowth and vascularisation due to an improved capacity to encourage gas, nutrient and waste exchange.

4.2 Experimental Section

4.2.1 Materials

Sample preparation. HDPE discs (⌀ 6 mm x 3 mm) were biopsy punched (Kai Medical, Gifu, Japan) out of MEDPOR® (Styker, NSW, Australia) (Fig. 4.2a), StarPore® (Melbourne, VIC, Australia) (Fig. 4.2b) and sintered StarPore® (Melbourne, VIC, Australia) (Fig. 4.2c). Printing parameters for the sintered scaffolds involved the use of a 30 W CO_2 (10.6 μm) laser engraver (Universal Laser Systems, Inc., USA) with a laser velocity of 100 mm/s, at 18 watts and a spot size of 127 μm, scanned with 1 mm hatch and layer spacing over 20 x 20 x 3 mm (XYZ) (Fig. 4.2d). Scaffolds for the simulated body fluid assay were printed in a slurry, outlined in Chapter 2, with and without 0.1, % and 1% w/v Bioglass S53P4 (53% SiO2, 4% P2O5, 20% CaO, 23% Na2O wt %). All scaffolds were sterilised by ethylene oxide (EtO) by Anatomics Pty Ltd (Melbourne, VIC, Australia).

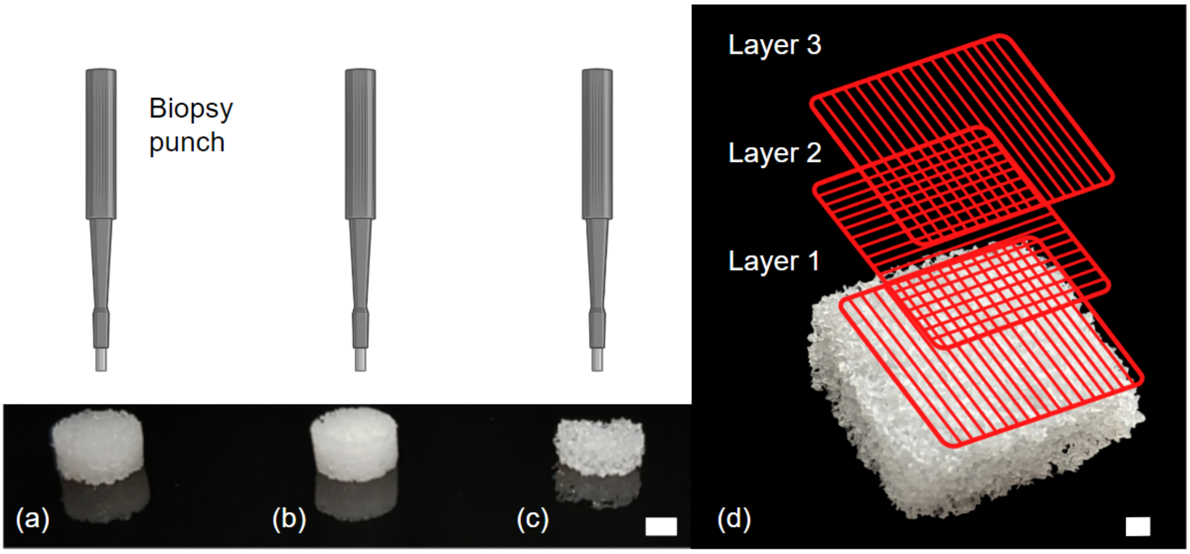

MEDPOR® StarPore® (m) StarPore® (s) Scan strategy for StarPore® (s)

Figure 4.2 (a-c) Images of the implanted scaffolds following biopsy punch, scale bar = 2 mm. (d) Schematic of scan strategy used to generate the sintered construct above the 20 x 20 x 3 mm scaffold, scale bar = 2mm.

4.2.2 *In vitro* Bioactivity

A simulated biological fluid (SBF) assay was conducted to assess the apatite forming capacity of scaffolds. Scaffolds were printed using the slurry-based method previously outlined, where 800 mg/ml of StarPore® powder was dispersed in DI water. The neat or virgin material was used as a negative control against 0.1 % w/v and 1 % w/v Bioglass® which was dispersed in the water prior to creating the slurry with StarPore®. Simulated biological fluid (SBF) was prepared using analytical grade reagents consisting of 5.403 g NaCl, 0.504 g $NaHCO_3$, 0.426 g $NaCO_3$, 0.225 g KCl, 0.230 g $K_2HPO_4{\cdot}3H_2O$, 0.311 g $MgCl2{\cdot}6H_2O$, 0.8 g NaOH, 0.293 g $CaCl_2$, 0.072 g Na_2SO_4 and 17.892 g HEPES as buffering agent (all purchased from Sigma-Aldrich). The pH was adjusted to 7.40 ± 0.05 using 1.0 M NaOH solution. Scaffolds were immersed in a 50 ml SBF solution and incubated at 37 ℃ (Fig. 4.3). Samples were removed at day 0, day 1 and day 7 then were rinsed with distilled water to remove excess salt and prevent further apatite formation, left to air dry for 24 hours and weighed, where n = 3. Scanning Electron Microscopy (SEM) images were taken using a

JEOL JSM-7500FA. Samples were prepared via sputter-coating to create a ~10 nm gold coating.

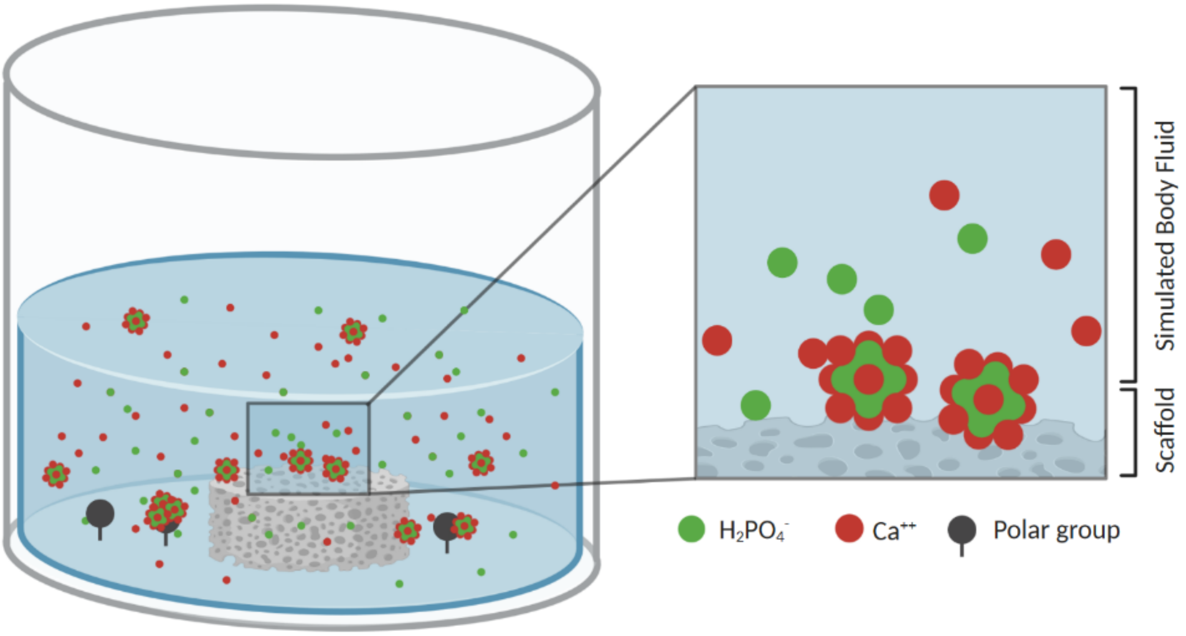

Figure 4.3 Illustration of SBF-mediated mineralisation. The dispersed calcium and phosphate ions begin to form nucleated crystals. Apatite crystals are formed and grow on the polar surface of the scaffold. Adapted from [317]

4.2.3 *In vivo* Subcutaneous Implantation

To assess tissue and vascular ingrowth, HDPE discs of MEDPOR®, StarPore® (M) and StarPore® (S) were subcutaneously implanted in rats at Queensland University of Technology's Medical Engineering Research Facility over 8 weeks (QUT Animal Ethics Approval #190000456). The implantation surgeries were performed on male skeletally-mature Sprague-Dawley rats that were 9 weeks old (n = 18). General anaesthesia (2% isoflurane, 1.5% oxygen) was administered through a nose cone. Pre-emptive analgesia and prophylactic antibiotics were administered via subcutaneous injection (0.1 mg/kg BW buprenorphine, 1 mg/kg body weight (BW) meloxicam, 20 mg/kg BW cefazoline, 0.5 mL warm sterile saline). The backs of the animals were shaved and prepared with povidone-iodine Using a scalpel, four paramedian incisions were made on the back of each animal, two on each side with approximately 2 cm between incisions. One sample of

MEDPOR®, StarPore® (moulded) or StarPore® (sintered); was inserted subcutaneously below the panniculus carnosus at each incision site, with each animal receiving 4 discs from different scaffold groups in the soft tissues of the back in distinct pockets, separated by at least 2 cm (implant location sites can be found in Fig 4.4). Irrigation with sterile normal saline was carried out to keep the exposed tissues moist and the incisions were closed with 4-0 prolene surgical sutures.

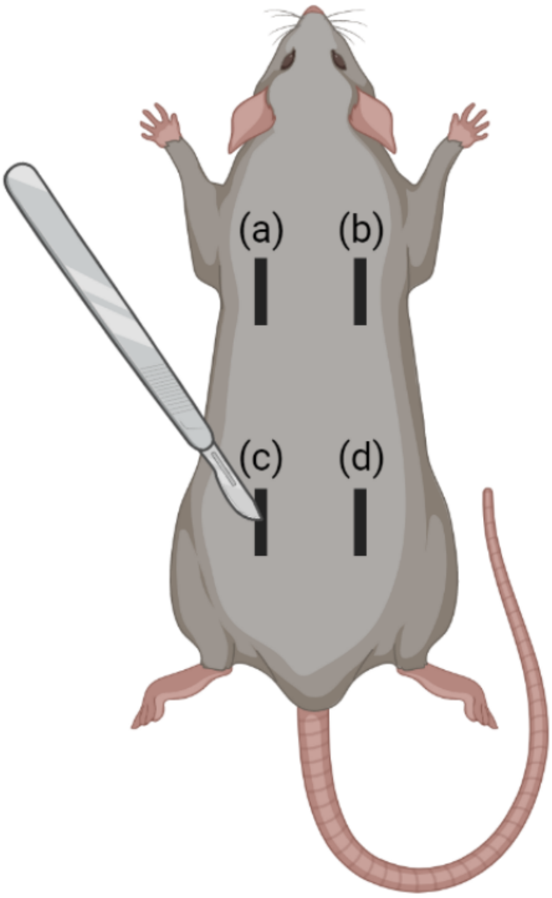

Figure 4.4 Schematic of rat subcutaneous implantation sites. (a) Left cranial or LCr, (b) Right cranial or RCr, (c) Left caudal or LCd and (d) Right caudal or RCd.

4.2.4 Immunohistochemical Analysis

Following removal of implants, scaffolds were fixed for 48 hrs in 4 % PFA. Of the 4 samples harvested from each group, 3 were embedded with the muscle beneath for parallel or horizontal sectioning. The remaining samples were cut sagittally to expose the internal inner face of implants and embedded surface down for vertical sectioning. A rotary microtome (RM 2135, Leica, Wetzlar, Germany) was used to slice 5 µm paraffin sections and 3 different immunohistochemical (IHC) stainings were used to identify specific proteins within the scaffolds. Haematoxylin and eosin (H&E) was used to gauge tissue morphology, with Masson's trichrome (MT) staining used for collagen and blood vessel identification, von Willebrand factor (vWF) glycoprotein as an endothelial cell marker to outline the presence of late stage blood vessels and CD68 marker to image macrophage activity.

Haematoxylin counterstaining was performed on IHC samples to visualise cell nuclei. Stained slides were then automatically scanned at 20x magnification (SCN400 High Throughput Slide Scanner, Leica, Wetzlar, Germany). Tissue content was quantified using colour thresholding in ImageJ. The percentage of ECM (from H&E), collagen or blood (MT) present within each scaffold was calculated by selecting the outer margins of the scaffold as the ROI and applying an automatic threshold to delineate specific colours present in the images which could be attributed to a general or specific tissue type, and was characterised by a peak in the colour intensity histogram (Appendix 4). Tissue content was calculated as a percentage of the scaffold ROI area, and reported as the average ± S.D. (where n = 3) for each scaffold group at each time point. Blood vessels were also visually identified in 5 40x-magnification ROIs from each sample in ImageJ and selected using an ellipse or freehand selection tool. The total number and area of blood vessels in each sample were calculated using the measuring tool in ImageJ and reported as the average ± S.D. for each scaffold group at each time point (where n = 3 rats, ROIs within each sample where n = 5). The diameter of blood cells in MT images was measured using a line tool and reported as average ± S.D. (where n = 20 RBCs)

4.2.5 Statistical Analysis

Statistical significance between experimental groups was calculated in Excel (Microsoft, Redmond WA, USA) using the student’s T-test function to calculate p-value and one-way ANOVA to identify differences between experimental parameters

4.3 Results and Discussion

4.3.1 *In vitro* Bioactivity

The bioactivity of sintered StarPore® scaffolds was assessed via an SBF assay. Pure or virgin StarPore® was compared to constructs with 0.1 % and 1 % w/v Bioglass® integrated into the structure (Fig. 4.5). Due to the lack of functionality on the surface of all scaffolds, only minor growth was observed (Fig. 4.6 d-f). The fabrication method as well as the low concentration of particles dispersed through the matrix meant that the polymer completely encapsulated the Bioglass® particles, limiting their interaction with the solution. Previous studies investigating the bioactivity of HDPE/Bioglass® composites have produced constructs with percentages above 20 % w/v of Bioglass® [318]. Additionally, they’re often fabricated by surface coating methods that expose higher specific areas of glass particles to the solution and enable rapid ion exchange [319].

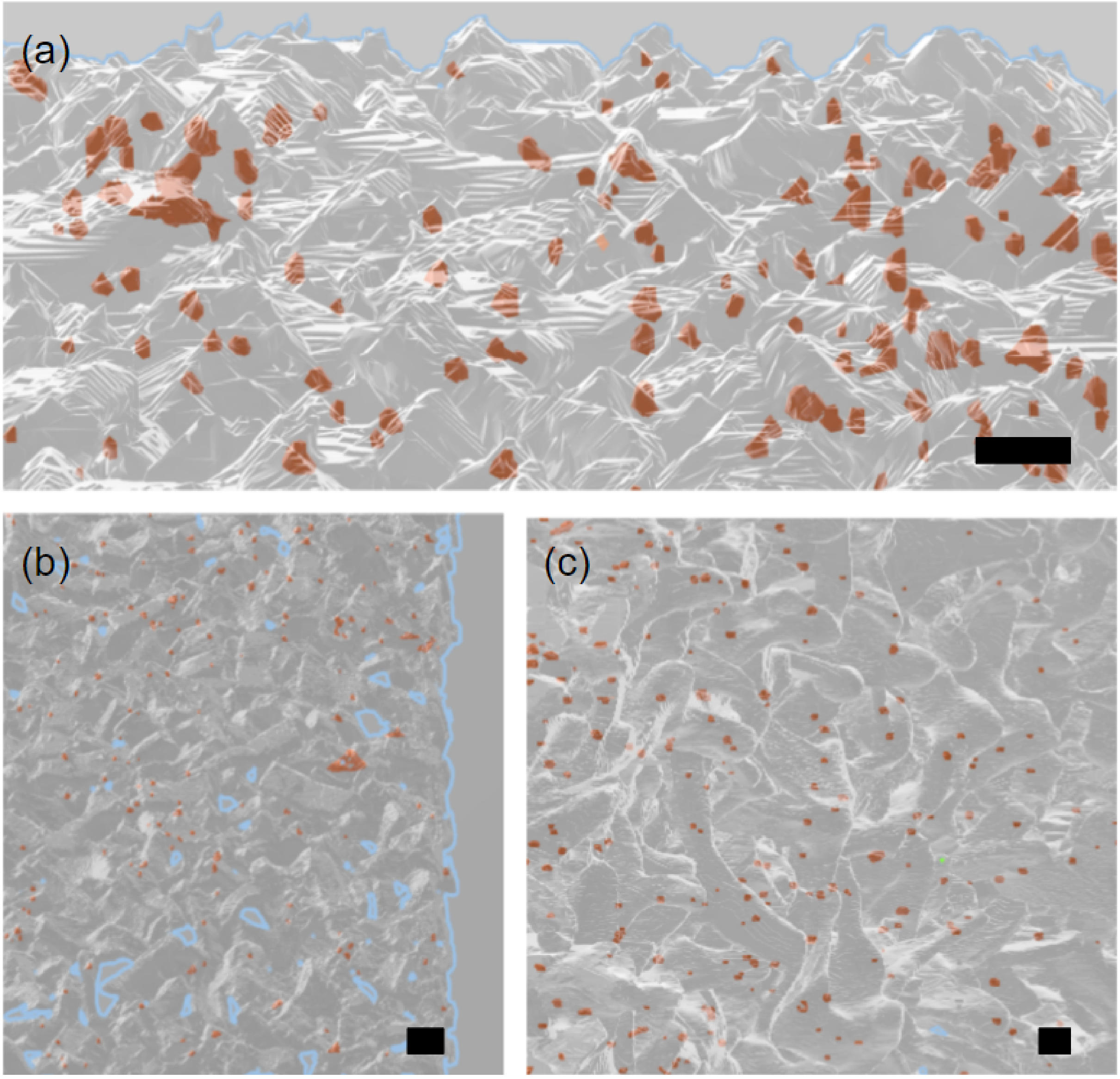

Figure 4.5 Reconstructed micro CT images of Bioglass® (orange) integrated within the polymer matrix of StarPore®. Scale bar = 100 µm.

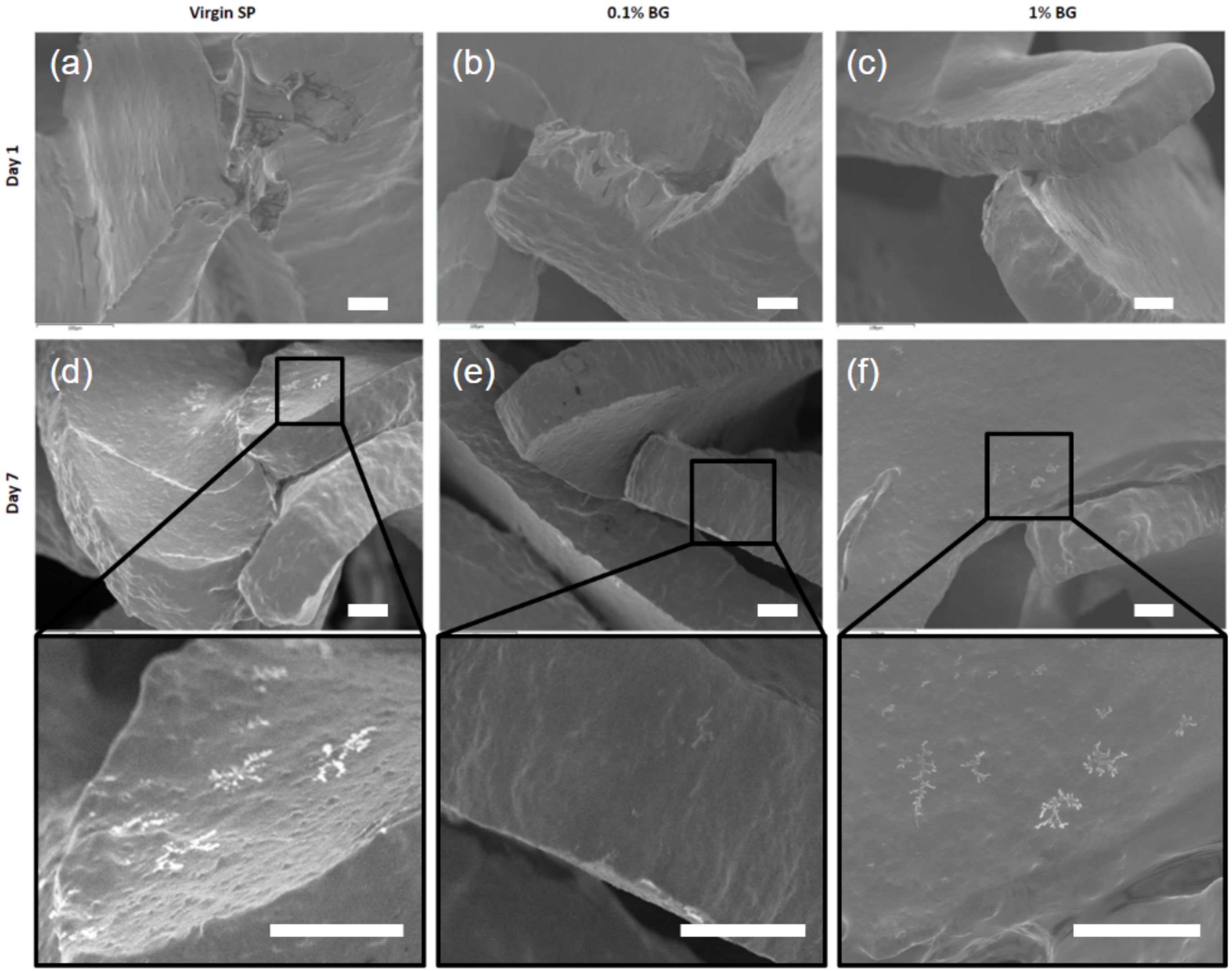

Figure 4.6 Scanning electron microscope images showing the surface morphology of StarPore®(s) scaffolds before (a-c) and after 7 days (d-f) immersed in SBF solution. (a), (d) don't contain Bioglass, whereas (b), (e) contain 0.1% w/v Bioglass and (c), (f) contain 1% w/v Bioglass.

4.3.1 *In vivo* Subcutaneous Implantation

4.3.1.1 Tissue Ingrowth

Throughout the implantation experiment the weight of the rats was closely monitored. It was revealed that all rats completely recovered from surgery and returned to their previous weight. Samples were harvested at 1, 4 and 8 weeks following euthanasia. Immediately after harvesting samples were embedded and fixed for immunohistochemical (IHC) analysis. H&E staining of samples, at the 8 week time point, revealed slight tissue ingrowth into all samples (Fig. 4.7). Interestingly, MEPORE® and StarPore® (M) samples showed a large amount of unfilled pore space (Fig. 4.7 d & e). The printed scaffolds on the other hand showed more connective tissue infiltration (Fig. 4.7 f). While the mechanical properties were found to be significantly reduced following compression tests within the printed constructs, this was found to be beneficial during implantation. This was directly associated with the interconnectivity and overall scaffold porosity.

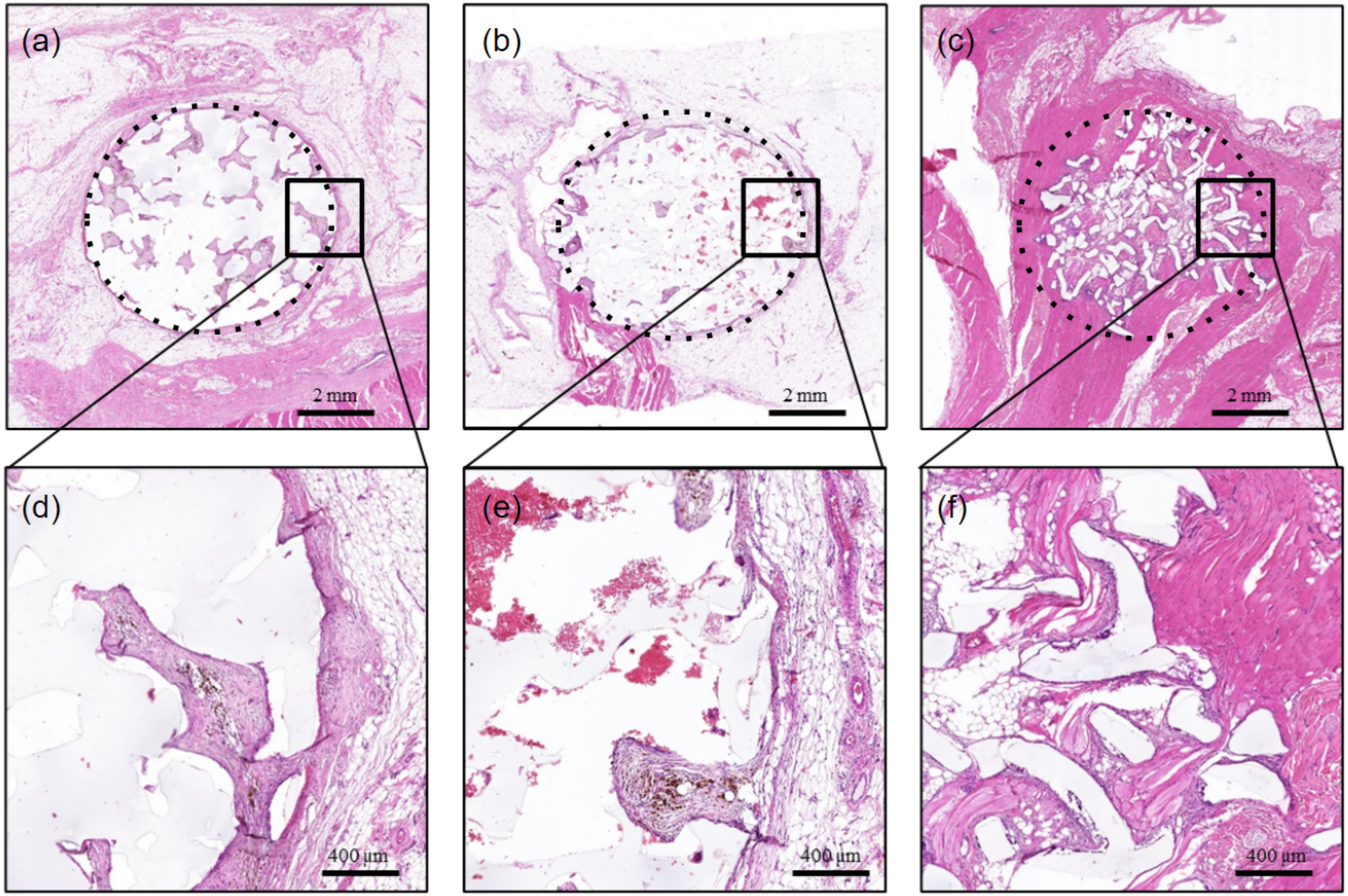

Figure 4.7 H&E stainings of implanted 6 mm scaffolds discs (a) MEDPOR®, (b) StarPore® (moulded) and (c) StarPore® (sintered) at week 8, accompanied by 20x magnification of regions of interest (d) MEDPOR®, (e) StarPore® (moulded) and (f) StarPore® (sintered). Cell nuclei are stained dark purple with haematoxylin, ECM and cytoplasm is stained pink with eosin.

Accounting for the density discrepancies between samples, the histology data was quantitatively assessed with ImageJ. Sample porosity was determined to be 35.9% ± 6.1%, 67.6% ± 11.2% and 82.4% ± 13.9% for MEDPOR®, StarPore® (M) and StarPore® (S), respectively. Thus within the regions of interest, the scaffolds occupied 64.1% for MEDPOR®, 32.4% for StarPore® (M) and 16.3% for StarPore® (S) (Fig. 4.8 a). After normalising tissue ingrowth against scaffold porosity for potential space available within each implant, we found pores filled in MEDPOR® to be 18.6%, in StarPore® (M) 24.9 % and StarPore® (S) 77.1 %. Accordingly, this revealed a connection between porosity and tissue ingrowth (Fig. 4.8 b). Interestingly, the highly porous printed scaffolds resulted in a 3.4-fold increase in percentage tissue infiltration, when compared to StarPore® (M), consistent with previous studies, demonstrating improved tissue ingrowth with higher pore size and porosity [320–322]. The commercially available HDPE scaffolds, MEDPOR® and StarPore® (M), were found to have a reduced capacity to promote tissue ingrowth (Fig. 4.8 c). While the differences observed in tissue ingrowth could be related to overall scaffold porosity, surface roughness has also been shown to provide anchorage points that influence cell attachment [323], particularly in SLS [177] and SLM [51] printed parts. Additionally, a porous interconnected structure provides a pathway for cell migration, however, these pores need to be small enough to enable a high specific surface [324]. Thus a porous hierarchical scaffold structure may be beneficial for bone tissue engineering applications [325–327].

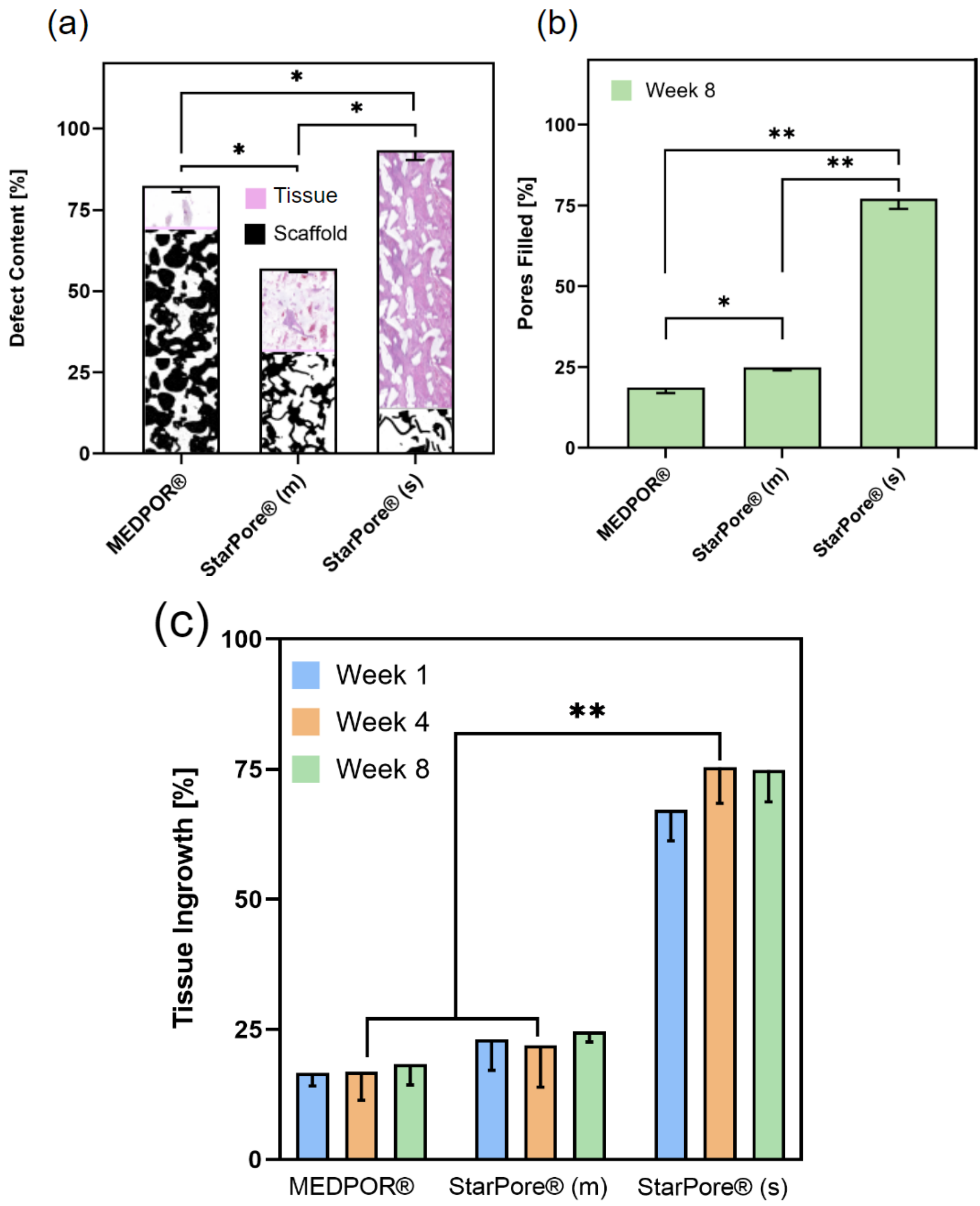

Figure 4.8 Quantification of tissue ingrowth of MEDPOR®, StarPore® (M) and StarPore®(S) samples determined from H&E sections. (a) A combination of scaffold and tissue infiltration within each defect region. (b) Normalised tissue infiltration accounting for variations in scaffold porosity. (c) Overall tissue ingrowth as a percentage of H&E staining within the region of interest measured at week 1, 4 and 8. All averages ± SD, where n = 3. * $p < 0.005$; ** $p < 0.0005$

4.3.1.2 Vascular tissue Ingrowth

To determine the presence of vascular tissue infiltration, Masson's Trichrome staining was employed. This is used to determine collagen (blue) in connective tissues, the existence of muscles and blood (red) as well as cell nuclei (dark purple). vWF (brown) staining was also used as an endothelial cell marker, with nuclei (light purple). StarPore® (m) scaffolds embedded in tissue can be seen in Fig. 4.9. A clear epidermal tissue layer can be seen on the right side of the image, with the white rectangular area seen in the dermal layer being a cross-section of the implant. Distinct red blood cells (RBCs) were dispersed throughout the pores of the scaffold (Fig. 4.9 a, b, d, e), identified by the red stained ellipsoids, approximately 3.7 ± 0.5 µm in diameter (where $n = 20$) an established hallmark in literature [328–331]. Additionally, voids between connective tissue were observed, thought to be associated with disorganised tissue (Fig. 4.9 b, d, e). Confirmation of this was seen through the endothelial cell marker vWF, where no clear collagen alignment or organisation was observed (Fig. 4.9 c & f).

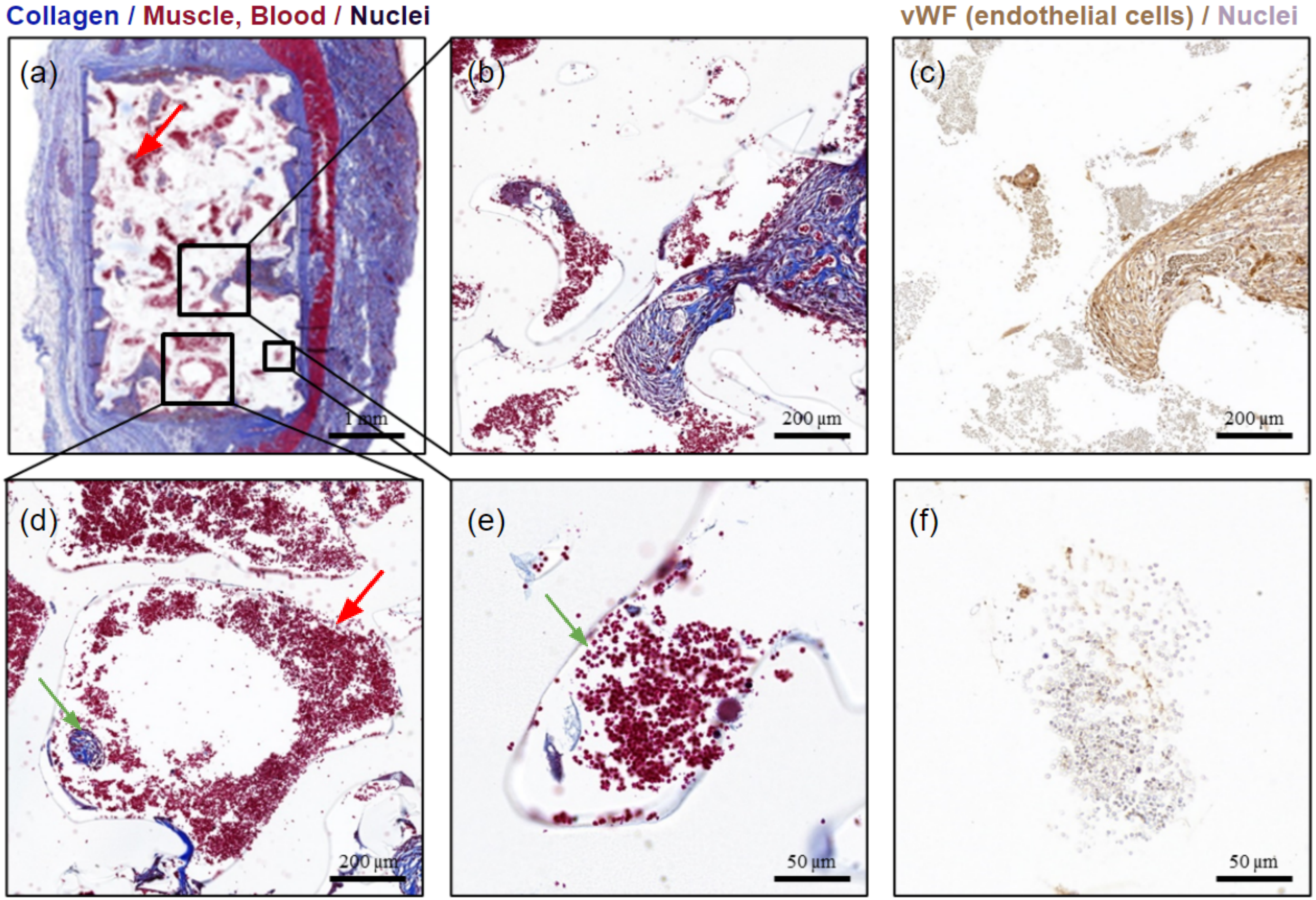

Figure 4.9 Protein staining of MT and vWF markers on StarPore® (m) scaffolds following the 8 week subcutaneous rat implantation. (a-g) All samples were sliced vertically with the epidermis seen on the right hand side, with muscle seen to the left. Red arrows indicate blood vessels outside vessels, with green indicative of those inside

StarPore® (s) scaffolds embedded in tissue can be seen in Fig. 4.10. A clear epidermal tissue layer can be seen on the right side of the image, with no discernible border at implant and tissue interface (Fig. 4.10 a). Clear indications of collagen fibre deposition and alignment was observed, with areas of dense tissue as well as loose connective tissue (Fig. 4.10 b, c, e). In the same vein, the endothelial marker vWF demonstrated clear organised vascular structures (Fig. 4.10 c & f).

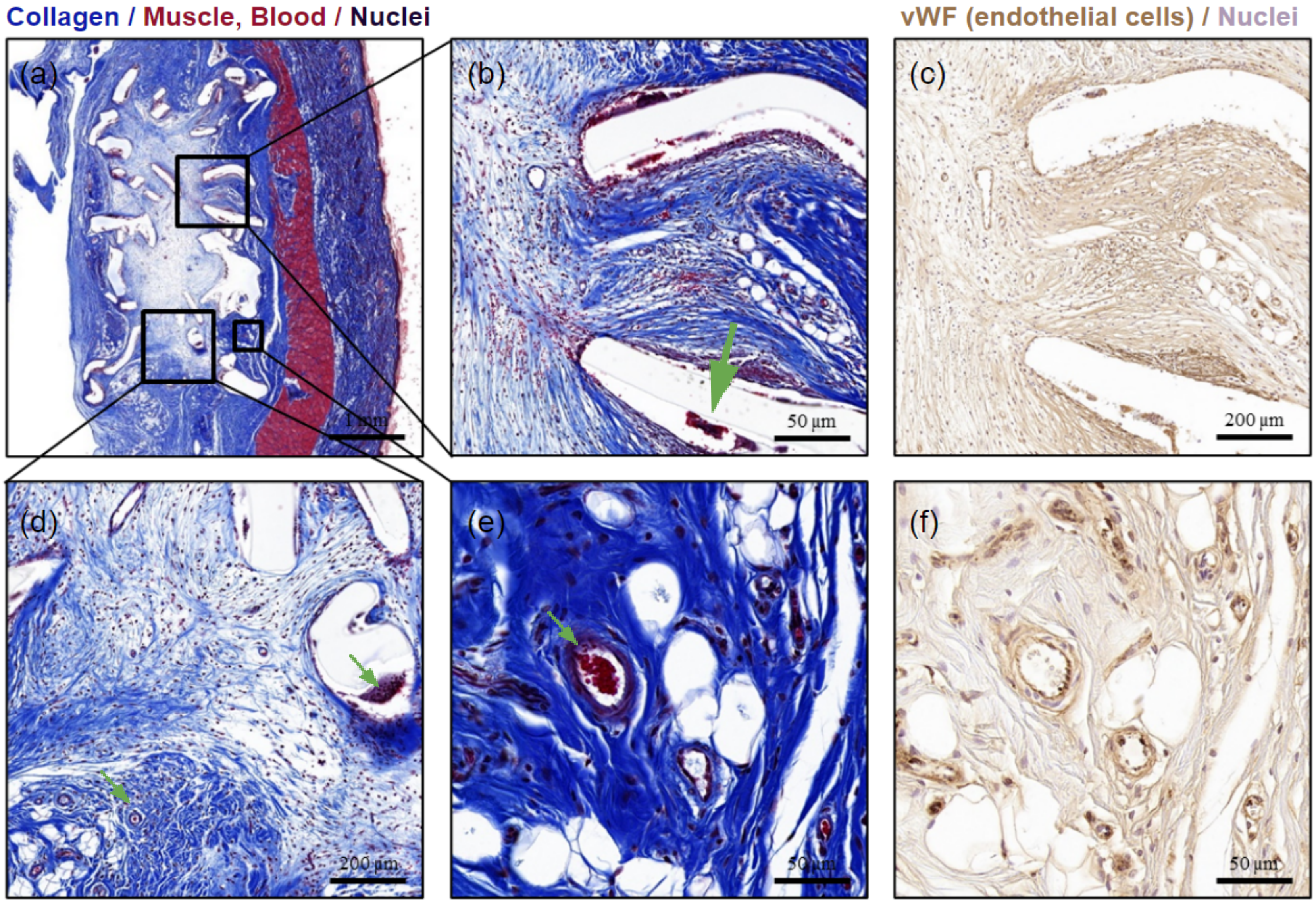

Figure 4.10 Protein staining of MT and vWF markers on StarPore® (s) scaffolds following the 8 week subcutaneous rat implantation. (a-g) All samples were sliced vertically with the epidermis seen on the right hand side, with muscle seen to the left. Red arrows indicate blood vessels outside vessels, with green indicative of those inside

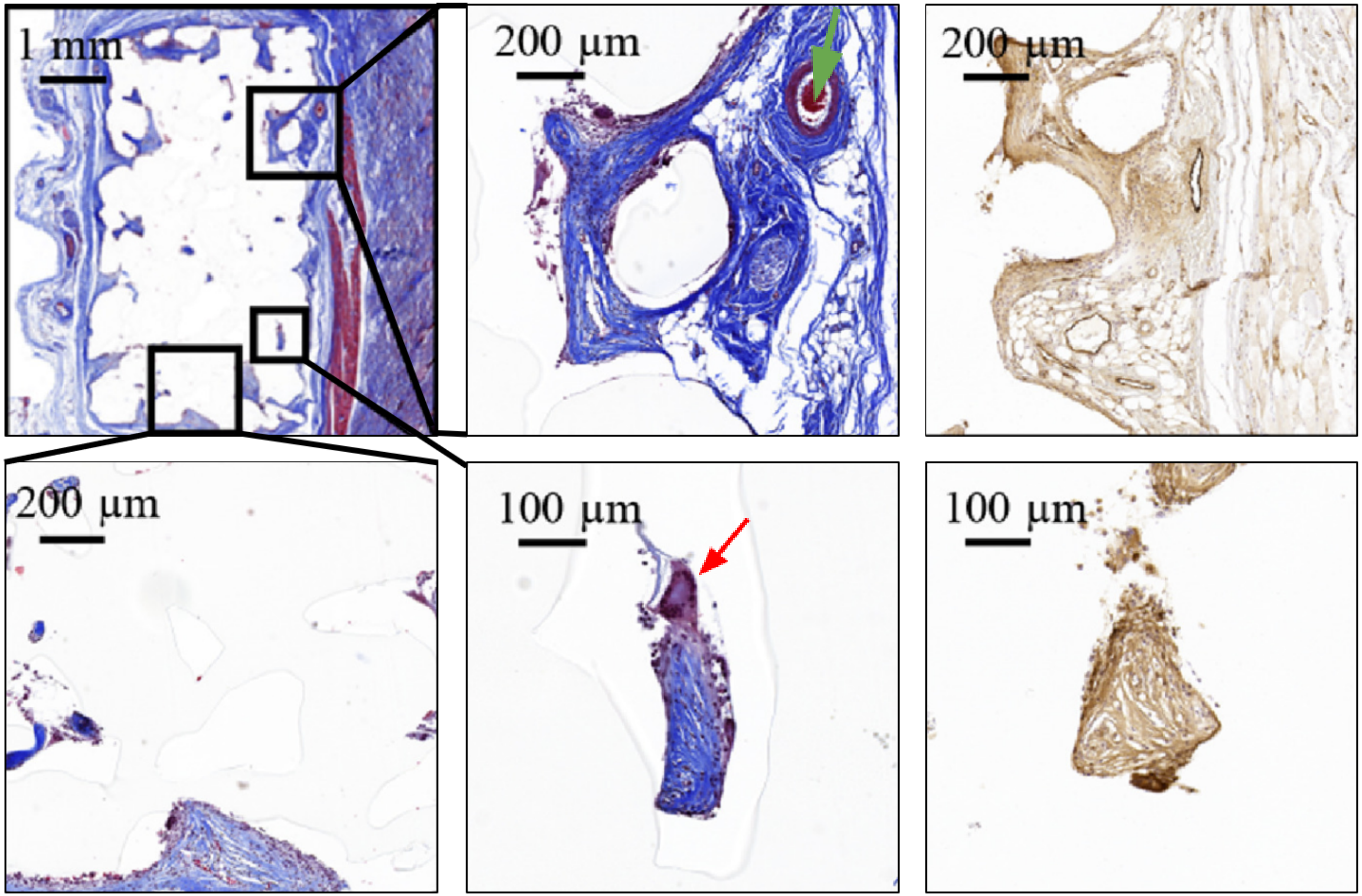

Figure 4.11 Protein staining of MT and vWF markers on MEDPOR® scaffolds following the 8 week subcutaneous rat implantation. (a-g) All samples were sliced vertically with the epidermis seen on the right hand side, with muscle seen to the left. Red arrows indicate blood vessels outside vessels, with green indicative of those inside

The quantity of each tissue type is reported as a percentage of the total scaffold surface area (Fig. 4.12), showing a significant increase in the blood content within StarPore® (M) scaffolds compared to the other two scaffold types ($p < 0.002$, where $n = 3$); on average, StarPore® (M) scaffolds contained 18.7 ± 2.3% red staining, identifiable as RBCs in the micrographs, compared to 5.5 ± 2.0% and 9.6 ± 3.1% for MEDPOR® and StarPore® (s) respectively. Given the significant difference in tissue ingrowth between samples of varying porosity, pore interconnectivity was quantified from μCT data by comparing the total volume of all interconnected pores with those not connected. It was found that the 35.9% pore volume within MEDPOR® scaffolds was predominantly one continuous pore structure, with remaining volume attributable to unconnected pores. It was calculated that 99.94 ± 0.01% of the pore volume was interconnected, while the remaining 0.06 ± 0.01% of the pore volume consisted of entirely closed pores, inaccessible to fluid flow or tissue infiltration. These results indicate that while the vast majority of the MEDPOR® scaffold structure is interconnected, the porosity limits the ability for tissue and fluid to infiltrate into some pores which may only be connected by small twisting voids in 3 dimensions.

The number of blood vessels after the 8 week implantation within MEDPOR® scaffolds was 12 ± 2.6, within StarPore® (m) to be 5 ± 1.3 and within StarPore® (s) was 15 ± 3.1. Through comparison of the average proportion of blood and collagen content between the scaffold groups, it was identified that there was a significantly high concentration of blood present in the StarPore® (M) samples ($n = 3$, $p < 0.002$). The cause of this significant increase in blood infiltration within the moulded samples is not well-understood. Similar findings are seldom reported in the literature other than in reference to scaffolds whereby ectopic bone formation was induced via the use of bioactive components or cells, which may then include the formation of a hematopoietic niche or immature bone marrow as a precursor to bone development [332]. However, no component of the implanted scaffold aimed to induce bone formation or haematopoiesis.

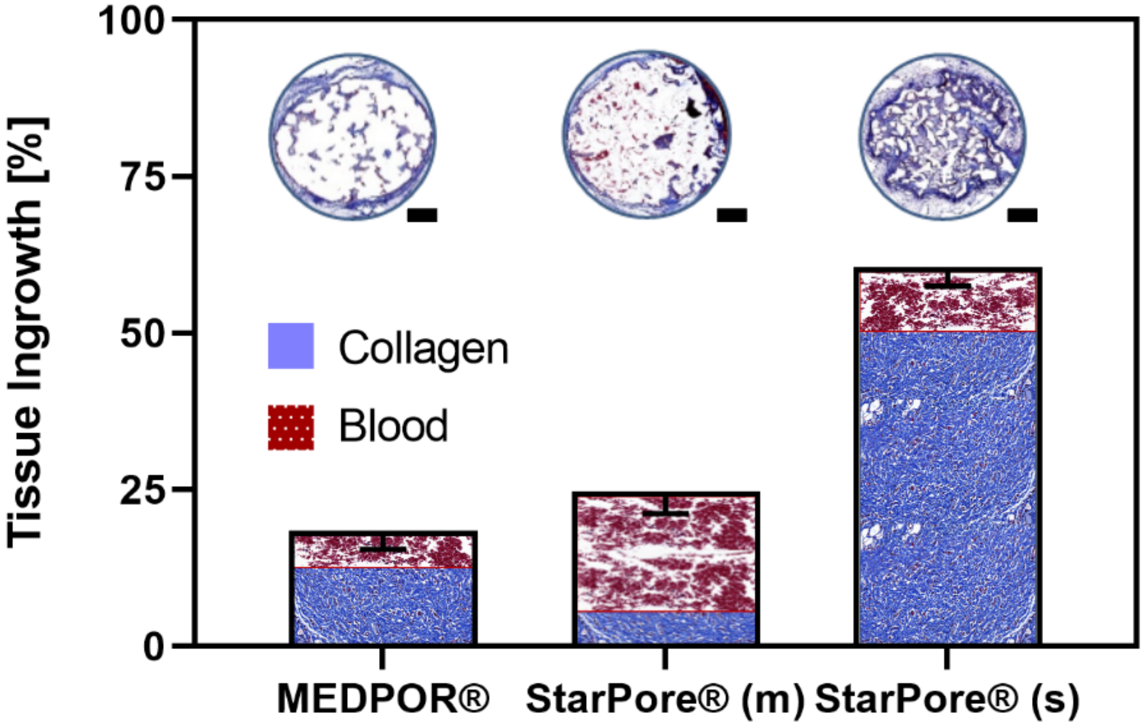

Figure 4.12 Comparison of collagen and blood tissue distribution in MT-stained sections of MEDPOR®, StarPore® (m) and StarPore® (s) after 8 weeks *in vivo*, accompanied by a cross section of each scaffold, scale bar = 1 mm.

4.3.1.3 Foreign Body Response

A distinct inflammatory response was observed at the interface between native tissue and implants. To determine the extent of the macrophage marker Cluster of Differentiation 68 or CD68 was used [333]. In such circumstances, mast cells and macrophages are recruited to the surface of the implant to 'clean' the wound site of bacterial, dead cells and microscopic particles. However, since they are unable to digest the macroscopic polymer structures, foreign body giant cells are formed to increase their functionality [334]. The cells involved in this inflammatory reaction modulate the local tissue response and regulate the function of fibroblasts, signalling an oversupply of collagen matrix deposition around the implant and creation of a fibrous capsule [335,336]. This has been previously characterised in similar animal models by the identification of dense collagen deposition encapsulating the implant using H&E and/or MT staining of histological sections [334]. The thickness of these dense collagen capsules has also been used to characterise the severity of the response [336]. In this study, a universal macrophage marker, CD68 was employed during IHC staining to identify macrophages within tissue at the 1 week time point to assess and compare inflammation responses between experimental groups. CD68 is expressed in monocyte lineages, most notably macrophages, and is routinely employed as an IHC marker in rat tissues to study inflammation.

To identify variabilities between implants in the initial inflammatory response of implants IHC was used. The presence of a fibrotic capsule after 1 week was determined through the use of CD68 and MT-stained sections on MEDPOR®, StarPore® (m) and StarPore® (s) (Fig. 4.13). A thicker fibrotic capsule was thought to be associated with a strong inflammatory response to the implants [337]. The presence of blood at the implant interface of the moulded StarPore® (m) samples was indicative of a heightened foreign body response (Fig. 4.13 b). The expression of CD68 in MEDPOR® and StarPore® (s) was determined to be less saturated when compared to StarPore® (m). The thickness of the capsules stained with CD68 were quantified at week 1, with StarPore® (m) leading to an approximate 3-fold thickness increase over StarPore® (s) and an approximate 2-fold increase in thickness when compared to MEDPOR® (Fig. 4.13 c). This suggests the body recruited a higher concentration of macrophages to the implant area in response to StarPore® (m). A dense network of collagen fibres was observed at the tissue-implant interface, as indicated by MT staining. Both the MEDPOR® and StarPore® (m) implants, at week 4, led to the production of a defined fibrous capsule surrounding the implants. The capsule was proportional to that of the CD68 staining observed at week 1, indicative of heightened inflammation in response to MEDPOR® and StarPore® (m) implants. On the other hand StarPore® (s) implants, a significantly thinner fibrotic capsule was evident at the tissue-implant interface. After a single week, CD68 staining demonstrated a reduced concentration of macrophages when compared to the MEDPOR® and StarPore® (m) implants. Additionally, connective tissue was able to develop throughout 80 % of the void space within the StarPore® (s) implants (Fig. 4.8 c).

While CD68 is useful a macrophage marker, alone it lacks the ability to identify M1 or M2-polarised macrophages, which can be used to determine pro-inflammatory and pro-healing functionality, respectively [338,339]. Though, given the distinct tissue morphology differences between StarPore® (m) (Fig. 4.9) and StarPore® (s) (Fig. 4.10) after 8-weeks, the CD68-positive staining was indicative of a reduced inflammatory response in the highly porous printed scaffolds, when compared to the moulded ones [340].

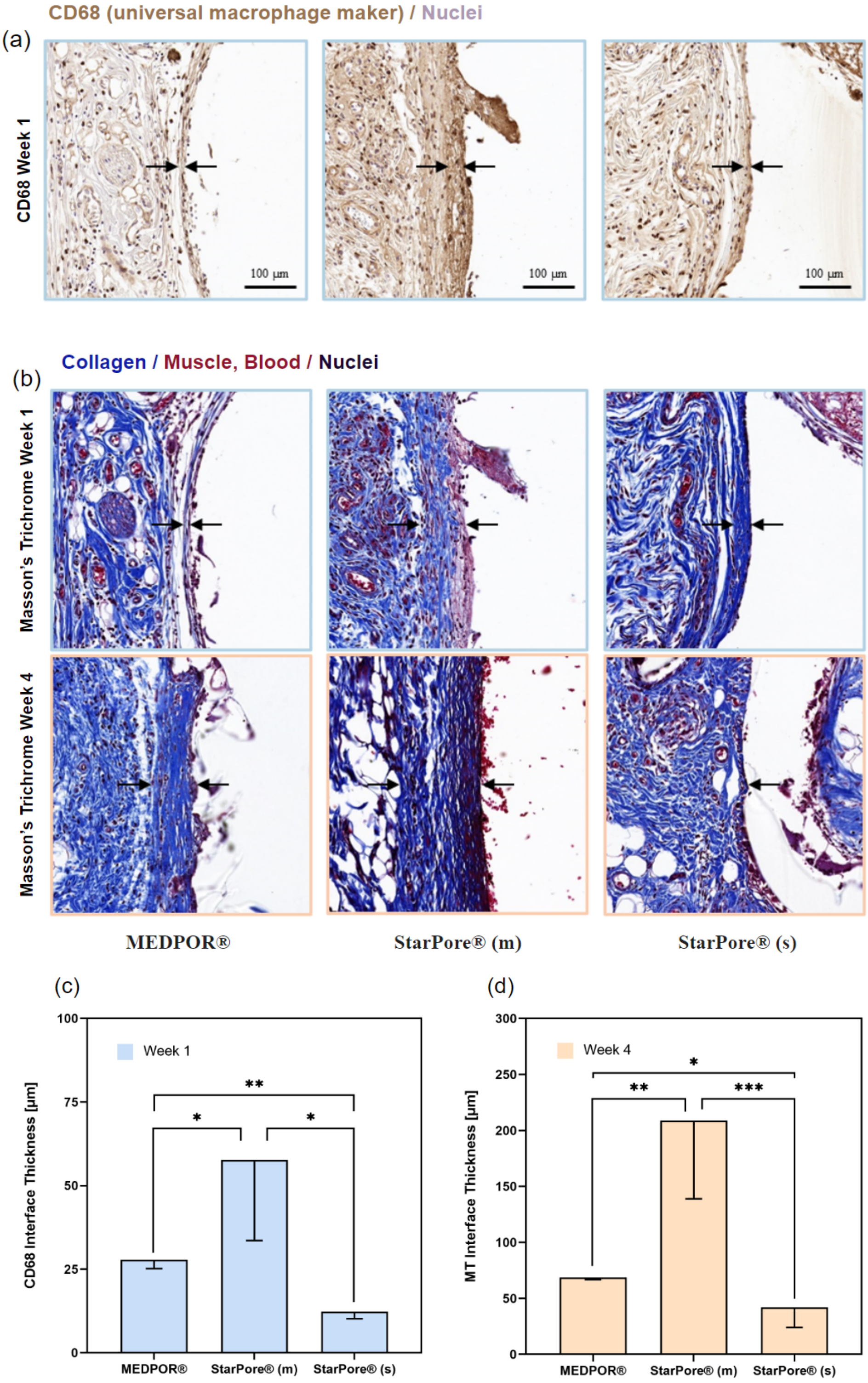

Figure 4.13 (a) Microscopy images of CD68-stained histology sections of scaffolds after 1 week of implantation. (b) Microscopy images of MT-stained histology sections of scaffolds after 1 week and 4 weeks of implantation. (c) The quantified thickness of the CD68 expression at the scaffold-tissue interface, avg ± S.D. (where n = 5). (d) The quantified thickness of the CD68 expression at the scaffold-tissue interface 1 week post implantation, avg ± S.D. (where n = 5) The quantified collagen capsule identified at the scaffold-tissue interface 4 weeks post implantation, avg ± S.D. (where n = 5). Where the arrows indicate the thickness of strong CD68 expression and collagen deposition.

4.4 Conclusions

The chapters preceding this outline how a novel SLS printing approach can be used to generate porous HDPE implants based on StarPore®. This chapter compares well established HDPE-based implant materials, MEDPOR® and StarPore®, which are fabricated by traditional manufacturing approaches against printed scaffolds.

Firstly, to investigate the influence of integrating Bioglass® into StarPore®, an SBF assay was conducted. While it was observed that early stages of apatite began to form on the surface, the inherent hydrophobicity of the polymer and polymers and general, resulted in no discernible differences between composites and pure HDPE scaffolds. Additionally, the complete encapsulation of Bioglass® particles within the polymer matrix, limiting any interactions of Bioglass® with the SBF solution. Future work should explore the use of bioactive glass particles at a higher concentration throughout the polymer matrix, while also employing surface polishing methods or plasma treatment to ensure Bioglass® particles are presented on the surface.

Returning to the original printing method established in Chapter 2 with pure HDPE, printed and commercially available scaffolds were implanted in a subcutaneous rat model over 8 weeks. Samples were extracted at timepoints of week 1, 4 and 8, which underwent IHC staining to outline tissue ingrowth, vascularisation and quantify any initial inflammatory response. While this *in vivo* model does not accurately reflect bone tissue ingrowth nor a site-specific tissue response, fibrotic tissue infiltration was greatly improved in the highly porous printed StarPore® scaffolds when compared to the commercial gold standard of MEDPOR® and the moulded StarPore® samples. This was thought to be associated with the high porosity, interconnectivity and rough surface morphology of printed scaffolds. The inflammatory response on the moulded StarPore® samples revealed the presence of a fibrotic capsule surrounding the implants, not as prominent around the MEDPOR® scaffolds. This response to the moulded StarPore® reduced any tissue infiltration and led to red blood cells populating the empty voids within the scaffold.

While there is no clear consensus on the ideal porosity, pore geometry, interconnectivity or surface morphology in the current scientific landscape, this work serves as a basis for the use of additive manufacturing in the fabrication of patient specific bone substitutes. Future studies should employ critical-sized bone defects *in vivo* models over a 3 - 6 month period to more accurately depict real-world implant performance.

As our knowledge develops so does our understanding of printer-material and material-immune system interactions. Not only does additive manufacturing offer the ability to utilise different materials and bioactive composites, it can pave the way for fabricating scaffolds with variations in porosity, pore size, pore geometry and surface morphology to more accurately recapitulate the tissue at the defect site. Coupled with the potential to generate patient-specific implants, additive manufacturing may hold the key to overcoming the current shortcomings of traditional implants, such as slow tissue integration and vascularisation, to ultimately generate the implants of the future.

CHAPTER 5

THE FUTURE

Chapter 5: The Future

Overview

The objective of this dissertation was to explore the use of powder bed fusion technology on a novel trilobal HDPE (StarPore®) for use as bone substitutes.

5.1 Summary

Chapter 1 outlined several SLS approaches previously utilised in bone tissue engineering applications, with a focus on the regenerative capacity of human bone through the use of polymers and composites capable of tackling bone tissue engineering obstacles. The chapter identified established print parameters specific to each material, accompanied by the physical characterisation and biological response of scaffolds, both *in vitro* and *in vivo*. From the literature analysis, SLS was deemed to be the most appropriate printing method for processing of high-density polyethylene, due to its thermochemical properties and difficult rheological attributes.

Chapter 2 investigated the development, design and testing of a dynamic and modular powder deposition system for use in laser engravers. The impact of key processing parameters such a laser beam path and energy density on the chemical and physical properties of the polymer were quantified through *in situ* imaging techniques as well as chemical analysis through DSC, TGA and FTIR. Within the ideal processing window, no significant impact on the polymer characteristics was observed. Increasing the energy density above 0.55 J/mm^2 resulted in the polymer powder melting, leading to unfavourable particle deformation and unpredictable print process outcomes. The higher energy densities also jeopardised implant porosity, a fundamental attribute for biological performance in vivo. While these drawbacks of increased energy density leading to higher part density may tarnish some biological performance, processing via these parameters could pave the way for a broader applicability of these implants, towards protective areas such as the skull and even towards more load bearing applications.

Chapter 3 explored the influence of print parameters on the physical and mechanical properties. Specifically, the compression and tensile strength, compared to moulded constructs. Laser sintered constructs were found to be one tenth the strength of those produced by moulding, this is due to having a porous print bed, the macromolecular structure of the material and unpredictable thermal behaviour. Additionally, printed constructs were found to have a porosity spanning 80 - 95 % compared to the 55 - 65 % observed in moulded constructs, having a significant impact on mechanical strength. The broader range of porosity in the printed constructs could be tuned to match the bone at the implant site. The density of bone changes depending upon several attributes, including age, hormone and mineral levels as well as with the amount and type of exercise an individual undergoes. Thus being able to tune the density and porosity of constructs as a gradient, with a rigid outer layer and more spongy-like internals, may hold the key to more accurately recapitulating the native form and function of human bone.

Chapter 4 aimed to compare the same printed constructs against moulded ones, specifically StarPore® and MEDPOR®, commercially available HDPE implants. A bioactivity assay was used to determine whether the integration of Bioglass® into the scaffolds during printing would improve the appetite forming capacity. Unfortunately due to the complete encapsulation of the Bioglass® particles, no differences were observed. Printed constructs were determined to have 82 % porosity, compared to that of 68 % and 36 %, of StarPore® and MEDPOR® respectively. Following an 8-week *in vivo* rat implantation, the highly porous printed scaffolds were found to improve fibrotic tissue ingrowth over the commercially available moulded scaffolds. Likewise, initial stages of neovascularisation were present within the printed scaffolds, while the moulded StarPore® led to a heightened immune response. Interestingly, although HDPE is bioinert, it was still found to trigger an immune response. This could be associated with either the sterilisation protocols, surface morphology, porosity or all of the above. Future work should include a critical size bone defect with a greater number of replicates as well as extended implantation, in the realm of 6 months to establish vascular and bone tissue infiltration into the scaffolds. Following this, more comprehensive stainings, micro CT analysis and mechanical tests could be conducted with the native tissue within the pores of the scaffolds to understand how host bone may stabilise the implant.

5.2 Conclusions

SLS-based approaches hold promise for a variety of tissue engineering applications. Bone tissue engineering in particular can benefit from the high strength parts produced by many powder bed fusion techniques. While HDPE is approved by regulatory bodies for human implantation, its use in powder bed fusion is sparse as the thermal and optical properties of the polymer don’t lend itself to laser sintering. Additionally, the obscure trilobal shape, large particle size and narrow sintering window meant that the polymer could easily distort when parameters were not finely controlled. The warping and deformation limited the print density, especially during dry sintering. The novel slurry-based approach alleviated any unpredictable thermal gradients while improving spreadability and surface morphology. Likewise, adding multiple raster scans within each layer helped overcome significant polymer shrinkage during sintering.

Morphology and porosity were found to be tunable through adjustments in layer height as well as variations in scan strategy. When compared to moulded constructs, which will always have a fixed porosity and surface finish, the printed scaffolds had approximately twice the roughness. The porosity was found to range between 76 - 92 %, compared to the 55 % and 26 % of the two distinct moulded scaffolds. The increased porosity, while known to be beneficial for nutrient and waste diffusion *in vivo*, was detrimental to scaffold stiffness and tensile strength. Moulded scaffolds based on StarPore® were found to be over 4-fold stronger than those printed, at every energy density and scan strategy tested, as the polymer couldn't be restricted in the Z-axis and tended to shrink and expand towards the laser during printing.

On the biological side however, the dynamic surface finish and high porosity was found to be beneficial for tissue infiltration and vascularisation. Compared to the current gold standard of HDPE implants, MEDPOR® and StarPore®, the sintered version of StarPore® stimulated a 3 to 4-fold improvement in tissue ingrowth over the 8 week implantation. Additionally, no significant immune response was observed from the host. Initial stages of neo-vascularisation were also prevalent in the printed constructs when compared to the traditionally moulded scaffolds.

3D printing technology is not perfect and requires existing knowledge in engineering and materials science to work efficiently. Together with a multidisciplinary team, new innovative techniques and materials may hold the key to future tissue engineering applications as have been outlined in this body of work.

5.3 Future Work

The novel slurry-based approach was found to overcome many of the shortcomings associated with unfavourable thermal properties of the polymer. Although not an entirely new concept, powder dispersion in a "liquid vehicle" is a known method for improving the packing density in a powder bed [341–343]. While conceptually similar to SLS, layerwise slurry deposition or LSD generates green ceramic parts using ceramic slurry as feedstock as opposed to a dry powder bed [343–345]. Additionally, the capillary forces and surface tension between particles and water within the print volume, enabled an improvement in the resulting print density. That said, the unsintered particles need to be dissolved out with water or other aqueous solvents unlike typical SLS or SLM methods. LSD generated parts are shown to be comparable to cast or moulded parts, with mechanical properties within the range of 70 - 80 MPa for similar parts [346]. The use of a slurry-based approach in SLS boasts extraordinary potential for the use of a diverse range of polymers or even composites, particularly those with narrow sintering windows or irregular shaped particles.

Polymers such as HDPE tend to be bioinert, lacking inherent bioactivity. Here, we outlined a method of printing two materials through a slurry-based approach that resulted in encapsulated bioactive glass particles dispersed throughout the polymer matrix. The same methodology could be applied to a biodegradable polymer such as PCL, with added bioactive elements such as bioglass®, tricalcium phosphate or even hydroxyapatite to stimulate rapid bone ingrowth and vascularisation. Manipulating the concentrations of bioactive compounds throughout the polymer matrix with gradients could be used to control the release of ions into the surrounding tissue, gradually recruiting cell types at established intervals. Additionally, the same methodology could be used to promote scaffold degradation, along with adjustments in structure thickness and porosity of constructs, to tailor the degradation profile of materials to coincide with the rate of tissue infiltration, such as bone ingrowth.

The *in situ* monitoring of printing, particularly in this body of work, provided great insights into the influence of energy density on scaffold printing. Other techniques such as X-ray imaging have also been utilised for *in situ* monitoring of additive manufacturing [347,348]. For the development of new and novel printing techniques, whether it be extrusion or light-based approaches, requires quantitative characterisation of materials, before, during and after printing. Recent innovations in machine learning and artificial intelligence may hold the key for rapid progress in this area [349–353]. Their use will be vital for hardware, software and material optimisations and the development of revolutionary 3D printing techniques that can be translated for use in the clinical environment at the point-of-care.

Bone is a dynamic tissue that, as outlined in the introduction, has a plethora of physical attributes and mechanical properties that vary depending on age, hormone levels, among others. The regenerative capacity of bone requires continual mechanical load to maintain function. This load can be in the form of compression, tension and torsion, under a variety of forces and frequencies. Once a bone substitute has been implanted, homoeostasis is disrupted. One example is pure titanium implants, which can lead to the phenomenon of stress shielding, where the stiff implant absorbs more of the load than the surrounding bone, resulting in bone degeneration at the bone-implant interface. On the other hand, polymeric implants like those based on StarPore®, can often be weaker than the surrounding bone, which may limit their use in load-bearing bone applications. Combining the stiffness of metals with the elastic properties of polymers may hold the key to more accurately recapitulating the mechanical properties of native human bone. For ongoing function, bone requires load, torsion, compression, etc, thus mechanical support from rigid materials, plus enhanced bioactivity from polymers and/or ceramics may provide the ideal environment for stimulating regeneration while being supported by robust materials. For instance, the SLS process has previously been used to generate green parts with carbon fibre coated polyamide, that have high compressive and flexural strength compared to typical parts produced by printing. Carbon fibre reinforcement can also be used to improve the anisotropic behaviour of SLS printed polyamide [340], alleviating many of the current shortcomings associated with single material SLS printing. Future work could apply similar reinforcement strategies to different polymers to improve the mechanical properties in certain geometrical planes for load-bearing bone tissue engineering applications.

Mechanical reinforcement can also be achieved through varying design strategies of prints. Computational modelling via finite element analysis enables the development of unit cell structures [354]. Unit cells can be used to specifically tune the topographical properties of lattices. Cuboid unit cells have been shown to have high elastic and low shear moduli, while octet unit cells have been shown to have high shear moduli and surface-volume ratios but low permeability [355]. Additionally, 3D printed unit cell structures have also been shown to improve anisotropic characteristics through the use of metamaterials [356]. Varying the design of unit cells hold significant potential for improving the mechanical properties of constructs with tunable biological properties capable of guiding tissue ingrowth [357].

The current implementation for implant design, from patient consultation, scanning, design and implantation, involves the back and forth communication from engineers and clinicians. The inefficiencies in this process prevent rapid repair and patient outcomes. For instance, the CAD software suites used are typically intended for industry and have technical user interfaces not approachable for clinicians without extensive experience. On the biomedical or bio-mechanical design side, engineers typically lack knowledge in designing physiologically relevant constructs. Future work could alleviate the need for technical CAD experience, with ease of use software for a clinical approach, as many of the features present in modern CAD software packages are irrelevant for clinical use cases. Additionally, such software could also integrate surgical planning functionality as well as anatomical models and surgical guides for incisions and screw mounting. 3D models can also be used to train surgeons during their education, with accurate material stiffnesses achievable through printing methods such as SLS and PolyJet™ [358].

The main obstacles associated with translating 3D printed patient-specific implants are:

- Financial investment
- Engagement from multidisciplinary professionals
- Robust logistical networks
- Compliance with regulatory standards, including software, hardware, transport and sterilisation

In practice, understanding a patient's needs is the first step to the clinical translation of 3D printed bone implants. Image acquisition, segmentation, surface rendering, and file conversion provide engineers and surgeons with all the relevant information to predict surgical outcomes. Several iterations of each implant can be conceptualised through modelling software and rapid prototyping of the implant itself, putting the device directly in the hands of patients and clinicians within a short time-frame to ultimately iron out any issues.

Within the medical device industry, the translation of 3D printed implants from research to application must undergo comprehensive regulatory assessment. The process of printing, from scanning to modelling to print execution, as well as the materials and printing technology, all need to be understood prior to implantation, as outlined in Section 1.3.1.3. Custom-made medical devices are currently given regulatory exemptions as they're bespoke and require consultation on a patient-to-patient basis. A framework for regulatory approval of bespoke printed bone implants could be as follows:

- Define the applicable regulations and standards
- Set up a solid quality management system
- Keep track of each step of manufacturing with documentation
- Maintenance and monitoring (24 months)
- Have regulatory intelligence integrated into your system

Recent advances in pharmaceutical fabrication have led to the use of SLS printing as drug development platforms. Tailoring morphological characteristics has the capacity to generate extended release profiles in drugs such as paracetamol [359] and irbesartan [360], as well as antibiotics [361]. The release profiles can also be tuned to have an initial rapid release followed by extended release, as seen in the cartilage cancer treatment composite drug made from PCL and fluorouracil [362]. The same concept could be applied to the next generation of drug impregnated implants. Anti-inflammatory drugs embedded within a scaffold with controllable release hold significant potential in improving the crucial phase of implantation, with a rapid initial release followed by a controlled extended release [363,364], with potential to release antibiotics into a localised area, potentially preventing side effects associated with disruption in the gut microbiome [365].

All of these avenues have limitless potential. The only way forward is through a multidisciplinary approach to fundamental research questions. As researchers we often lose sight of the bigger picture, the picture of delivering hope and real clinical outcomes to patients. This is the key, this is the reason we do what we do. What’s required? The marriage of communal knowledge from scientists, engineers, regulators, industry, government, clinicians, the community and patients, from every corner of the earth. Together, we will be able to convene, develop, fabricate and deliver the implants of tomorrow to those in need in a timely manner with reduced costs and high accessibility.

6.0 References

1. Tatangelo G, Watts J, Lim K, Connaughton C, Abimanyi-Ochom J, Borgström F, et al. The Cost of Osteoporosis, Osteopenia, and Associated Fractures in Australia in 2017. J Bone Miner Res. 2019;34: 616–625.

2. Eppley BL, Pietrzak WS, Blanton MW. Allograft and alloplastic bone substitutes: a review of science and technology for the craniomaxillofacial surgeon. J Craniofac Surg. 2005;16: 981–989.

3. Hutmacher DW. Scaffolds in tissue engineering bone and cartilage. The Biomaterials: Silver Jubilee Compendium. Elsevier Ltd; 2000. pp. 175–189.

4. Liu X, Ma PX. Polymeric scaffolds for bone tissue engineering. Ann Biomed Eng. 2004;32: 477–486.

5. Kashirina A, Yao Y, Liu Y, Leng J. Biopolymers as bone substitutes: a review. Biomater Sci. 2019;7: 3961–3983.

6. Sharma S, Sudhakara P, Singh J, Ilyas RA, Asyraf MRM, Razman MR. Critical Review of Biodegradable and Bioactive Polymer Composites for Bone Tissue Engineering and Drug Delivery Applications. Polymers . 2021;13. doi:10.3390/polym13162623

7. Amini AR, Laurencin CT, Nukavarapu SP. Bone tissue engineering: recent advances and challenges. Crit Rev Biomed Eng. 2012;40: 363–408.

8. Kantaros A, Chatzidai N, Karalekas D. 3D printing-assisted design of scaffold structures. Int J Adv Manuf Technol. 2016;82: 559–571.

9. Thayaparan GK, Lewis PM, Thompson RG, D'Urso PS. Patient-specific implants for craniomaxillofacial surgery: A manufacturer's experience. Ann Med Surg (Lond). 2021;66: 102420.

10. Elsevier. Principles of Bone Biology - 3rd Edition. [cited 9 Oct 2019]. Available: https://www.elsevier.com/books/principles-of-bone-biology/bilezikian/978-0-12-373884-4

11. Bigham-Sadegh A, Oryan A. Basic concepts regarding fracture healing and the current options and future directions in managing bone fractures. International Wound Journal. Blackwell Publishing Ltd; 2015. pp. 238–247. doi:10.1111/iwj.12231

12. Caplan AI. Tissue engineering designs for the future: new logics, old molecules. Tissue Eng. 2000;6: 1–8.

13. Reddi AH. Morphogenetic messages are in the extracellular matrix: Biotechnology from bench to bedside. Biochemical Society Transactions. Portland Press Ltd; 2000. pp. 345–349.

14. WHO Scientific Group on the Burden of Musculoskeletal Conditions at the Start of the New Millennium. The burden of musculoskeletal conditions at the start of the new millennium. World Health Organ Tech Rep Ser. 2003;919: i–x, 1–218, back cover.

15. Yunus Basha R, Sampath SK, Doble M. Design of biocomposite materials for bone tissue regeneration. Materials Science and Engineering C. Elsevier Ltd; 2015. pp. 452–463.

doi:10.1016/j.msec.2015.07.016

16. Khetani SR, Bhatia SN. Microscale culture of human liver cells for drug development. Nat Biotechnol. 2008;26: 120–126.

17. Kumar G, Narayan B. Morbidity at bone graft donor sites. Classic Papers in Orthopaedics. Springer-Verlag London Ltd; 2014. pp. 503–505.

18. Behnam Manesh S, Omani Samani R, Behnam Manesh S. Ethical issues of transplanting organs from transgenic animals into human beings. Cell J. 2014;16: 353–360.

19. Griesemer A, Yamada K, Sykes M. Xenotransplantation: Immunological hurdles and progress toward tolerance. Immunological Reviews. 2014. pp. 241–258. doi:10.1111/imr.12152

20. Khorasani M, Janbaz P, Rayati F. Maxillofacial reconstruction with Medpor porous polyethylene implant: a case series study. J Korean Assoc Oral Maxillofac Surg. 2018;44: 128–135.

21. Paxton NC, Allenby MC, Lewis PM, Woodruff MA. Biomedical applications of polyethylene. Eur Polym J. 2019;118: 412–428.

22. Bose S, Vahabzadeh S, Bandyopadhyay A. Bone tissue engineering using 3D printing. Materials Today. 2013. pp. 496–504. doi:10.1016/j.mattod.2013.11.017

23. Lai Y-S, Chen W-C, Huang C-H, Cheng C-K, Chan K-K, Chang T-K. The effect of graft strength on knee laxity and graft in-situ forces after posterior cruciate ligament reconstruction. PLoS One. 2015;10: e0127293.

24. Palágyi K, Németh G, Kardos P. Topology Preserving Parallel 3D Thinning Algorithms. In: Brimkov VE, Barneva RP, editors. Digital Geometry Algorithms: Theoretical Foundations and Applications to Computational Imaging. Dordrecht: Springer Netherlands; 2012. pp. 165–188.

25. Wang X, Nyman JS, Dong X, Leng H, Reyes M. Fundamental Biomechanics in Bone Tissue Engineering. Synthesis Lectures on Tissue Engineering. 2010;2: 1–225.

26. Reznikov N, Bilton M, Lari L, Stevens MM, Kröger R. Fractal-like hierarchical organization of bone begins at the nanoscale. Science. 2018;360. doi:10.1126/science.aao2189

27. Galante J, Rostoker W, Ray RD. Physical properties of trabecular bone. Calcif Tissue Res. 1970;5: 236–246.

28. Roesler H. The history of some fundamental concepts in bone biomechanics. J Biomech. 1987;20: 1025–1034.

29. Chen J-H, Liu C, You L, Simmons CA. Boning up on Wolff's Law: mechanical regulation of the cells that make and maintain bone. J Biomech. 2010;43: 108–118.

30. Eriksen EF. Cellular mechanisms of bone remodeling. Rev Endocr Metab Disord. 2010;11: 219–227.

31. Karageorgiou V, Kaplan D. Porosity of 3D biomaterial scaffolds and osteogenesis. Biomaterials. 2005;26: 5474–5491.

32. Park SA, Lee SJ, Seok JM, Lee JH, Kim WD, Kwon IK. Fabrication of 3D Printed PCL/PEG Polyblend Scaffold Using Rapid Prototyping System for Bone Tissue Engineering Application. J

Bionic Eng. 2018;15: 435–442.

33. Le Huec JC, Schaeverbeke T, Clement D, Faber J, Le Rebeller A. Influence of porosity on the mechanical resistance of hydroxyapatite ceramics under compressive stress. Biomaterials. 1995;16: 113–118.

34. Blokhuis TJ, Termaat MF, den Boer FC, Patka P, Bakker FC, Haarman HJ. Properties of calcium phosphate ceramics in relation to their in vivo behavior. J Trauma. 2000;48: 179–186.

35. Murphy CM, Haugh MG, O'Brien FJ. The effect of mean pore size on cell attachment, proliferation and migration in collagen-glycosaminoglycan scaffolds for bone tissue engineering. Biomaterials. 2010;31: 461–466.

36. Rustom LE, Boudou T, Lou S, Pignot-Paintrand I, Nemke BW, Lu Y, et al. Micropore-induced capillarity enhances bone distribution in vivo in biphasic calcium phosphate scaffolds. Acta Biomater. 2016;44: 144–154.

37. Bohner M, Baroud G, Bernstein A, Döbelin N, Galea L, Hesse B, et al. Characterization and distribution of mechanically competent mineralized tissue in micropores of β-tricalcium phosphate bone substitutes. Mater Today. 2017;20: 106–115.

38. Bidan CM, Kommareddy KP, Rumpler M, Kollmannsberger P, Bréchet YJM, Fratzl P, et al. How linear tension converts to curvature: geometric control of bone tissue growth. PLoS One. 2012;7: e36336.

39. Bidan CM, Kollmannsberger P, Gering V, Ehrig S, Joly P, Petersen A, et al. Gradual conversion of cellular stress patterns into pre-stressed matrix architecture during in vitro tissue growth. J R Soc Interface. 2016;13. doi:10.1098/rsif.2016.0136

40. Ripamonti U, Roden LC, Renton LF. Osteoinductive hydroxyapatite-coated titanium implants. Biomaterials. 2012;33: 3813–3823.

41. Diao J, OuYang J, Deng T, Liu X, Feng Y, Zhao N, et al. 3D-plotted beta-tricalcium phosphate scaffolds with smaller pore sizes improve in vivo bone regeneration and biomechanical properties in a critical-sized calvarial defect rat model. Adv Healthc Mater. 2018;7: 1800441.

42. Torres FG, Nazhat SN, Sheikh Md Fadzullah SH, Maquet V, Boccaccini AR. Mechanical properties and bioactivity of porous PLGA/TiO2 nanoparticle-filled composites for tissue engineering scaffolds. Compos Sci Technol. 2007;67: 1139–1147.

43. Goshulak P, Samiezadeh S, Aziz MSR, Bougherara H, Zdero R, Schemitsch EH. The biomechanical effect of anteversion and modular neck offset on stress shielding for short-stem versus conventional long-stem hip implants. Med Eng Phys. 2016;38: 232–240.

44. Chanlalit C, Shukla DR, Fitzsimmons JS, An K-N, O'Driscoll SW. Stress shielding around radial head prostheses. J Hand Surg Am. 2012;37: 2118–2125.

45. Sumner DR. Long-term implant fixation and stress-shielding in total hip replacement. J Biomech. 2015;48: 797–800.

46. Bragdon CR, Burke D, Lowenstein JD, O'Connor DO, Ramamurti B, Jasty M, et al. Differences in stiffness of the interface between a cementless porous implant and cancellous bone in vivo in dogs due to varying amounts of implant motion. J Arthroplasty. 1996;11: 945–951.

47. Maniatopoulos C, Pilliar RM, Smith DC. Threaded versus porous‑surfaced designs for implant

stabilization in bone‑endodontic implant model. J Biomed Mater Res. 1986;20: 1309–1333.

48. Cheng L, Suresh K S, He H, Rajput RS, Feng Q, Ramesh S, et al. 3D Printing of Micro- and Nanoscale Bone Substitutes: A Review on Technical and Translational Perspectives. Int J Nanomedicine. 2021;16: 4289–4319.

49. Boyan BD, Lossdörfer S, Wang L, Zhao G, Lohmann CH, Cochran DL, et al. Osteoblasts generate an osteogenic microenvironment when grown on surfaces with rough microtopographies. Eur Cell Mater. 2003;6: 22–27.

50. Masuda T, Yliheikkilä PK, Felton DA, Cooper LF. Generalizations regarding the process and phenomenon of osseointegration. Part I. In vivo studies. Int J Oral Maxillofac Implants. 13: 17–29.

51. Chen H, Wang C, Zhu X, Zhang K, Fan Y, Zhang X. Fabrication of porous titanium scaffolds by stack sintering of microporous titanium spheres produced with centrifugal granulation technology. Mater Sci Eng C Mater Biol Appl. 2014;43: 182–188.

52. Anselme K, Bigerelle M. Topography effects of pure titanium substrates on human osteoblast long-term adhesion. Acta Biomater. 2005;1: 211–222.

53. Torstrick FB, Lin ASP, Potter D, Safranski DL, Sulchek TA, Gall K, et al. Porous PEEK improves the bone-implant interface compared to plasma-sprayed titanium coating on PEEK. Biomaterials. 2018;185: 106–116.

54. Cerardi A, Caneri M, Meneghello R, Concheri G, Ricotta M. Mechanical characterization of polyamide cellular structures fabricated using selective laser sintering technologies. Mater Des. 2013;46: 910–915.

55. Mukherjee K, Gupta S. Bone ingrowth around porous-coated acetabular implant: a three-dimensional finite element study using mechanoregulatory algorithm. Biomech Model Mechanobiol. 2016;15: 389–403.

56. ISO 10993-1:2018. In: ISO [Internet]. 2021 [cited 18 Feb 2022]. Available: https://www.iso.org/standard/68936.html

57. Daigle B, Torsekar M. The EU Medical Device Regulation and the US Medical Device Industry. J Int'l Com & Econ. 2019; 1.

58. Darrow JJ, Avorn J, Kesselheim AS. FDA Regulation and Approval of Medical Devices: 1976-2020. JAMA. 2021;326: 420–432.

59. Food US. Biological Responses to Metal Implants. doi:10.1016/j.jmig.2011.04.009

60. Delloye C, Cornu O, Druez V, Barbier O. Bone allografts. What they can offer and what they cannot. Journal of Bone and Joint Surgery - Series B. 2007. pp. 574–579. doi:10.1302/0301-620X.89B5.19039

61. Asa'ad F, Pagni G, Pilipchuk SP, Giannì AB, Giannobile WV, Rasperini G. 3D-Printed Scaffolds and Biomaterials: Review of Alveolar Bone Augmentation and Periodontal Regeneration Applications. Int J Dent. 2016;2016: 1239842.

62. Rotatori D, Lee EJ, Sleeva S. The evolution of the workforce during the fourth industrial revolution. Human Resource Development International. 2021;24: 92–103.

63. Kumar L, Haleem A, Tanveer Q, Javaid M, Shuaib M, Kumar V. Rapid manufacturing: Classification and recent development. Int j adv eng res sci. 2017;4: 29–40.

64. Akilbekova D, Mektepbayeva D. Patient specific in situ 3D printing. 3D Printing in Medicine. 2017; 91–113.

65. Rengier F, Mehndiratta A, von Tengg-Kobligk H, Zechmann CM, Unterhinninghofen R, Kauczor H-U, et al. 3D printing based on imaging data: review of medical applications. Int J Comput Assist Radiol Surg. 2010;5: 335–341.

66. Liu Z, Wang Y, Wu B, Cui C, Guo Y, Yan C. A critical review of fused deposition modeling 3D printing technology in manufacturing polylactic acid parts. Int J Adv Manuf Technol. 2019;102: 2877–2889.

67. Lee H, Lim CHJ, Low MJ, Tham N, Murukeshan VM, Kim Y-J. Lasers in additive manufacturing: A review. Int J Precis Eng Manuf-Green Technol. 2017;4: 307–322.

68. Hofland EC, Baran I, Wismeijer DA. Correlation of Process Parameters with Mechanical Properties of Laser Sintered PA12 Parts. Advances in Materials Science and Engineering. 2017;2017. doi:10.1155/2017/4953173

69. Tolochko NK, Khlopkov YV, Mozzharov SE, Ignatiev MB, Laoui T, Titov VI. Absorptance of powder materials suitable for laser sintering. Rapid Prototyping Journal. 2000;39: 88.

70. Kruth J, Mercelis P, Van Vaerenbergh J, Froyen L, Rombouts M. Binding mechanisms in selective laser sintering and selective laser melting. Rapid Prototyping Journal. 2005;39: 88.

71. Józwik J, Ostrowski D, Milczarczyk R, Krolczyk GM. Analysis of relation between the 3D printer laser beam power and the surface morphology properties in Ti-6Al-4V titanium alloy parts. J Brazil Soc Mech Sci Eng. 2018;40: 215.

72. Gu H, Gong H, Pal D, Rafi K, Starr T, Stucker B, et al. Influences of energy density on porosity and microstructure of selective laser melted 17-4PH stainless steel. 2013 Solid Freeform Fabrication Symposium. utw10945.utweb.utexas.edu; 2013. Available: http://utw10945.utweb.utexas.edu/Manuscripts/2013/2013-37-Gu.pdf

73. Ho HCH, Cheung WL, Gibson I. Morphology and Properties of Selective Laser Sintered Bisphenol A Polycarbonate. Ind Eng Chem Res. 2003;42: 1850–1862.

74. Tan KH, Chua CK, Leong KF, Cheah CM, Cheang P, Abu Bakar MS, et al. Scaffold development using selective laser sintering of polyetheretherketone–hydroxyapatite biocomposite blends. Biomaterials. 2003;24: 3115–3123.

75. Schmid M, Amado A, Wegener K. Materials perspective of polymers for additive manufacturing with selective laser sintering. J Mater Res. 2014;29: 1824–1832.

76. Nelson JC, Vail NK, Barlow JW, Beaman JJ, Bourell DL, Marcus HL. Selective laser sintering of polymer-coated silicon carbide powders. Ind Eng Chem Res. 1995;34: 1641–1651.

77. Kruth J-P, Vandenbroucke B, Van Vaerenbergh J, Naert I. Digital manufacturing of biocompatible metal frameworks for complex dental prostheses by means of SLS/SLM. Proc of 2nd Int Conf on Advanced Research in Virtual and Rapid Prototyping, Leiria. research.utwente.nl; 2005. pp. 139–145.

78. Chalancon A, Bourell D. Measured energy densities for polyamide 12 and comparison of values

calculated for laser sintering. Proceedings of the Solid Freeform Fabrication Symposium, Austin, Texas, USA. utw10945.utweb.utexas.edu; 2016. pp. 2217–2223.

79. Scipioni Bertoli U, Wolfer AJ, Matthews MJ, Delplanque J-PR, Schoenung JM. On the limitations of Volumetric Energy Density as a design parameter for Selective Laser Melting. Mater Des. 2017;113: 331–340.

80. Sampson R, Lancaster R, Sutcliffe M, Carswell D, Hauser C, Barras J. An improved methodology of melt pool monitoring of direct energy deposition processes. Opt Laser Technol. 2020;127: 106194.

81. Thanki A, Goossens L, Mertens R, Probst G. Study of keyhole-porosities in selective laser melting using X-ray computed tomography. Proceedings of iCT. 2019. Available: https://lirias.kuleuven.be/retrieve/530678

82. Yadav P, Rigo O, Arvieu C, Le Guen E, Lacoste E. In Situ Monitoring Systems of The SLM Process: On the Need to Develop Machine Learning Models for Data Processing. Crystals. 2020;10: 524.

83. Alkahari MR, Furumoto T, Ueda T, Hosokawa A, Tanaka R, Abdul Aziz MS. Thermal conductivity of metal powder and consolidated material fabricated via selective Laser Melting. Key Eng Mater. 2012;523-524: 244–249.

84. Mertens R, Vrancken B, Holmstock N, Kinds Y, Kruth J-P, Van Humbeeck J. Influence of Powder Bed Preheating on Microstructure and Mechanical Properties of H13 Tool Steel SLM Parts. Phys Procedia. 2016;83: 882–890.

85. Bai C, Spontak RJ, Koch CC, Saw CK, Balik CM. Structural changes in poly(ethylene terephthalate) induced by mechanical milling. Polymer . 2000;41: 7147–7157.

86. Jonna S, Lyons J. Processing and properties of cryogenically milled post-consumer mixed plastic waste. Polym Test. 2005;24: 428–434.

87. Wu J, Xu X, Zhao Z, Wang M, Zhang J. Study in performance and morphology of polyamide 12 produced by selective laser sintering technology. Rapid Prototyping Journal. 2018;24: 813–820.

88. Duan B, Cheung WL, Wang M. Optimized fabrication of Ca–P/PHBV nanocomposite scaffolds via selective laser sintering for bone tissue engineering. Biofabrication. 2011;3: 015001.

89. Tan XP, Tan YJ, Chow CSL, Tor SB, Yeong WY. Metallic powder-bed based 3D printing of cellular scaffolds for orthopaedic implants: A state-of-the-art review on manufacturing, topological design, mechanical properties and biocompatibility. Materials Science and Engineering: C. 2017;76: 1328–1343.

90. Zhou Z, Liu Y, Liu X, Zhan Q, Wang K. Microstructure evolution and mechanical properties of in-situ Ti6Al4V–TiB composites manufactured by selective laser melting. Composites Part B. 2021;207: 108567.

91. Gu D, Zhang H, Dai D, Xia M, Hong C, Poprawe R. Laser additive manufacturing of nano-TiC reinforced Ni-based nanocomposites with tailored microstructure and performance. Composites Part B. 2019;163: 585–597.

92. Shi Y, Li Z, Sun H, Huang S, Zeng F. Effect of the properties of the polymer materials on the quality of selective laser sintering parts. Proc Inst Mech Eng Part L J Mat Des Appl. 2004;218:

247–252.

93. Schmid M, Amado A, Wegener K. Polymer powders for selective laser sintering (SLS). AIP Conference Proceedings. American Institute of Physics Inc.; 2015. doi:10.1063/1.4918516

94. Wudy K, Drummer D. Aging effects of polyamide 12 in selective laser sintering: Molecular weight distribution and thermal properties. Additive Manufacturing. 2019;25: 1–9.

95. Drummer D, Harder RG, Witt G, Wegner A, … KW-. IJ, 2015 U. Long-term Properties of Laser Sintered Parts of Polyamide 12-Influence of Storage Time and Temperature on the Aging Behavior. International Journal of Recent Contributions from Engineering, Science & IT (iJES). 2015; 20–27.

96. Benedetti L, Brulé B, Decreamer N, Evans KE, Ghita O. Shrinkage behaviour of semi-crystalline polymers in laser sintering: PEKK and PA12. Materials and Design. 2019;181. doi:10.1016/j.matdes.2019.107906

97. Winnacker M. Polyamides and their functionalization: recent concepts for their applications as biomaterials. Biomater Sci. 2017;5: 1230–1235.

98. Xiang C, Etrick NR, Frey MW, Norris EJ, Coats JR. Structure and Properties of Polyamide Fabrics with Insect-Repellent Functionality by Electrospinning and Oxygen Plasma-Treated Surface Coating. Polymers. 2020;12: 2196.

99. Niu X, Qin M, Xu M, Zhao L, Wei Y, Hu Y, et al. Coated electrospun polyamide-6/chitosan scaffold with hydroxyapatite for bone tissue engineering. Biomed Mater. 2021;16: 025014.

100. McKeen LW. 1 - Introduction to Plastics and Polymers. In: McKeen LW, editor. Film Properties of Plastics and Elastomers (Fourth Edition). William Andrew Publishing; 2017. pp. 1–24.

101. Wudy K, Drummer D, Kühnlein F, Drexler M. Influence of degradation behavior of polyamide 12 powders in laser sintering process on produced parts. AIP Conf Proc. 2014;1593: 691–695.

102. Goodridge RD, Tuck CJ, Hague RJM. Laser sintering of polyamides and other polymers. Prog Mater Sci. 2012;57: 229–267.

103. Bai J, Goodridge RD, Hague RJM, Song M. Improving the mechanical properties of laser‐sintered polyamide 12 through incorporation of carbon nanotubes. Polymer Engineering & Science. 2013;53: 1937–1946.

104. Brandt M. Laser Additive Manufacturing: Materials, Design, Technologies, and Applications. Woodhead Publishing; 2016.

105. Griessbach S, Lach R, Grellmann W. Structure–property correlations of laser sintered nylon 12 for dynamic dye testing of plastic parts. Polym Test. 2010;29: 1026–1030.

106. Bourell DL, Watt TJ, Leigh DK, Fulcher B. Performance Limitations in Polymer Laser Sintering. Phys Procedia. 2014;56: 147–156.

107. Meyer K-RD, Hornung K-HD, Feldmann RD, Smigerski H-JD. Verfahren zur herstellung von pulverfoermigen beschichtungsmitteln auf der basis von polyamiden mit mindestens 10 aliphatisch gebundenen kohlenstoffatomen pro carbonamidgruppe. Patent. AT:1820:T, 1982.

Available: https://patents.google.com/patent/AT1820T/en-20US4325121.pdf

108. Senff H, Gaboriau C. Method for preparing polyamide powder by anionic polymerisation. US Patent. 20100113661:A1, 2010. Available: https://patentimages.storage.googleapis.com/ff/1b/bf/1d071c259b1681/US20100113661A1.pdf

109. Vidal B de C. Using the FT-IR linear dichroism method for molecular order determination of tendon collagen bundles and nylon 6. Acta Histochem. 2013;115: 686–691.

110. Vidal B de C, Mello MLS. Collagen type I amide I band infrared spectroscopy. Micron. 2011;42: 283–289.

111. Das S, Hollister SJ, Flanagan C, Adewunmi A, Bark K, Chen C, et al. Freeform fabrication of Nylon‐6 tissue engineering scaffolds. Rapid Prototyping Journal. 2003;9: 43–49.

112. Das S, Hollister SJ, Flanagan C, Adewunmi A, Bark K, Chen C, et al. Computational Design, Freeform Fabrication and Testing of Nylon-6 Tissue Engineering Scaffolds. MRS Online Proceedings Library (OPL). 2002;758. doi:10.1557/PROC-758-LL5.7

113. Chen X, Lian T, Zhang B, Du Y, Du K, Xiang N, et al. Design and Mechanical Compatibility of Nylon Bionic Cancellous Bone Fabricated by Selective Laser Sintering. Materials . 2021;14. doi:10.3390/ma14081965

114. Woodruff MA, Hutmacher DW. The return of a forgotten polymer—Polycaprolactone in the 21st century. Prog Polym Sci. 2010;35: 1217–1256.

115. Nuyken O, Pask SD. Ring-Opening Polymerization—An Introductory Review. Polymers . 2013;5: 361–403.

116. Chuenjitkuntaworn B, Osathanon T, Nowwarote N, Supaphol P, Pavasant P. The efficacy of polycaprolactone/hydroxyapatite scaffold in combination with mesenchymal stem cells for bone tissue engineering. J Biomed Mater Res A. 2016;104: 264–271.

117. Bahl S, Dolma J, Jyot Singh J, Sehgal S. Biodegradation of plastics: A state of the art review. Materials Today: Proceedings. 2021;39: 31–34.

118. BaoLin G, Ma PX. Synthetic biodegradable functional polymers for tissue engineering: a brief review. Sci China Chem. 2014;57: 490–500.

119. Górecka Ż, Idaszek J, Kołbuk D, Choińska E, Chlanda A, Święszkowski W. The effect of diameter of fibre on formation of hydrogen bonds and mechanical properties of 3D-printed PCL. Mater Sci Eng C Mater Biol Appl. 2020;114: 111072.

120. Bartnikowski M, Dargaville TR, Ivanovski S, Hutmacher DW. Degradation mechanisms of polycaprolactone in the context of chemistry, geometry and environment. Prog Polym Sci. 2019;96: 1–20.

121. Sailema-Palate GP, Vidaurre A, Campillo-Fernández AJ, Castilla-Cortázar I. A comparative study on Poly(ε-caprolactone) film degradation at extreme pH values. Polym Degrad Stab. 2016;130: 118–125.

122. Aoyama T, Uto K, Shimizu H, Ebara M, Kitagawa T, Tachibana H, et al. Development of a new poly-ε-caprolactone with low melting point for creating a thermoset mask used in radiation therapy. Sci Rep. 2021;11: 20409.

123. Wang Q, Ye W, Ma Z, Xie W, Zhong L, Wang Y, et al. 3D printed PCL/β-TCP cross-scale scaffold with high-precision fiber for providing cell growth and forming bones in the pores. Materials Science and Engineering: C. 2021;127: 112197.

124. Kade JC, Dalton PD. Polymers for Melt Electrowriting. Adv Healthc Mater. 2021;10: e2001232.

125. Kinstlinger IS, Bastian A, Paulsen SJ, Hwang DH, Ta AH, Yalacki DR, et al. Open-Source Selective Laser Sintering (OpenSLS) of Nylon and Biocompatible Polycaprolactone. Eddington DT, editor. PLoS One. 2016;11: e0147399.

126. Mazzoli A, Ferretti C, Gigante A, Salvolini E, Mattioli-Belmonte M. Selective laser sintering manufacturing of polycaprolactone bone scaffolds for applications in bone tissue engineering. Rapid Prototyping Journal. 2015;21: 386–332.

127. Yamada H, Evans, F, G. Strength of biological materials. Baltimore, Williams & Wilkins; 1970.

128. Gu X, Zha Y, Li Y, Chen J, Liu S, Du Y, et al. Integrated polycaprolactone microsphere-based scaffolds with biomimetic hierarchy and tunable vascularization for osteochondral repair. Acta Biomater. 2022;141: 190–197.

129. Liang X, Duan P, Gao J, Guo R, Qu Z, Li X, et al. Bilayered PLGA/PLGA-HAp Composite Scaffold for Osteochondral Tissue Engineering and Tissue Regeneration. ACS Biomater Sci Eng. 2018;4: 3506–3521.

130. Demirors M. The History of Polyethylene. In: Strom, T, E, Rasmussen, S, C, editors. 100+ Years of Plastics Leo Baekeland and Beyond. American Chemical Society; 2011. pp. 115–145.

131. González-Aguilar GA, Cruz R, Baez R, Wang CY. Storage quality of bell peppers pretreated with hot water and polyethylene packaging. J Food Qual. 1999;22: 287–299.

132. Hamadouche M, Biau DJ, Huten D, Musset T, Gaucher F. The use of a cemented dual mobility socket to treat recurrent dislocation. Clin Orthop Relat Res. 2010;468: 3248–3254.

133. Vasile C, Pascu M, Rapra Technology Limited. Practical guide to polyethylene. RAPRA Technology; 2005. p. 176.

134. Sharma RK. Use of HDPE implants in facial skeletal augmentation: Should we rush for it? Indian J Plast Surg. 2010;43: 40–41.

135. Hindy P, Hong J, Lam-Tsai Y, Gress F. A comprehensive review of esophageal stents. Gastroenterol Hepatol . 2012;8: 526–534.

136. Langlois J, Hamadouche M. Recent update on crosslinked polyethylene in total hip arthroplasty. SICOT J. 2020;6: 13.

137. Wegner A. New Polymer Materials for the Laser Sintering Process: Polypropylene and Others. Phys Procedia. 2016;83: 1003–1012.

138. Amorim Fred L. Selective laser sintering of Mo-CuNi composite to be used as EDM electrode. Rapid Prototyping Journal. 2014;20: 59–68.

139. Khalil Y, Kowalski A, Hopkinson N. Influence of energy density on flexural properties of

laser-sintered UHMWPE. Additive Manufacturing. 2016;10: 67–75.

140. Ferrage L, Bertrand G, Lenormand P, Grossin D, Ben-Nissan B. A review of the additive manufacturing (3DP) of bioceramics: Alumina, zirconia (PSZ) and hydroxyapatite. Journal of the Australian Ceramic Society. Springer International Publishing; 2017. pp. 11–20. doi:10.1007/s41779-016-0003-9

141. Salmoria GV, Ahrens CH, Klauss P, Paggi RA, Oliveira RG, Lago A. Rapid manufacturing of polyethylene parts with controlled pore size gradients using selective laser sintering. Mater Res. 2007;10: 211–214.

142. Paxton NC, Dinoro J, Ren J, Ross MT, Daley R, Zhou R, et al. Additive manufacturing enables personalised porous high-density polyethylene surgical implant manufacturing with improved tissue and vascular ingrowth. Applied Materials Today. 2021;22: 100965.

143. Salmoria GV, Leite JL, Ahrens CH, Lago A, Pires ATN. Rapid manufacturing of PA/HDPE blend specimens by selective laser sintering: Microstructural characterization. Polym Test. 2007;26: 361–368.

144. Salmoria GV, Leite JL, Paggi RA, Lago A, Pires ATN. Selective laser sintering of PA12/HDPE blends: Effect of components on elastic/plastic behavior. Polym Test. 2008;27: 654–659.

145. Salmoria GV, Leite JL, Vieira LF, Pires ATN, Roesler CRM. Mechanical properties of PA6/PA12 blend specimens prepared by selective laser sintering. Polym Test. 2012;31: 411–416.

146. Goodridge RD, Hague RJM, Tuck CJ. An empirical study into laser sintering of ultra-high molecular weight polyethylene (UHMWPE). J Mater Process Technol. 2010;210: 72–80.

147. Rimell JT, Marquis PM. Selective laser sintering of ultra high molecular weight polyethylene for clinical applications. J Biomed Mater Res. 2000;53: 414–420.

148. Haleem A, Javaid M. Polyether ether ketone (PEEK) and its 3D printed implants applications in medical field: An overview. Clinical Epidemiology and Global Health. 2019;7: 571–577.

149. Puppi D, Chiellini F, Piras AM, Chiellini E. Polymeric materials for bone and cartilage repair. Prog Polym Sci. 2010;35: 403–440.

150. Haleem A, Javaid M, Vaish A, Vaishya R. Three-Dimensional-Printed Polyether Ether Ketone Implants for Orthopedics. Indian J Orthop. 2019;53: 377–379.

151. Zhang H. Fire-safe polymers and polymer composites. Office of Aviation Research, Federal Aviation Administration; 2004.

152. Berretta S, Evans KE, Ghita O. Processability of PEEK, a new polymer for High Temperature Laser Sintering (HT-LS). Eur Polym J. 2015;68: 243–266.

153. Nazarov A, Skornyakov I, Shishkovsky I. The Setup Design for Selective Laser Sintering of High-Temperature Polymer Materials with the Alignment Control System of Layer Deposition. Machines. 2018;6: 11.

154. Yazdani B, Chen B, Benedetti L, Davies R, Ghita O, Zhu Y. A new method to prepare composite powders customized for high temperature laser sintering. Compos Sci Technol. 2018;167: 243–250.

155. Berretta S, Evans K, Ghita O. Additive manufacture of PEEK cranial implants: Manufacturing considerations versus accuracy and mechanical performance. Materials and Design. 2018;139: 141–152.

156. Chen P, Cai H, Li Z, Li M, Wu H, Su J, et al. Crystallization kinetics of polyetheretherketone during high temperature-selective laser sintering. Additive Manufacturing. 2020;36: 101615.

157. Shackleford ASD, Williams RJ, Brown R, Wingham JR, Majewski C. Degradation of Laser Sintered polyamide 12 parts due to accelerated exposure to ultraviolet radiation. Additive Manufacturing. 2021;46: 102132.

158. Akande SO, Dalgarno KW, Munguia J, Pallari J. Assessment of tests for use in process and quality control systems for selective laser sintering of polyamide powders. J Mater Process Technol. 2016;229: 549–561.

159. Roskies M, Jordan JO, Fang D, Abdallah M-N, Hier MP, Mlynarek A, et al. Improving PEEK bioactivity for craniofacial reconstruction using a 3D printed scaffold embedded with mesenchymal stem cells. J Biomater Appl. 2016;31: 132–139.

160. Feng P, Wu P, Gao C, Yang Y, Guo W, Yang W, et al. A Multimaterial Scaffold With Tunable Properties: Toward Bone Tissue Repair. Adv Sci. 2018;5: 1700817.

161. Savalani MM, Hao L, Dickens PM, Zhang Y, Tanner KE, Harris RA. The effects and interactions of fabrication parameters on the properties of selective laser sintered hydroxyapatite polyamide composite biomaterials. Rapid Prototyping Journal. 2012;18: 16–27.

162. Hui D, Goodridge RD, Scotchford CA, Grant DM. Laser sintering of nano-hydroxyapatite coated polyamide 12 powders. Additive Manufacturing. 2018;22: 560–570.

163. Ramu M, Ananthasubramanian M, Kumaresan T, Gandhinathan R, Jothi S. Optimization of the configuration of porous bone scaffolds made of Polyamide/Hydroxyapatite composites using Selective Laser Sintering for tissue engineering applications. Biomed Mater Eng. 2018;29: 739–755.

164. Chung H, Das S. Processing and properties of glass bead particulate-filled functionally graded Nylon-11 composites produced by selective laser sintering. Materials Science and Engineering: A. 2006;437: 226–234.

165. Goodridge RD, Shofner ML, Hague RJM, McClelland M, Schlea MR, Johnson RB, et al. Processing of a Polyamide-12/carbon nanofibre composite by laser sintering. Polym Test. 2011;30: 94–100.

166. Bonfield W, Grynpas MD, Tully AE, Bowman J, Abram J. Hydroxyapatite reinforced polyethylene--a mechanically compatible implant material for bone replacement. Biomaterials. 1981;2: 185–186.

167. Bonfield W, Doyle C, Tanner KE. In vivo evaluation of hydroxyapatite reinforced polyethylene composites. Biological and Biomedical Performence of Biomaterials. Elsevier, Amsterdam; 1986. pp. 153–159.

168. Savalani MM, Hao L, Harris RA. Evaluation of CO2 and Nd:YAG Lasers for the Selective Laser Sintering of HAPEX®. Proc Inst Mech Eng Pt B: J Eng Manuf. 2006;220: 171–182.

169. Milazzo M, Contessi Negrini N, Scialla S, Marelli B, Farè S, Danti S, et al. Additive

manufacturing approaches for hydroxyapatite‐reinforced composites. Adv Funct Mater. 2019;29: 1903055.

170. Du Y, Liu H, Yang Q, Wang S, Wang J, Ma J, et al. Selective laser sintering scaffold with hierarchical architecture and gradient composition for osteochondral repair in rabbits. Biomaterials. 2017;137: 37–48.

171. Xia Y, Zhou P, Cheng X, Xie Y, Liang C, Li C, et al. Selective laser sintering fabrication of nano-hydroxyapatite/poly-ε-caprolactone scaffolds for bone tissue engineering applications. Int J Nanomedicine. 2013;8: 4197–4213.

172. Eshraghi S, Das S. Micromechanical finite-element modeling and experimental characterization of the compressive mechanical properties of polycaprolactone-hydroxyapatite composite scaffolds prepared by selective laser sintering for bone tissue engineering. Acta Biomater. 2012;8: 3138–3143.

173. Doyle H, Lohfeld S, McHugh P. Evaluating the effect of increasing ceramic content on the mechanical properties, material microstructure and degradation of selective laser sintered polycaprolactone/β-tricalcium phosphate materials. Med Eng Phys. 2015;37: 767–776.

174. Wang G, Qian G, Zan J, Qi F, Zhao Z, Yang W, et al. A co-dispersion nanosystem of graphene oxide @silicon-doped hydroxyapatite to improve scaffold properties. Mater Des. 2021;199: 109399.

175. Shuai C, Wu P, Zhong Y, Feng P, Gao C, Huang W, et al. Polyetheretherketone/poly (glycolic acid) blend scaffolds with biodegradable properties. J Biomater Sci Polym Ed. 2016;27: 1434–1446.

176. Shuai C, Huang W, Feng P, Gao C, Shuai X, Xiao T, et al. Tailoring properties of porous Poly (vinylidene fluoride) scaffold through nano-sized 58s bioactive glass. J Biomater Sci Polym Ed. 2016;27: 97–109.

177. XiaoHui S, Wei L, PingHui S, QingYong S, QingSong W, YuSheng S, et al. Selective laser sintering of aliphatic-polycarbonate/hydroxyapatite composite scaffolds for medical applications. Int J Adv Manuf Technol. 2015;81: 15–25.

178. Kuznetsova DS, Timashev PS, Dudenkova VV, Meleshina AV, Antonov EA, Krotova LI, et al. Comparative Analysis of Proliferation and Viability of Multipotent Mesenchymal Stromal Cells in 3D Scaffolds with Different Architectonics. Bull Exp Biol Med. 2016;160: 535–541.

179. Wiria FE, Chua CK, Leong KF, Quah ZY, Chandrasekaran M, Lee MW. Improved biocomposite development of poly(vinyl alcohol) and hydroxyapatite for tissue engineering scaffold fabrication using selective laser sintering. J Mater Sci Mater Med. 2008;19: 989–996.

180. Liao HT, Lee MY, Tsai WW, Wang HC, Lu WC. Osteogenesis of adipose‐derived stem cells on polycaprolactone–β‐tricalcium phosphate scaffold fabricated via selective laser sintering and surface coating with collagen type I. Journal of tissue. 2016;10: e337–E353.

181. Moiduddin K, Mian SH, Alkhalefah H, Umer U. Digital Design, Analysis and 3D Printing of Prosthesis Scaffolds for Mandibular Reconstruction. Metals . 2019;9: 569.

182. Salmoria GV, Klauss P, Zepon KM, Kanis LA. The effects of laser energy density and particle size in the selective laser sintering of polycaprolactone/progesterone specimens: morphology and

drug release. Int J Adv Manuf Technol. 2013;66: 1113–1118.

183. Awad A, Fina F, Goyanes A, Gaisford S, Basit AW. Advances in powder bed fusion 3D printing in drug delivery and healthcare. Adv Drug Deliv Rev. 2021;174: 406–424.

184. Salmoria GV, Cardenuto MR, Roesler CRM, Zepon KM, Kanis LA. PCL/Ibuprofen Implants Fabricated by Selective Laser Sintering for Orbital Repair. Procedia CIRP. 2016;49: 188–192.

185. Sun Z, Wu F, Gao H, Cui K, Xian M, Zhong J, et al. A Dexamethasone-Eluting Porous Scaffold for Bone Regeneration Fabricated by Selective Laser Sintering. ACS Appl Bio Mater. 2020;3: 8739–8747.

186. Thakkar R, Jara MO, Swinnea S, Pillai AR, Maniruzzaman M. Impact of Laser Speed and Drug Particle Size on Selective Laser Sintering 3D Printing of Amorphous Solid Dispersions. Pharmaceutics. 2021;13: 1149.

187. Kulinowski P, Malczewski P, Pesta E, Łaszcz M, Mendyk A, Polak S, et al. Selective laser sintering (SLS) technique for pharmaceutical applications—Development of high dose controlled release printlets. Additive Manufacturing. 2021;38: 101761.

188. Groll J, Boland T, Blunk T, Burdick JA, Cho D-W, Dalton PD, et al. Biofabrication: reappraising the definition of an evolving field. Biofabrication. 2016;8: 013001.

189. Grzeszczak A, Lewin S, Eriksson O, Kreuger J, Persson C. The Potential of Stereolithography for 3D Printing of Synthetic Trabecular Bone Structures. Materials . 2021;14. doi:10.3390/ma14133712

190. Zhou T, Zhang L, Yao Q, Ma Y, Hou C, Sun B, et al. SLA 3D printing of high quality spine shaped β-TCP bioceramics for the hard tissue repair applications. Ceram Int. 2020;46: 7609–7614.

191. Zhang J, Huang D, Liu S, Dong X, Li Y, Zhang H, et al. Zirconia toughened hydroxyapatite biocomposite formed by a DLP 3D printing process for potential bone tissue engineering. Mater Sci Eng C Mater Biol Appl. 2019;105: 110054.

192. Xu F, Ren H, Zheng M, Shao X, Dai T, Wu Y, et al. Development of biodegradable bioactive glass ceramics by DLP printed containing EPCs/BMSCs for bone tissue engineering of rabbit mandible defects. J Mech Behav Biomed Mater. 2020;103: 103532.

193. Zhang B, Gui X, Song P, Xu X, Guo L, Han Y, et al. Three-dimensional printing of large-scale, high-resolution bioceramics with micronano inner porosity and customized surface characterization design for bone regeneration. ACS Appl Mater Interfaces. 2022;14: 8804–8815.

194. Zhang B, Wang L, Song P, Pei X, Sun H, Wu L, et al. 3D printed bone tissue regenerative PLA/HA scaffolds with comprehensive performance optimizations. Mater Des. 2021;201: 109490.

195. Kim CG, Han KS, Lee S, Kim MC, Kim SY, Nah J. Fabrication of Biocompatible Polycaprolactone–Hydroxyapatite Composite Filaments for the FDM 3D Printing of Bone Scaffolds. NATO Adv Sci Inst Ser E Appl Sci. 2021;11: 6351.

196. Wang W, Zhang B, Li M, Li J, Zhang C, Han Y, et al. 3D printing of PLA/n-HA composite scaffolds with customized mechanical properties and biological functions for bone tissue engineering. Composites Part B. 2021;224: 109192.

197. Zhao D, Liang H, Han C, Li J, Liu J, Zhou K, et al. 3D printing of a titanium-tantalum Gyroid scaffold with superb elastic admissible strain, bioactivity and in-situ bone regeneration capability. Additive Manufacturing. 2021;47: 102223.

198. Kelly CN, Francovich J, Julmi S, Safranski D, Guldberg RE, Maier HJ, et al. Fatigue behavior of As-built selective laser melted titanium scaffolds with sheet-based gyroid microarchitecture for bone tissue engineering. Acta Biomater. 2019;94: 610–626.

199. Zhao L, Pei X, Jiang L, Hu C, Sun J, Xing F, et al. Bionic design and 3D printing of porous titanium alloy scaffolds for bone tissue repair. Composites Part B. 2019;162: 154–161.

200. DiNoro JN, Paxton NC, Skewes J, Yue Z, Lewis PM, Thompson RG, et al. Laser sintering approaches for bone tissue engineering. Polymers . 2022;14: 2336.

201. Hashmi S. Comprehensive Materials Processing. Newnes; 2014.

202. Peng X, Kuang X, Roach DJ, Wang Y, Hamel CM, Lu C, et al. Integrating digital light processing with direct ink writing for hybrid 3D printing of functional structures and devices. Additive Manufacturing. 2021;40: 101911.

203. Lupone F, Padovano E, Casamento F, Badini C. Process Phenomena and Material Properties in Selective Laser Sintering of Polymers: A Review. Materials . 2021;15. doi:10.3390/ma15010183

204. Roberts IA, Wang CJ, Esterlein R, Stanford M, Mynors DJ. A three-dimensional finite element analysis of the temperature field during laser melting of metal powders in additive layer manufacturing. Int J Mach Tools Manuf. 2009;49: 916–923.

205. Barbosa-Cánovas GV, Ortega-Rivas E, Juliano P, Yan H. Food Powders: Physical Properties, Processing, and Functionality. Springer, Boston, MA; 2005.

206. Schmid M, Amado F, Levy G, Wegener K. Flowability of powders for selective laser sintering (SLS) investigated by round robin test. High Value Manufacturing: Advanced Research in Virtual and Rapid Prototyping: Proceedings of the 6th International Conference on Advanced Research in Virtual and Rapid Prototyping. books.google.com; 2013. p. 95.

207. Universal Laser PLS6MW Laser System. [cited 13 Oct 2021]. Available: https://www.pdi3d.com/Universal_Laser_PLS6MW_Laser_System_p/ul-pls6mw.htm

208. VEVOR 40W Co2 Laser 12" x 8" USB Port Laser Engraving Machine Air Exhaust Fan Laser Cutter High Precise Stepping Motor (40W CO2 Laser).

209. Sillani F, Wagner D, Aaron SM, Haferkamp L, Bernardus SA, Schmid M, et al. Compaction behavior of powder bed fusion feedstock for metal and polymer additive manufacturing. Rapid Prototyping Journal. 2021;27: 58–66.

210. Baesso I, Karl D, Spitzer A, Gurlo A, Günster J, Zocca A. Characterization of powder flow behavior for additive manufacturing. Additive Manufacturing. 2021;47: 102250.

211. Haferkamp L, Haudenschild L, Spierings A, Wegener K, Riener K, Ziegelmeier S, et al. The Influence of Particle Shape, Powder Flowability, and Powder Layer Density on Part Density in Laser Powder Bed Fusion. Metals . 2021;11: 418.

212. Van den Eynde M. Expanding the polymer material palette for Laser Sintering: The importance of powder flowability. 2018 [cited 21 Oct 2021]. Available:

https://lirias.kuleuven.be/2274960?limo=0

213. Verbelen L. Towards scientifically based screening criteria for polymer laser sintering. 2016 [cited 21 Oct 2021]. Available: https://lirias.kuleuven.be/1941361?limo=0

214. Prescott, J.K. and Barnum, R.A. On powder flowability. Pharm Technol. 2000;24: 60–60.

215. Spierings AB, Voegtlin M, Bauer T, Wegener K. Powder flowability characterisation methodology for powder-bed-based metal additive manufacturing. Progress in Additive Manufacturing. 2016;1: 9–20.

216. Berretta S, Ghita O, Evans KE. Morphology of polymeric powders in Laser Sintering (LS): From Polyamide to new PEEK powders. Eur Polym J. 2014;59: 218–229.

217. Khazaee S, Kiani A, Badrossamay M, Foroozmehr E. Selective Laser Sintering of Polystyrene: Preserving Mechanical Properties without Post-processing. J Mater Eng Perform. 2021;30: 3068–3078.

218. Sih SS. The thermal and optical properties of powders in selective laser sintering. University of Texas at Austin. 1996.

219. Shishkovskii IV, Kupriyanov NL. Thermal fields in metal-polymer powder compositions during laser treatment. High Temp. 1997;35: 710–714.

220. Taylor CM, Childs T. Thermal experiments in direct metal laser sintering. Proceedings of Euro RP 2001. 2001.

221. Gusarov AV, Laoui T, Froyen L, Titov VI. Contact thermal conductivity of a powder bed in selective laser sintering. Int J Heat Mass Transf. 2003;46: 1103–1109.

222. Hobbs ER, Bailin PL, Wheeland RG, Ratz JL. Superpulsed lasers: minimizing thermal damage with short duration, high irradiance pulses. J Dermatol Surg Oncol. 1987;13: 955–964.

223. Ready J. Effects of High-Power Laser Radiation. Elsevier; 2012.

224. Bai J, Zhang B, Song J, Bi G, Wang P, Wei J. The effect of processing conditions on the mechanical properties of polyethylene produced by selective laser sintering. Polym Test. 2016;52: 89–93.

225. Jhabvala J, Boillat E, Antignac T, Glardon R. On the effect of scanning strategies in the selective laser melting process. Virtual Phys Prototyp. 2010;5: 99–109.

226. Jia H, Sun H, Wang H, Wu Y, Wang H. Scanning strategy in selective laser melting (SLM): a review. Int J Adv Manuf Technol. 2021;113: 2413–2435.

227. Luo Z, Zhao Y. A survey of finite element analysis of temperature and thermal stress fields in powder bed fusion Additive Manufacturing. Additive Manufacturing. 2018;21: 318–332.

228. Bassoli E, Gatto A, Iuliano L. Joining mechanisms and mechanical properties of PA composites obtained by selective laser sintering. Rapid Prototyping Journal. 2012;18: 100–108.

229. Fávaro SL, Rubira AF, Muniz EC, Radovanovic E. Surface modification of HDPE, PP, and PET films with KMnO4/HCl solutions. Polym Degrad Stab. 2007;92: 1219–1226.

230. Costa CS, Muñoz M, Ribeiro MR, Silva JM. A thermogravimetric study of HDPE conversion

under a reductive atmosphere. Catal Today. 2021;379: 192–204.

231. Vasquez M, Haworth B, Hopkinson N. Methods for quantifying the stable sintering region in laser sintered polyamide-12. Polym Eng Sci. 2013;53: 1230–1240.

232. Saini DR, Shenoy AV. Melt Rheology of Some Specialty Polymers. J Elastomers Plast. 1985;17: 189–217.

233. Scaffaro R, La Mantia FP, Botta L, Morreale M, Tz. Dintcheva N, Mariani P. Competition between chain scission and branching formation in the processing of high-density polyethylene: Effect of processing parameters and of stabilizers. Polym Eng Sci. 2009;49: 1316–1325.

234. Fairbrother A, Hsueh H-C, Kim JH, Jacobs D, Perry L, Goodwin D, et al. Temperature and light intensity effects on photodegradation of high-density polyethylene. Polym Degrad Stab. 2019;165: 153–160.

235. Liu X, Gao C, Sangwan P, Yu L, Tong Z. Accelerating the degradation of polyolefins through additives and blending. J Appl Polym Sci. 2014;131. doi:10.1002/app.40750

236. Wencke YL, Proes F, Imgrund P, Luinstra GA. Toward the direct synthesis of HDPE powders for powder bed fusion based additive manufacturing. Macromol Mater Eng. 2021; 2100477.

237. Munaro M, Akcelrud L. Correlations between composition and crystallinity of LDPE/HDPE blends. J Polym Res. 2008;15: 83–88.

238. Sahu AK, Sudhakar K, Sarviya RM. Influence of U.V light on the thermal properties of HDPE/Carbon black composites. Case Studies in Thermal Engineering. 2019;15: 100534.

239. Wong AC-Y, Lam F. Study of selected thermal characteristics of polypropylene/polyethylene binary blends using DSC and TGA. Polym Test. 2002;21: 691–696.

240. Yaagoubi H, Abouchadi H, Janan MT. Review on the modeling of the laser sintering process for Polyamide 12. E3S Web of Conferences. 2021;234: 00006.

241. Wendel B, Dallner C, Schmachtenberg E. New developments in selective laser sintering of polymers. Proc 5th Laser Assisted Net-shape Engineering Conf(LANE 2007), Erlangen. 2007. pp. 323–331.

242. Tan LJ, Zhu W, Sagar K, Zhou K. Comparative study on the selective laser sintering of polypropylene homopolymer and copolymer: processability, crystallization kinetics, crystal phases and mechanical properties. Additive Manufacturing. 2021;37: 101610.

243. Rosso S, Meneghello R, Biasetto L, Grigolato L, Concheri G, Savio G. In-depth comparison of polyamide 12 parts manufactured by Multi Jet Fusion and Selective Laser Sintering. Additive Manufacturing. 2020;36: 101713.

244. Sivadas, B.O., Ashcroft, I., Khlobystov, A.N. and Goodridge, R.D. Laser sintering of polymer nanocomposites. Advanced Industrial and Engineering Polymer Research. 2021;4: 277–300.

245. Bellehumeur CT, Bisaria MK, Vlachopoulos J. An experimental study and model assessment of polymer sintering. Polym Eng Sci. 1996;36: 2198–2207.

246. Muller JD, Lamnawar K, Maazouz A. Relationship between rheological and surface properties for the sintering process of polymers. Journal of Materials Science. 2012;47: 121–131.

247. Mueller B. Additive manufacturing technologies – rapid prototyping to direct digital manufacturing. Assem autom. 2012;32. doi:10.1108/aa.2012.03332baa.010

248. Schmid M, Amado A, Wegener K. Polymer powders for selective laser sintering (SLS). AIP Conference proceedings. AIP Publishing LLC; 2015. p. 160009.

249. Koutny D, Palousek D, Pantelejev L, Hoeller C, Pichler R, Tesicky L, et al. Influence of Scanning Strategies on Processing of Aluminum Alloy EN AW 2618 Using Selective Laser Melting. Materials . 2018;11. doi:10.3390/ma11020298

250. Wohlgemuth F, Lellinger D, Alig I. Modelling of Pore Collapse during Polymer Sintering: Viscoelastic Model with Enclosed Gas. Materials . 2021;14. doi:10.3390/ma14092182

251. Kontopoulou M, Vlachopoulos J. Bubble dissolution in molten polymers and its role in rotational molding. Polym Eng Sci. 1999;39: 1189–1198.

252. Gogos G. Bubble removal in rotational molding. Polym Eng Sci. 2004;44: 388–394.

253. Ly H-B, Monteiro E, Le T-T, Le VM, Dal M, Regnier G, et al. Prediction and Sensitivity Analysis of Bubble Dissolution Time in 3D Selective Laser Sintering Using Ensemble Decision Trees. Materials . 2019;12. doi:10.3390/ma12091544

254. David Kingery W, Bowen HK, Uhlmann DR. Introduction to Ceramics. John Wiley & Sons; 1976.

255. Kontopoulou M, Vlachopoulos J. Melting and densification of thermoplastic powders. Polym Eng Sci. 2001;41: 155–169.

256. Chaudhary BI, Takács E, Vlachopoulos J. Processing enhancers for rotational molding of polyethylene. Polym Eng Sci. 2001;41: 1731–1742.

257. Pereira TF, Silva MAC, Oliveira MF, Maia IA, Silva JVL, Costa MF, et al. Effect of process parameters on the properties of selective laser sintered Poly(3-hydroxybutyrate) scaffolds for bone tissue engineering. Virtual Phys Prototyp. 2012;7: 275–285.

258. Lisi Leite J, Salmoria GV, Paggi RA, Ahrens CH, Pouzada AS. Microstructural characterization and mechanical properties of functionally graded PA12/HDPE parts by selective laser sintering. Int J Adv Manuf Technol. 2012;59: 583–591.

259. Senthilkumaran K, Pandey PM, Rao PVM. Influence of building strategies on the accuracy of parts in selective laser sintering. Mater Des. 2009;30: 2946–2954.

260. Lin J-H, Pan Y-J, Liu C-F, Huang C-L, Hsieh C-T, Chen C-K, et al. Preparation and Compatibility Evaluation of Polypropylene/High Density Polyethylene Polyblends. Materials . 2015;8: 8850–8859.

261. Hu E, Yuan H, Du Y, Chen X. LDPE and HDPE Microplastics Differently Affect the Transport of Tetracycline in Saturated Porous Media. Materials. 2021;14: 1757.

262. Jung MR, Horgen FD, Orski SV. V. Rodriguez C, KL Beers, GH Balazs, TT Jones, TM Work, KC Brignac, S.-J. Royer, KD Hyrenbach, BA Jensen, JM Lynch, Validation of ATR FT-IR to identify polymers of plastic marine debris, including those ingested by marine organisms. Mar Pollut Bull. 2018;127: 704–716.

263. Morais JA de, Gadioli R, De Paoli M-A. Curaua fiber reinforced high-density polyethylene

composites: effect of impact modifier and fiber loading. Polímeros. 2016;26: 115–122.

264. Czelusniak T, Amorim FL. Influence of energy density on selective laser sintering of carbon fiber-reinforced PA12. Int J Adv Manuf Technol. 2020;111: 2361–2376.

265. Zhang J, Adams A. Understanding thermal aging of non-stabilized and stabilized polyamide 12 using 1H solid-state NMR. Polym Degrad Stab. 2016;134: 169–178.

266. Demontiero O, Vidal C, Duque G. Aging and bone loss: new insights for the clinician. Ther Adv Musculoskelet Dis. 2012;4: 61–76.

267. Ashammakhi N, Ahadian S, Darabi MA, El Tahchi M, Lee J, Suthiwanich K, et al. Minimally Invasive and Regenerative Therapeutics. Adv Mater. 2019;31: e1804041.

268. Vos T, Abajobir AA, Abate KH, Abbafati C, Abbas KM, Abd-Allah F, et al. Global, regional, and national incidence, prevalence, and years lived with disability for 328 diseases and injuries for 195 countries, 1990--2016: a systematic analysis for the Global Burden of Disease Study 2016. Lancet. 2017;390: 1211–1259.

269. Tao O, Kort-Mascort J, Lin Y, Pham HM, Charbonneau AM, ElKashty OA, et al. The Applications of 3D Printing for Craniofacial Tissue Engineering. Micromachines. 2019;10: 480.

270. Keaveny TM, Morgan EF, Niebur GL, Yeh OC. Biomechanics of trabecular bone. Annu Rev Biomed Eng. 2001;3: 307–333.

271. Heaney RP, Donald Whedon G. Bone. Encyclopedia Britannica. 2019. Available: https://www.britannica.com/science/bone-anatomy

272. Martini F, Nath J, Bartholomew E. Fundamentals of Anatomy and Physiology. Global Edition. Harlow. United Kingdom: Pearson Education Canada; 2018.

273. Yaszemski MJ, Payne RG, Hayes WC, Langer R, Mikos AG. Evolution of bone transplantation: molecular, cellular and tissue strategies to engineer human bone. Biomaterials. 1996;17: 175–185.

274. Rahim TNAT, Abdullah AM, Akil H, Mohamad D. Comparison of mechanical properties for polyamide 12 composite-based biomaterials fabricated by fused filament fabrication and injection molding. AIP Conference Proceedings. American Institute of Physics; 2016. p. 020007.

275. Nordin M. Basic Biomechanics of the Musculoskeletal System. Lippincott Williams & Wilkins; 2020.

276. Carter DR, Hayes WC. Compact bone fatigue damage: a microscopic examination. Clin Orthop Relat Res. 1977; 265–274.

277. Keaveny TM, Hayes WC. A 20-year perspective on the mechanical properties of trabecular bone. J Biomech Eng. 1993;115: 534–542.

278. Grimal Q, Laugier P. Quantitative Ultrasound Assessment of Cortical Bone Properties Beyond Bone Mineral Density. IRBM. 2019;40: 16–24.

279. Zioupos P, Cook RB, Hutchinson JR. Some basic relationships between density values in cancellous and cortical bone. J Biomech. 2008;41: 1961–1968.

280. Morgan EF, Bayraktar HH, Keaveny TM. Trabecular bone modulus–density relationships

depend on anatomic site. J Biomech. 2003;36: 897–904.

281. Wright TM, Hayes WC. Fracture mechanics parameters for compact bone—Effects of density and specimen thickness. J Biomech. 1977;10: 419–430.

282. Zioupos P, Currey JD. Changes in the stiffness, strength, and toughness of human cortical bone with age. Bone. 1998;22: 57–66.

283. Zioupos P, Currey JD, Hamer AJ. The role of collagen in the declining mechanical properties of aging human cortical bone. J Biomed Mater Res. 1999;45: 108–116.

284. McCalden RW, McGeough JA, Barker MB, Court-Brown CM. Age-related changes in the tensile properties of cortical bone. The relative importance of changes in porosity, mineralization, and microstructure. J Bone Joint Surg Am. 1993;75: 1193–1205.

285. Burstein AH, Reilly DT, Martens M. Aging of bone tissue: mechanical properties. J Bone Joint Surg Am. 1976;58: 82–86.

286. Launey ME, Buehler MJ, Ritchie RO. On the mechanistic origins of toughness in bone. Annu Rev Mater Res. 2010;40: 25–53.

287. Yadroitsev I, Gusarov A, Yadroitsava I, Smurov I. Single track formation in selective laser melting of metal powders. J Mater Process Technol. 2010;210: 1624–1631.

288. Zarringhalam H, Hopkinson N, Kamperman NF, de Vlieger JJ. Effects of processing on microstructure and properties of SLS Nylon 12. Materials Science and Engineering: A. 2006;435-436: 172–180.

289. Liu K, Shi Y, He W, Li C, Wei Q, Liu J. Densification of alumina components via indirect selective laser sintering combined with isostatic pressing. The International Journal of Advanced Manufacturing Technology. 2013;67: 2511–2519.

290. Kruth J-P, Levy G, Klocke F, Childs THC. Consolidation phenomena in laser and powder-bed based layered manufacturing. CIRP Ann. 2007;56: 730–759.

291. Khairallah SA, Anderson AT, Rubenchik A. Laser powder-bed fusion additive manufacturing: Effects of main physical processes on dynamical melt flow and pore formation from mesoscopic powder …. arXiv. Lawrence Livermore National Laboratory; 2015.

292. Silva MJ, Gibson LJ. The effects of non-periodic microstructure and defects on the compressive strength of two-dimensional cellular solids. Int J Mech Sci. 1997;39: 549–563.

293. Yamada H, Evans FG. Strength of biological materials,(1970). Baltimore, MD: Williams & Wilkens.

294. Tomar, Dave, Chandekar. Advances in tissue engineering approaches for craniomaxillofacial bone reconstruction. and Functional Tissue …. 2020. Available: https://www.intechopen.com/chapters/73880

295. Kruth, J.P., Levy, G., Schindel, R., Craeghs, T. and Yasa, E. Consolidation of polymer powders by selective laser sintering. Proceedings of the 3rd international conference on polymers and moulds innovations. lirias.kuleuven.be; 2008. pp. 15–30.

296. Faes M, Wang Y, Lava P, Moens D. Variability, heterogeneity, and anisotropy in the

quasi-static response of laser sintered PA12 components. Strain. 2017;53: e12219.

297. Soe SP, Eyers DR, Setchi R. Assessment of non-uniform shrinkage in the laser sintering of polymer materials. Int J Adv Manuf Technol. 2013;68: 111–125.

298. Lücking TH, Sambale F, Beutel S, Scheper T. 3D-printed individual labware in biosciences by rapid prototyping: A proof of principle. Eng Life Sci. 2015;15: 51–56.

299. Ullsperger T, Wencke YL, Yürekli B, Matthäus G, Rettenmayr M, Luinstra GA, et al. Laser powder bed fusion of ultra-high molecular weight polyethylene (UHMWPE) using near-infrared ultrashort laser pulses. Mater Des. 2021;210: 110048.

300. Bolnick HJ, Bui AL, Bulchis A, Chen C, Chapin A, Lomsadze L, et al. Health-care spending attributable to modifiable risk factors in the USA: an economic attribution analysis. Lancet Public Health. 2020;5: e525–e535.

301. Dimitriou R, Jones E, McGonagle D, Giannoudis PV. Bone regeneration: Current concepts and future directions. BMC Medicine. 2011. doi:10.1186/1741-7015-9-66

302. Battafarano G, Rossi M, De Martino V, Marampon F, Borro L, Secinaro A, et al. Strategies for Bone Regeneration: From Graft to Tissue Engineering. Int J Mol Sci. 2021;22. doi:10.3390/ijms22031128

303. Clarke B. Normal bone anatomy and physiology. Clin J Am Soc Nephrol. 2008;3 Suppl 3: S131–9.

304. Standring S. Gray's Anatomy E-Book: The Anatomical Basis of Clinical Practice. Elsevier Health Sciences; 2015.

305. Haglund WD. Forensic taphonomy: The postmortem fate of human remains. Sorg MH, Haglund WD, editors. Boca Raton, FL: CRC Press; 1996. doi:10.1201/9781439821923

306. Davis L. Student-centered design components in body physics: Motion to metabolism. In: Body Physics: Motion to Metabolism [Internet]. pdxscholar.library.pdx.edu; 2019 [cited 27 Jul 2022]. Available: https://pdxscholar.library.pdx.edu/cgi/viewcontent.cgi?article=1023&context=oer_symposium

307. The Editors of Encyclopedia Britannica. Cancellous bone. In: Encyclopedia Britannica [Internet]. 16 Apr 2015 [cited 24 May 2022]. Available: https://www.britannica.com/science/cancellous-bone

308. Hart NH, Nimphius S, Rantalainen T, Ireland A, Siafarikas A, Newton RU. Mechanical basis of bone strength: influence of bone material, bone structure and muscle action. J Musculoskelet Neuronal Interact. 2017;17: 114–139.

309. Morgan EF, Unnikrisnan GU, Hussein AI. Bone Mechanical Properties in Healthy and Diseased States. Annu Rev Biomed Eng. 2018;20: 119–143.

310. Gupte MJ, Ma PX. Nanofibrous Scaffolds for Dental and Craniofacial Applications. J Dent Res. 2012;91: 227–234.

311. Martín-del-Campo, M., Rosales-Ibañez, R. and Rojo, L. Biomaterials for cleft lip and palate regeneration. International journal of. 2019;20: 2176.

312. Tevlin R, McArdle A, Atashroo D, Walmsley GG, Senarath-Yapa K, Zielins ER, et al.

Biomaterials for craniofacial bone engineering. J Dent Res. 2014;93: 1187–1195.

313. Hung, B.P., Naved, B.A., Nyberg, E.L., Dias, M., Holmes, C.A., Elisseeff, J.H., Dorafshar, A.H. and Grayson, W.L. Three-dimensional printing of bone extracellular matrix for craniofacial regeneration. ACS biomaterials. 2016;2: 1806–1816.

314. Ribeiro VP, Silva-Correia J, Nascimento AI, da Silva Morais A, Marques AP, Ribeiro AS, et al. Silk-based anisotropical 3D biotextiles for bone regeneration. Biomaterials. 2017;123: 92–106.

315. Chen W, Thein-Han W, Weir MD, Chen Q, Xu HHK. Prevascularization of biofunctional calcium phosphate cement for dental and craniofacial repairs. Dent Mater. 2014;30: 535–544.

316. Goodridge RD, Dalgarno KW, Wood DJ. Indirect selective laser sintering of an apatite-mullite glass-ceramic for potential use in bone replacement applications. Proc Inst Mech Eng H. 2006;220: 57–68.

317. Shin K, Acri T, Geary S, Salem AK. Biomimetic Mineralization of Biomaterials Using Simulated Body Fluids for Bone Tissue Engineering and Regenerative Medicine. Tissue Eng Part A. 2017;23: 1169–1180.

318. Huang J, Silvio LDI, Wang M, Rehman I, Ohtsuki C, Bonfield W. Evaluation of in vitro bioactivity and biocompatibility of Bioglass®-reinforced polyethylene composite. J Mater Sci Mater Med. 1997;8: 809–813.

319. Maçon ALB, Kim TB, Valliant EM, Goetschius K, Brow RK, Day DE, et al. A unified in vitro evaluation for apatite-forming ability of bioactive glasses and their variants. J Mater Sci Mater Med. 2015;26: 115.

320. Chimutengwende-Gordon M, Dowling R, Pendegrass C, Blunn G. Determining the porous structure for optimal soft-tissue ingrowth: An in vivo histological study. PLoS One. 2018;13: e0206228.

321. Bandyopadhyay A, Espana F, Balla VK, Bose S, Ohgami Y, Davies NM. Influence of porosity on mechanical properties and in vivo response of Ti6Al4V implants. Acta Biomater. 2010;6: 1640–1648.

322. Spece H, Basgul C, Andrews CE, MacDonald DW, Taheri ML, Kurtz SM. A systematic review of preclinical in vivo testing of 3D printed porous Ti6Al4V for orthopedic applications, part I: Animal models and bone ingrowth outcome measures. J Biomed Mater Res B Appl Biomater. 2021;109: 1436–1454.

323. D'Lima DD, Lemperle SM, Chen PC, Holmes RE, Colwell CW Jr. Bone response to implant surface morphology. J Arthroplasty. 1998;13: 928–934.

324. O'Brien FJ. Biomaterials & scaffolds for tissue engineering. Mater Today. 2011;14: 88–95.

325. Zhang H, Zhang H, Xiong Y, Dong L, Li X. Development of hierarchical porous bioceramic scaffolds with controlled micro/nano surface topography for accelerating bone regeneration. Mater Sci Eng C Mater Biol Appl. 2021;130: 112437.

326. Wang Z, Florczyk SJ. Freeze-FRESH: A 3D Printing Technique to Produce Biomaterial Scaffolds with Hierarchical Porosity. Materials. 2020;13: 354.

327. Jia, G., Huang, H., Niu, J., Chen, C., Weng, J., Yu, F., Wang, D., Kang, B., Wang, T., Yuan, G.

and Zeng, H. Exploring the interconnectivity of biomimetic hierarchical porous Mg scaffolds for bone tissue engineering: Effects of pore size distribution on mechanical …. J Magnes Alloy. 2021;9: 1954–1966.

328. Engström KG, Ohlsson L. Morphology and filterability of red blood cells in neonatal and adult rats. Pediatr Res. 1990;27: 220–226.

329. Engström KG, Löfvenberg E. Treatment of myeloproliferative disorders with hydroxyurea: effects on red blood cell geometry and deformability. Blood. 1998;91: 3986–3991.

330. Viallat A, Abkarian M. Dynamics of Blood Cell Suspensions in Microflows. CRC Press; 2019.

331. Windberger U. Blood suspensions in animals. Dynamics of Blood Cell Suspensions in Microflows. Boca Raton : CRC Press, [2020] j Includes bibliographical references and index.: CRC Press; 2019. pp. 371–419.

332. McGovern JA, Griffin M, Hutmacher DW. Animal models for bone tissue engineering and modelling disease. Dis Model Mech. 2018;11. doi:10.1242/dmm.033084

333. Anderson. Biological responses to materials. Annu Rev Mater Res. 2001. Available: https://my.bme.utah.edu/~pat/Courses/Biomaterials/BiologicalResponse.pdf

334. Ibrahim M, Bond J, Medina MA, Chen L, Quiles C, Kokosis G, et al. Characterization of the Foreign Body Response to Common Surgical Biomaterials in a Murine Model. Eur J Plast Surg. 2017;40: 383–392.

335. Ratner BD. Reducing capsular thickness and enhancing angiogenesis around implant drug release systems. J Control Release. 2002;78: 211–218.

336. Rujitanaroj P-O, Jao B, Yang J, Wang F, Anderson JM, Wang J, et al. Controlling fibrous capsule formation through long-term down-regulation of collagen type I (COL1A1) expression by nanofiber-mediated siRNA gene silencing. Acta Biomater. 2013;9: 4513–4524.

337. Goreish HH, Lewis AL, Rose S, Lloyd AW. The effect of phosphorylcholine-coated materials on the inflammatory response and fibrous capsule formation: in vitro and in vivo observations. J Biomed Mater Res A. 2004;68: 1–9.

338. Hardison SE, Herrera G, Young ML, Hole CR, Wozniak KL, Wormley FL Jr. Protective immunity against pulmonary cryptococcosis is associated with STAT1-mediated classical macrophage activation. J Immunol. 2012;189: 4060–4068.

339. Pettersen JS, Fuentes-Duculan J, Suárez-Fariñas M, Pierson KC, Pitts-Kiefer A, Fan L, et al. Tumor-associated macrophages in the cutaneous SCC microenvironment are heterogeneously activated. J Invest Dermatol. 2011;131: 1322–1330.

340. Sussman EM, Halpin MC, Muster J, Moon RT, Ratner BD. Porous implants modulate healing and induce shifts in local macrophage polarization in the foreign body reaction. Ann Biomed Eng. 2014;42: 1508–1516.

341. Sachs EM, Haggerty JS, Cima MJ, Williams PA. Three-dimensional printing techniques. US Patent. 5204055, 1993. Available: https://patentimages.storage.googleapis.com/9e/92/4c/16485de942a672/US5204055.pdf

342. Sachs EM, Cima MJ, Caradonna MA, Grau J, Serdy JG, Saxton PC, et al. Jetting layers of

powder and the formation of fine powder beds thereby. US Patent. 6596224, 2003. Available: https://patentimages.storage.googleapis.com/d7/11/1b/148400e0b1f237/US6596224.pdf

343. Gunster J, Engler S, Heinrich JG. Forming of complex shaped ceramic products via layer-wise slurry deposition. Bull Eur Ceram Soc. 2003; 25–28.

344. Gahler A, Heinrich JG, Guenster J. Direct laser sintering of Al2O3--SiO2 dental ceramic components by layer-wise slurry deposition. J Am Ceram Soc. 2006;89: 3076–3080.

345. Tian X, Günster J, Melcher J, Li D, Heinrich JG. Process parameters analysis of direct laser sintering and post treatment of porcelain components using Taguchi's method. J Eur Ceram Soc. 2009;29: 1903–1915.

346. Lima P, Zocca A, Acchar W, Günster J. 3D printing of porcelain by layerwise slurry deposition. J Eur Ceram Soc. 2018;38: 3395–3400.

347. Rafailovich M, Shmueli Y, Jiang J. In-situ X-ray and thermal imaging of 3D printed PLA. APS March Meeting. 2019. Available: https://ui.adsabs.harvard.edu/abs/2019APS..MARA49001R/abstract

348. Shmueli Y, Lin Y-C, Zuo X, Guo Y, Lee S, Freychet G, et al. In-situ X-ray scattering study of isotactic polypropylene/graphene nanocomposites under shear during fused deposition modeling 3D printing. Compos Sci Technol. 2020;196: 108227.

349. Nguyen PD, Nguyen TQ, Tao QB, Vogel F. A data-driven machine learning approach for the 3D printing process optimisation. Virtual Phys Prototyp. 2022; 1–19.

350. Goh GD, Sing SL, Yeong WY. A review on machine learning in 3D printing: applications, potential, and challenges. Artificial Intelligence Review. 2021;54: 63–94.

351. Elbadawi M, McCoubrey LE, Gavins FKH. Disrupting 3D printing of medicines with machine learning. Trends in. 2021;42: 745–757.

352. Ruberu K, Senadeera M, Rana S, Gupta S, Chung J, Yue Z, et al. Coupling machine learning with 3D bioprinting to fast track optimisation of extrusion printing. Applied Materials. 2021;22: 100914.

353. Kim DH, Zohdi TI. Tool path optimization of selective laser sintering processes using deep learning. Comput Mech. 2022;69: 383–401.

354. Sala R, Regondi S, Pugliese R. Design Data and Finite Element Analysis of 3D Printed Poly(ε-Caprolactone)-Based Lattice Scaffolds: Influence of Type of Unit Cell, Porosity, and Nozzle Diameter on the Mechanical Behavior. Eng. 2021;3: 9–23.

355. Egan PF, Gonella VC, Engensperger M, Ferguson SJ, Shea K. Computationally designed lattices with tuned properties for tissue engineering using 3D printing. PLoS One. 2017;12: e0182902.

356. Cui H, Hensleigh R, Yao D, Maurya D, Kumar P, Kang MG, et al. Three-dimensional printing of piezoelectric materials with designed anisotropy and directional response. Nat Mater. 2019;18: 234–241.

357. Onal E, Frith JE, Jurg M, Wu X, Molotnikov A. Mechanical Properties and In Vitro Behavior of Additively Manufactured and Functionally Graded Ti6Al4V Porous Scaffolds. Metals .

2018;8: 200.

358. Frithioff A, Frendø M, Pedersen DB, Sørensen MS, Wuyts Andersen SA. 3D-Printed Models for Temporal Bone Surgical Training: A Systematic Review. Otolaryngol Head Neck Surg. 2021;165: 617–625.

359. Gueche YA, Sanchez-Ballester NM, Bataille B, Aubert A, Leclercq L, Rossi J-C, et al. Selective Laser Sintering of Solid Oral Dosage Forms with Copovidone and Paracetamol Using a CO2 Laser. Pharmaceutics. 2021;13. doi:10.3390/pharmaceutics13020160

360. Madžarević, M., Medarević, Đ., Pavlović, S., Ivković, B., Đuriš, J. and Ibrić, S. Understanding the Effect of Energy Density and Formulation Factors on the Printability and Characteristics of SLS Irbesartan Tablets—Application of the Decision Tree …. Pharmaceutics. 2021;13: 1969.

361. Cox SC, Jamshidi P, Eisenstein NM, Webber MA, Hassanin H, Attallah MM, et al. Adding functionality with additive manufacturing: Fabrication of titanium-based antibiotic eluting implants. Materials Science and Engineering: C. 2016;64: 407–415.

362. Gv S, Fe V, Gb G, Ms M, La K. 3D printing of PCL/Fluorouracil tablets by selective laser sintering: Properties of implantable drug delivery for cartilage cancer treatment. Rheumatol Orthop Med. 2017;2. doi:10.15761/rom.1000121

363. Costa BL, Machado R de R, Paiva MRB, Serakides R, Coelho M de M, Silva-Cunha A, et al. Sirolimus-loaded biodegradable implants induce long lasting anti-inflammatory and antiangiogenic effects. J Drug Deliv Sci Technol. 2018;44: 373–379.

364. Lee D, Park K, Seo J. Recent advances in anti-inflammatory strategies for implantable biosensors and medical implants. Biochip J. 2020;14: 48–62.

365. Borbet TC, Pawline MB, Zhang X, Wipperman MF, Reuter S, Maher T, et al. Influence of the early-life gut microbiota on the immune responses to an inhaled allergen. Mucosal Immunol. 2022. doi:10.1038/s41385-022-00544-5

Appendices

Appendix 1

The G-code use used to control the Arduino in the re-coater

G-Code V1.4
Automated Recoater

NB ; there's two Z-axis instead of X
Recoat with high frequecy stepping to ensure powder settling
Be sure to drop Z before re-winding recoater

G/M → Blue Text is a G- or M-command
F → Speed
X/Y/Z → Coordinates
E → Feeder movement

Typical Marlin Codes

G Code
G0 Rapid Movement
G1 Coordinated Movement
G2 CW ARC
G3 CCW ARC
G4 Dwell S<seconds> or P<milliseconds>
G10 retract filament according to settings of M207
G11 retract recover filament according to settings of M208
G28 Home all Axis
G29 Detailed Z-Probe, probes the bed at 3 or more points. Will fail if you haven't homed yet.
G30 Single Z Probe, probes bed at current XY location.
G31 Dock sled (Z PROBE SLED only)
G32 Undock sled (Z PROBE SLED only)
G90 Use Absolute Coordinates
G91 Use Relative Coordinates
G92 Set current position to coordinates given

M Codes

M0 Unconditional stop
M1 Same as M0
M17 Enable/Power all stepper motors
M18 Disable all stepper motors; same as M84
M20 List SD card
M21 Init SD card
M22 Release SD card
M23 Select SD file (M23 filename.g)
M24 Start/resume SD print
M25 Pause SD print
M26 Set SD position in bytes (M26 S12345)
M27 Report SD print status
M28 Start SD write (M28 filename.g)
M29 Stop SD write
M30 Delete file from SD (M30 filename.g)
M31 Output time since last M109 or SD card start to serial
M32 Select file and start SD print (Can be used _while_ printing from SD card files):
M42 Change pin status via gcode Use M42 Px Sy to set pin x to value y, when omitting Px the onboard led will be used.
M80 Turn on Power Supply
M81 Turn off Power Supply
M82 Set E codes absolute (default)
M83 Set E codes relative while in Absolute Coordinates (G90) mode
M84 Disable steppers until next move,or use S<seconds> to specify an inactivity timeout, after which the steppers will be
disabled. S0 to disable the timeout.
M85 Set inactivity shutdown timer with parameter S<seconds>. To disable set zero (default)
M92 Set axis_steps_per_unit same syntax as G92
M104 Set extruder target temp
M105 Read current temp
M106 Fan on
M107 Fan off
M109 S## Wait for extruder current temp to reach target temp. Waits only when heating. R## Wait for extruder current temp
to reach target temp. Waits when heating and cooling IF AUTOTEMP is enabled, S<mintemp> B<maxtemp> F<factor>.
Exit autotemp by any M109 without F
M112 Emergency stop
M114 Output current position to serial port
M115 Capabilities string
M117 display message
M119 Output Endstop status to serial port

M126 Solenoid Air Valve Open (BariCUDA support by jmil)
M127 Solenoid Air Valve Closed (BariCUDA vent to atmospheric pressure by jmil)
M128 EtoP Open (BariCUDA EtoP = electricity to air pressure transducer by jmil)
M129 EtoP Closed (BariCUDA EtoP = electricity to air pressure transducer by jmil)
M140 Set bed target temp
M150 Set BlinkM Color Output R: Red<0-255> U(!): Green<0-255> B: Blue<0-255> over i2c, G for green does not work.
M190 S## Wait for bed current temp to reach target temp. Waits only when heating R## Wait for bed current temp to reach target temp. Waits when heating and cooling
M200 D<millimeters> set filament diameter and set E axis units to cubic millimeters (use S0 to set back to millimeters).
M201 Set max acceleration in units/s^2 for print moves (M201 X1000 Y1000)
M202 Set max acceleration in units/s^2 for travel moves (M202 X1000 Y1000) Unused in Marlin!!
M203 Set maximum feedrate that your machine can sustain (M203 X200 Y200 Z300 E10000) in mm/sec
M204 Set default acceleration: S normal moves T filament only moves (M204 S3000 T7000) in mm/sec^2 also sets minimum segment time in ms (B20000) to prevent buffer under-runs and M20 minimum feedrate
M205 advanced settings: minimum travel speed S=while printing T=travel only, B=minimum segment time X= maximum xy jerk, Z=maximum Z jerk, E=maximum E jerk
M206 set additional homing offset
M207 set retract length S[positive mm] F[feedrate mm/min] Z[additional zlift/hop], stays in mm regardless of M200 setting
M208 set recover=unretract length S[positive mm surplus to the M207 S*] F[feedrate mm/sec]
M209 S<1=true/0=false> enable automatic retract detect if the slicer did not support G10/11: every normal extrude-only move will be classified as retract depending on the direction.
M218 set hotend offset (in mm): T<extruder_number> X<offset_on_X> Y<offset_on_Y>
M220 S<factor in percent> set speed factor override percentage
M221 S<factor in percent> set extrude factor override percentage
M226 P<pin number> S<pin state> Wait until the specified pin reaches the state required
M240 Trigger a camera to take a photograph
M250 Set LCD contrast C<contrast value> (value 0..63)
M280 set servo position absolute. P: servo index, S: angle or microseconds
M300 Play beep sound S<frequency Hz> P<duration ms>
M301 Set PID parameters P I and D
M302 Allow cold extrudes, or set the minimum extrude S<temperature>.

M303 PID relay autotune S<temperature> sets the target temperature. (default target temperature = 150C)
M304 Set bed PID parameters P I and D
M400 Finish all moves
M401 Lower z-probe if present
M402 Raise z-probe if present
M404 N<dia in mm> Enter the nominal filament width (3mm, 1.75mm) or will display nominal filament width without parameters
M405 Turn on Filament Sensor extrusion control. Optional D<delay in cm> to set delay in centimeters between sensor and extruder
M406 Turn off Filament Sensor extrusion control
M407 Displays measured filament diameter
M500 stores parameters in EEPROM
M501 reads parameters from EEPROM (if you need reset them after you changed them temporarily).
M502 reverts to the default "factory settings". You still need to store them in EEPROM afterwards if you want to.
M503 print the current settings (from memory not from EEPROM)
M540 Use S[0|1] to enable or disable the stop SD card print on endstop hit (requires ABORT_ON_ENDSTOP_HIT_FEATURE_ENABLED)
M600 Pause for filament change X[pos] Y[pos] Z[relative lift] E[initial retract] L[later retract distance for removal]
M665 set delta configurations
M666 set delta endstop adjustment
M605 Set dual x
M700 Turn off print pressure to syringe 0 RMH 10/31/14
M701 Turn on print pressure to syringe 0 RMH 10/31/14
M702 Turn off purge pressure to syringe 0 RMH 10/31/14
M703 Turn on purge pressure to syringe 0 RMH 10/31/14
M750 Turn off vaccuum pump RMH 10/31/14
M751 Turn on vaccuum pump RMH 10/31/14
M907 Set digital trimpot motor current using axis codes.
M908 Control digital trimpot directly.
M350 Set microstepping mode.
M351 Toggle MS1 MS2 pins directly.

Appendix 2

Appendix Table 1.Theoretical Sintering Model of spherical HDPE powders, used to estimate sintering parameters of StarPore®.

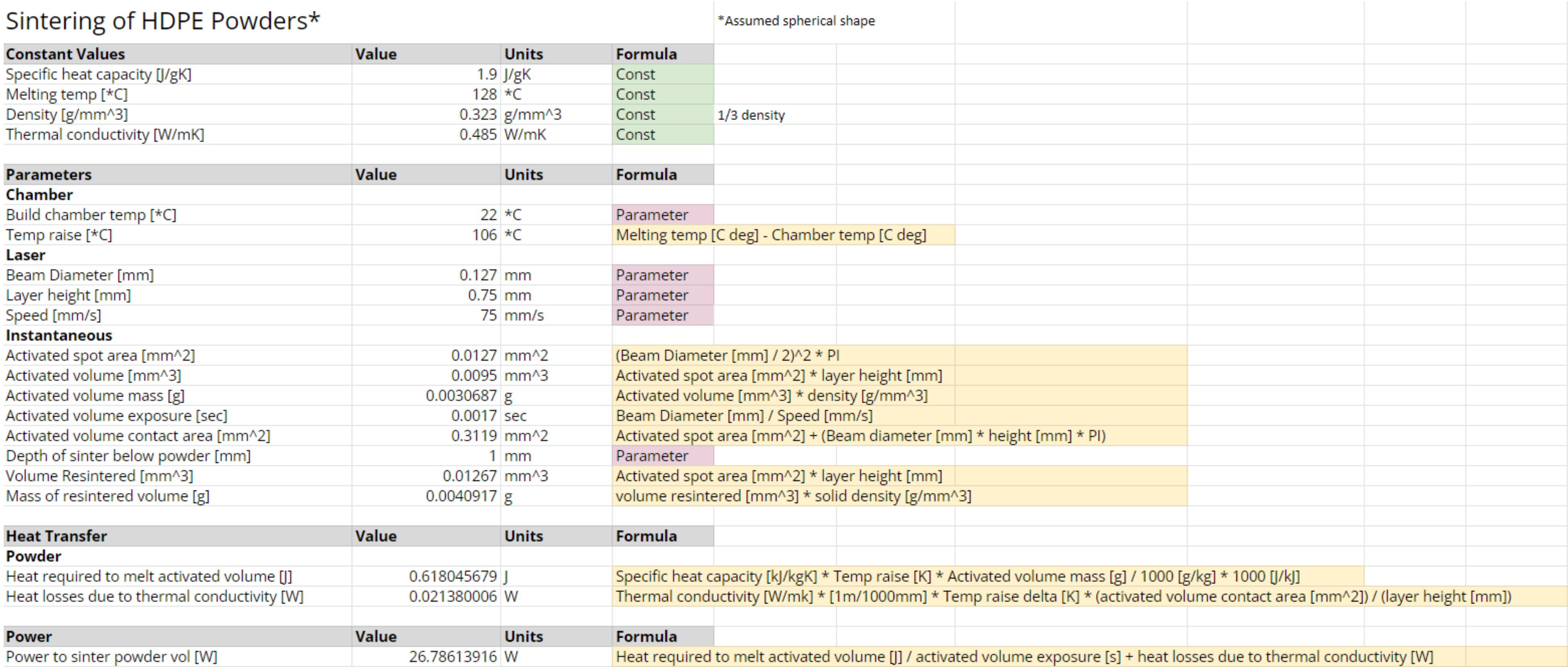

Sintering of HDPE Powders*

*Assumed spherical shape

Constant Values	**Value**	**Units**	**Formula**	
Specific heat capacity [J/gK]	1.9	J/gK	Const	
Melting temp [*C]	128	*C	Const	
Density [g/mm^3]	0.323	g/mm^3	Const	1/3 density
Thermal conductivity [W/mK]	0.485	W/mK	Const	
Parameters	**Value**	**Units**	**Formula**	
Chamber				
Build chamber temp [*C]	22	*C	Parameter	
Temp raise [*C]	106	*C	Melting temp [C deg] - Chamber temp [C deg]	
Laser				
Beam Diameter [mm]	0.127	mm	Parameter	
Layer height [mm]	0.75	mm	Parameter	
Speed [mm/s]	75	mm/s	Parameter	
Instantaneous				
Activated spot area [mm^2]	0.0127	mm^2	(Beam Diameter [mm] / 2)^2 * PI	
Activated volume [mm^3]	0.0095	mm^3	Activated spot area [mm^2] * layer height [mm]	
Activated volume mass [g]	0.0030687	g	Activated volume [mm^3] * density [g/mm^3]	
Activated volume exposure [sec]	0.0017	sec	Beam Diameter [mm] / Speed [mm/s]	
Activated volume contact area [mm^2]	0.3119	mm^2	Activated spot area [mm^2] + (Beam diameter [mm] * height [mm] * PI)	
Depth of sinter below powder [mm]	1	mm	Parameter	
Volume Resintered [mm^3]	0.01267	mm^3	Activated spot area [mm^2] * layer height [mm]	
Mass of resintered volume [g]	0.0040917	g	volume resintered [mm^3] * solid density [g/mm^3]	
Heat Transfer	**Value**	**Units**	**Formula**	
Powder				
Heat required to melt activated volume [J]	0.618045679	J	Specific heat capacity [kJ/kgK] * Temp raise [K] * Activated volume mass [g] / 1000 [g/kg] * 1000 [J/kJ]	
Heat losses due to thermal conductivity [W]	0.021380006	W	Thermal conductivity [W/mk] * [1m/1000mm] * Temp raise delta [K] * (activated volume contact area [mm^2]) / (layer height [mm])	
Power	**Value**	**Units**	**Formula**	
Power to sinter powder vol [W]	26.78613916	W	Heat required to melt activated volume [J] / activated volume exposure [s] + heat losses due to thermal conductivity [W]	

Appendix 3

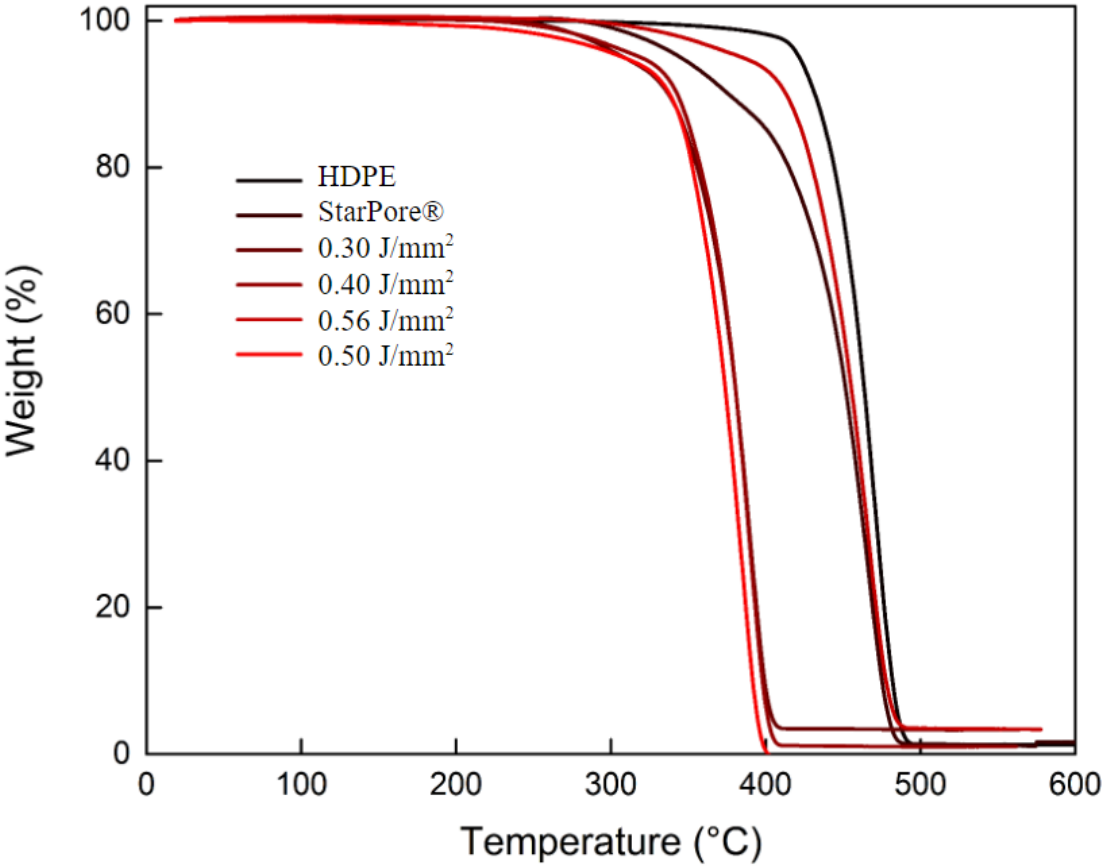

Appendix Figure 1. Thermogravimetric analysis comparing HDPE in a pellet form against, StarPore® and sintered StarPore® at energy densities ranging from 0.30 J/mm^2 to 0.50 J/mm^2

Appendix 4

Threshold adjustments used to estimate different tissues from the MT IHC sections (A Fig. 2).

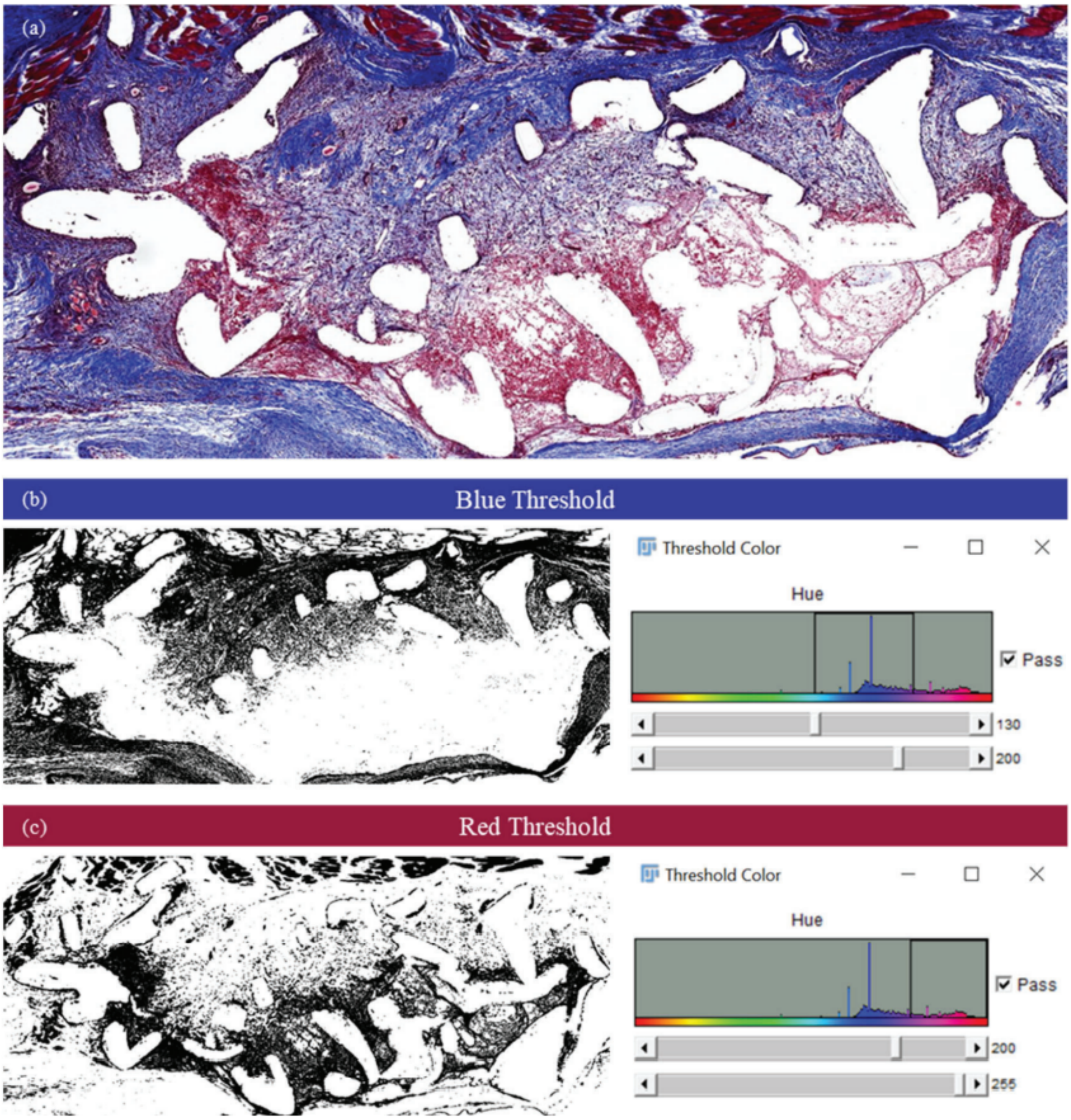

Appendix Figure 2. Representative images of the MT-stained tissue surrounding the HDPE implant within the region of interest (a), where (b) is the blue threshold and (c) is the red threshold.